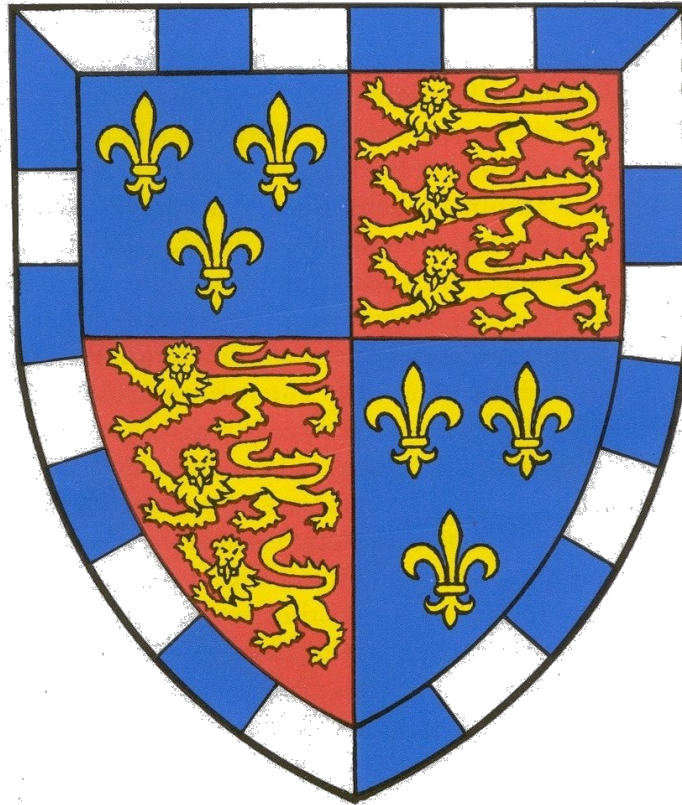# Coordination Cages:
Beyond The Solution State

Hugh Patrick Ryan

Christ's College

June 2021

This thesis is submitted for the degree of Doctor of Philosophy

Declaration

I hereby declare that this dissertation, entitled "*Coordination Cages: Beyond The Solution State*", is the result of work which I have undertaken at the Department of Chemistry, University of Cambridge between October 2017 and June 2021. Except where stated to the contrary, the work presented herein was conducted by me, Hugh Patrick Ryan; those results which have been obtained by other parties have been accredited to the named authors within the text. Figures which have been reproduced or adapted from other sources are indicated in their figure captions. Some aspects of the work presented herein have been published in peer-reviewed journals and the original publications have been cited in the main text; a list of publications is also included. This dissertation has not been, nor is currently being, submitted for any other degree, diploma, or academic qualification at this or any other university. It does not exceed 60,000 words in length.

Hugh Patrick Ryan, June 2021

Summary

Name: Hugh Patrick Ryan

Title: Coordination Cages: Beyond The Solution State

Metal-organic coordination cages can be assembled from simple building blocks to form a wide range of structure types such as Platonic and Archimedean solids. Such architectures are able to encapsulate a diverse array of molecular guests in the solution state, from both organic and aqueous media. This thesis investigates the application of metal-organic coordination cages in the solid-supported physisorbed and neat liquid states and the host-guest chemistry of the resulting materials. This thesis is divided into three main sections are these are outlined below:

Chapter 1 presents a brief introduction to the history and development of supramolecular chemistry and metal-organic architectures. A particular emphasis is placed on the formation of coordination cages and the factors unpinning their guest encapsulation properties.

Chapter 3, the first research chapter, investigates the adsorption of coordination cages on to alumina supports, *via* solution depletion, from water and acetonitrile. The adsorbed cages are analysed spectroscopically and their host-guest chemistry is probed *via* a series of guest displacement experiments under flow conditions. Finally, it is demonstrated that adsorbed cages can be used to store reactive molecular guests for subsequent release and reaction.

Chapter 4, the second research chapter, presents the current progress towards the development of a new generation of porous liquids based on coordination cage scaffolds peripherally-functionalised with polymer chains. The first section explores the use of a coordination cage ion metathesis reaction in the formation of a cage salt. The second section investigates the effect of the peripheral chain length on the thermal properties of the resulting cage materials.

List of Publications

1. Ryan H., Haynes C., Smith A., Grommet A., Nitschke J., "*Guest Encapsulation with Surface-Adsorbed Self-Assembled Cages*", *Advanced Materials*, **2021**, 2004192, 33(1).

2. Jie K., Zhou Y., Ryan H., Dai S., Nitschke J., "*Engineering Permanent Porosity into Liquids*", *Advanced Materials*, **2021**, 2005745, 33(18).

3. Nguyen B., Thoburn J., Grommet A., Howe D., Ronson T., Ryan H., Bolliger J., Nitschke J., "*Coordination Cages Selectively Transport Molecular Cargoes Across Liquid Membranes*", *Journal of the American Chemical Society,* **2021**, 143(31), 12175 – 12180.

Acknowledgements

In a meeting of early 2018, Jonathan Nitschke asked me very seriously if I was confident in continuing with my project on the adsorption of coordination cages. There was no accusation in this question only concern for the productivity of my time in the laboratory. In response, I recall mumbling that I would keep going with it even though internally I was far from sure if I could see it through to fruition. That was the push I needed. Thank you, Jonathan, for giving me the freedom to explore what I found interesting whilst always prompting me to explain why I thought each experiment was worthwhile. As someone who strongly dislikes being micromanaged, I could not have asked for more input in my own PhD experience.

This next section is for the many, many wonderful people of Lab 353/354, the Department of Chemistry, and those further afield who have helped in my research. When I started my PhD back in October 2017 I was highly unsure of my own laboratory skills; my now co-authors Dr Angela Grommet and Dr Cally Haynes took me into their charge and never failed to make time for me. I cannot thank you enough for your support. I would also have floundered without Dr Tanya Ronson, even up to the completion of this thesis, and I shall miss her gentle New Zealand accent proclaiming tea-time at 11:00 each day. I would also like to thank my academic collaborators - Alyssa Smith, Dr Tom Bennett, Georgie Robertson, and Dr Angela Stelson - as well as those poor unfortunate souls who have suffered under my supervision - Dani Besenyöi, Matt Price, and Jiantao Zhou. Finally, a big thank you to the NMR service, Duncan Howe and Andrew Mason, without whom I would have broken Auchentoshan (née Lady Florence) many times over.

In the great tradition of acknowledgments sections, my next thanks go to Fiammetta Doria and Camilla Ryan, my mother and sister. Whilst being the third child in my family to undertake a PhD clearly means that I lack originality, my mother has been a source of constant support and food in equal measure. Furthermore, I could not have wanted for a better lockdown companion; as we have said amongst ourselves on numerous occasions, I don't think that I've ever felt more fortunate and privileged than when I was able to spend the early throes of the pandemic in such good company. When I started my PhD, Camilla counselled me that "a PhD is a marathon not a sprint" – wise words indeed, even if this 25th mile has felt a bit more like the latter! Hopefully the final 26th will be less furious! Camilla, you've been a constant in my life for 26 years (shockingly) and I would not have it any other

way. I'm so proud of all that we've both achieved and hopefully now we will both be able to enjoy life after studenthood.

When Angela and Cally left the group it fell to Dr Lillian Ma to soak up all of my crazy; Lillian, you are the best. You might be many thousands of miles away now but, wherever I am, you'll always be welcome. Lillian left and then it came to Dr Larissa Von Krbek to take care of this hot mess. Larissa, you were a star even if you freely admit that sometimes you had no idea what I was saying. Big shouts also go to the grumpy old men, Dr Jake Greenfield and Dr John Carpenter, and to Dr Marion Kieffer even though we're still clearing up your pararosaniline mess - for those of you who don't know, pararosaniline is BRIGHT PINK.

Whilst the high quality of this thesis will suggest that I spent every waking minute in the laboratory, I have spent a not inconsiderable proportion of my time at university dancing with the Cambridge University DanceSport Team (CUDT). If you had told me before I arrived in Cambridge that I would spend most of my "free" time and "disposable income" on competitive dance then I would probably have corpsed with laughter. I'm not laughing now. CUDT has given me the most wonderful extra-curricular life and I am incredibly thankful to David Mallabone, Paul Walker, Crystal Main, and Jemma Girling for their coaching and support over the past 7 years. It's been a privilege. Ballroom and Latin dance styles are partnered, however, so it would be remiss of me not to mention the wonderful women, and one man, who have been attached to my right hip; in no particular order, thank you Maddi Morelli-Batters, Jasmin Silver, Tessa Teo, Liam Pattullo, and Anna Lippert. Please also bear in mind that I possess video footage of all of you dancing with me and thus remember me in your future successes for fear of public shaming.

This last section is for Annie, Klara, Andreas, and Tomáš, my household crew of 2020-2021. The pandemic forced us to spend our evenings and weekends together and it turns out that you're not a bad bunch.

Abbreviations and Symbols

c – concentration

CD_3CN – deuterated acetonitrile

CH_3CN/MeCN – acetonitrile

DCM – DiChloroMethane

DMF – DiMethylFormamide

DOSY – Diffusion-Ordered SpectroscopY

DSC – Differential Scanning Calorimetry

D_2O – deuterated water

EDX – Energy-Dispersive X-ray spectroscopy

EtOH - ethanol

G' – storage modulus

G" – loss modulus

H_2O – water

ITC – Isothermal Titration Calorimetry

k – rate constant

k_B – Boltzmann constant

K_L – adsorbate-adsorbate binding constant

K_S – surface-adsorbate binding constant

M – molar ($mol\ dm^{-3}$)

MS – Mass Spectrometry

NMR – Nuclear Magnetic Resonance (spectroscopy)

NTf_2^- – triflimide/bis(trifluoromethanesulfonyl)imide anion

PALS – Positron Annihilation Lifetime Spectroscopy

SO_4^{2-} – sulphate anion

t – time

T – Temperature

T_g – glass transition Temperature

TGA – ThermoGravimetric Analysis

TMA^+ – TetraMethylAmmonium cation

UV-Vis – UltraViolet-Visible

wt% – weight percentage

XPS – X-ray Photoelectron Spectroscopy

δ – chemical shift (ppm)

ΔG – Gibbs free energy change

$\Delta G^{\neq}$ – activation Barrier

$\Delta\Delta G$ – a difference in Gibbs free energy changes

ΔH – Enthalpy Change

$\Delta\Delta H$ – a difference in enthalpy changes

θ – total surface coverage

θ_{MONO} – monolayer surface coverage

θ_{MAX} – maximum surface coverage

$\subset$ – (denotes guest binding)

Table of Contents

Chapter 1: Introduction

This section introduces the field of supramolecular chemistry with a particular focus on the history of the field and on metal-organic structures. Some of the most prevalent approaches to the synthesis of metal-organic structures are illustrated with a series of examples. Emphasis is placed on the synthesis of metal-organic coordination cages, their host-guest chemistry, and their applications. Finally, the research aims of this thesis are outlined.

1.1 Introduction to Supramolecular Chemistry

Supramolecular chemistry is the study of systems interacting *via* non-covalent forces and thus has come to be known, somewhat ubiquitously, as chemistry "beyond the molecule".[1] Intermolecular forces (*ca.* 2 - 40 kJ mol^{-1}), such as hydrogen bonding, π-π interactions,[2] and Van der Waals forces, are typically significantly weaker that the covalent bonds formed in traditional organic synthesis (*ca.* 240 – 480 kJ mol^{-1}).[3] These interactions form the basic arsenal of supramolecular synthesis and their inherent lability engenders reversibility within the systems formed. The resulting supramolecular systems are therefore often dynamic and able to explore their energy landscapes (energy barriers, $\Delta G^{\neq}$ < thermal energy, $k_B T$) thereby existing under thermodynamic control and can also respond to external stimuli such as heat and light.[4,5] Thermodynamic control is not universal, however, and there are numerous examples of systems existing under kinetic control, in which the systems may either be kinetically trapped ($\Delta G^{\neq} \gg k_B T$) or evolve *via* a series of metastable states ($\Delta G^{\neq} \sim k_B T$).[6–8]

The foundations of synthetic supramolecular chemistry were established in the 1960s by researchers such as Pedersen, Lehn, and Cram. In 1967, Pedersen reported the synthesis of cyclic polyethers, termed "crown" ethers, which bound cations such as Li$^+$ and NH$_4^+$ within the centre of the crown ether ring due to the favourable interaction of the cationic charge of the guest with the partial negative charges of the oxygen atoms in the host (Figure 1.1a).[9] Shortly after, in 1969, Lehn reported the formation of "cryptand" molecules which defined regions of closed, electron-rich space in which inorganic cations could also be bound (Figure 1.1b).[10] Following on from the work of Pedersen and Lehn, Cram then extended the concept of molecular hosts to the design and synthesis of rigid, pre-organised analogues of crown ethers, which he termed "spherands" (Figure 1.1c).[11] It was for these advances in molecular vessels that Pedersen, Lehn, and Cram were awarded the 1987 Nobel Prize in Chemistry thereby paving the way for the development of modern supramolecular chemistry. The Nobel Prize in

Chemistry was awarded in supramolecular chemistry again in 2016 to Sauvage, Stoddart, and Feringa for their work on metallo-catenanes,[12] rotaxanes ("molecular shuttles"),[13] and molecular motors,[14] respectively. Today the library of supramolecular systems continues to diversify within ongoing research into architectures such as molecular motors,[15] supramolecular polymers,[16] supramolecular gels,[17] and coordination cages.[18]
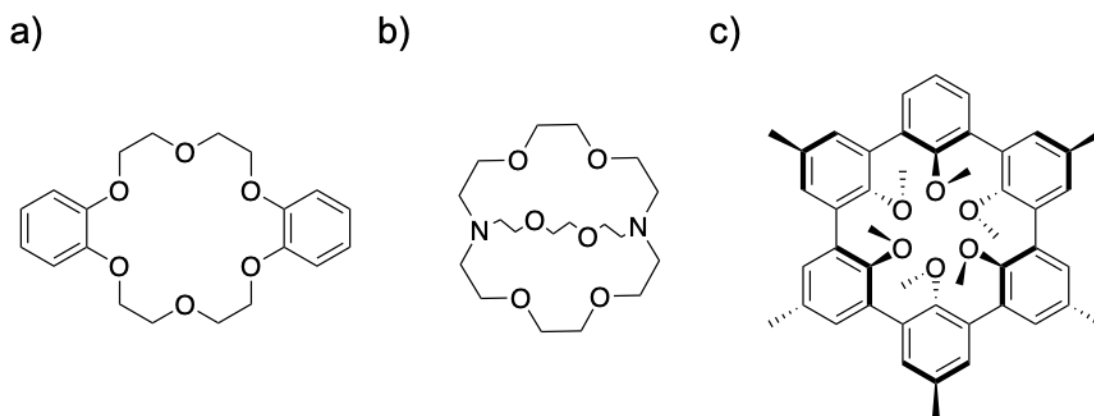
Figure 1.1: a) Cyclic polyether dibenzo-18-crown-6 reported by Pedersen, b) Cryptand molecule [2.2.2]-cryptand reported by Lehn, c) Spherand molecule reported by Cram.[9–11]

1.2 Formation of Metal-Organic Structures

The introduction of metal-ligand bonds into supramolecular systems has resulted in the formation of a wide range of architectures.[3] Whilst they are typically much stronger (*ca.* 60 – 200 kJ mol^{-1}) than other intermolecular forces, metal-ligand bonds remain sufficiently labile to support the "error-checking" observed in self-assembling systems. In particular, great success has been achieved *via* the use of the well-defined coordination geometries of transition metals with organic donor species. A number of approaches have been developed for the assembly of metal-organic architectures and the most prevalent of these are outlined below.

The *symmetry interaction* approach considers the point symmetry of the desired architecture and its individual components. The canonical example of the symmetry interaction approach is that of the M_2L_3 triple helicate; in order to form a helicate with D_3 symmetry, the C_3 and C_2 axes of the metal centres and bis(bidentate) ligands, respectively, must be orthogonal and thus the chelate-plane of each metal centre – defined as the plane orthogonal to the major

symmetry axis of the metal complex – lies parallel to the C_2 axes of the ligands (Figure 1.2a).[3,19] For example, Raymond *et al.* reported the formation of triple helicate **1.1** from bis-catechol ligands and gallium (Figure 1.2b). In contrast, the formation of an M_4L_6 tetrahedron, in which the ligands span the edges of the tetrahedron, requires an idealised angle of 70.6° between the coordinate vectors of the ligands, such as in Raymond's bis-catechol-based tetrahedron **1.2** (Figure 1.2d); the coordinate vector is defined as the vector which describes the interaction between the metal and the ligand (Figure 1.2c).
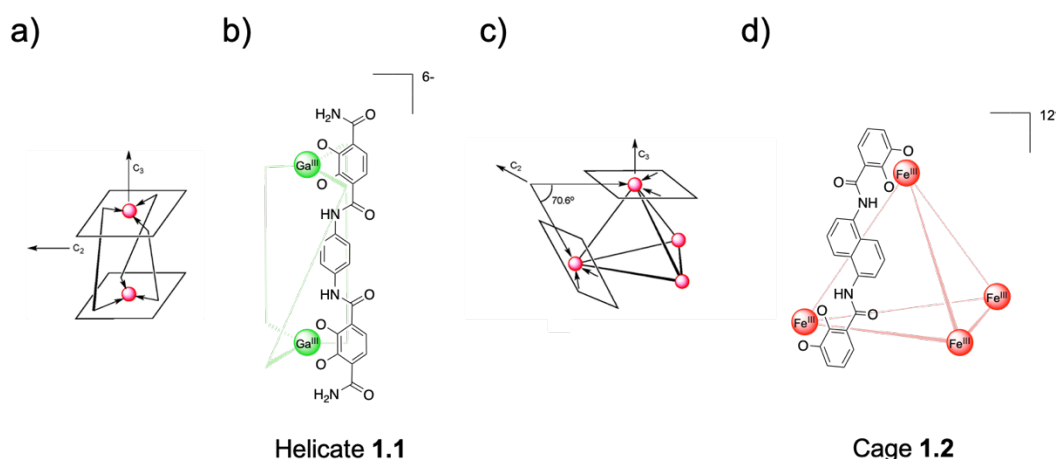
Figure 1.2: a) Symmetry interaction approach to forming helicates, b) Raymond's bis-catechol triple helicate (negative charges on oxygen atoms are excluded for clarity), c) Symmetry interaction approach to forming tetrahedra, d) Raymond's bis-catechol tetrahedron (negative charges on oxygen atoms are excluded for clarity).[3,19] Figures 1.2a and 1.2c reproduced with permission from reference 3.

The *directional bonding* approach is focussed on achieving the geometry of the desired architecture *via* the bite angles and stoichiometries of the system components.[3] Within this approach, the combination of three ditopic ligands with a bite angle of 60° with three linear ditopic ligands (with suitable donor-acceptor interactions) would be expected to result in the formation of a supramolecular triangle (Figure 1.3a); in contrast, the inclusion of polytopic ligands would be expected to result in the formation of three-dimensional architectures (Figure 1.3b). For example, Schalley *et al.* reported a study of the effect of temperature, concentration, and solvent polarity on systems formed from linear bis-pyridyl ligands and cis-protected metal centres (Figure 1.4).[3,20] Cis-protected metal centres are metal centres in which the entropic favourability of the cis-coordination of bidentate ligands to a metal, *i.e.* the chelate effect, results in persistence of this interaction in the presence of additional coordinating species, such

as the metal centres in triangle **1.3** and square **1.4**. In Schalley's systems, the directional bonding approach predicted the formation of supramolecular squares; in reality, a mixture of triangles (**1.3**) and squares (**1.4**) was formed. Schalley observed that, whilst squares were favoured enthalpically due to reduced strain in the ligands, the predominance of triangles in these systems was due to the increased entropy of four triangles relative to three squares. The directional bonding approach is thus subject to caveats such as ligand flexibility.
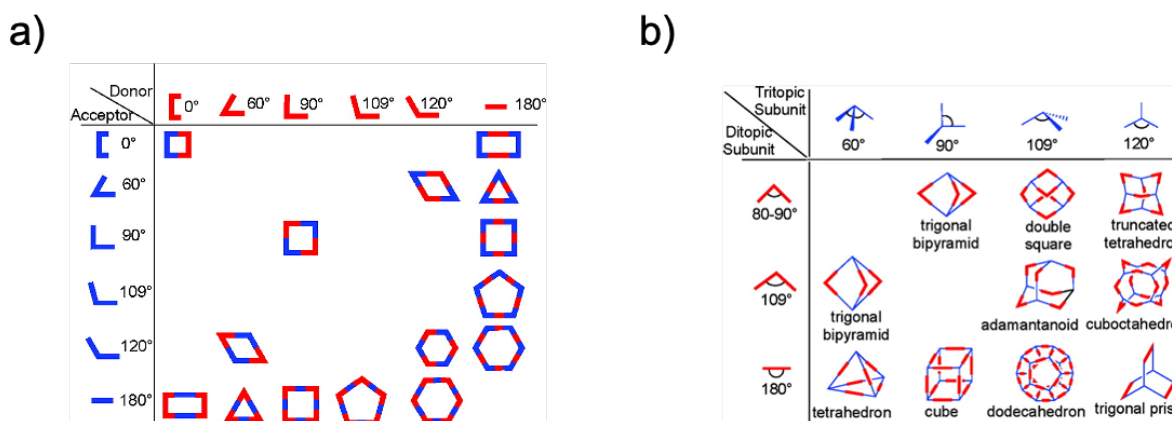
Figure 1.3: a) 2D directional bonding approach to forming supramolecular architectures, b) 3D directional bonding approach to forming supramolecular architectures.[3] Figure reproduced with permission from reference 3.
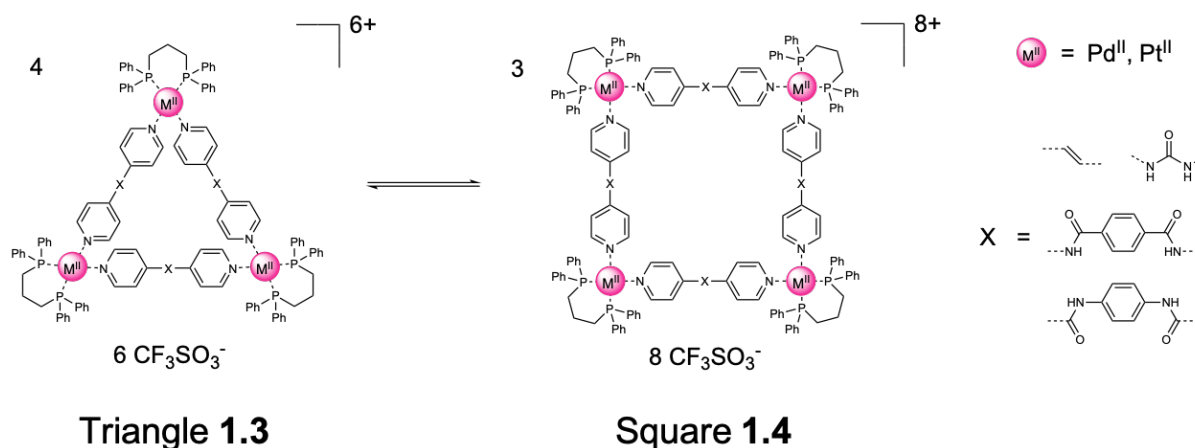

Figure 1.4: Schalley's supramolecular triangle/square system within the directional bonding approach. Whilst squares are favoured enthalpically on grounds of ligand flexibility, triangles are favoured entropically.[20]

The final methodology considered herein is the *panelling* approach. This approach utilises molecular components which constitute the faces of a desired structure. For example, a tetrahedron can be formed from four triangular faces, whereas a cube requires six square faces.[3] These molecular faces are then "stitched" together *via* the use of suitable vertex components. An example of the panelling approach is presented in the following section.

1.3 Coordination Cages

The approaches to the formation of metal-organic structures described in the previous section have been employed to great effect in the design and synthesis of three-dimensional metal-organic ensembles termed "coordination cages". These coordination cages define an enclosed region of space which can be used to bind guest species such as neutral compounds and ions.

One of the earliest examples of a coordination cage was reported by Fujita *et al.* in 1995. In this system, 4 equivalents of a tridentate pyridine-based ligand were combined with 6 equivalents of cis-protected palladium (II) in water resulting in the quantitative formation of octahedral cage **1.5** (Figure 1.5a).[3,21] Cage **1.5** was observed to bind 4 molecules of adamantyl carboxylate in its cavity; the addition of adamantyl carboxylate to **1.5** in water resulted in the appearance of a set of guest peaks in the ^{1}H NMR spectrum, upfield-shifted by approximately 8 ppm. This observation was confirmed by X-ray crystallography. Cage **1.5** exemplifies the panelling approach to metal-organic structures in which the 4 tridentate ligands span 4 of the 8 faces of an octahedron (*vide supra*). The geometry of **1.5** is also consistent with the assembly expected from components possessing bite angles of 120° and 90°, for the tridentate ligand and cis-protected Pd^{II} centres respectively, in the directional bonding approach.
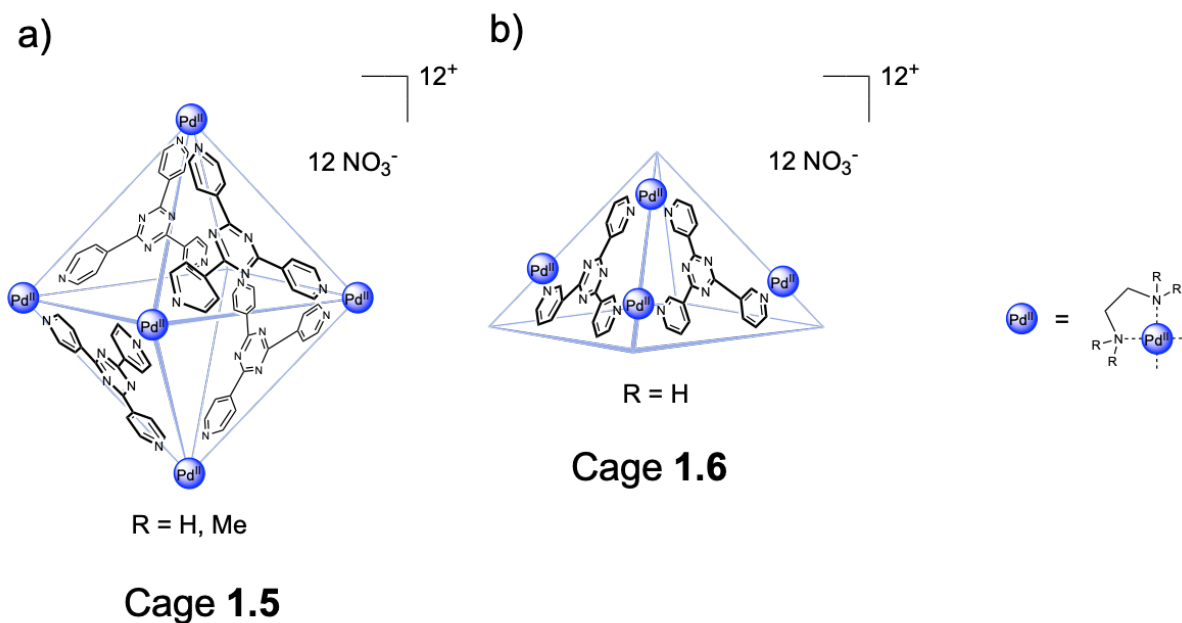
Figure 1.5: a) Fujita's octahedral cage, demonstrating the panelling approach, b) Fujita's square-pyramidal bowl.[21–23]

The work of Nitschke *et al.* utilises metal-ligand coordination bonds in conjunction with dynamic covalent bonds; dynamic covalent bonds are bonds which form under thermodynamic control and thus they are well-suited to the "error-checking" commonly involved in supramolecular systems.[24] Many of the cages formed in Nitschke's group utilise ligands with a bidentate pyridyl-imine motif in which the imine bond (and thus the ligand) forms *in situ* from the condensation of an aniline and an aldehyde. This bidentate motif then coordinates to metal centres to form the overall cage architecture. This approach to the formation of metal-organic coordination cages is known as *subcomponent self-assembly*. For example, Nitschke recently reported the assembly of tetrahedral cage **1.7** in which the edges of the tetrahedron were formed from bis-bidentate ligands bearing antiaromatic panels based on nickelated-norcorrole (Figure 1.6).[25] Nitschke demonstrated that the magnetic properties of the antiaromatic panels reinforced each other, resulting in a highly antiaromatic environment which shifted the ^{1}H NMR signals of encapsulated guests by up to 15 ppm.

Cage **1.7**

Figure 1.6: Nitschke's anti-aromatic tetrahedral coordination cage, formed *via* subcomponent self-assembly from nickelated-norcorrole ligands.[25] Figure adapted with permission from reference 25.

1.4 Host-Guest Chemistry

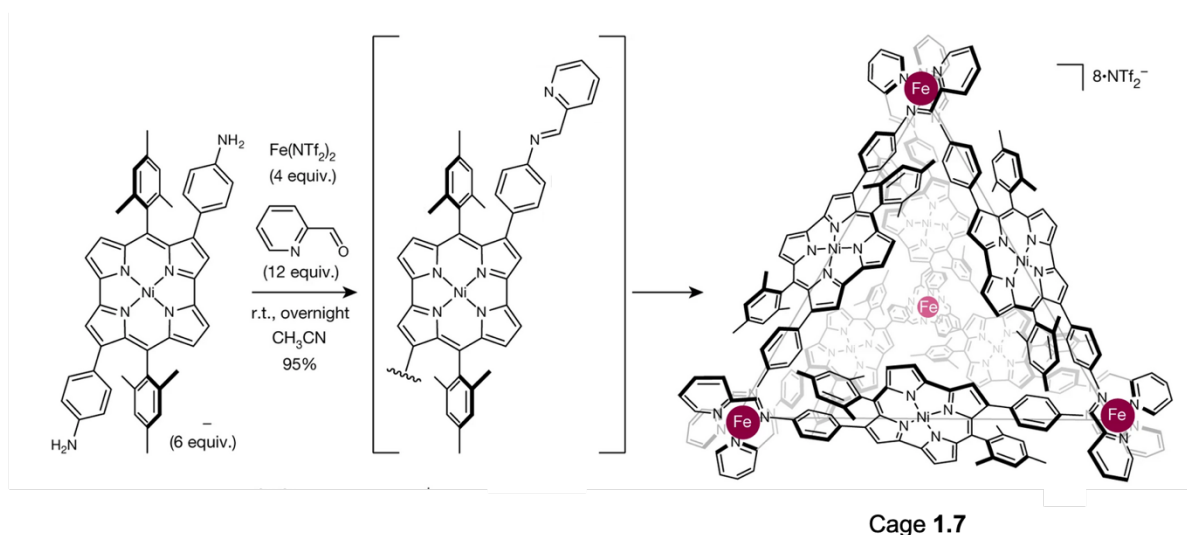The volume of space enclosed by metal-organic coordination cages is often able to host molecular guests. The affinity of a supramolecular host for a given guest species can be influenced by a number of factors, some of which are outlined below.

In 1998, Julius Rebek reported an investigation of the binding constants of a number of aliphatic guests within a supramolecular dimer in organic media.[26] Rebek observed that the guests which bound most strongly within the dimer occupied (55 ± 9) % of the volume of the dimer's cavity; this is now known commonly as the "55% Rule". A similar phenomenon was also observed in a study by Hunter and Ward *et al.,* in which the binding constants were obtained for a series of cyclic ketones inside the M_8L_{12} cube **1.8** (Figure 1.7a, 7b).[27–29] Hunter and Ward found that cycloundecanone, occupying *ca*. 50% of the cavity of **1.8**, bound more strongly than the other cyclic ketones investigated, in alignment with Rebek's rule. The crystal structure of cycloundecanone⊂**1.8** revealed that the carbonyl group of the guest was oriented towards one of the vertices of the cube in order to form a favourable electrostatic interaction and the alkyl backbone of the guest made contacts with the interior cage surface. Hunter and Ward observed that, from cyclopentanone to cycloundecanone, each additional methylene group in the alkyl backbone contributed *ca*. 5 kJ mol^{-1} to the free energy of encapsulation due to the increase in hydrophobic surface area of the guest (Figure 1.7c), whereas guests larger

than cycloundecanone, up to cyclotetradecanone, bound less strongly on steric grounds. The size match of a guest for a given cage cavity can thus act a first step in understanding guest binding.
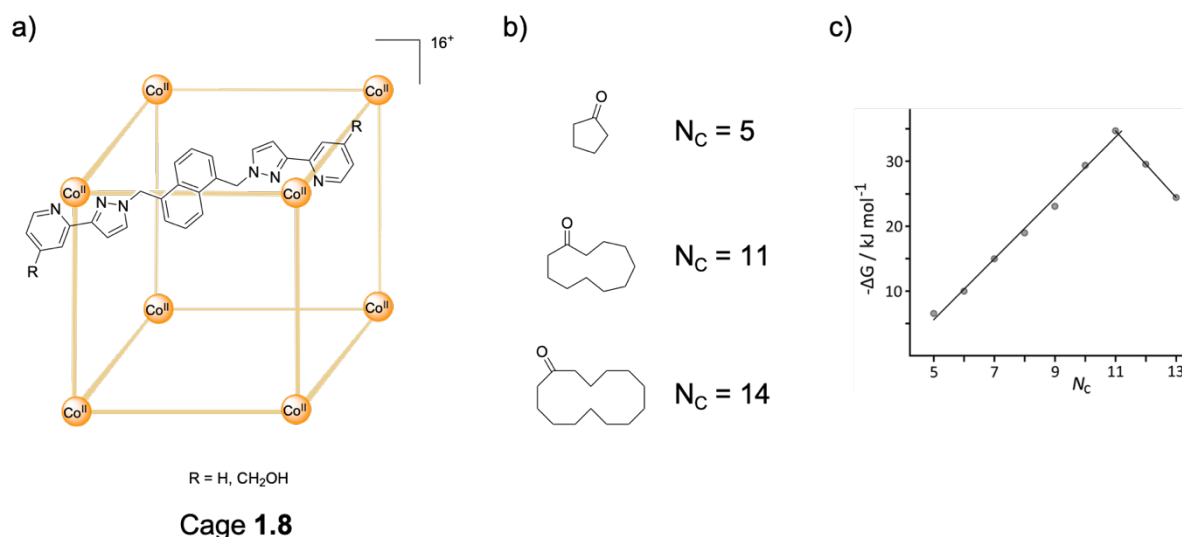

Figure 1.7: a) Ward's cubic cage, b) Representative sample of the cyclic ketones studied - cyclopentanone (N_c = 5), cycloundecanone (N_c = 11), and cyclotetradecanone (N_c = 14), c) Plot of free energy of complexation (ΔG) against number of carbon atoms in the cyclic ketone backbone (N_C).[27–29] Figure 1.7c reproduced with permission from reference 27.

The strength of a given host-guest interaction is strongly influenced by the *hydrophobic effect*. In its broadest sense, the hydrophobic effect is the observed tendency of apolar molecules to aggregate when in aqueous media.[30] Whilst a full exploration of the hydrophobic effect is beyond the scope of this introduction, it is nevertheless important to note that the hydrophobic effect does not originate simply from unfavourable interactions between water and apolar solutes but rather from a balance of enthalpic and entropic contributions. At a rudimentary level, the combination of an empty host and a free guest to form a single host-guest complex is entropically disfavoured due to the loss of degrees of freedom (*e.g.* translational, vibrational, and rotational). Whilst it would be logical to assume that an enthalpic gain must compensate for this entropic penalty, the role of the solvent must be considered. A study by Raymond *et al.* investigated the interplay of the enthalpic and entropic contributions in guest-binding within the M_4L_6 tetrahedron **1.2** (*vide supra*).[31] Raymond concluded that, in polar, protic solvents, such as water and methanol, solvent rearrangement is the driving force for supramolecular encapsulation processes. In order for a guest to enter the capsule's cavity, both the guest and

the interior of the capsule must be de-solvated. This desolvation process represents an enthalpic penalty – recalling that the hydrophobic effect is not due to unfavourable solvent-solute interactions – but an entropic gain due to the liberation of solvent molecules.[31,32] The liberated solvent molecules then form hydrogen bonds with the bulk solvent thereby forming enthalpically favourable but entropically unfavourable interactions, and thus there is a compensation between enthalpy and entropy. The encapsulation of large guest species results in a large void in the bulk solvent and the formation of many new hydrogen bonds, hence enthalpic gain compensates for entropic loss; conversely, smaller, well-solvated guests leave behind smaller voids and the entropic gain from solvent liberation compensates for the enthalpic penalty of desolvation. Ward *et al.* have also reported a study in which the encapsulation of a series of cyclic ketones was driven by the release of "high-energy" water molecules from cubic cage **1.8** (Figure 1.7a).[33] In the absence of additional guest species, the crystal structure of cubic cage **1.8** indicated that the cage cavity was occupied by 10 water molecules; these 10 molecules formed an average of 0.5 fewer hydrogen bonds per molecule than in the bulk solution. Upon the introduction of a molecular guest, these "high-energy" water molecules were released into the bulk and formed additional hydrogen bonds, thereby contributing an enthalpic gain. This hypothesis was supported by a Van't Hoff analysis of the binding constants for the cyclic ketones, which demonstrated that the difference in the free energies of encapsulation, $\Delta\Delta G$, was due primarily to the differences in the enthalpies of encapsulation, $\Delta\Delta H$. The hydrophobic effect and the behaviour of solvent molecules thus play a critical role in understanding the strength of host-guest chemistry in coordination cages.

In addition to the discussions of sterics and the hydrophobic effect above, Nitschke *et al.* have reported a study of the factors affecting guest binding within aromatic-walled M_4L_6 coordination cages.[34] Nitschke observed that large, offset diamine ligands assembled into cages with a greater degree of surface enclosure than those formed from smaller, linear ligands and thus the former showed a greater propensity for guest binding due to improved host-guest interactions (Figure 1.8). Additionally, Fujita *et al.* have recently reported the encapsulation of cationic species within the formally cationic cage **1.5** following "capping" with tripodal anions (Figure 1.9).[35] This study neatly demonstrated the power of electrostatics in supramolecular host-guest chemistry, in this case both between the charged metal centres and the tripodal anions and also between the cationic guests and the tripodal anions.
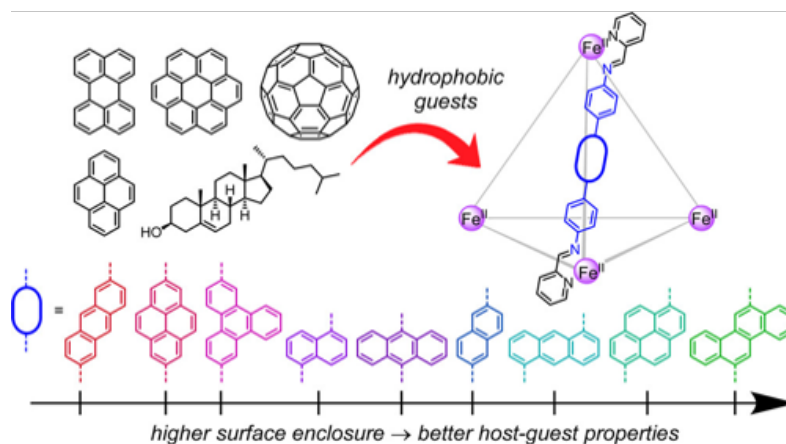
Figure 1.8: The conclusions from Nitschke's study on the effect of surface enclosure on guest binding properties; aromatic panels which enclosed a region of hydrophobic space more fully exhibited greater host-guest properties when assembled into coordination cages.[34] Figure reproduced with permission from reference 34.
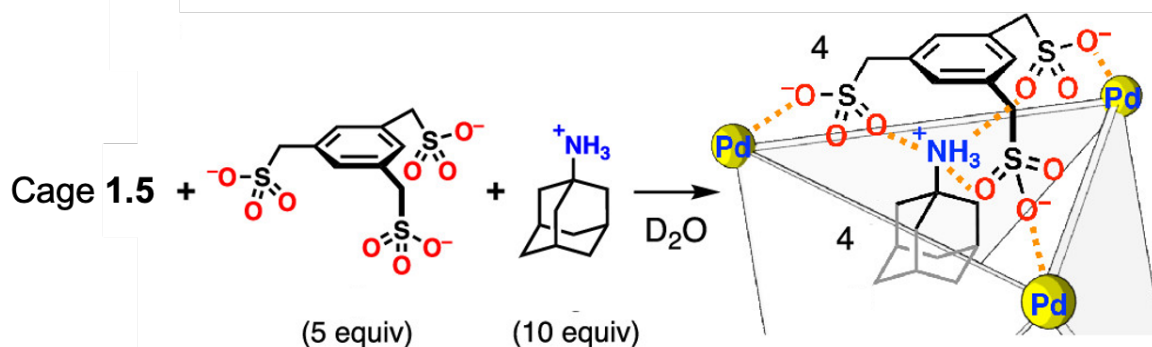
Figure 1.9: The combination of Fujita's cationic cage with 4 equivalents of a tripodal anion results in the encapsulation of cationic species in aqueous media.[35] Figure adapted with permission from reference 35.

1.5 Applications of Coordination Cages

The host-guest chemistry of supramolecular coordination cages has been employed in a number of applications such as the stabilisation of reactive species[36], low-energy chemical separations,[37] and catalysis[38,39] from both organic and aqueous media.[18,40] Some examples of these applications are illustrated below. Further examples, more pertinent to this work, are provided in the introductions to Chapters 3 and 4.

The octahedral cage **1.5** reported by Fujita *et al.* was observed to catalyse the Diels-Alder reaction between N-cyclohexylmaleimide and anthracen-9-ylmethanol in water (Figure

1.10a).[23] Anthracene, when acting as the diene in a Diels-Alder reaction in the absence of a host species, is known to react *via* its central ring (carbon positions 9 and 10) due to the high π electron density at these carbon atoms.[41,42] In the presence of cage **1.5**, however, the Diels-Alder reaction occurred at carbon positions 1 and 4 of the anthracene; this alternative regioselectivity was attributed to the proximity of the terminal anthracene ring and the maleimide when both of the guests were bound simultaneously inside **1.5**. In contrast, Fujita also demonstrated that the square-pyramidal bowl **1.6** could be used to catalyse the same Diels-Alder reaction but with the conventional regiochemistry (Figure 1.10c). A later work by Fujita showed that cage **1.5** promoted the [2+2] olefin cross photoaddition between fluoranthene and N-cyclohexylmaleimide (Figure 1.10b).[43] Furthermore, the use of a chiral source of cis-protected palladium (II) led to a chiral deformation in the cage cavity, resulting in subsequent asymmetric induction in the [2+2] photoaddition. Mukherjee *et al.* have also recently reported the assembly of an enantiopure $M_{12}L_6$ tetrahedron from tetrazole linkers and a source of chiral Pd^{II}, which showed binding selectivity between the enantiomers of diethyl-BINOL ((R/S)-2,2′-diethoxy-1,1′-binaphthalene).[44] Thus supramolecular hosts have been employed to catalyse both new and existing reactions and show great promise for asymmetric catalysis.
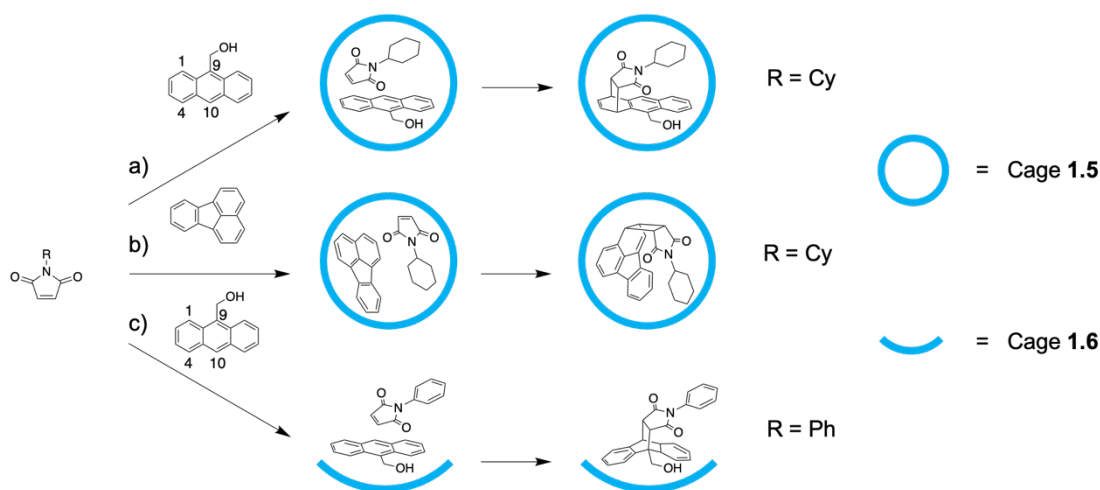
Figure 1.10: a) Fujita's octahedral cage **1.5** catalyses the Diels-Alder reaction between N-cyclohexylmaleimide and anthracen-9-ylmethanol with unusual regioselectively, b) Fujita's octahedral cage **1.5** promotes [2+2] olefin cross photoaddition, c) Fujita's square-pyramidal bowl **1.6** catalyses the Diels-Alder reaction between N-phenylmaleimide and anthracen-9-ylmethanol with usual regioselectivity.[23,43] The structures of cages **1.5** and **1.6** can be found in Figure 1.5.

A recent report by Stang and Wang *et al.* demonstrated that coordination cages could be used for intracellular protein delivery.[45] Stang and Wang formed cage **1.9** from palladium (II) and a bis-pyridyl ligand with a pendant oligo(ethylene glycol) chain and a terminal adamantane group (Figure 1.11). These adamantane termini then formed host-guest interactions with β-cyclodextrin groups along a polyethylenimine backbone, resulting in the formation of supramolecular nanoparticles. These supramolecular nanoparticles were also assembled in the presence of green fluorescent protein (GFP) and RNase A-NBC (the latter being a cytotoxic protein conjugate) and confocal laser scanning microscopy and flow cytometry demonstrated that these nanoparticles could be used to deliver the protein payload to the cytosol of HeLa cells. In the case of RNase A-NBC, the delivery of the protein reduced the cell viability to 50 % of that of the non-treated cells. Stang and Wang also demonstrated that their nanoparticles were able to deliver CRISPR/Cas9 to human embryonic kidney cells. This study thus illustrates the potential of coordination cages for future applications in therapeutics and genome editing.
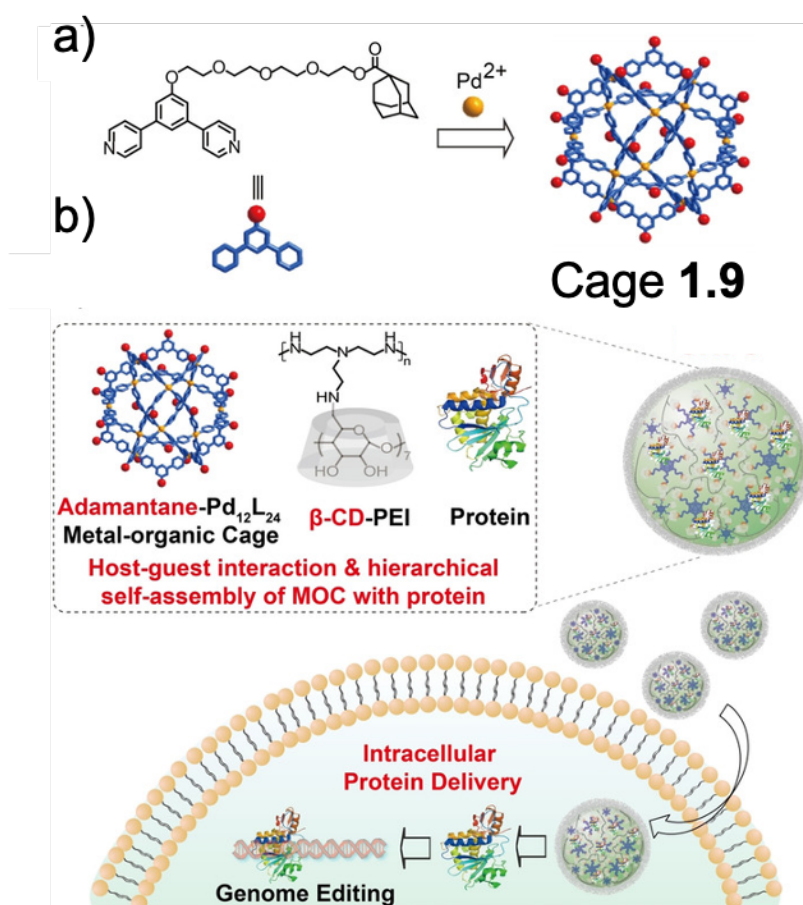
Figure 1.11: a) Assembly of Stang and Wang's adamantane-terminated coordination cage, b) Nanoparticles composed of coordination cage, β-cyclodextrin-functionalised polyethylenimine, and protein cargo are delivered intracellularly.[45] Figure adapted with permission from reference 45.

Finally, a report by Nitschke *et al.* demonstrated that a coordination cage **1.10** functionalised with poly(ethylene) glycol chains was able to transfer between aqueous and organic phases in response to temperature (Figure 1.12).[46] Additionally, the coordination cage bound fluoroadamantane and this guest remained bound following phase transfer. |The judicious application of a temperature stimulus then resulted in the directional motion of both the cage and its molecular cargo within a multi-phase system. Nitschke has also shown previously that the reversible phase transfer of cages and their cargoes can be stimulated *via* anion exchange; in this study, hydrophilic sulphate counterions promoted water solubility whereas hydrophobic tetrakis(pentafluoro-phenyl)-borate counterions engendered cage solubility in ethyl acetate.[47]

13

Coordination cages thus present a means by which low-energy chemical separations can be achieved.
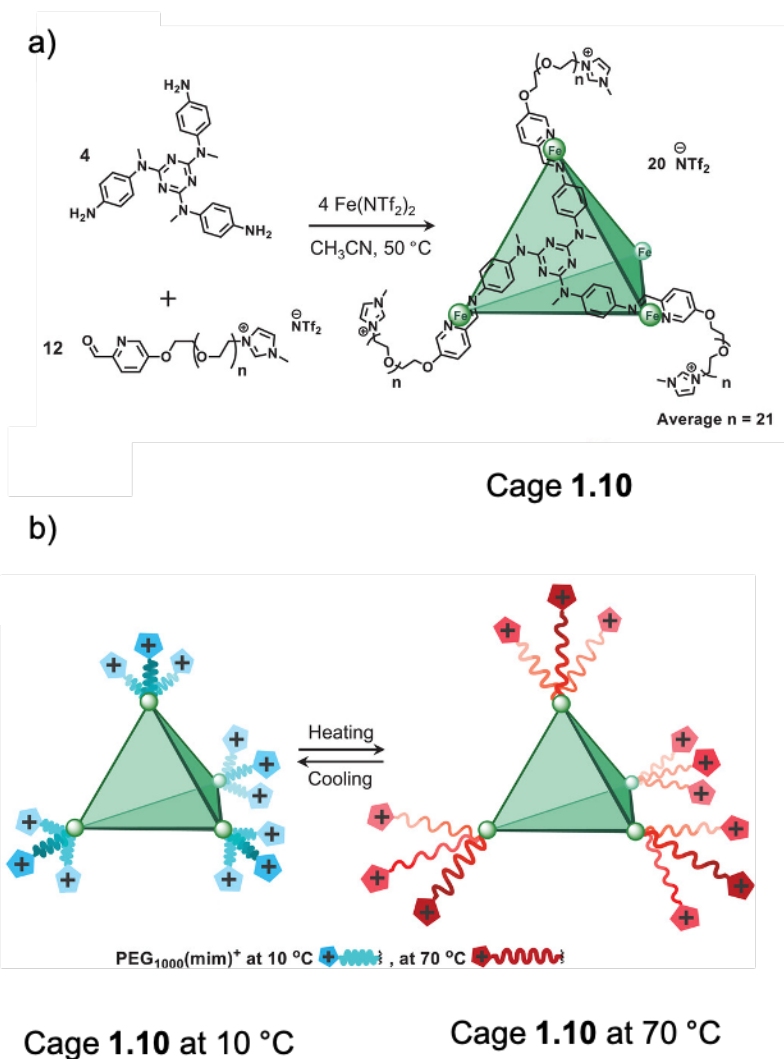

Figure 1.12: a) Self-assembly of Nitschke's thermally-transportable coordination cage **1.10**, b) Heating and cooling of cage **1.10** results in uncoiling and coiling, respectively, of the pendant poly(ethylene glycol) chains thereby triggering phase transfer.[46] Figure adapted with permission from reference 46.

1.6 Research Aims

This chapter has given a brief introduction to the early history of supramolecular chemistry and the more recent formation of metal-organic architectures. As discussed above, there has been considerable interest in the development of coordination cages with well-defined host-guest chemistry. The work of Nitschke *et al.* is primarily focussed on the synthesis, host-guest chemistry, and applications of metal-organic coordination cages formed *via* subcomponent self-assembly. The coordination cages of Nitschke's group are typically studied in the solution state on the NMR scale (*ca.* 0.5 – 1 mL, 0.5 – 2 mM). This thesis adopts a more materials chemistry approach to new applications of Nitschke's coordination cages in phases other than the solution state in order to achieve new behaviour and function. The remaining chapters of this thesis are outlined below.

Chapter 2 details the instrumentation and experimental techniques employed in the projects reported herein. Details of some of the theory underpinning these techniques are provided in the Appendix.

Chapter 3 presents an investigation of coordination cages adsorbed on activated alumina (aluminium oxide). The surface of alumina consists of hydroxylated aluminium atoms, thus alumina is amphoteric, and has been shown to be a good substrate for the electrostatic adsorption of highly charged coordination cages.[48] The adsorption isotherms of coordination cages and mononuclear complexes on activated alumina are collected *via* the solution depletion method and it is demonstrated that the cages remain intact and functional following adsorption. Finally, some applications of the adsorbed cages are explored.

Chapter 4 presents an investigation of coordination cages as scaffolds for permanently porous liquids. Previous work has already shown that coordination cages can form porous liquids and this chapter investigates a new generation of these materials.[49] The work on liquid materials in this thesis is broadly divided into two sections. The first section focusses on the progress, to-date, towards the formation of a new type of porous ionic liquid in which both ionic components are metal-organic coordination cages. The second section investigates the tuning of the glass transition temperature of liquid/glass-like cages.

1.7 References

1. Lehn, J.-M. From supramolecular chemistry towards constitutional dynamic chemistry and adaptive chemistry. *Chemical Society Reviews* **36**, 151–160 (2007).

2. Hunter, C. A. & Sanders, J. K. M. The Nature of π-π Interactions. *Journal of the American Chemical Society* **112**, 5525–5534 (1990).

3. Chakrabarty, R., Mukherjee, P. S. & Stang, P. J. Supramolecular Coordination: Self-Assembly of Finite Two- and Three-Dimensional Ensembles. *Chemical Reviews* **111**, 6810–6918 (2011).

4. Jones, C. D. & Steed, J. W. Gels with sense: Supramolecular materials that respond to heat, light and sound. *Chemical Society Reviews* **45**, 6546–6596 (2016).

5. Yan, X., Wang, F., Zheng, B. & Huang, F. Stimuli-responsive supramolecular polymeric materials. *Chemical Society Reviews* **41**, 6042–6065 (2012).

6. Korevaar, P. A. *et al.* Pathway complexity in supramolecular polymerization. *Nature* **481**, 492–496 (2012).

7. Mattia, E. & Otto, S. Supramolecular systems chemistry. *Nature Nanotechnology* **10**, 111–119 (2015).

8. Wehner, M. & Würthner, F. Supramolecular polymerization through kinetic pathway control and living chain growth. *Nature Reviews Chemistry* **4**, 38–53 (2020).

9. Pedersen, C. J. Cyclic polyethers and their complexes with metal salts. *Journal of the American Chemical Society* **89**, 7017–7036 (1967).

10. Dietrich, B., Lehn, J. M. & Sauvage, J. P. Les Cryptates. *Tetrahedron Letters* **10**, 2889–2892 (1969).

11. Cram, D. J., Takahiro, K., Helgeson, R. C. & Lein, G. M. Spherands-Ligands Whose Binding of Cations Relieves Enforced Electron-Electron Repulsions1. *Journal of the American Chemical Society* **101**, 6752–6754 (1979).

12. Dietrich-Buchecker, C. O., Sauvage, J. P. & Kintzinger, J. P. Une nouvelle famille de molecules : les metallo-catenanes. *Tetrahedron Letters* **24**, 5095–5098 (1983).

13. Anelli, P. L., Spencer, N. & Stoddart, J. F. A molecular shuttle. *Journal of the American Chemical Society* **113**, 5131–5133 (1991).

14. Feringa, B. L., Jager, W. F., de Lange, B. & Meijer, E. W. Chiroptical molecular switch. *Journal of the American Chemical Society* **113**, 5468–5470 (1991).

15. Kassem, S. *et al.* Artificial molecular motors. *Chemical Society Reviews* **46**, 2592–2621 (2017).

16. Hartlieb, M., Mansfield, E. D. H. & Perrier, S. A guide to supramolecular polymerizations. *Polymer Chemistry* **11**, 1083–1110 (2020).

17. Chivers, P. R. A. & Smith, D. K. Shaping and structuring supramolecular gels. *Nature Reviews Materials* **4**, 463–478 (2019).

18. Zhang, D., Ronson, T. K. & Nitschke, J. R. Functional Capsules via Subcomponent Self-Assembly. *Accounts of Chemical Research* **51**, 2423–2436 (2018).

19. Caulder, D. L. & Raymond, K. N. Supermolecules by design. *Accounts of Chemical Research* **32**, 975–982 (1999).

20. Weilandt, T., Troff, R. W., Saxell, H., Rissanen, K. & Schalley, C. A. Metallo-supramolecular self-assembly: The case of triangle-square equilibria. *Inorganic Chemistry* **47**, 7588–7598 (2008).

21. Fujita, M. *et al.* Self-assembly of ten molecules into nanometre-sized organic host frameworks. *Nature* **378**, 469–471 (1995).

22. Umemoto, K., Yamaguchi, K. & Fujita, M. Molecular Paneling via Coordination: Guest-Controlled Assembly of Open Cone and Tetrahedron Structures from Eight Metals and Four Ligands. *Journal of the American Chemical Society* **122**, 7150–7151 (2000).

23. Yoshizawa, M., Tamura, M. & Fujita, M. Diels-Alder in aqueous molecular hosts: Unusual regioselectivity and efficient catalysis. *Science* **312**, 251–254 (2006).

24. Rowan, S. J., Cantrill, S. J., Cousins, G. R. L., Sanders, J. K. M. & Stoddart, J. F. Dynamic Covalent Chemistry. *Angewandte Chemie International Edition* **41**, 898–952 (2002).

25. Yamashina, M. *et al.* An antiaromatic-walled nanospace. *Nature* **574**, 511–515 (2019).

26. Mecozzi, S. & Rebek, Jr., J. The 55 % Solution: A Formula for Molecular Recognition in the Liquid State. *Chemistry - A European Journal* **4**, 1016–1022 (1998).

27. Turega, S., Cullen, W., Whitehead, M., Hunter, C. A. & Ward, M. D. Mapping the internal recognition surface of an octanuclear coordination cage using guest libraries. *Journal of the American Chemical Society* **136**, 8475–8483 (2014).

28. Tidmarsh, I. S. *et al.* Octanuclear cubic coordination cages. *Journal of the American Chemical Society* **130**, 15167–15175 (2008).

29. Whitehead, M., Turega, S., Stephenson, A., Hunter, C. A. & Ward, M. D. Quantification of solvent effects on molecular recognition in polyhedral coordination cage hosts. *Chemical Science* **4**, 2744–2751 (2013).

30. Blokzijl, W. & Engberts, J. B. F. N. Hydrophobic Effects. Opinions and Facts. *Angewandte Chemie International Edition in English* **32**, 1545–1579 (1993).

31. Leung, D. H., Bergman, R. G. & Raymond, K. N. Enthalpy-entropy compensation reveals solvent reorganization as a driving force for supramolecular encapsulation in water. *Journal of the American Chemical Society* **130**, 2798–2805 (2008).

32. Rizzuto, F. J., von Krbek, L. K. S. & Nitschke, J. R. Strategies for binding multiple guests in metal–organic cages. *Nature Reviews Chemistry* **3**, 204–222 (2019).

33. Metherell, A. J., Cullen, W., Williams, N. H. & Ward, M. D. Binding of Hydrophobic Guests in a Coordination Cage Cavity is Driven by Liberation of "High-Energy" Water. *Chemistry - A European Journal* **24**, 1554–1560 (2018).

34. Ronson, T. K., Meng, W. & Nitschke, J. R. Design Principles for the Optimization of Guest Binding in Aromatic-Paneled $Fe^{II}_4L_6$ Cages. *Journal of the American Chemical Society* **139**, 9698–9707 (2017).

35. Takezawa, H., Tabuchi, R., Sunohara, H. & Fujita, M. Confinement of Water-Soluble Cationic Substrates in a Cationic Molecular Cage by Capping the Portals with Tripodal Anions. *Journal of the American Chemical Society* **142**, 17919–17922 (2020).

36. Galan, A. & Ballester, P. Stabilization of reactive species by supramolecular encapsulation. *Chemical Society Reviews* **45**, 1720–1737 (2016).

37. Zhang, D., Ronson, T. K., Zou, Y. Q. & Nitschke, J. R. Metal–organic cages for molecular separations. *Nature Reviews Chemistry* **5**, 168–182 (2021).

38. Tan, C. *et al.* Supramolecular Coordination Cages for Asymmetric Catalysis. *Chemistry – A European Journal* **25**, 662–672 (2019).

39. Fang, Y. *et al.* Catalytic reactions within the cavity of coordination cages. *Chemical Society Reviews* **48**, 4707–4730 (2019).

40. Percástegui, E. G., Ronson, T. K. & Nitschke, J. R. Design and Applications of Water-Soluble Coordination Cages. *Chemical Reviews* **120**, 13480–13544 (2020).

41. Cheng, M. F. & Li, W. K. A computational study of the Diels-Alder reactions involving acenes: Reactivity and aromaticity. *Chemical Physics Letters* **368**, 630–638 (2003).

42. Fringuelli, F. & Taticchi, A. *The Diels-Alder Reaction*. (John Wiley & Sons, Ltd, 1988).

43. Nishioka, Y., Yamaguchi, T., Kawano, M. & Fujita, M. Asymmetric [2 + 2] olefin cross photoaddition in a self-assembled host with remote chiral auxiliaries. *Journal of the American Chemical Society* **130**, 8160–8161 (2008).

44. Howlader, P., Zangrando, E. & Mukherjee, P. S. Self-Assembly of Enantiopure Pd_{12} Tetrahedral Homochiral Nano-Cages with Tetrazole Linkers and Chiral Recognition. *Journal of the American Chemical Society* **142**, 9070–9078 (2020).

45. Liu, J. *et al.* Hierarchical Self-assembly of Discrete Metal–Organic Cages into Supramolecular Nanoparticles for Intracellular Protein Delivery. *Angewandte Chemie International Edition* **60**, 5429–5435 (2021).

46. Nguyen, B.-N. T., Grommet, A. B., Tron, A., Georges, M. C. A. & Nitschke, J. R. Heat Engine Drives Transport of an $Fe^{II}_4L_4$ Cage and Cargo. *Advanced Materials* **32**, 1907241 (2020).

47. Grommet, A. B. *et al.* Anion Exchange Drives Reversible Phase Transfer of Coordination Cages and Their Cargoes. *Journal of the American Chemical Society* **140**, 14770–14776 (2018).

48. Tsyganenko, A. A. & Mardilovich, P. P. Structure of alumina surfaces. *Journal of the Chemical Society, Faraday Transactions* **92**, 4843–4852 (1996).

49. Ma, L. *et al.* Coordination cages as permanently porous ionic liquids. *Nature Chemistry* **12**, 270–275 (2020).

Chapter 2: Materials and Methods

2.1 Materials

All reagents and solvents were obtained from commercial sources unless otherwise stated. Deuterated water (D_2O) was obtained from Sigma-Aldrich. Deuterated acetonitrile (CD_3CN) was obtained from Fluorochem. "Acidic alumina" (Aluminium oxide. activated, acidic, Brockmann I, standard grade, ~150 mesh) was purchased from Sigma-Aldrich with a measured surface area of (146.4 ± 0.3) $m^2\ g^{-1}$ (BET analysis). "Basic alumina" (Aluminium oxide 90 standardised) was purchased from Merck with a measured surface area of (171.3 ± 0.6) $m^2\ g^{-1}$ (BET analysis).

2.2 Nuclear Magnetic Resonance Spectroscopy (NMR)

^{1}H, ^{13}C, and ^{19}F NMR spectra were recorded on a 400 MHz Avance III HD Smart Probe Spectrometer at 298 K or on a 500 MHz AVIII HD Smart Probe Spectrometer, unless otherwise stated. Chemical shifts (δ) are reported in parts per million (ppm). Spectra are referenced to residual solvent peaks unless otherwise stated. Coupling constants (J) are recorded in hertz (Hz). The following splitting abbreviations are used: s – singlet, d – doublet, t – triplet, q – quartet, qn – quintet, sx – sextet, m – multiplet, bs – broad singlet.

DOSY spectra were acquired with the pulse program 'ledbpgp2s' from the standard Bruker Topspin 3.2 library on a 400 MHz Avance III HD Smart Probe Spectrometer. 'ledbpgp2s' is a 2D sequence for diffusion measurements using a stimulated echo and longitudinal eddy-current delay (LED) using bipolar gradient pulses for diffusion and 2 spoil gradients. 16 increments using a quadratic gradient ramp (type q) going from 10 to 80% of the gradient systems maximum power of 10A. Each increment used 16 transients; a 90 degree rotation required a ^{1}H pulse of 400.1324710 MHz applied for 11.1 microseconds and 13 Watts. Other pulses defined in the pulse program are derived from these values. A spectral window of 8012.820 Hz was acquired around an irradiation frequency of 400.1324710 MHz, digitising 32768 K points over 2.0447233 seconds. The maximum field strength was 5.01 G/cm A.[1]

Many thanks to Duncan Howe and Andrew Mason at the NMR facility (Department of Chemistry, University of Cambridge) for all of their help and time.

2.3 UV-Vis Spectroscopy (UV-Vis)

UV-Vis spectra were recorded on an Agilent Technologies Cary Series UV-Vis-NIR-Spectrophotometer at ambient temperature. The samples were recorded in a 1 mm quartz cuvette unless otherwise stated. Spectra were collected in double beam mode, with samples placed in the front analyte position and air in the back reference position. A background of neat solvent was used. Samples were zeroed at a specified wavelength prior to the collection of spectra.

2.4 Transmission Spectroscopy

Transmission spectroscopy was conducted with Alyssa Smith in the Vignolini Bio-Inspired Photonics Group at the Department of Chemistry, University of Cambridge. All transmission spectra were recorded at ambient temperature using an Ocean Optics HPX-2000 light source and a LabSphere Inc integrating sphere with an Avantes HS2048 spectrometer and Thorlabs optical fibres. The samples for transmission spectroscopy were prepared by sandwiching an aqueous suspension of cage on alumina in NVH immersion oil between two glass slides. Adsorbed cages were measured relative to the bare alumina substrates. Data were smoothed in Origin Pro 2017 using the Adjacent Averaging method at the 10 point level.

2.5 X-Ray Photoemission Spectroscopy (XPS)

XPS experiments were performed by Mohamed Al-Hada at the Maxwell Centre, University of Cambridge, on a Thermo Fisher Scientific Escalab 250XI spectrometer, using a flood gun for charge compensation. Many thanks also to Carmen Fernandez-Posada at the Maxwell Centre, University of Cambridge for her help with data analysis.

2.6 Gas Adsorption Isotherms

Nitrogen adsorption isotherms were collected by Antonio Serrano at the Department of Chemical Engineering and Biotechnology, University of Cambridge, on a Micromeritics ASAP 2020.

2.7 Thermogravimetric Analysis (TGA)

TGA data were collected with a TA Instruments SDT650 at a heating rate of 10 °C min^{-1} and a nitrogen flow rate of 50 mL min^{-1}. Data were collected by Georgie Robertson, Department of Materials Science and Metallurgy, University of Cambridge, unless otherwise stated. TGA data were analysed with TA Instruments Universal Analysis 2000, version 4.5A, build 4.5.0.5 (2007).

2.8 Differential Scanning Calorimetry (DSC)

DSC data were collected with a TA Instruments Q2000 DSC at a heating rate of 10 °C min^{-1} and a nitrogen flow rate of 50 mL min^{-1}. Data were collected by Georgie Robertson, Department of Materials Science and Metallurgy, University of Cambridge, unless otherwise stated. DSC data were analysed with TA Instruments Universal Analysis 2000, version 4.5A, build 4.5.0.5 (2007).

2.9 Mass Spectrometry

Mass spectrometry was performed by the Department of Chemistry Mass Spectrometry service, University of Cambridge, unless otherwise stated, on one of a Waters Synapt G2-Si, Waters Xevo GS-2, or Agilent 6230 LC/TOF, using either Electrospray (ESI) or Atmospheric Solids Analysis Probe (ASAP) ionisation mode. Instrumentation is stated for each sample.

2.10 Single Crystal X-Ray Diffraction

Data were collected at Beamline I19 of Diamond Light Source employing silicon double crystal monochromated synchrotron radiation (0.6889 Å) with ω and ψ scans at 100(2) K.[2] Data integration and reduction were undertaken with Xia2.[3,4] Subsequent computations were carried

out using the WinGX-32 graphical user interface.[5] A multi-scan empirical absorption correction using spherical harmonics was applied to the data using DIALS.[4] The structure was solved by intrinsic phasing using SHELXT[6] then refined and extended with SHELXL.[7] Carbon-bound hydrogen atoms were included in idealised positions and refined using a riding model. Hydrogen atoms were not applied to disordered ethanol or water molecules. Disorder was modelled using standard crystallographic methods including constraints, restraints, and rigid bodies where necessary. Crystal structure images were prepared using PyMOL Molecular Graphics System, Version 1.4.1.

2.11 Other

Flash column chromatography was performed on a Biotage Isolera Four Advanced Automated Flash Purification System with pre-packed silica cartridges unless otherwise stated. Flow experiments were conducted with a World Precision Instruments Programmable Syringe Pump.

2.12 References

1. Wu, D. H., Chen, A. & Johnson, C. S. An Improved Diffusion-Ordered Spectroscopy Experiment Incorporating Bipolar-Gradient Pulses. *Journal of Magnetic Resonance, Series A* **115**, 260–264 (1995).

2. Allan, D. *et al.* A Novel Dual Air-Bearing Fixed-χ Diffractometer for Small-Molecule Single-Crystal X-ray Diffraction on Beamline I19 at Diamond Light Source. *Crystals* **7**, 336 (2017).

3. Winter, G. Xia2: An expert system for macromolecular crystallography data reduction. *Journal of Applied Crystallography* **43**, 186–190 (2010).

4. Winter, G. *et al.* DIALS: Implementation and evaluation of a new integration package. *Acta Crystallographica Section D: Structural Biology* **74**, 85–97 (2018).

5. Farrugia, L. J. WinGX and ORTEP for Windows: An update. *Journal of Applied Crystallography* **45**, 849–854 (2012).

6. Sheldrick, G. M. SHELXT - Integrated space-group and crystal-structure determination. *Acta Crystallographica Section A: Foundations of Crystallography* **71**, 3–8 (2015).

7. Sheldrick, G. M. Crystal structure refinement with SHELXL. *Acta Crystallographica Section C: Structural Chemistry* **71**, 3–8 (2015).

Chapter 3: Adsorption of Coordination Cages formed *via* Subcomponent Self-Assembly

The work of Nitschke et al. is primarily focussed on the assembly and function of coordination cages in the solution state. This chapter explores the electrostatic adsorption of coordination cages on activated alumina from aqueous and organic media. The adsorptive loading of cages on to alumina was quantified via adsorption isotherms and kinetics. Visible transmission, energy-dispersive X-ray, and X-ray photoelectron spectroscopies were employed to further characterise the adsorbed cages. Furthermore, guest displacement experiments under flow conditions were used to demonstrate that the cages retain their ability to bind and release molecular guests following adsorption. Finally, adsorbed cages were used to separate a mixture of guests and non-guests and to compartmentalise the components of a Diels-Alder reaction for subsequent release and reaction.

3.1 Introduction

3.1.1 Surface Networks

In his 1918 paper concerning the adsorption of gases on plane surfaces, Langmuir derived a basic model of adsorption in which he assumed that the occupation of one adsorption site did not affect the occupation of a neighbouring site, *i.e.* no cooperativity/intermolecular interactions.[1] Later work by Everett extended this adsorption model to the solution state; Everett showed that, for strongly binding adsorbates, the same functional form of adsorption isotherm was expected for adsorption from solution phases (see Appendix).[2] In reality, however, the presence of non-covalent interactions has led to the formation of supramolecular architectures, both discrete and continuous, at interfaces, the study of which has been facilitated by the development of surface techniques such as Scanning Tunnelling Microscopy (STM).[3,4] This section outlines some of these examples of supramolecular chemistry on surfaces.

The formation of extended two-dimensional networks on solid surfaces has been achieved *via* non-covalent interactions such as Van der Waals forces[5] and hydrogen bonding.[6] In 2003, Champness and Beton *et al.* reported a particularly striking system in which perylene tetra-carboxylic di-imide and melamine were co-adsorbed on to silver-terminated silicon to form a hexagonal network held together by hydrogen bonds (Figure 3.1).[7] This hexagonal

network then templated the formation of fullerene (C_{60}) heptamers within the pores of the network (Figure 3.1c) and thus the supramolecular network was able to control the patterning of the fullerenes on the surface.
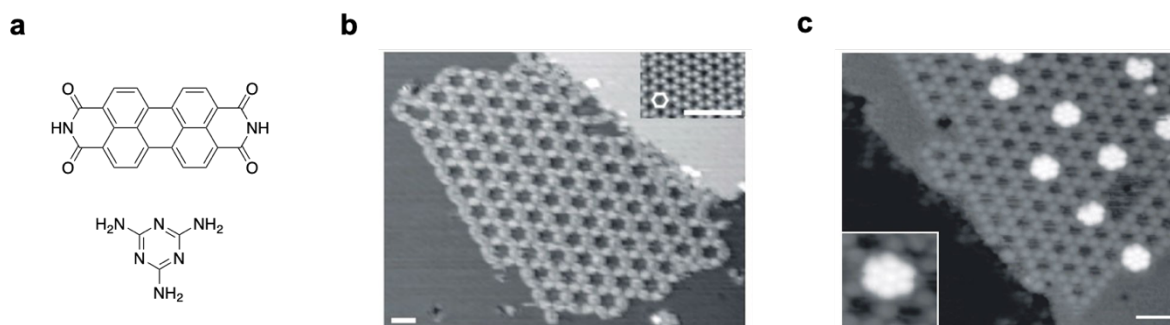

Figure 3.1: a) Perylene tetra-carboxylic di-imide and melamine, b) STM image of the hexagonal network on silver-terminated silicon, inset, Ag/Si(111) - √3 × √3 R30° substrate surface, c) C_{60} heptamers in the surface network.[7] Figures 3.1b and 3.1c reproduced with permission from reference 7.

In contrast to the network reported by Champness and Beton, Hammer and Linderoth *et al.* utilised π-π interactions between non-planar triazole molecules to assemble discrete supramolecular corrals on the surfaces of copper, silver, and gold.[8] Unlike in the studies of adsorption of aromatic species by Fasel and Enders *et al.*, in which the aromatic moieties adsorbed coplanar with the surface, triazoles are known to chemisorb to the surface of copper, *via* the triazole nitrogen atoms, with only a small energetic barrier penalty to tilting.[9–11] Hammer and Linderoth investigated the adsorption of a non-planar 1,5-triazole, the aromatic moieties of which did not lie coplanar with the surface, which formed annular corrals of 11-18 molecules, *via* π-π interactions between the biphenyl and phenanthrene units, and the two conformers of the triazole, P and M, resulted in the formation of oppositely handed corrals (Figure 3.2). Hammer and Linderoth concluded that such corrals might find future applications in the quantum confinement of surface states or in the formation of surface "reaction pockets".
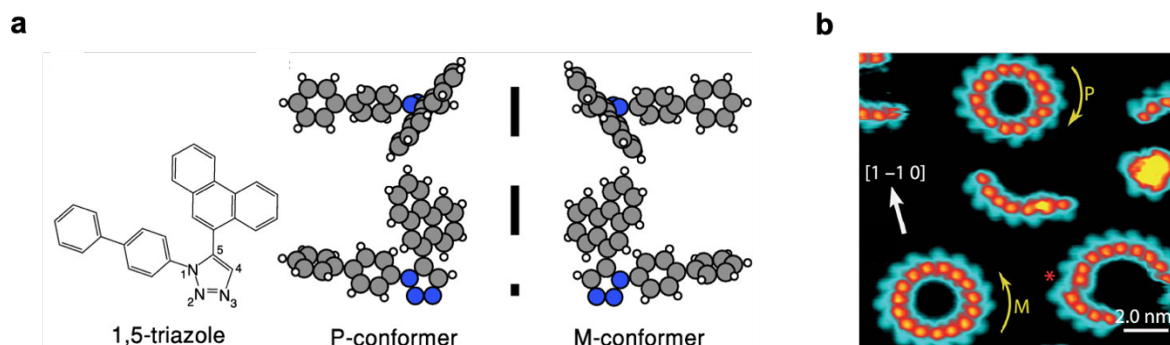
Figure 3.2: a) 1-([1,1'-biphenyl]-4-yl)-5-(phenanthren-9-yl)-1*H*-1,2,3-triazole and its P- and M-conformers, b) Corrals formed from M-conformers (15-mer) and P-conformers (14-mer) of the triazole.[8] Figures 3.2a and 3.2b reproduced and adapted with permission from reference 8.

3.1.2 Immobilised Coordination Cages

The literature also contains examples of supramolecular hosts on solid surfaces. Cave *et al.* recently reported a study in which a novel co-pillar[4+1]arene, functionalised with two pendant bromo-octyl chains per molecule, was tethered to the surface of chromatographic silica.[12] The surface-functionalised silica was then used to separate a mixture of aromatic hydrocarbons, including ortho-, meta-, and para-xylene, with the most strongly binding guests possessing the longest retention times (Figure 3.3). Dalcanale *et al.* have reported a number of studies on the assembly of cavitand-based coordination cages with platinum and palladium on silica[13] and gold[14,15] in which the cages were grafted to the surfaces *via* the chemistry of self-assembled monolayers (Figure 3.4). Dalcanale then demonstrated the persistence of the structural integrity of the cages *via* Atomic Force Microscopy (AFM). In contrast, however, the literature contains few examples of adsorbed coordination cages. Clever *et al.* have demonstrated, *via* Surface-Enhanced Raman Spectroscopy (SERS), that Pd_4L_8 phenothiazine-based cages remain structurally intact following adsorption on gold.[16] Additionally, Ramamurthy *et al.* have shown that organic host-guest species can self-assemble on the surface of silica from their molecular components and that the mobility of the adsorbed components was important for subsequent host formation.[17]
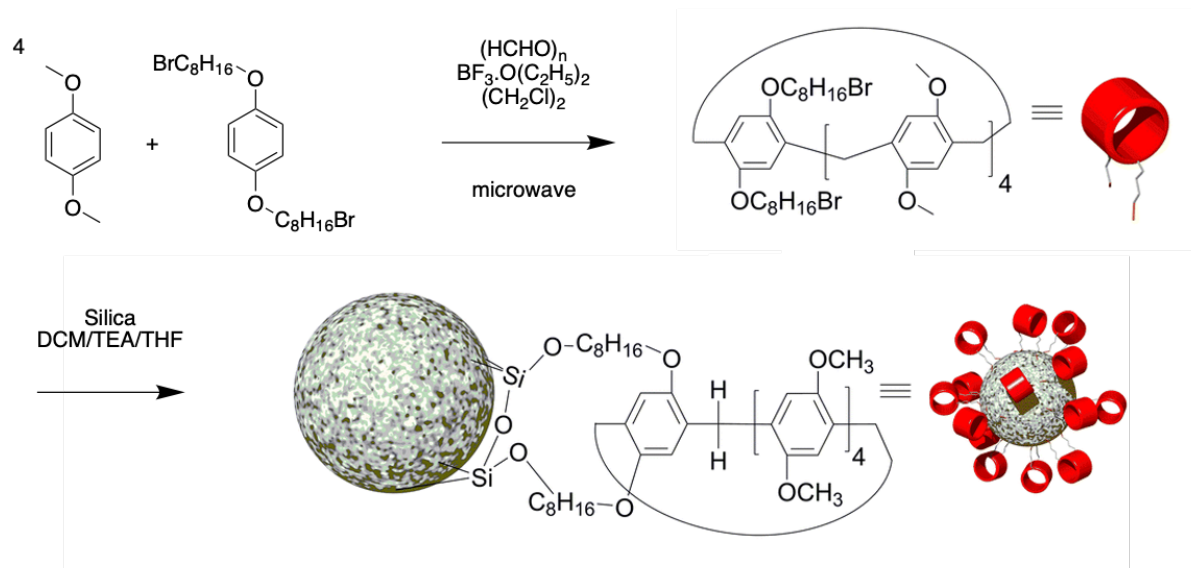
Figure 3.3: Preparation of Cave's co-pillar[4+1]arene-functionalised silica; The co-pillar[4+1]arene is formed *via* microwave synthesis and then grafted to the silica surface in DCM/TEA/THF.[12] Figure 3.3 was reproduced and adapted with permission from reference 12.
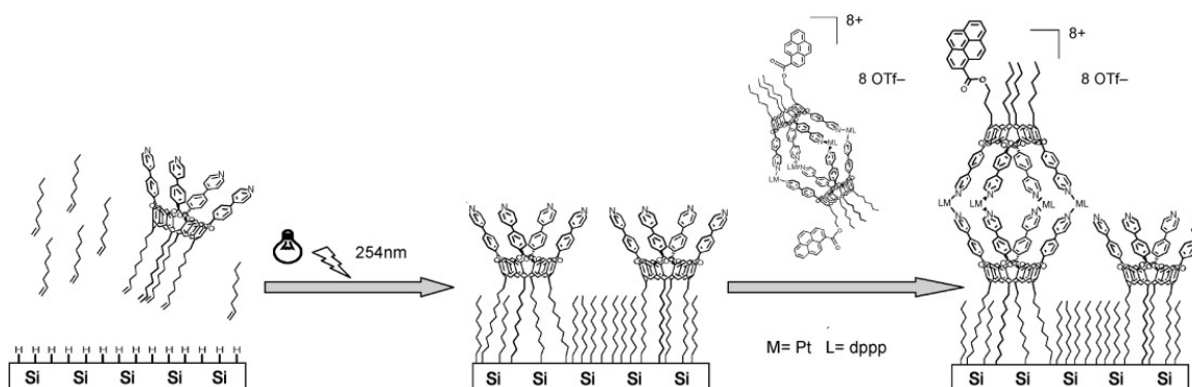

Figure 3.4: Preparation of Dalcanale's cavitand-based coordination cage on silica; a mixed octane/cavitand monolayer is formed on the silica surface followed by a ligand exchange reaction to form surface-bound cages.[13] Figure 3.4 was reproduced and adapted with permission from reference 13.

More recently, in 2020, Bergman, Raymond, and Toste *et al.* reported the electrostatic immobilisation of anionic assemblies on cationic polymers.[18] The authors demonstrated that an anionic M_4L_6 gallium (III) assembly could be immobilised on polymer supports functionalised with ammonium moieties with loadings of up to 0.1 mmol g^{-1}, depending on the composition of the polymer support (Figure 3.5a). The immobilised assemblies were then

employed to heterogeneously catalyse aza-Prins and aza-Cope reactions under flow conditions. Furthermore, the gallium (III) assembly was enantioresolved with (−)-N'-methylnicotinium iodide and the resulting immobilised enantioenriched assembly enabled asymmetric catalysis.

Entry	Catalyst	Loading (mol %)	CD₃OD:D₂O	Yield
1	Cage, **P1**, R = Me	8	10:1	63
2	Cage, **P1**, R = Et	8	10:1	63
3	Cage, **P2**, R = Me	8	10:1	86
4	Cage, **P2**, R = Me	8	1:1	58
5	Cage, **P2**, R = Et	8	10:1	77
6	Cage, **P2**, R = n-Bu	8	10:1	13
7	**P1**, R = Me	0	10:1	0
8	**P2**, R = Me	0	10:1	0
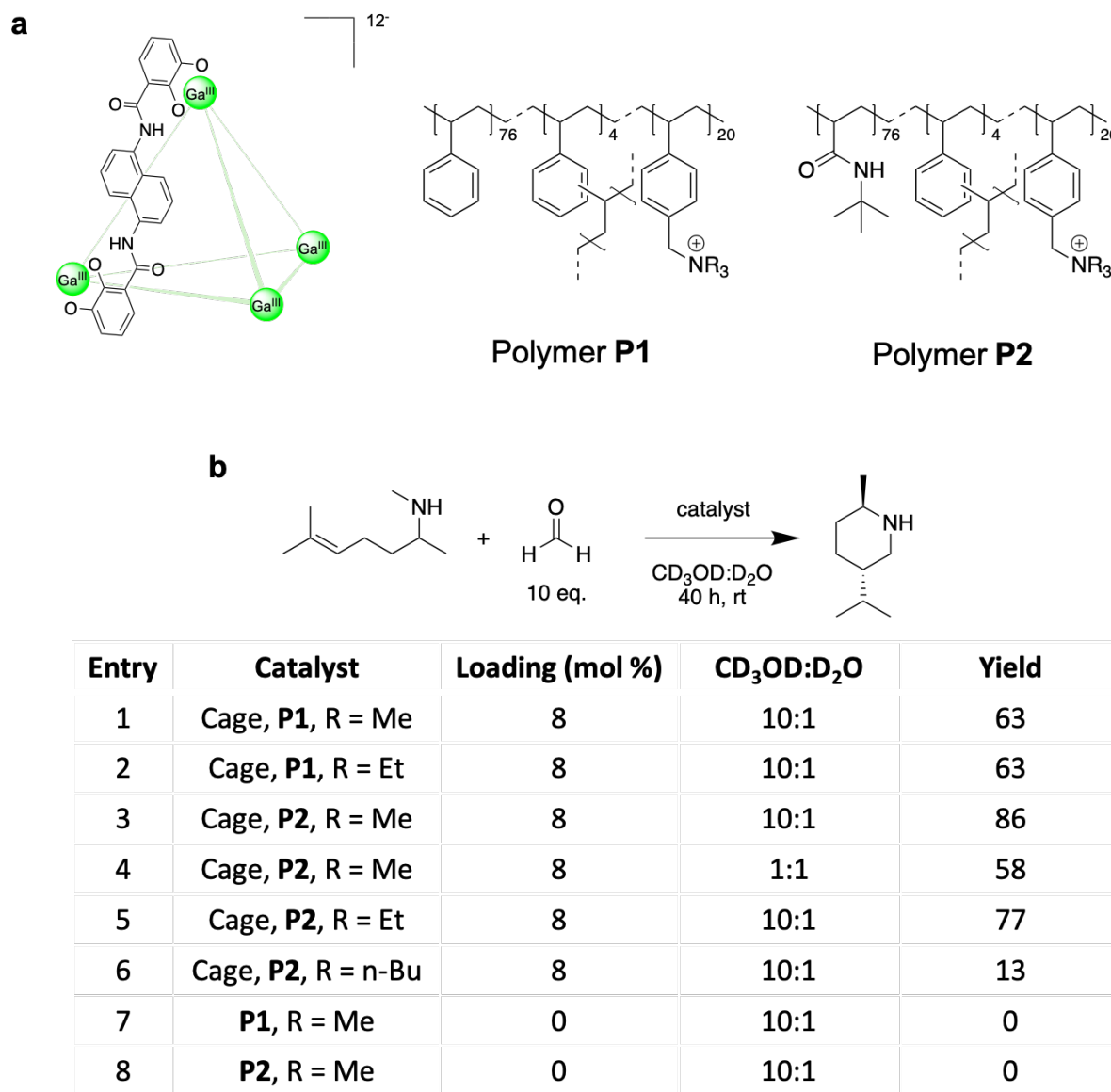
Figure 3.5: a) Bergman, Raymond, and Toste's gallium (III) coordination cage and co-polymers for immobilisation, b) Aza-Prins reaction catalysed by the gallium (III) assembly immobilised on co-polymer supports.[18]

3.1.3 Aims and Objectives

The field of supramolecular chemistry contains many instances of coordination cages in the solution state. In contrast, as illustrated in the previous section, there are far fewer examples of coordination cages immobilised on solid supports. Nitschke has demonstrated that coordination cages, formed *via* subcomponent self-assembly, have extensive host-guest chemistry and can be employed in a number of applications such as phase transfer[19] and the recovery of precious materials.[20] This chapter presents an investigation of the adsorption and function of Nitschke's coordination cages on alumina (aluminium oxide) in which the cages are electrostatically physisorbed on to the surface *via* solution depletion.

3.2 Adsorption From Water

This section draws on material published in "*Guest Encapsulation within Surface-Adsorbed Self-Assembled Cages*".

3.2.1 Preliminary Work

The surface of alumina consists of hydroxylated aluminium atoms when under aqueous conditions.[21] It should be noted, however, that alumina surfaces are typically highly complex and are thought to consist of surface hydroxyl groups bonded to up to three tetrahedrally/octahedrally-coordinated aluminium atoms. Alumina is thus amphoteric and polar as a result of these surface hydroxyl groups and has seen use as an adsorbent in the adsorption of both ionic and aromatic species.[22,23] The Point of Zero Charge (PZC) is defined as the pH at which a given surface's net charge density is zero.[24] Commercial alumina has been observed to have PZC's in the region of pH 5-6, thus a net positive surface charge should be expected for aqueous slurries of alumina with pH < 5 and net negative surface charge should be expected for slurries with pH > 6. We thus hypothesised that anionic cages would adsorb electrostatically on acidic activated alumina (pH 4.0 – 5.0, 10 % w/v in water) and cationic cages would adsorb on basic activated alumina (pH 9.0 – 10.0, 10 % w/v in water).

Prior to this thesis, in unpublished work, Dr Jonathan Foster investigated the adsorption of anionic cage **3.1** (Figure 3.6a, *vide infra*) and two cationic cages, not described herein, on alumina, silica, and polymer supports from a variety of solvents. Dr Foster observed that cage **3.1** adsorbed on acidic alumina from water with an estimated loading of 0.02 – 0.03 mmol g^{-1}. This quantification of cage loading on alumina was performed by one-point mass balance (see

Solution Depletion Method in the Appendix), TGA, Elemental Analysis, and by weight (the alumina support was weighed before and after cage adsorption). Dr Foster concluded his work on the project with some attempted host-guest chemistry with the adsorbed cages; in his final report, however, he commented that he obtained no definitive evidence for the intact adsorption of the cages or subsequent host-guest chemistry. This system thus formed the basis for initial investigations of suitable cage and adsorbent systems.
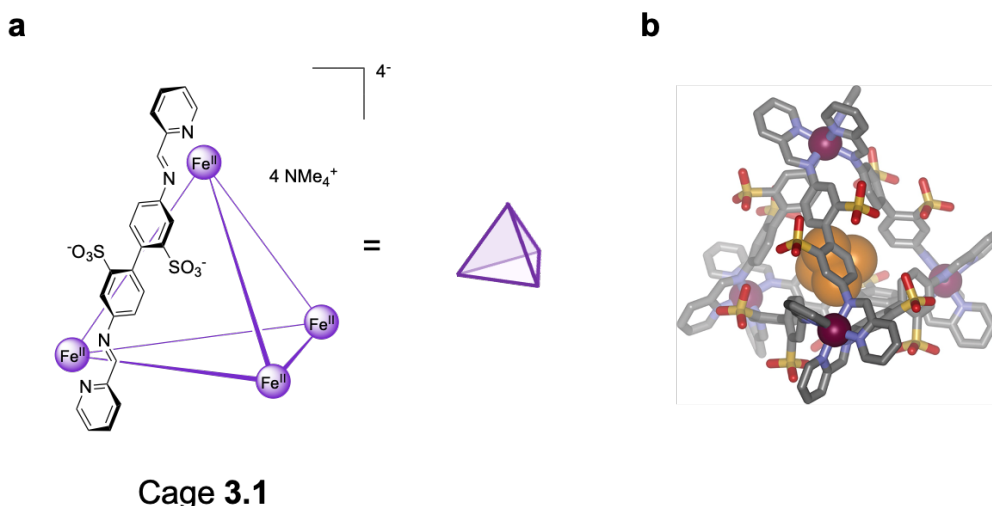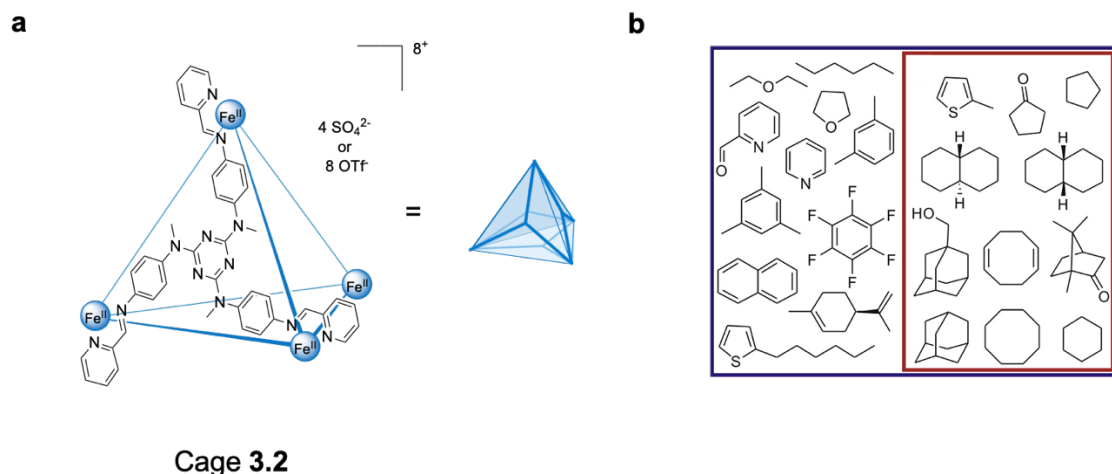

Figure 3.6: a) Nitschke's tetrahedral coordination cage **3.1**, assembled from a commercial sulphonated dianiline, and its schematic representation, b) Crystal structure of white phosphorus, P_4, bound within **3.1**.[25] Figure 3.6b was reproduced with permission from reference 25.

3.2.2 Cage Systems Studied

In 2008, Nitschke reported the self-assembly of water-soluble $Fe^{II}_4L_6$ tetrahedral cage **3.1** (Figure 3.6a).[25] **3.1** bound small aliphatic molecules such as cyclohexane and cyclopentane and could be reversibly disassembled and re-assembled upon acidification and basification of the cage solution, respectively. Subsequent work with cage **3.1** showed that it could bind white phosphorous (P_4), a component of munitions, thereby rendering the pyrophoric phosphorus both air-stable and water-soluble (Figure 3.6b).[26] A later study published in 2013 investigated the factors affecting the thermodynamics and kinetics of guest binding in cage **3.1**. The study concluded that, as seen originally by Rebek (*vide supra*), the size of the guest acted as a gross selection rule for binding, with no binding observed for guests with more than 6 carbon atoms.[27] Principal Component Analysis (PCA), a method by which high-dimensionality data can be reduced to fewer dimensions, was then used to elucidate the factors affecting the strength and

kinetics of binding.[28] PCA indicated that $\log K_a$, in which K_a is the thermodynamic binding constant in the host-guest equilibrium, was correlated with the octanol:water partition coefficient ($\log P$) and the dipole moment (μ) of the guest; strongly binding guests, *i.e.* $K_a \gg 1$, typically had large partition coefficients, *i.e.* they were hydrophobic species, and small dipole moments and thus were a good match for the hydrophobic cavity of cage **3.1**. In contrast, the rate of guest uptake was dependent on the guest volume (V) and asphericity (Ω_A) with small, aspherical guests binding more quickly than larger, more spherical species. These results are shown in the quadrant plot below (Figure 3.7).
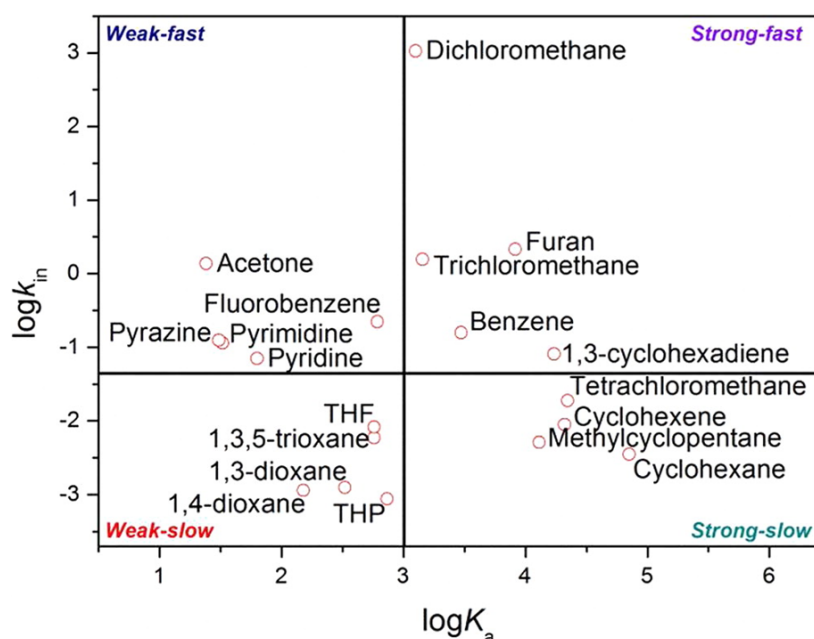
Figure 3.7: Quadrant plot of the guest ingress rate constant, k_{in}, against the guest binding constant, K_a, for the guests studied in cage **3.1**.[27] Figure 3.7 was reproduced with permission from reference 27.

In 2014, Nitschke reported the self-assembly of $Fe^{II}_4L_4$ tetrahedral cage **3.2** from a triazine-centred triamine ligand, which was soluble in acetonitrile and water with triflate and sulphate counterions respectively (Figure 3.8a).[29] Cage **3.2** bound guest molecules in both water and acetonitrile, with a greater variety of guest species encapsulated in water due to the hydrophobic effect (Figure 3.8b). The extensive host-guest chemistry of cage **3.2** was attributed to the efficient enclosure of the cage cavity by the face-capping triazine panels; other studies by Nitschke have demonstrated that hydrophobic guests are more effectively encapsulated by cages formed from ligands which more fully define a region of hydrophobic space.[30]

Cage **3.2**

Figure 3.8: a) Nitschke's tetrahedral coordination cage **3.2**, assembled from a triazine-centred trianiline, and its schematic representation, b) The guest species which were observed to bind within cage **3.2** from water (blue box) and acetonitrile (red box).[29] Figure 3.8b was reproduced with permission from reference 29.

The excellent host-guest chemistry of the cages described above suggested that these cages would be interesting candidates for adsorption studies. The following sections explore the quantification, characterisation, and utility of anionic cage **3.1** and cationic cage **3.2** adsorbed on acidic and basic alumina, respectively, from aqueous media.

It should be noted, however, that additional work by Nitschke has demonstrated that other coordination cages with sulphate counterions are metastable in water, both *via* direct assembly with sulphate salts and also *via* anion exchange.[31,32] For example, a zinc(II)-porphyrin M_8L_6 cube was observed to be stable in water indefinitely at room temperature when assembled with nickel (II), whilst the same cage assembled with cadmium (II) decomposed on a timescale of minutes. Furthermore, the observed trend in water metastability was consistent with the Irving-Williams series with the exception of the ordering of iron (II) and cobalt (II);[33] this latter observation was attributed to the low-spin iron (II) centres in the porphyrin cube, which formed stronger metal-ligand bonds than the high-spin iron (II) originally considered by Irving and Williams. Thus, Nitschke's water-soluble coordination cages are not limited to cages **3.1** and **3.2**. Furthermore, the literature contains a wide range of water-soluble architectures and hence the methods developed in the following sections may find future application in a number of other systems.[31]

3.2.3 Adsorption Isotherms

Adsorption isotherms for cages **3.1** and **3.2** on acidic and basic alumina, respectively, were obtained *via* the solution depletion method (Section 3.5.4 and Appendix) in which UV-Vis spectroscopy was used to determine the concentrations of the supernatant solutions (Figure 3.10a-b). The adsorption isotherms of cationic mononuclear complex **3.3** on basic alumina and anionic mononuclear complex **3.4** on acidic alumina were also obtained; in the following sections, **3.3** and **3.4** are used as control coordination species with no cage cavities (Figures 3.9, 3.10c-d). In keeping with a consideration of electrostatics, minimal adsorption was observed for **3.1** and **3.4** on basic alumina and **3.2** and **3.3** on acidic alumina. Cage **3.1** was assembled *via* a modified literature procedure in which the cage counterion was sodium instead of tetramethylammonium;[25] sodium counterions were chosen to ensure good water solubility. **3.2** and **3.3** were prepared *via* literature procedures and **3.4** was synthesised for this work.[29,34] The adsorption isotherms in Figure 3.10 were fitted to a solution analogue of the BET isotherm, developed by Ebadi *et al.*, with the following form (also see Appendix):[35]

$$\theta = \theta_{\text{MONO}} \left(\frac{K_S c}{(1 - K_L c)(1 - K_L c + K_S c)} \right) \qquad \text{Equation 3.1}$$

in which θ is the total surface coverage ($\mu\text{mol}_{\text{adsorbate}} \text{ g}^{-1}_{\text{alumina}}$), θ_{MONO} is the monolayer surface coverage ($\mu\text{mol}_{\text{adsorbate}} \text{ g}^{-1}_{\text{alumina}}$), K_S is the surface-adsorbate binding constant (M^{-1}), K_L is the adsorbate-adsorbate binding constant (M^{-1}), and c is the equilibrium adsorbate concentration (M).
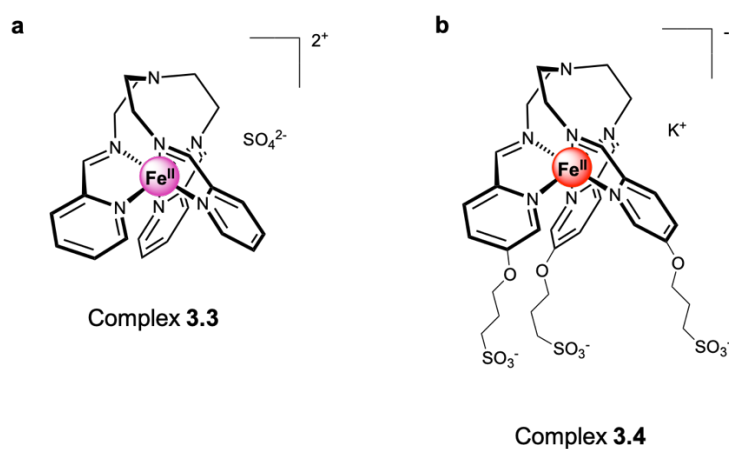
Figure 3.9: Control species; a) Cationic mononuclear complex **3.3**, b) Anionic mononuclear complex **3.4**.[34]

a

Adsorption Isotherm:
3.1 / Acidic Alumina / D_2O

b

Adsorption Isotherm:
3.2 / Basic Alumina / D_2O

c

Adsorption Isotherm:
3.3 / Basic Alumina / D_2O

d

Adsorption Isotherm:
3.4 / Acidic Alumina / D_2O
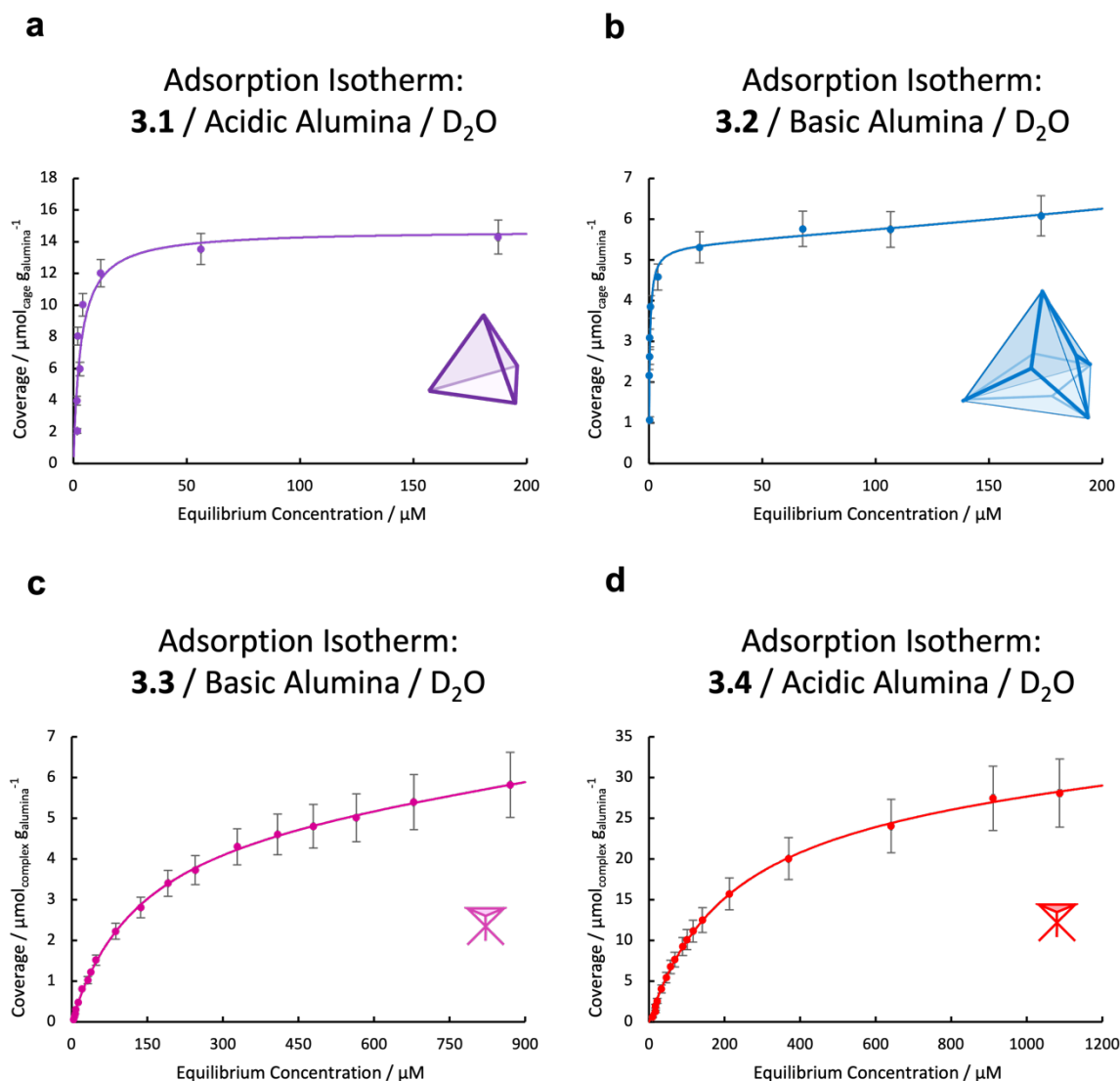
Figure 3.10: a) Adsorption isotherm of cage **3.1** on acidic alumina from water, b) Adsorption isotherm of cage **3.2** on basic alumina from water, c) Adsorption isotherm of complex **3.3** on basic alumina from water, d) Adsorption isotherm of complex **3.4** on acidic alumina from water. The isotherm data were fitted to Equation 3.1.

The values of the fitted parameters for the adsorption isotherms of **3.1** – **3.4** are given in Table 3.1

Table 3.1: Fitted parameter values for the solution-phase BET model applied to adsorption isotherms of **3.1** – **3.4**

System	θ_{MONO} / μmol$_{\text{adsorbate}}$ g^{-1}$_{\text{alumina}}$	K_S / M^{-1}	K_L / M^{-1}
Cage **3.1** / Acidic Alumina	15(1)	$3(1) \times 10^5$	~ 0
Cage **3.2** / Basic Alumina	5.3(5)	$2.3(7) \times 10^6$	$7(6) \times 10^2$
Complex **3.3** / Basic Alumina	5.5(2)	$7.4(4) \times 10^3$	$1.9(2) \times 10^2$
Complex **3.4** / Acidic Alumina	30(2)	$4.8(4) \times 10^3$	$8(4) \times 10^1$

The lower values of K_S for complexes **3.3** and **3.4**, relative to those for cages **3.1** and **3.2**, are attributed to a lower overall charge density of the mononuclear complexes. The non-zero values of K_L for **3.2** and **3.3** suggest the gradual formation of electrostatic multilayers of cations and anions at the alumina surface as the equilibrium adsorbate concentration increases; the large fractional error in these values is likely to have resulted from the multilayer stacking being significantly weaker than the monolayer interaction. In contrast, little multilayer adsorption, *i.e.* monolayer adsorption only, was observed for cage **3.1** which suggests that the spherical sodium counterions may be too well hydrated to support the formation of electrostatic multilayers. Similarly, in the case of complex **3.4** the small value of K_L suggests only the weak formation of electric multilayers perhaps again due to solvation of the potassium counterions.

3.2.4 Adsorption Kinetics

The solution depletion method was also used to investigate the kinetics of the adsorption of cage **3.1** on acidic alumina by varying the length of time for which a series of samples were allowed to equilibrate (Figure 3.11). The data in Figure 3.11 were fitted to the model of second order adsorption kinetics developed by Blanchard *et al.*:[36]

$$\theta = \theta_{MAX} \left(1 - \frac{1}{\theta_{MAX}kt + 1}\right) \qquad \text{Equation 3.2}$$

in which θ is again the total surface coverage (μmol$_{\text{adsorbate}}$ g^{-1}$_{\text{alumina}}$), θ_{MAX} is the maximum surface coverage (μmol$_{\text{adsorbate}}$ g^{-1}$_{\text{alumina}}$), k is the second-order rate constant (M^{-1} s^{-1}), and t is the equilibration time (s).

Equation 3.2 can be re-arranged into the following linear form:

$$\frac{1}{\theta} = \frac{1}{\theta_{MAX}} + \frac{1}{\theta_{MAX}^2 kt} \qquad \text{Equation 3.3}$$

From Equation 3.3 it is clear that a plot of inverse surface coverage against inverse equilibration time should be a straight line.

The data in Figure 3.11a indicate that the surface coverage of **3.1** on acidic alumina reached over 95% of its maximum value within 5 minutes, thereby indicating that cage adsorption occurs rapidly. Figure 3.11b shows that the data are consistent with Blanchard's model of second order adsorption kinetics by transforming the data to the form of Equation 3.3.
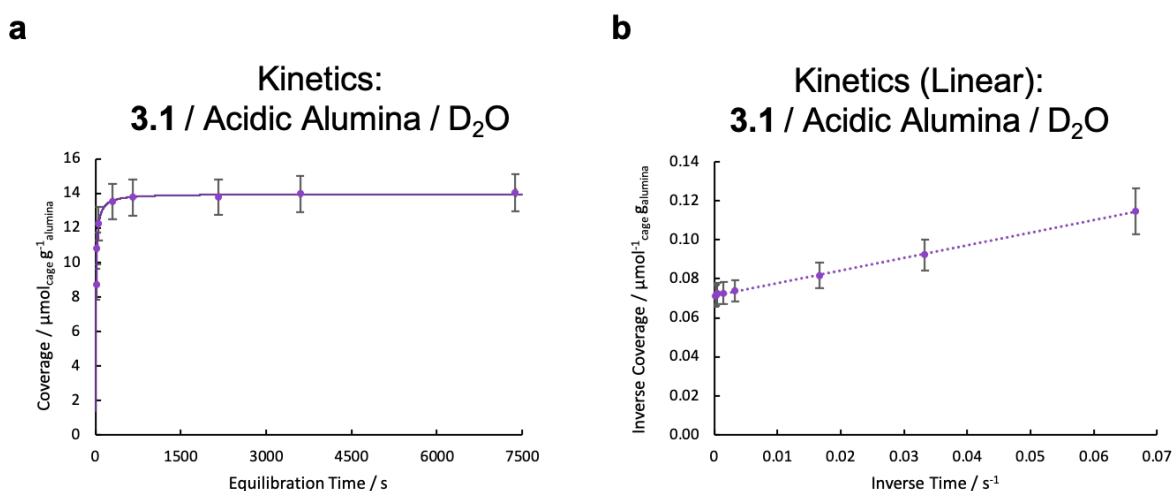

a Kinetics:
3.1 / Acidic Alumina / D_2O

b Kinetics (Linear):
3.1 / Acidic Alumina / D_2O

Figure 3.11: a) Plot of the surface coverage of cage **3.1** on acidic alumina as a function of equilibration time, b) Plot of the inverse of the coverage of cage **3.1** on acidic alumina against inverse time. The data in Figure 3.10a are fitted Equation 3.2, $\theta_{MAX} = 13.97(3)$ $\mu mol_{adsorbate}$ $g^{-1}_{alumina}$, $k = 8.1(2) \times 10^{-3}$ s^{-1}. The data in Figure 3.11b have been transformed to the form of Equation 3.3, $y = 0.6406\,x + 0.0715$, $R^2 = 0.9992$.

3.2.5 Cage Desorption

Sections 3.2.3 and 3.2.4 demonstrated that anionic cage **3.1** adsorbed under acidic conditions, *i.e.* a positively charged alumina surface, and cationic cage **3.2** adsorbed under basic conditions, *i.e.* a negatively charged alumina surface, in keeping with intuition from a consideration of electrostatics. Thus, it was postulated that adsorbed cages **3.1** and **3.2** would desorb from their alumina supports under basic and acidic conditions, respectively.

Accordingly, the suspension of cage **3.1** on acidic alumina in aqueous sodium hydroxide resulted in desorption of the intact cage at pD *ca*. 9-10 (by indicator paper), as observed by [1]H

NMR (Figure 3.12a). Likewise, the suspension of cage **3.2** on basic alumina in aqueous hydrochloric acid resulted in the desorption of the intact cage at pD *ca.* 4-5 (by indicator paper), as observed by ^{1}H NMR (Figure 3.12b).
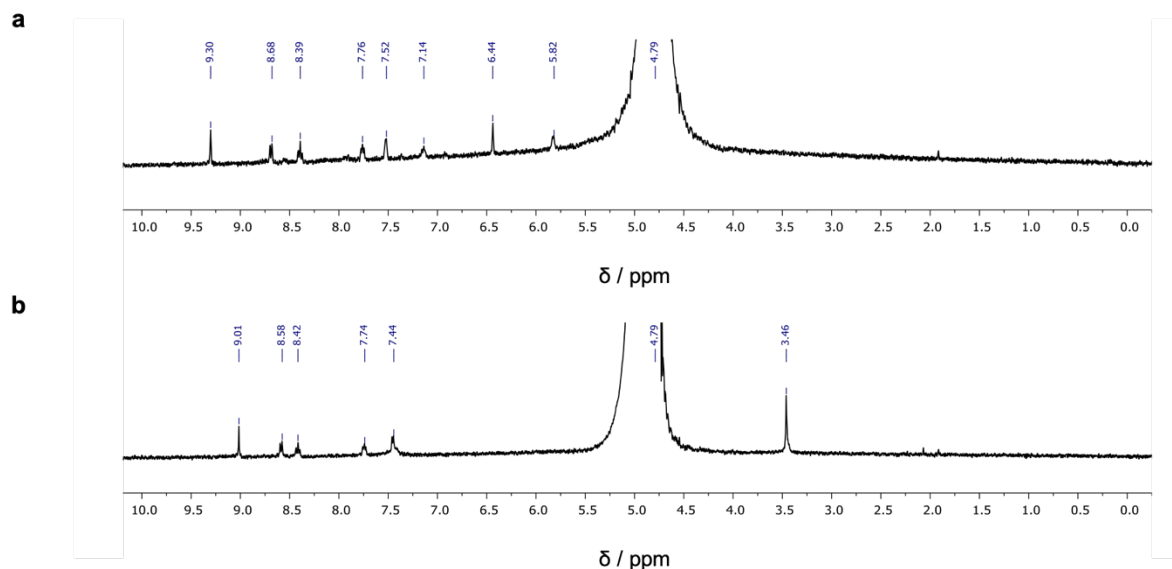
Figure 3.12: a) ^{1}H NMR (400 MHz, 298 K) spectrum of the supernatant solution after cage **3.1** on acidic alumina was suspended in aqueous NaOH (*ca.* 11.3 mM, pD 9-10 by indicator paper), b) ^{1}H NMR (400 MHz, 298 K) spectrum of the supernatant solution after cage **3.2** on basic alumina was suspended in aqueous HCl (*ca.* 1.1 mM, pD 4-5 by indicator paper).

3.2.6 Spectroscopic Analysis

The arsenal of analytic techniques typically employed in the study of metal-organic coordination cages includes ^{1}H NMR spectroscopy, single-crystal X-ray diffraction, and mass spectrometry. In the case of the adsorption of cages on to particulate alumina, however, these techniques are less directly applicable and hence alternative methods were sought.

The coordination of iron(II) to the bidentate pyridyl-imine motif results in a Metal-Ligand Charge Transfer (MLCT) band in the visible region of the electromagnetic spectrum. Species **3.1** – **3.4** are thus strongly coloured; **3.1** and **3.2** are purple (local absorption maxima at 572 and 571 nm, respectively), **3.3** is hot pink (local maximum at 559 nm), and **3.4** is red (local maximum at 536 nm) in aqueous solution (Figure 3.13). Following the adsorption of **3.1** – **3.4**, the white alumina substrates became purple (**3.1**, **3.2**), pink (**3.3**), and red (**3.4**) and hence the visible transmission spectra of the solid samples were recorded (Figure 3.14). The visible

transmission spectra show that the MLCT bands of **3.1** – **3.4** persist once adsorbed on the alumina, indicating that the iron(II) centres remained bound to the pyridyl-imine motifs, with red-shifts of *ca*. 13, 8, 7, and 6 nm observed for **3.1**, **3.2**, **3.3**, and **3.4** respectively. The surface MLCT band of cage **3.1** was observed to persist over the timescale of weeks/months but the band for cage **3.2** decayed spectroscopically and by inspection over the period of 24 hours (see Section 3.5.6); these observations suggest that cage **3.1** remained intact on the surface over a long period of time whereas cage **3.2** is likely to have decomposed possibly due to strong electrostatic forces on the alumina surface.
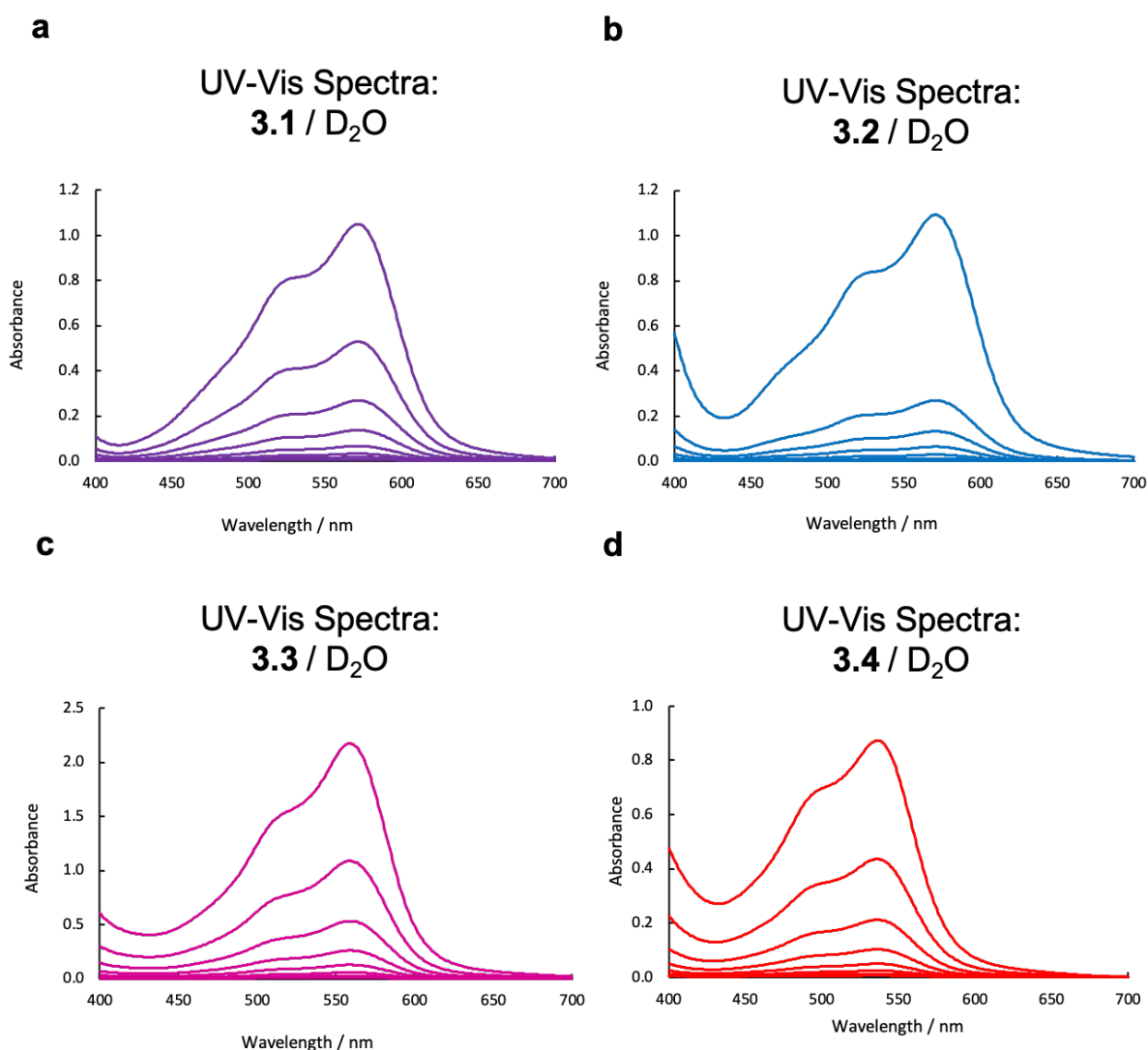
Figure 3.13: a) UV-Vis spectra of cage **3.1** in D_2O in the range 0 – 0.5 mM, UV-Vis spectra of cage **3.2** in D_2O in the range 0 – 0.4 mM, c) UV-Vis spectra of complex **3.3** in D_2O in the range 0 – 2 mM, d) UV-Vis spectra of complex **3.4** in D_2O in the range 0 – 1.6 mM. The data in Figures 3.13a-c were collected by Dr Cally Haynes using samples prepared by Mr Hugh Ryan.

a

Transmission Spectrum: 3.1 / Acidic Alumina

b

Transmission Spectrum: 3.2 / Basic Alumina

c

Transmission Spectrum: 3.3 / Basic Alumina

d

Transmission Spectrum: 3.4 / Acidic Alumina
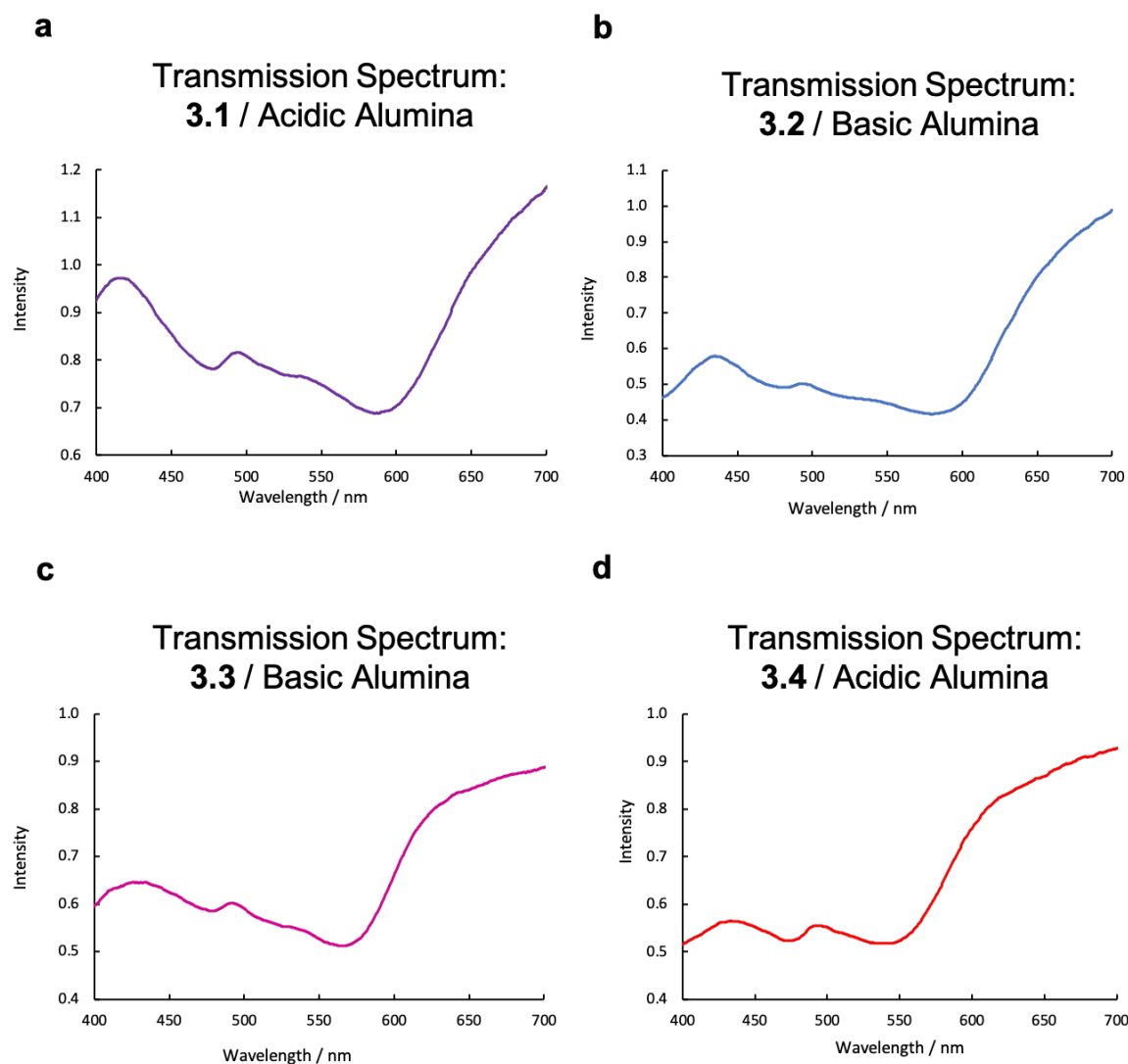
Figure 3.14: a) Visible transmission spectrum of cage **3.1** on acidic alumina, referenced to bare acidic alumina, b) Visible transmission spectrum of cage **3.2** on basic alumina, referenced to bare basic alumina, c) Visible transmission spectrum of complex **3.3** on basic alumina, referenced to bare basic alumina, d) Visible transmission spectrum of complex **3.4** on acidic alumina, referenced to bare acidic alumina. The data in Figures 3.14a-d were collected by Ms Alyssa Smith using samples prepared by Mr Hugh Ryan.

The X-ray photoelectron spectra of **3.1** on acidic alumina and bare acidic alumina were also recorded (Figure 3.15). Cage **3.1** on acidic alumina was chosen for this experiment because this system contains the greatest surface coverage of iron(II); whilst the monolayer surface coverage of **3.4** on acidic alumina is larger than that of **3.1** on acidic alumina, each unit of **3.1** contains four times as many iron atoms. The spectrum of **3.1** on acidic alumina indicates the presence of iron and nitrogen on the alumina surface following the adsorption of **3.1** at binding energies of 728 and 399 eV, respectively. Tables 3.2 and 3.3 present the relative abundances

of the elements identified in each system. The atomic percentage of iron (0.23 %) is also broadly consistent with the value of monolayer coverage of 15 $\mu mol_{adsorbate}$ $g^{-1}_{alumina}$ derived from the adsorption isotherm of **3.1** on acidic alumina (see Appendix). The sum of the atomic percentages in Table 3.3 is not equal to unity, most likely due to the trace presence of other elements.
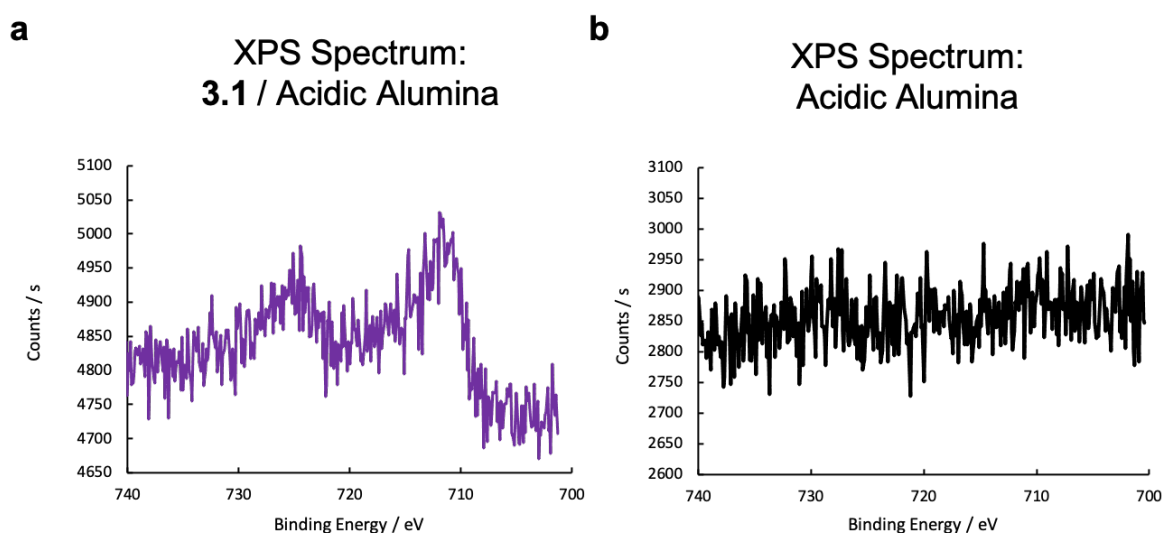
Figure 3.15: a) XPS spectrum of cage **3.1** on acidic alumina in the Fe2p region, b) XPS spectrum of bare acidic alumina in the Fe2p region. The data in Figures 3.15a-b were collected by Dr Mohamed Al-Hada using samples prepared by Mr Hugh Ryan.

Table 3.2: Elemental composition of cage **3.1** on acidic alumina

Element (Orbital)	Binding Energy / eV	Atomic Percentage
Aluminium (2p)	75.16	20.3
Carbon (1s)	285.89	42.8
Nitrogen (1s)	399.08	0.9
Oxygen (1s)	531.73	35.8
Iron (2p)	727.82	0.2

Table 3.3: Elemental composition of bare acidic alumina

Element (Orbital)	Binding Energy / eV	Atomic Percentage
Aluminium (2p)	75.12	36.7
Carbon (1s)	285.29	7.0
Oxygen (1s)	531.85	56.3

The energy-dispersive X-Ray spectra of **3.1**, **3.2**, and **3.4** on alumina likewise show the presence of iron on the alumina surface following adsorption (Figure 3.16 – 3.19). The spectra of **3.1** and **3.4** on acidic alumina show the presence of surface sulphur due to the sulphonate groups present in these complexes and the presence of surface chlorine due to the acidic activation of the alumina. In the case of complex **3.3** on basic alumina, however, the net surface coverage of iron (II) was too low to be detected; whilst the monolayer surface coverages of **3.2** and **3.3** on basic alumina are comparable (see Table 3.1), the iron (II) content of **3.3** is four times less than that of **3.2** and thus the iron content of **3.3** on basic alumina is an order of magnitude lower than that of the other systems studied. Additionally, the spectra of the bare acidic and basic aluminas do not show the presence of iron prior to adsorption of **3.1** – **3.4** (Figures 3.20 and 3.21).
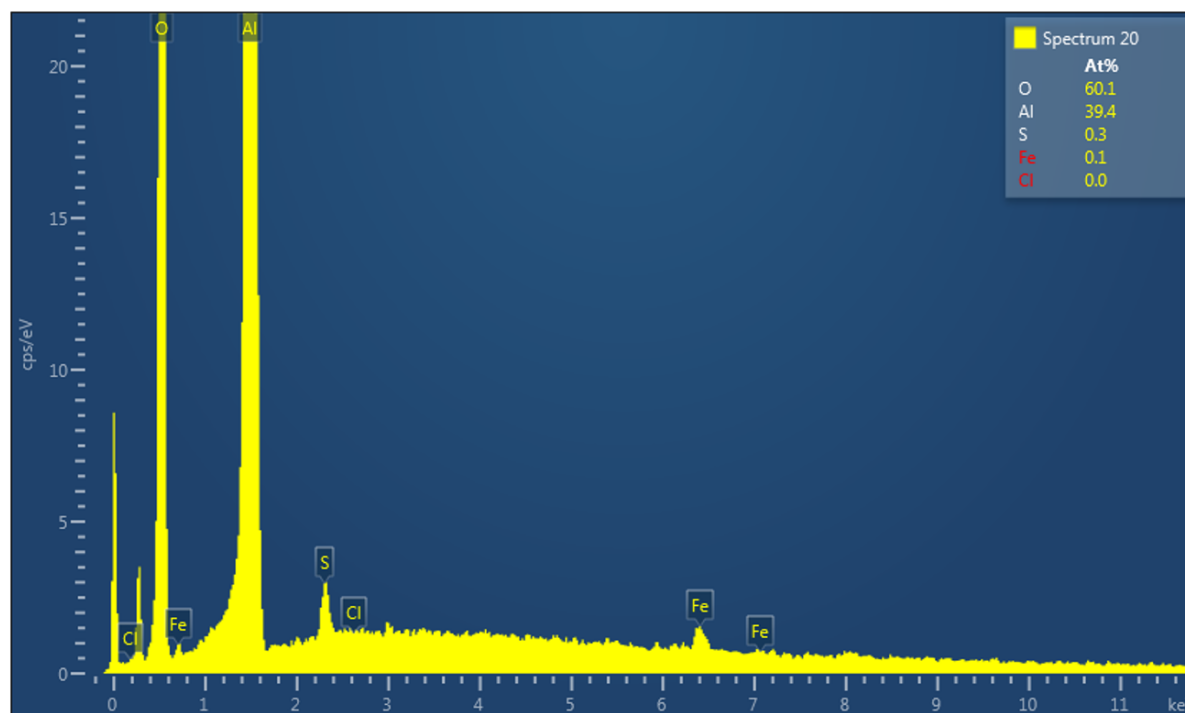
Figure 3.16: EDX spectrum of cage **3.1** on acidic alumina. The data were collected by Dr Heather Greer using a sample prepared by Mr Hugh Ryan.
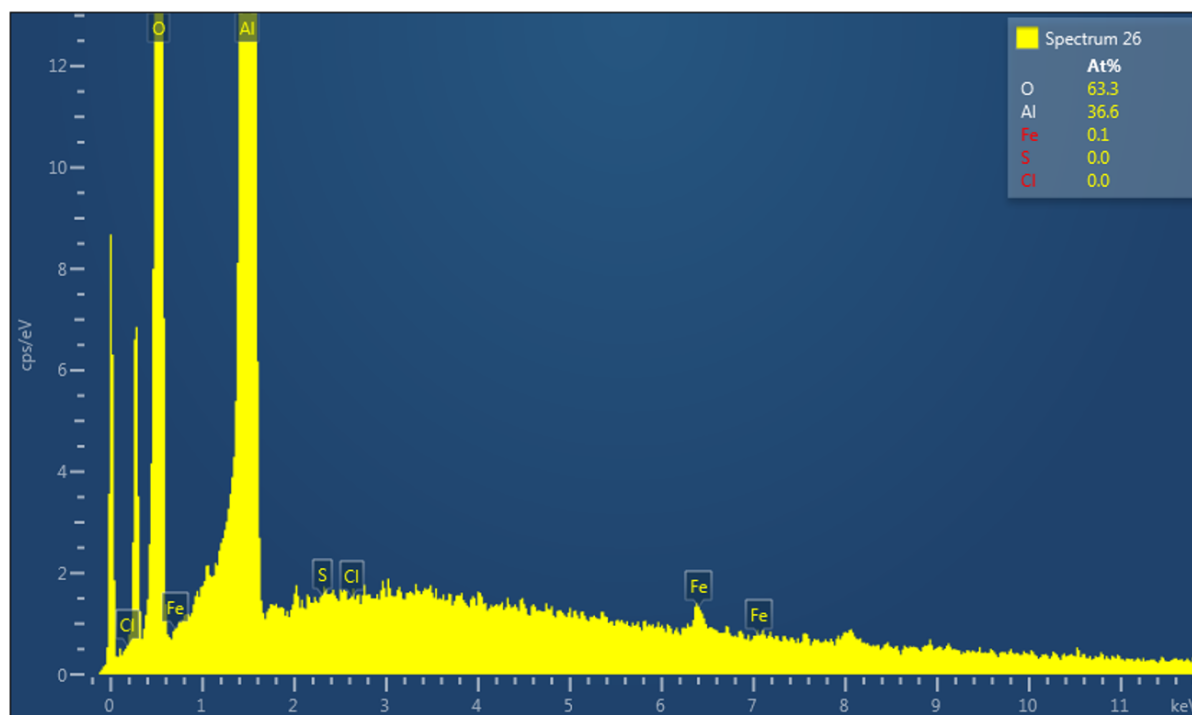
Figure 3.17: EDX spectrum of cage **3.2** on basic alumina. The data were collected by Dr Heather Greer using a sample prepared by Mr Hugh Ryan.
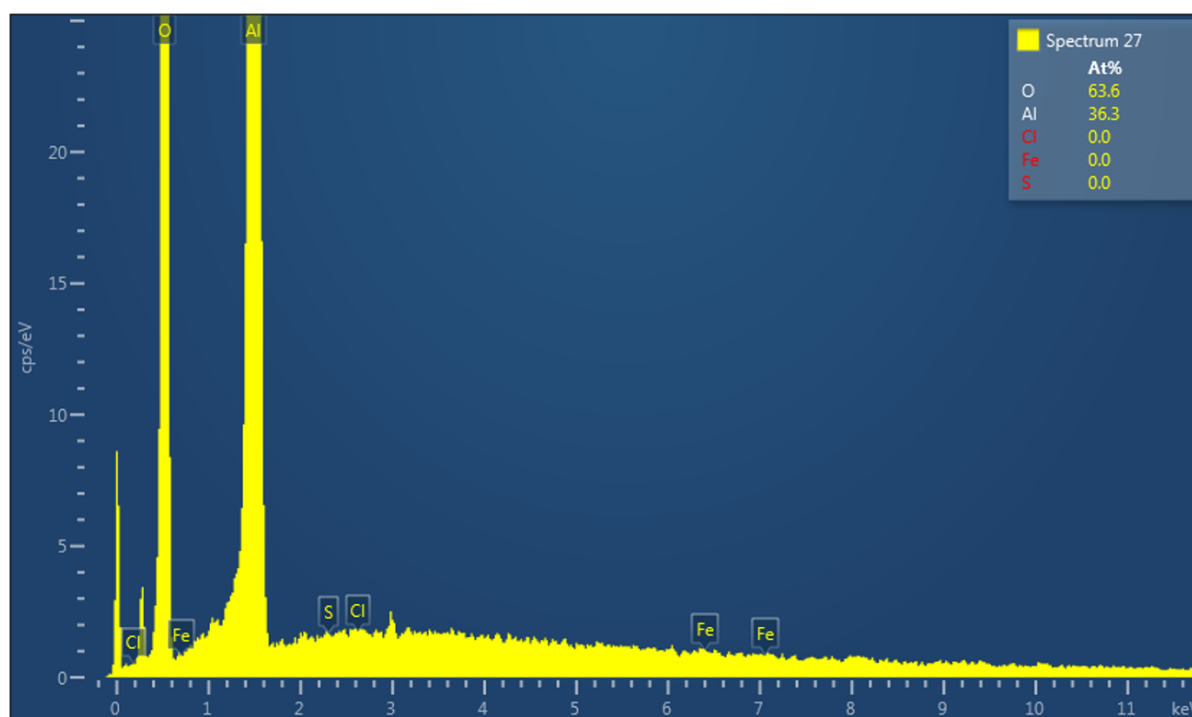
Figure 3.18: EDX spectrum of complex **3.3** on basic alumina. The data were collected by Dr Heather Greer using a sample prepared by Mr Hugh Ryan.
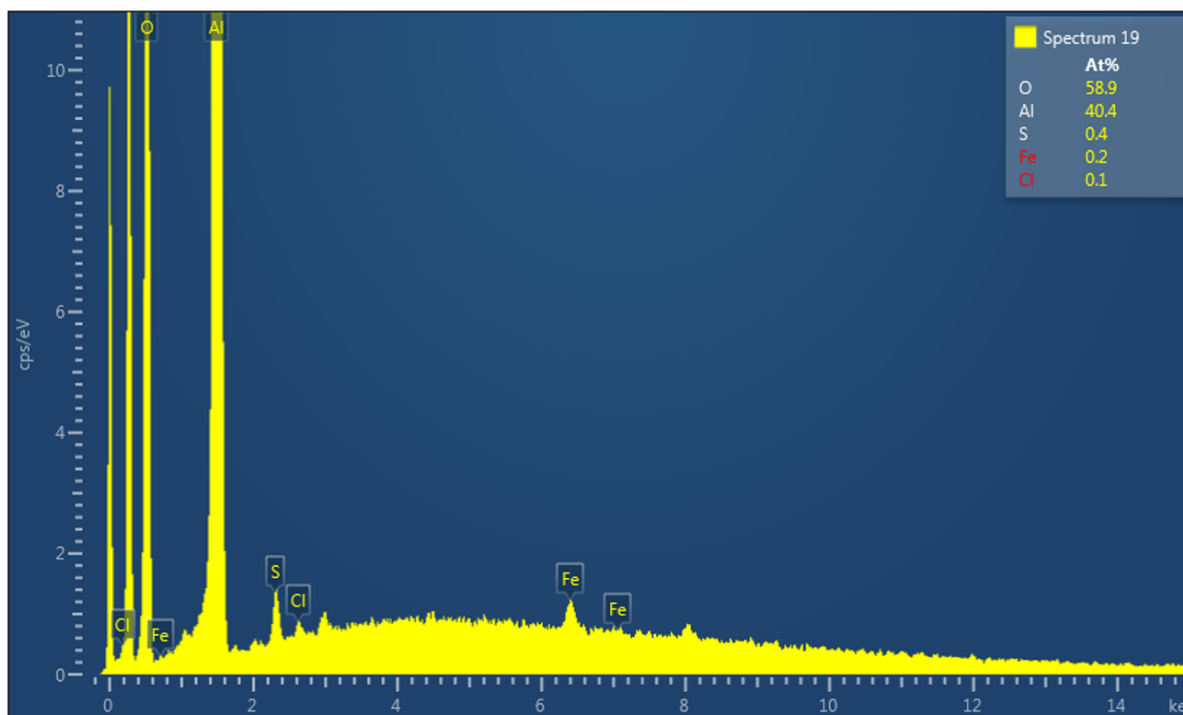
Figure 3.19: EDX spectrum of complex **3.4** on acidic alumina. The data were collected by Dr Heather Greer using a sample prepared by Mr Hugh Ryan.
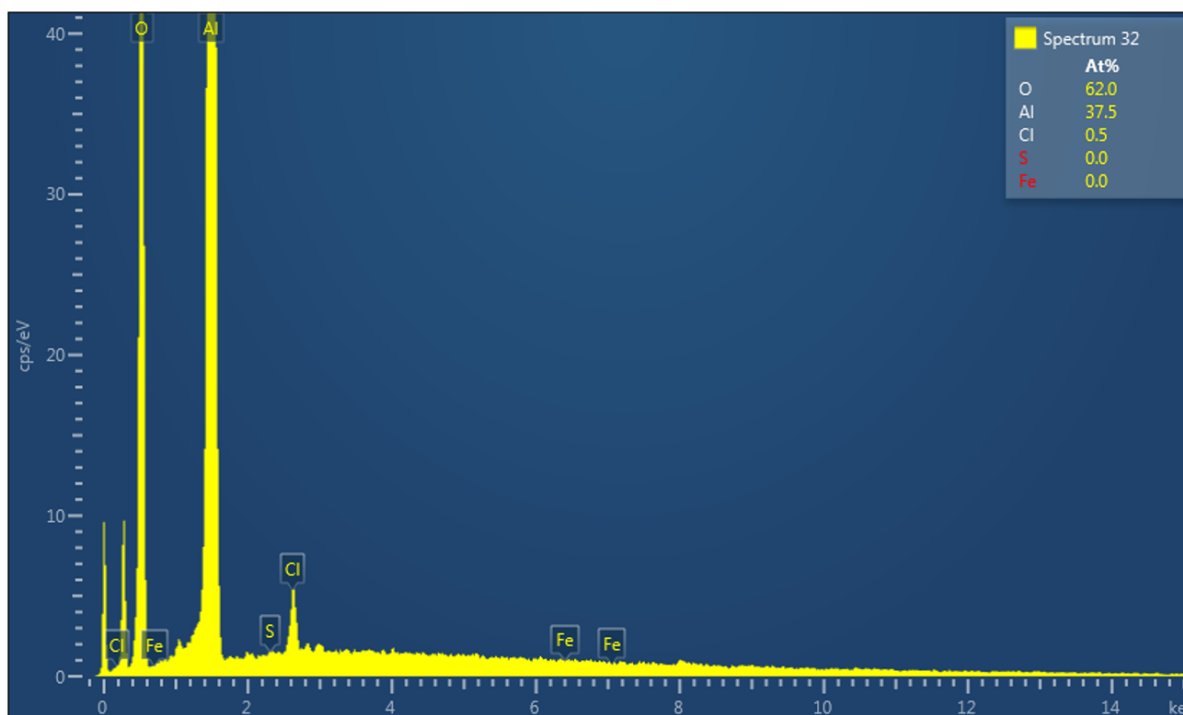
Figure 3.20: EDX spectrum of bare acidic alumina. The data were collected by Dr Heather Greer.
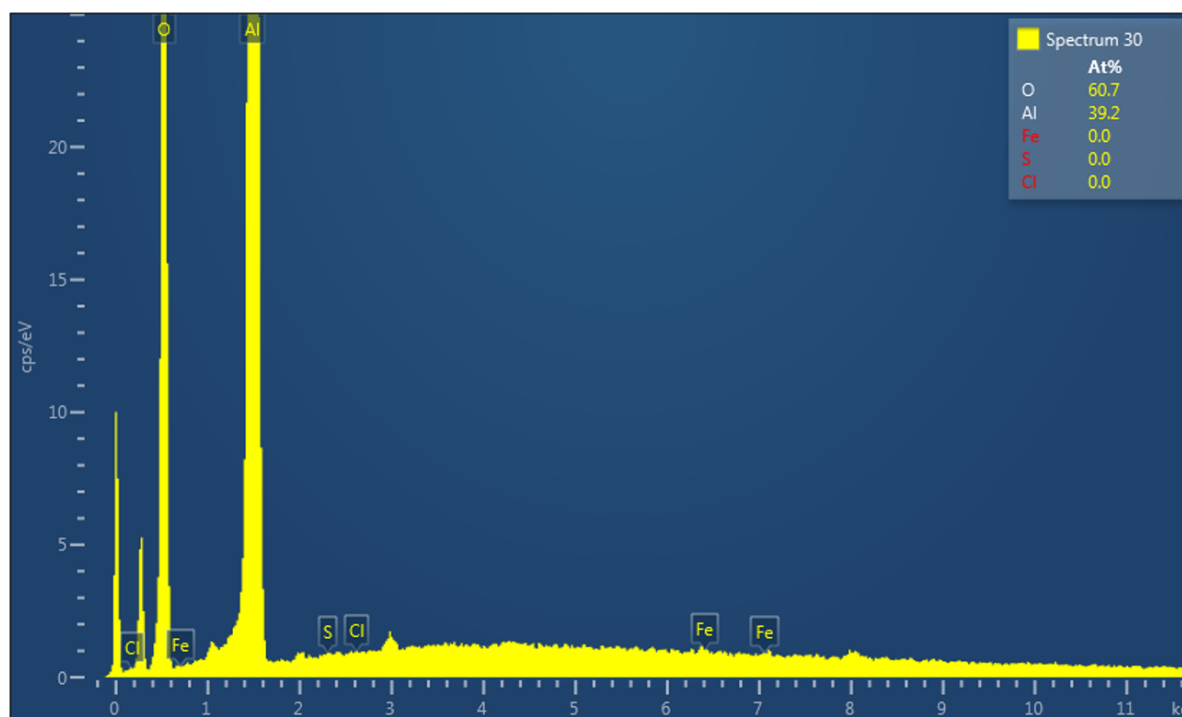
Figure 3.21: EDX spectrum of bare basic alumina. The data were collected by Dr Heather Greer.

3.2.7 Guest Displacement Under Flow

The known solution-state host-guest chemistry of cages **3.1** and **3.2** was used to demonstrate the preservation of their cage cavities, following adsorption, *via* a series of guest displacement experiments under flow conditions.[27,29] Alumina-bound cage was loaded into a syringe plugged with cotton wool and eluted with an aqueous solution of a known guest (Figure 3.22a). The "cage column" was then washed with water to remove the excess guest and subsequently eluted with an aqueous solution of a competitive guest species. The eluates of the cage column were then analysed *via* ^{1}H NMR spectroscopy.

45
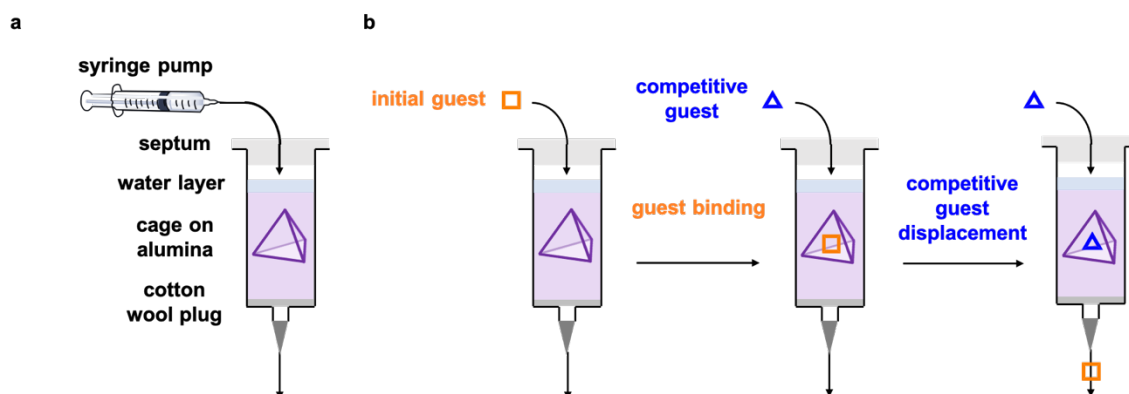
Figure 3.22: a) The "cage column" setup, b) Guest displacement schematic – an initial guest is bound within the adsorbed cage and is subsequently displaced upon the addition of a competitive guest.[37] Figure 3.22 was reproduced and adapted with permission from reference 37.

The method described above was used to demonstrate that fluorobenzene (K_a = 610 M^{-1})[27] could be displaced from cage **3.1** adsorbed on acidic alumina upon elution of the cage column with aqueous dichloromethane (K_a = 1300 M^{-1})[27]. This guest displacement process was repeated 3 times, thereby indicating that the adsorbed cage **3.1** could be recycled (see Section 3.5.11). In contrast, no fluorobenzene was observed to elute from columns of **3.4** on acidic alumina or a column of bare acidic alumina, in which no cage cavities were present (Figure 3.23). It was thus concluded that the presence of fluorobenzene in the cage column eluate was due to the displacement of fluorobenzene from the preserved cavities of **3.1** following the addition of the competitive dichloromethane guest. In the same way, fluorobenzene was also displaced from cage **3.2** adsorbed on basic alumina (Figure 3.24) whilst no fluorobenzene was observed to elute from columns of **3.3** on basic alumina and bare basic alumina.
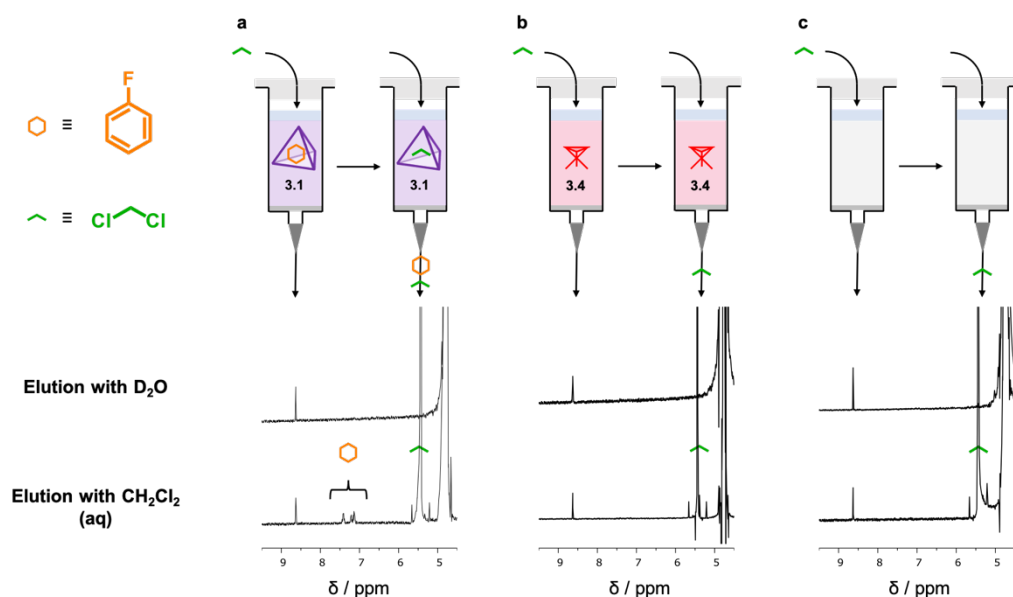
Figure 3.23: a) Schematic and partial ^{1}H NMR (400 MHz, 298 K) of fluorobenzene displaced from cage **3.1** on acidic alumina when eluted with D$_2$O and aqueous dichloromethane, b) Schematic and partial ^{1}H NMR (400 MHz, 298 K) of control experiment with complex **3.4** on acidic alumina, c) Schematic and partial ^{1}H NMR (400 MHz, 298 K) of control experiment with bare acidic alumina.[37] The peak at 8.63 ppm corresponds to pyrazine capillary. Full spectra are given in the Experimental. Figure 3.23 was reproduced and adapted with permission from reference 37.
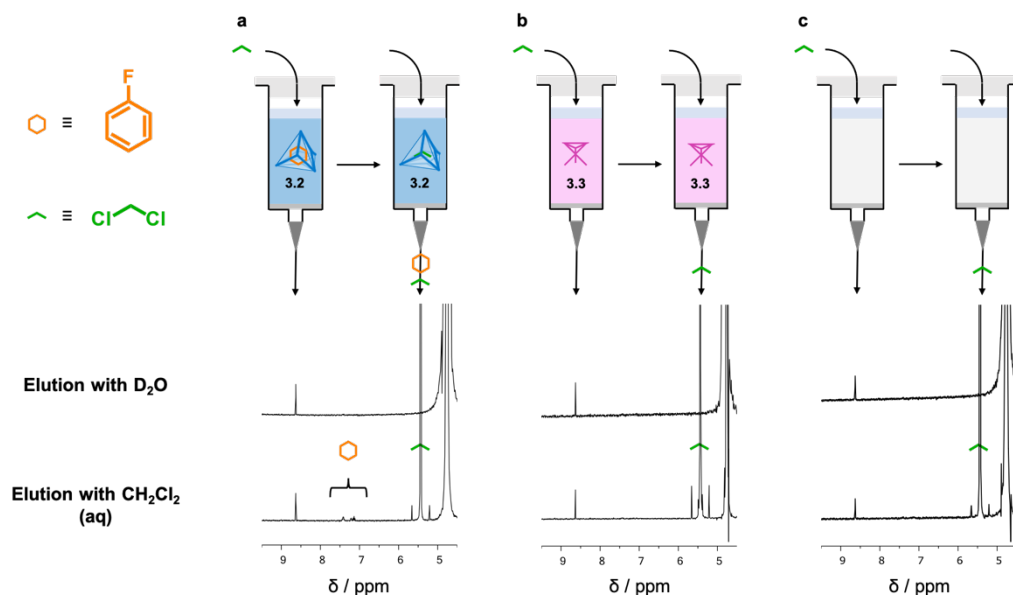
Figure 3.24: a) Schematic and partial ^{1}H NMR (400 MHz, 298 K) of fluorobenzene displaced from cage **3.2** on basic alumina when eluted with D$_2$O and aqueous dichloromethane, b) Schematic and partial ^{1}H NMR (400 MHz, 298 K) of control experiment with complex **3.3** on basic alumina, c) Schematic and partial ^{1}H NMR (400 MHz, 298 K) of control experiment with bare basic alumina. Peak at 8.63 ppm corresponds to pyrazine capillary. Full spectra are given in the Experimental.

47

In contrast, when a cage column of **3.1** on acidic alumina was first eluted with non-guest species, *i.e.* molecules which were not observed to bind *via* ^{1}H NMR such as phloroglucinol, pentaerythritol, and trifluorobenzene, no non-guest was present in the eluate upon subsequent elutions with aqueous dichloromethane (Figure 3.25). These experiments demonstrated that the non-guest species were not retained on the column following the washing steps, *i.e.* they were not bound within adsorbed **3.1**, thereby further supporting the preservation of the cage cavities following adsorption.
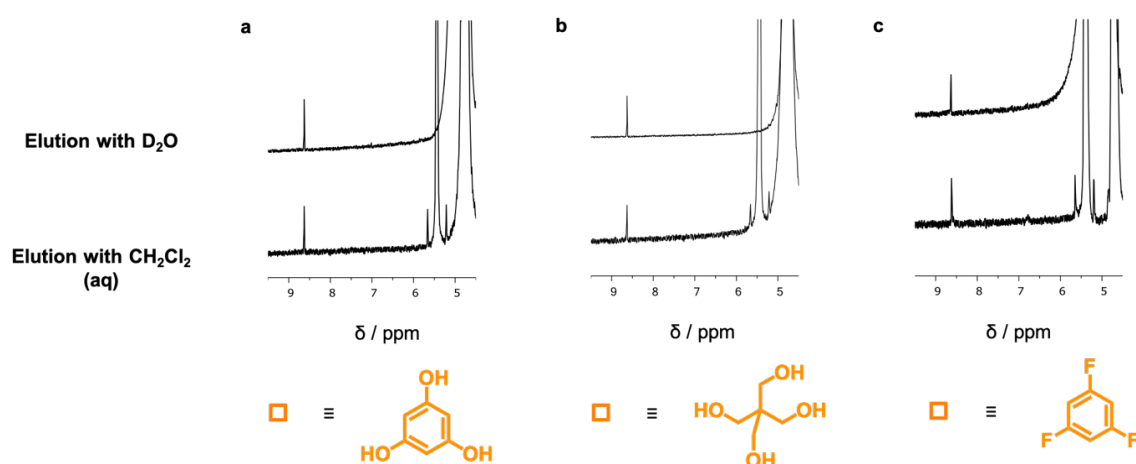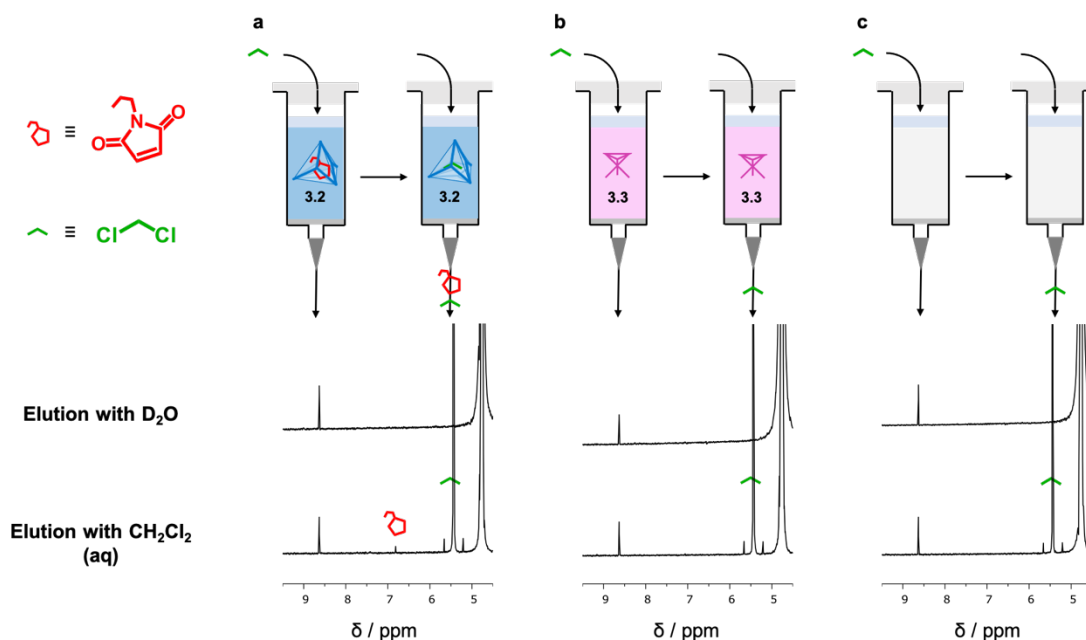

Figure 3.25: a) Partial ^{1}H NMR (400 MHz, 298 K) of cage column of **3.1** on acidic alumina "loaded" with initial non-guest phloroglucinol, b) Partial ^{1}H NMR (400 MHz, 298 K) of cage column of **3.1** on acidic alumina "loaded" with initial non-guest pentaerythritol, c) Partial ^{1}H NMR (400 MHz, 298 K) of cage column of **3.1** on acidic alumina "loaded" with initial non-guest trifluorobenzene. Peak at 8.63 ppm corresponds to pyrazine capillary. Full spectra are given in the Experimental.

A cage column of **3.1** on acidic alumina was also used to separate a mixture of guest and non-guest. The cage column was eluted with a mixture of fluorobenzene and trifluorobenzene (see Section 3.5.10) and then eluted with aqueous dichloromethane. The eluates were analysed by ^{1}H and ^{19}F NMR spectroscopy and contained mostly fluorobenzene with only a trace concentration of trifluorobenzene, the latter most likely due to adsorption to the alumina or weak association with the adsorbed cage (Figure 3.26). A column of adsorbed cage **3.1** was thus able to separate a mixture of guest and non-guest.
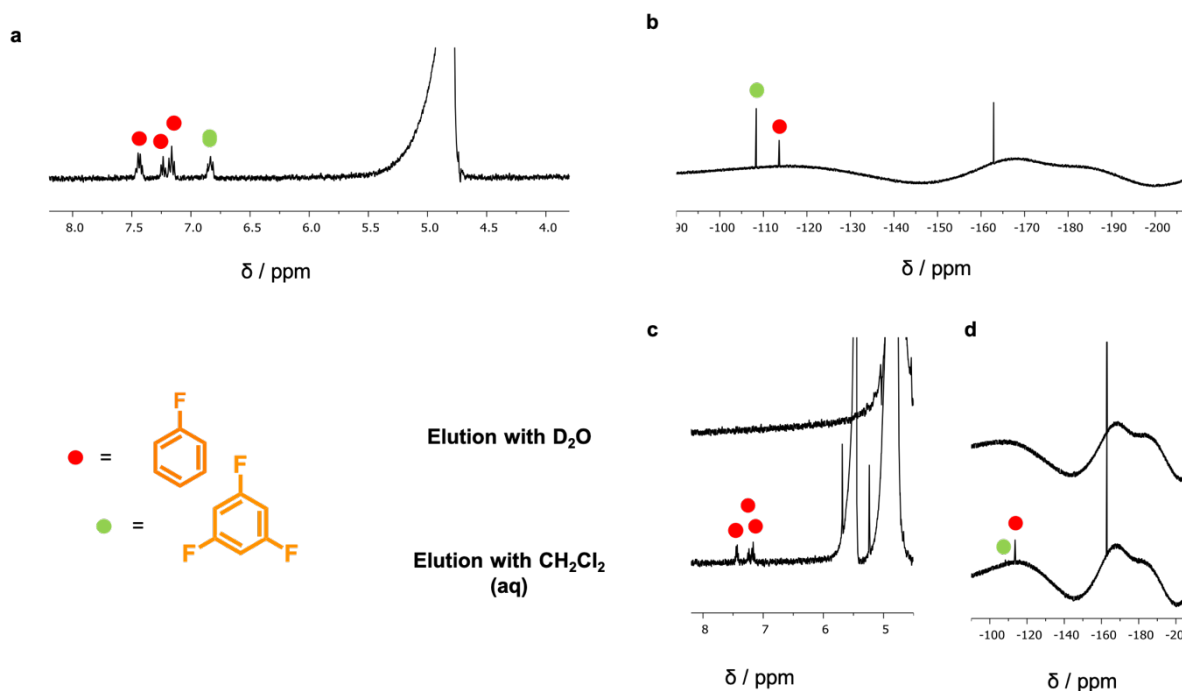
Figure 3.26: a) ^{1}H NMR (400 MHz, 298 K) spectrum of an aqueous mixture of fluorobenzene (*ca.* 2 mM, peaks at 7.43, 7.23, 7.16 ppm) and trifluorobenzene (*ca.* 2 mM, peak at 6.83 ppm) for guest separation experiment (referenced to residual solvent at 4.79 ppm), b) ^{19}F NMR (400 MHz, 298 K) spectrum of an aqueous mixture of fluorobenzene (*ca.* 2 mM, peak at -113.6 ppm) and trifluorobenzene (*ca.* 2 mM, peak at -108.4 ppm) for guest separation experiment (referenced to hexafluorobenzene at -162.9 ppm), c) Partial ^{1}H NMR (400 MHz, 298 K) spectra of guest separation when the cage column was eluted with aqueous dichloromethane, d) Partial ^{19}F NMR (400 MHz, 298 K) spectra of guest separation when the cage column with eluted with aqueous dichloromethane. Full spectra are given in the Experimental.

Finally, a system of adsorbed cages **3.1** and **3.2** was used to spatially separate the components of a Diels-Alder reaction for subsequent release and reaction. In solution, cages **3.1** and **3.2** bound cyclopentadiene and N-propyl maleimide with estimated binding constants of 1500 M^{-1} and 1200 M^{-1} and estimated ingress rate constants of $1.90(2) \times 10^{-3}$ M^{-1} s^{-1} and $2.6(1) \times 10^{-3}$ M^{-1} s^{-1}, respectively, *via* ^{1}H NMR spectroscopy (see Section 3.5.8). The guest loading and displacement procedure described above was thus used to show that cyclopentadiene and N-propyl maleimide could be loaded on to and subsequently displaced from columns of adsorbed **3.1** and **3.2**, respectively (Figures 3.27 and 3.28); in contrast, no guest release was observed from columns of adsorbed **3.3**, adsorbed **3.4**, or bare alumina.
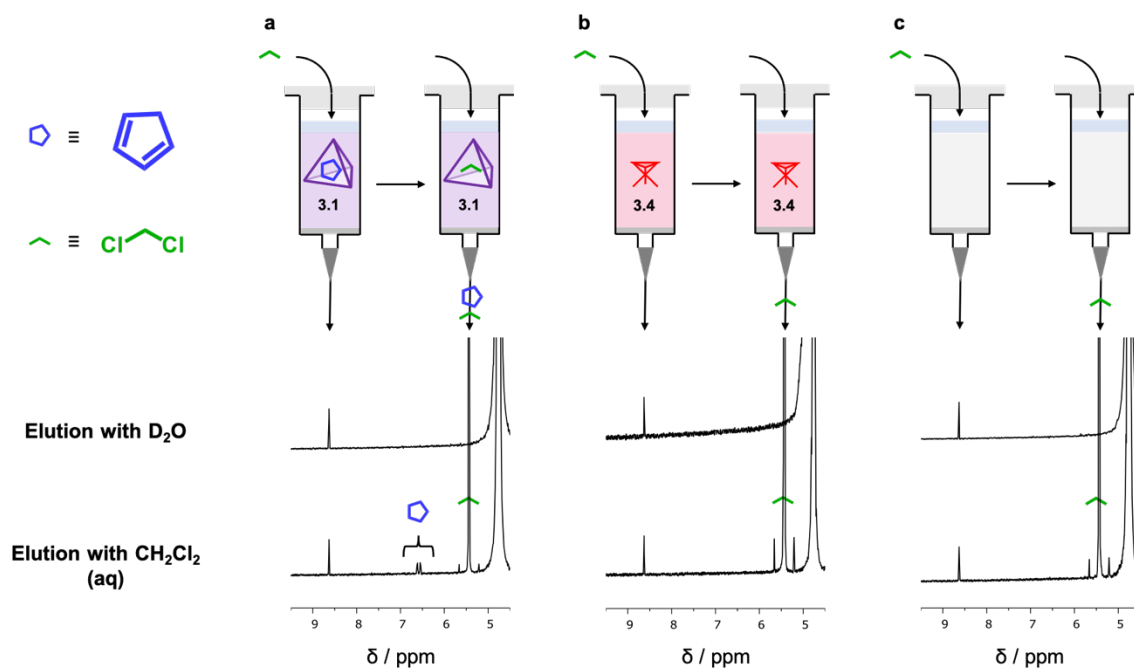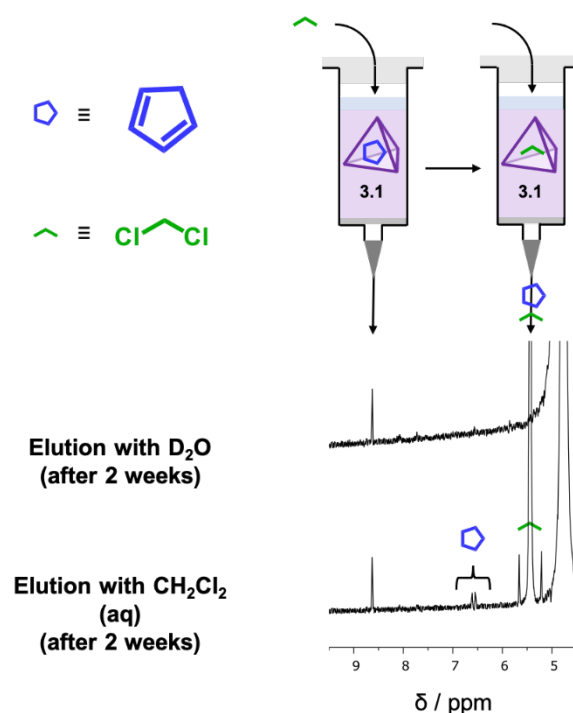
Figure 3.27: a) Schematic and partial ^{1}H NMR (400 MHz, 298 K) of cyclopentadiene displaced from cage **3.1** on acidic alumina when eluted with aqueous dichloromethane, b) Schematic and partial ^{1}H NMR (400 MHz, 298 K) of control experiment with complex **3.4** on acidic alumina, c) Schematic and partial ^{1}H NMR (400 MHz, 298 K) of control experiment with bare acidic alumina. Peak at 8.63 ppm corresponds to pyrazine capillary. Full spectra are given in the Experimental.

Figure 3.28: a) Schematic and partial ^{1}H NMR (400 MHz, 298 K) of N-propyl maleimide displaced from cage **3.2** on basic alumina when eluted with aqueous dichloromethane, b) Schematic and partial ^{1}H NMR (400 MHz, 298 K) of control experiment with complex **3.3** on basic alumina, c) Schematic and partial ^{1}H NMR (400 MHz, 298 K) of control experiment with bare basic alumina. Peak at 8.63 ppm corresponds to pyrazine capillary. Full spectra are given in the Experimental.

Furthermore, cyclopentadiene is a highly reactive species which is known to dimerise in the neat state on the timescale of hours; with cage **3.1** on acidic alumina, however, the monomeric cyclopentadiene could be loaded on to the column and still be released intact after two weeks (Figure 3.29).

Figure 3.29: Schematic and partial ^{1}H NMR (400 MHz, 298 K) of cyclopentadiene displaced from cage **3.1** on acidic alumina when eluted with aqueous dichloromethane, 2 weeks after the initial loading. Peak at 8.63 ppm corresponds to pyrazine capillary. Full spectra are given in the Experimental.

In order to separate the Diels-Alder components, cage columns of adsorbed **3.1** and **3.2** were loaded separately with cyclopentadiene and N-propyl maleimide, respectively, using the same loading procedure described in Figure 3.22, and then connected in series. The entire "double" cage column was then eluted with aqueous dichloromethane and subsequently the Diels-Alder adduct was observed in the eluate (Figure 3.30b). This experiment was also conducted with the cage columns connected in series prior to loading with the diene and dienophile, yielding a similar result (Figure 3.30c).
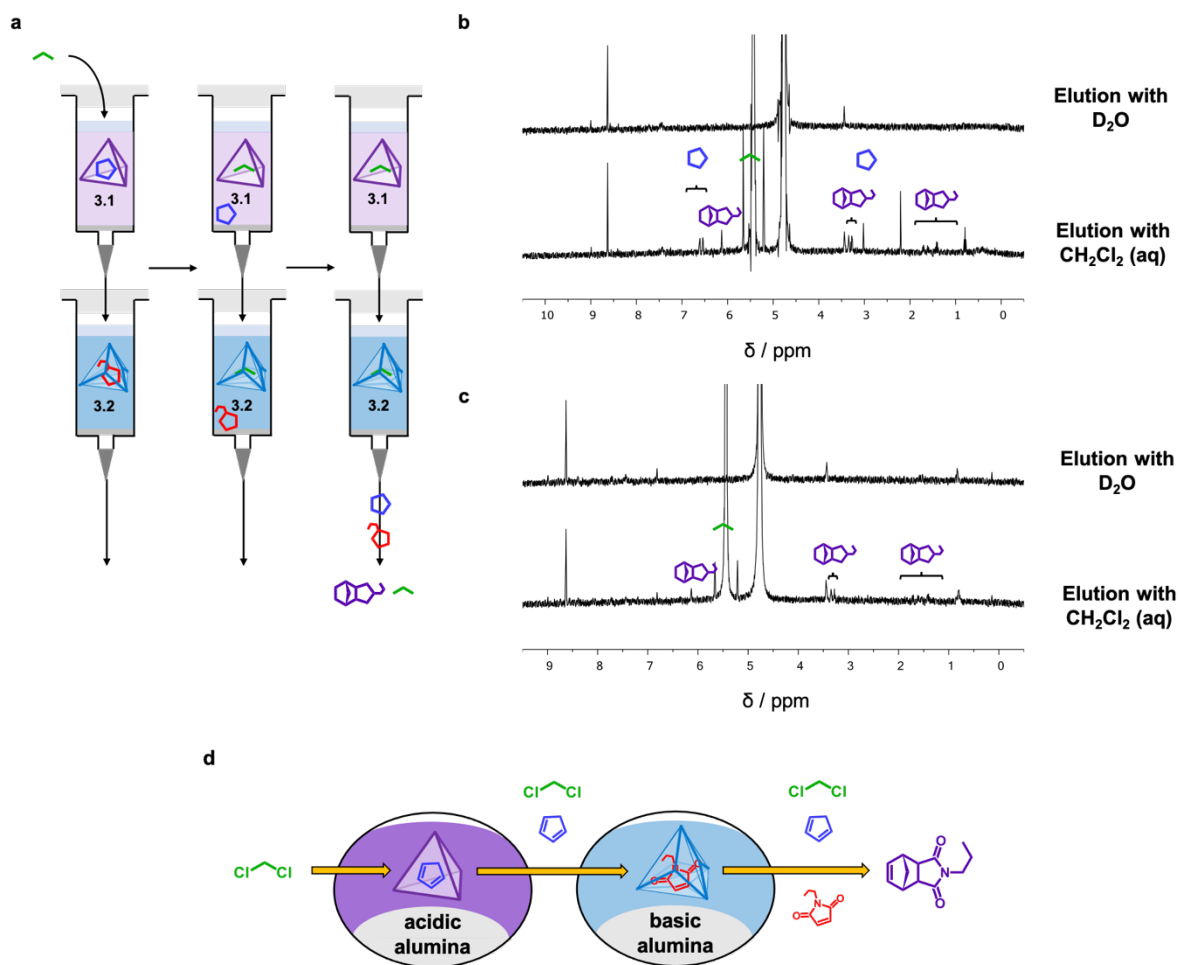
Figure 3.30: a) Schematic of displacement of cyclopentadiene and N-propylmaleimide from adsorbed cages **3.1** and **3.2**, respectively, upon the addition of aqueous dichloromethane, b) Partial ^{1}H NMR (400 MHz, 298 K) of system elution with D$_2$O and aqueous dichloromethane when initially loaded separately (peak at 8.63 ppm corresponds to pyrazine capillary), c) Partial ^{1}H NMR (400 MHz, 298 K) of system elution with D$_2$O and aqueous dichloromethane when initially loaded pre-stacked (peak at 8.63 ppm corresponds to pyrazine capillary), d), Schematic of overall Diels-Alder component separation and subsequent reaction.[37] Full spectra are given in the Experimental. Figures 3.30a, 3.30b, and 3.30d were reproduced and adapted with permission from reference 37.

3.3 Adsorption From Acetonitrile

3.3.1 Cage Systems Studied

The previous section detailed the adsorption of two tetrahedral coordination cages from water. In general, however, the polytopic organic subcomponents used in the self-assembly process are typically poorly soluble in water and thus organic solvents are preferred. Furthermore, the dynamic covalent nature of the pyridyl-imine binding motif renders the imine bond highly susceptible to hydrolysis. Whilst water-solubility can be achieved *via* the use of sulphate counterions (*vide supra*), this method is not universally successful at forming indefinitely (meta)stable water-soluble structures. Thus, the majority of Nitschke's cages continue to be assembled and manipulated in organic solvents, such as acetonitrile, nitromethane, and DMF, with non-coordinating anions such as trifluoromethanesulphonate (triflate) and bis(trifluoromethane)sulphonimide (triflimide/bistriflimide). It is therefore instructive to consider the adsorption of coordination cages from organic media so that a wider array of coordination cages may be accessed for future studies.

This section explores the quantification and characterisation of the adsorption of three cationic coordination cages, **3.5 – 3.7**, on alumina from acetonitrile (Figure 3.31). Cages **3.5 – 3.7** are all based on the same triazine-centred triamine ligand as cage **3.2** but are instead assembled as triflimide salts in order to engender solubility in acetonitrile. Cages **3.5 – 3.7** were chosen for these experiments in order to investigate what effect, if any, the choice of metal vertex has on the adsorption on the cages on to alumina.
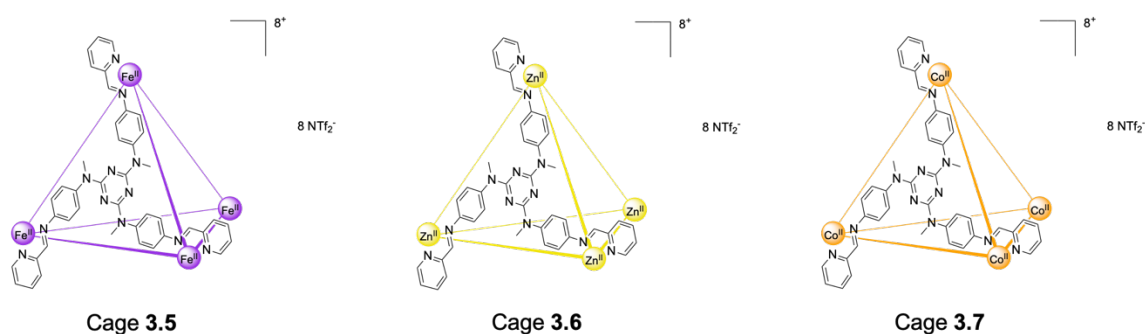
Figure 3.31: Cages **3.5 – 3.7**, based on Bolliger's triazine-centred triamine.[29,38]

3.3.2 Adsorption Isotherms

The adsorption isotherms of cages **3.5** – **3.7** on acidic and basic alumina were obtained *via* the solution depletion method (Figure 3.32), as in Section 3.2.3 (also see Experimental section 3.5.4). Cages **3.5** – **3.7** were assembled *via* modified literature procedures.[29,38] Unlike the isotherms in Section 3.2.3, the adsorption profiles of cages **3.5** – **3.7** were not consistent with Ebadi *et al.*'s solution-phase BET isotherm model and instead were more consistent with the empirical Freundlich isotherm:[39]

$$\theta = A \; c^{\frac{1}{n}} \qquad \text{Equation 3.4}$$

in which θ is again the total surface coverage (here in $\mu mol_{adsorbate} \; g^{-1}_{alumina}$) and A and n are fitted constants. The constant n is not required to have an integer value and thus, in this work, only the magnitudes of the constants A and n are reported and not their units.
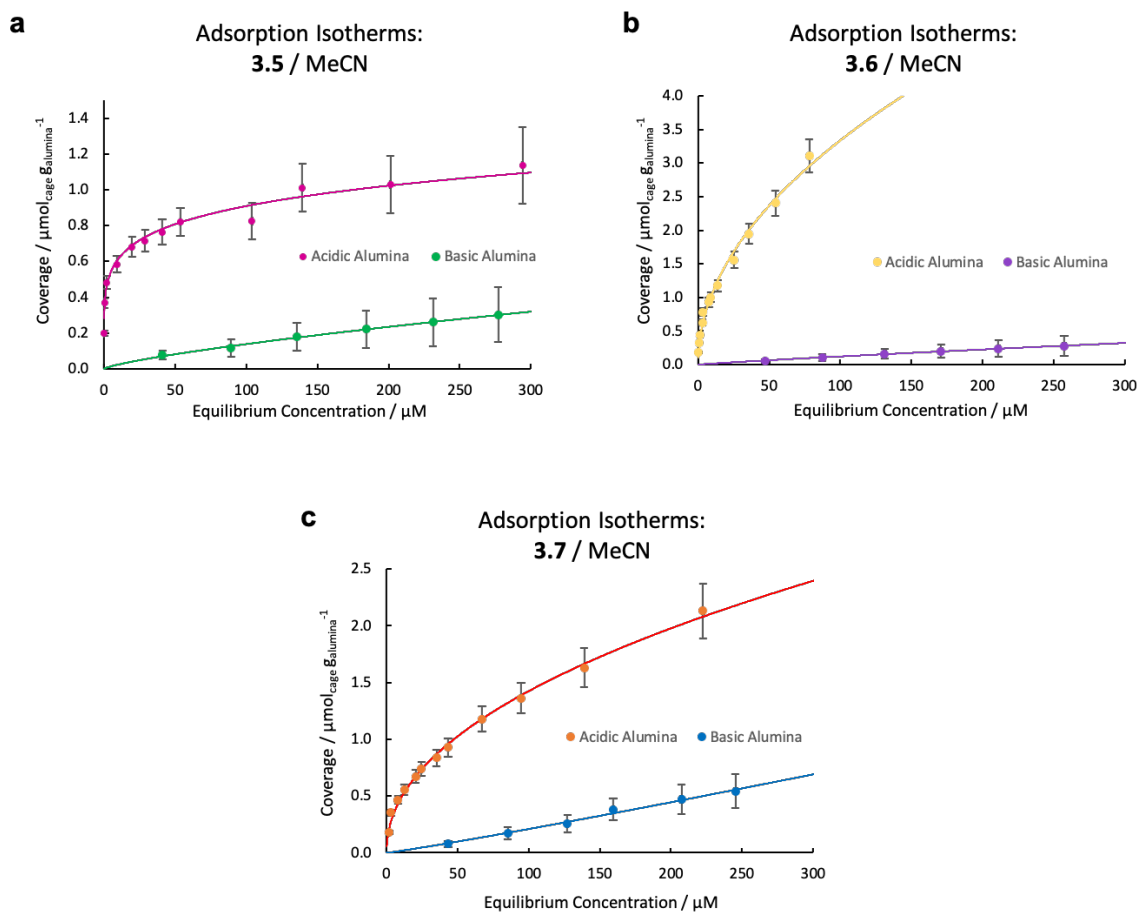
Figure 3.32: a) Adsorption isotherms of cage **3.5** on acidic and basic alumina from acetonitrile, b) Adsorption isotherms of cage **3.6** on acidic and basic alumina from acetonitrile, c) Adsorption isotherms of cage **3.7** on acidic and basic alumina from acetonitrile. The data in Figure 3.32 were fitted to Equation 3.4.

Table 3.4 summarises the values of the fitted parameters for the adsorption isotherms of **3.5** – **3.7**:

Table 3.4: Fitted parameter values for the Freundlich model applied to adsorption isotherms of **3.5** – **3.7**

System	A	n
Cage **3.5** / Acidic Alumina	$4.2(2) \times 10^{-1}$	5.9(3)
Cage **3.5** / Basic Alumina	$4.1(8) \times 10^{-3}$	1.31(7)
Cage **3.6** / Acidic Alumina	-	-
Cage **3.6** / Basic Alumina	$2.1(4) \times 10^{-3}$	1.13(5)
Cage **3.7** / Acidic Alumina	$1.61(9) \times 10^{-1}$	2.11(5)
Cage **3.7** / Basic Alumina	$1.4(6) \times 10^{-3}$	0.92(7)

Notably, as shown in Figure 3.32 and Table 3.4, cationic cages **3.5** – **3.7** adsorbed more strongly on acidic alumina than on basic alumina. This is contrary to the adsorption isotherms from water in Section 3.2.3 in which cationic species **3.2** and **3.3** adsorbed on basic alumina, *i.e.* positively charged adsorbates adsorbed on to a negatively charged substrate. One possible explanation for this observation is that, when adsorbing on acidic alumina, the first layer of material which adsorbed was actually the triflimide counterions and cage adsorption was present in the first electric multilayer; this hypothesis would also explain why the observed cage surface coverages were an order of magnitude lower than those observed under aqueous conditions.

The stabilities of cages **3.5** – **3.7** when exposed to acidic and basic alumina in acetonitrile were assessed by analysing the supernatants of 10 % w/v slurries of acidic and basic alumina in solutions of cages **3.5** – **3.7** in CD$_3$CN by ^{1}H NMR (Figure 3.33 – 3.35). Cages **3.5** and **3.7** remained intact when exposed to both acidic and basic alumina; the addition of acidic/basic alumina did not result in the disappearance of the imine peak (*ca.* 8.9 and 246 ppm for cages **3.5** and **3.7**, respectively) or the appearance of a picolinaldehyde aldehyde proton peak at *ca.* 10 ppm. In contrast, the addition of acidic alumina to a solution of cage **3.6** resulted in significant decomposition and a significant increase in the concentration of picolinaldehyde

and thus it was inferred that the cage decomposed significantly; for this reason, the values of *A* and *n* in Table 3.4 for cage **3.6** on acidic alumina are not given. This decomposition of cage **3.6** under acidic conditions might be due to the increased lability of the zinc coordination sphere, relative to those of iron and cobalt. The decomposition also explains why the surface coverage of cage **3.6** on acidic alumina is artificially larger than those of cages **3.5** and **3.7** on acidic alumina.
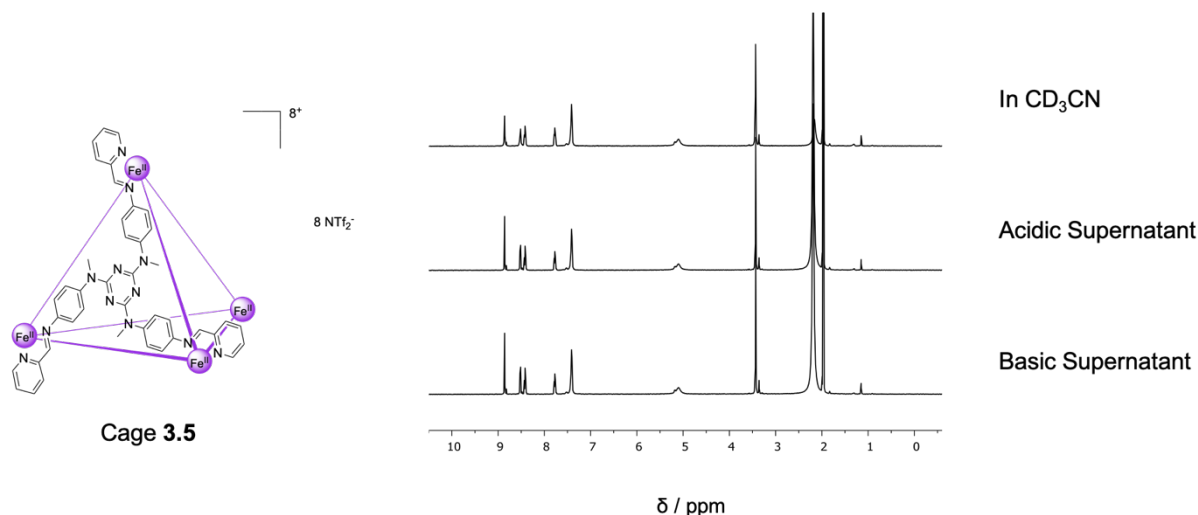
Figure 3.33: ^{1}H NMR (500 MHz, 298 K) spectra of cage **3.5** in CD$_3$CN and after exposure to acidic and basic alumina.
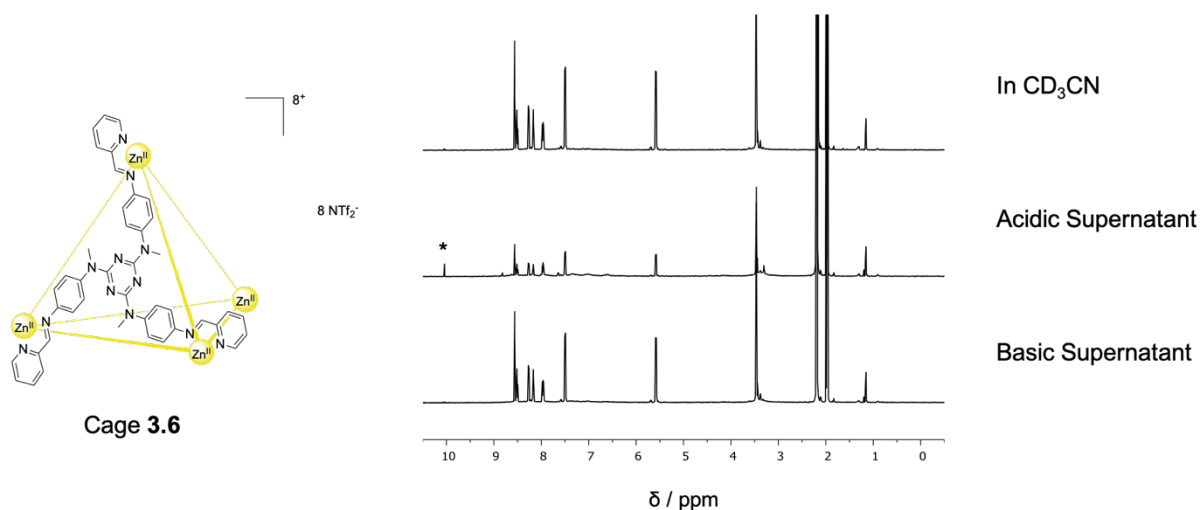
Figure 3.34: ^{1}H NMR (500 MHz, 298 K) spectra of cage **3.6** in CD$_3$CN and after exposure to acidic and basic alumina. The peak marked with "*" corresponds to the aldehyde proton of picolinaldehyde.
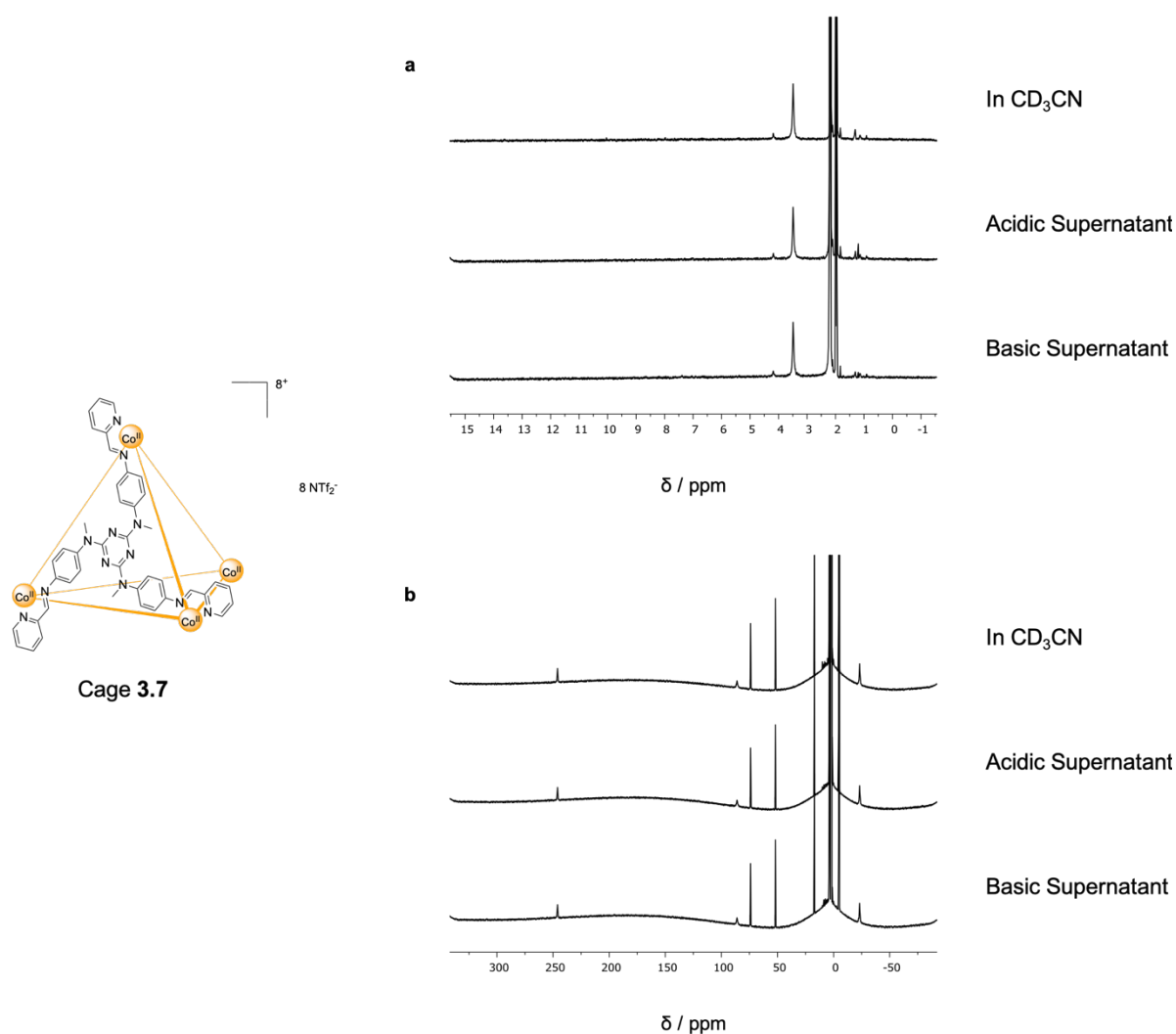
Cage **3.7**

Figure 3.35: ^{1}H NMR (500 MHz, 298 K) spectra of cage **3.7** in CD$_3$CN and after exposure to acidic and basic alumina; a) diamagnetic region, b) wide-sweep scan.

3.3.3 Change of Solvent System

The majority of the coordination cages formed in the Nitschke group are assembled and subsequently manipulated in acetonitrile, as discussed in Section 3.3.1. As discussed in Section 1.4, however, the binding of guest species within metal-organic coordination cages is often driven by the hydrophobic effect, *e.g.* cage **3.2/3.5** (Figure 3.8), and thus it is desirable to manipulate cages in water for host-guest studies. It was hypothesised that it might be possible to achieve aqueous host-guest chemistry with cages not themselves soluble in water by first adsorbing the cages on to alumina in acetonitrile and then filtering the resulting slurry and re-immersing it in water. To investigate the effect of changing solvent system on cages adsorbed from acetonitrile, "cage columns" of cage **3.5** on acidic alumina were eluted with a variety of

58

solvents (see Experimental). When a cage column of **3.5** on acidic alumina was eluted with D_2O the cage rapidly desorbed intact (Figure 3.36). Likewise, cage **3.5** on acidic alumina also desorbed intact when a column was eluted with ethanol (Figure 3.37). Finally, when a column of cage **3.5** on acidic alumina was first eluted with d_8-THF and then with water the cage remained adsorbed in d_8-THF but desorbed with water; furthermore, the presence of picolinaldehyde in the eluate indicated that the cage had decomposed significantly (Figure 3.38). Thus it was not possible to simply switch from acetonitrile to water either directly or *via* an intermediate solvent which was miscible with both acetonitrile and water. The EDX spectrum of bare acidic alumina (Figure 3.20) shows a significant signal for chlorine due to the acidic activation of the alumina; one possible explanation for the cage desorption observed is that the cage counterions were exchanged from triflimide to chloride upon exposure to water thereby rendering the cage water-soluble; this hypothesis has not been investigated. These cationic water-soluble cages then desorbed under the acidic conditions due to electrostatic repulsion, *i.e.* the alumina surface is positively charged under acidic conditions.
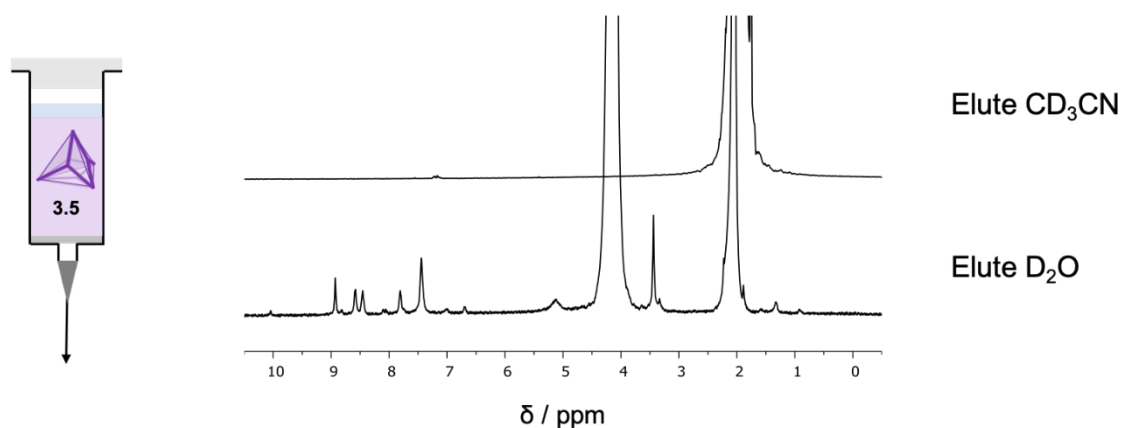
Figure 3.36: ^{1}H NMR (400 MHz, 298 K) spectra of elutions of a cage column of cage **3.5** on acidic alumina with CD_3CN and then D_2O. Spectra referenced to residual solvent peaks (1.94 ppm for acetonitrile, 4.79 ppm for water).
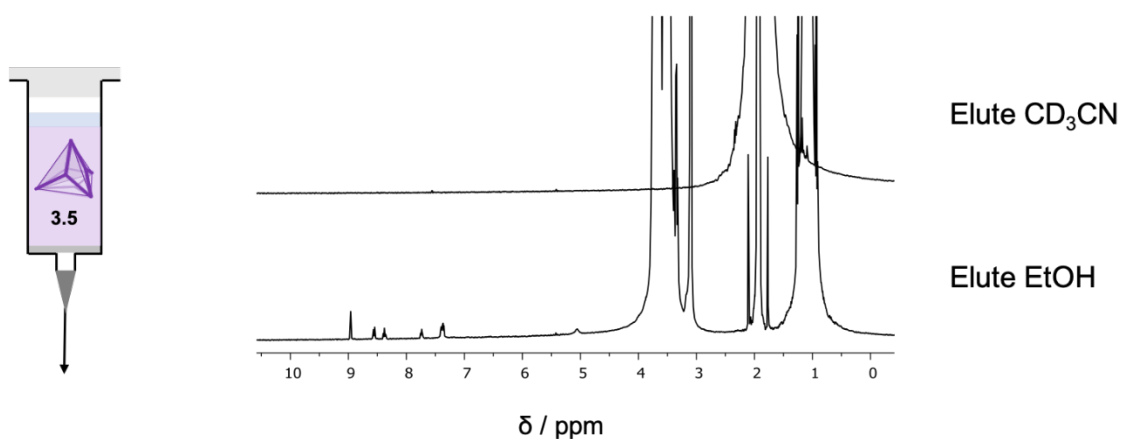
Figure 3.37: ^{1}H NMR (400 MHz, 298 K) spectra of elutions of a cage column of cage **3.5** on acidic alumina with CD_3CN and then EtOH. Spectra referenced to residual solvent peaks (1.94 ppm for acetonitrile).
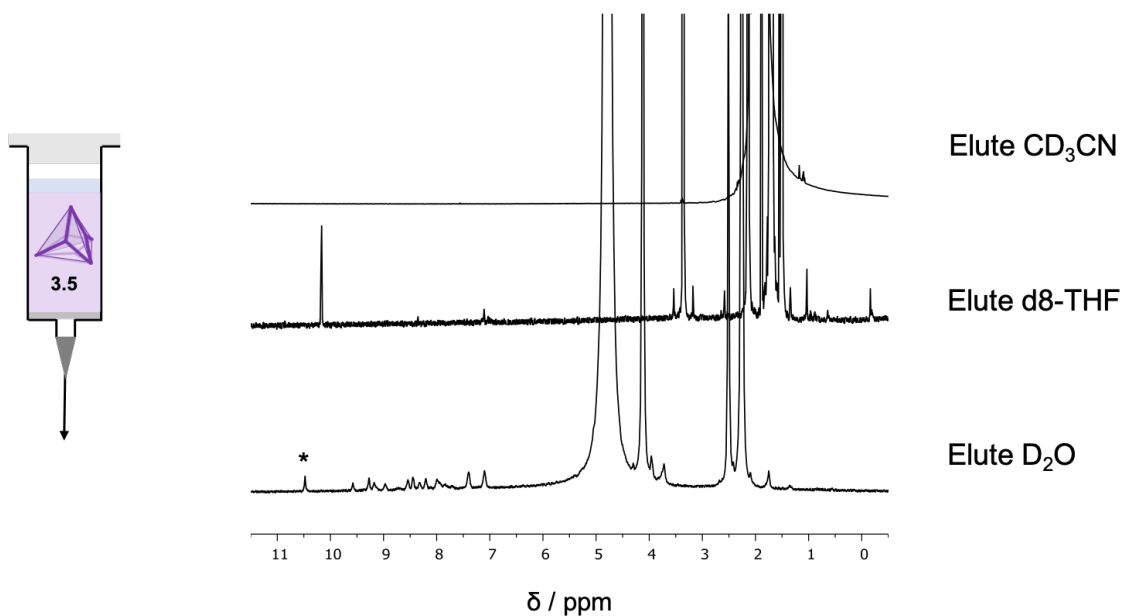
Figure 3.38: ^{1}H NMR (400 MHz, 298 K) spectra of elutions of a cage column of cage **3.5** on acidic alumina with CD_3CN, then d8-THF, and then D_2O. Spectra referenced to residual solvent peaks (1.94 ppm for acetonitrile, 4.79 ppm for water). The peak marked with "*" corresponds to the aldehyde proton of picolinaldehyde.

Finally, the adsorption of cage **3.5** from mixed acetonitrile/water was considered as a route to guest binding within cages not normally soluble in water. When cage **3.5** was dissolved in 1:1 $CD_3CN:D_2O$, however, the ^{1}H NMR spectrum indicated the presence of picolinaldehyde

shortly after dissolution and which suggests that the cage was not stable in this solvent mixture (Figure 3.39). Hence, the adsorption of cages in mixed acetonitrile/water was not pursued.
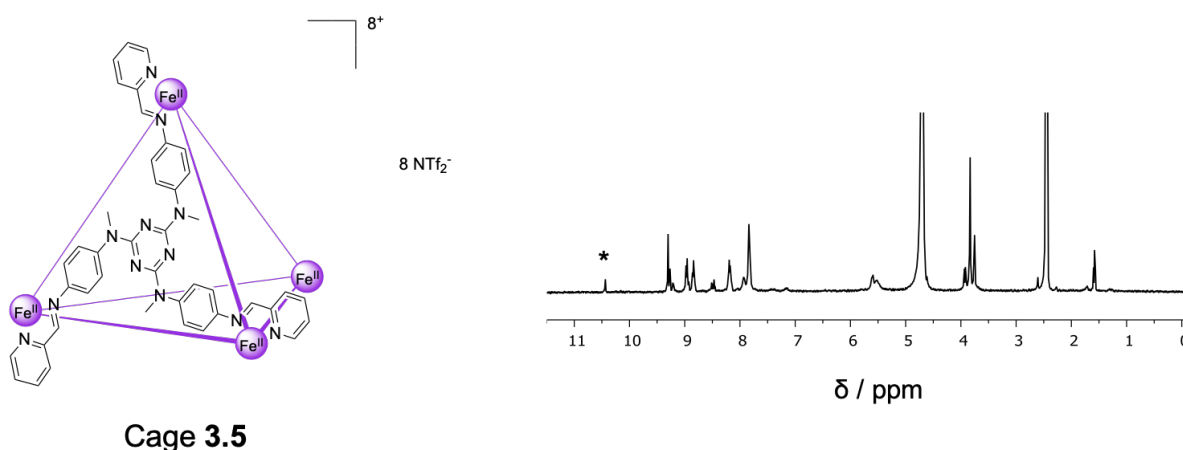
Cage **3.5**

Figure 3.39: ^{1}H NMR (400 MHz, 298 K) spectra of cage **3.5** in 1:1 CD$_3$CN:D$_2$O. The peak marked with "*" corresponds to the aldehyde proton of picolinaldehyde.

3.3.4 Guest Displacement Under Flow

The method described in Section 3.2.7 was used to investigate the uptake and release of molecular guests from cage **3.5** on acidic alumina. ^{1}H and ^{19}F NMR indicated that cage **3.5** bound fluorobenzene in acetonitrile and thus, as in Section 3.2.7, fluorobenzene was used as an inert guest to probe the preservation of the cage cavities following adsorption (Figure 3.23). Cage **3.5** on acidic alumina was loaded with fluorobenzene (see Experimental), washed with clean acetonitrile, and then eluted with DCM in acetonitrile. Unlike in Section 3.2.7, however, the ^{1}H NMR spectra of the DCM elutions did not show the presence of fluorobenzene in the eluate (Figure 3.40) and thus this experiment did not indicate the preservation of the cage cavities following adsorption. This could be due to the mechanical disassembly of the cage or a poor choice of guest displacement conditions, *i.e.* weak binding of the initial guest might result in the removal of any initially encapsulated guest during the column washing steps. Future experiments to demonstrate the preservation of cage cavities following adsorption from acetonitrile should therefore investigate different initial and competing guests and also different timescales for guest uptake and displacement.
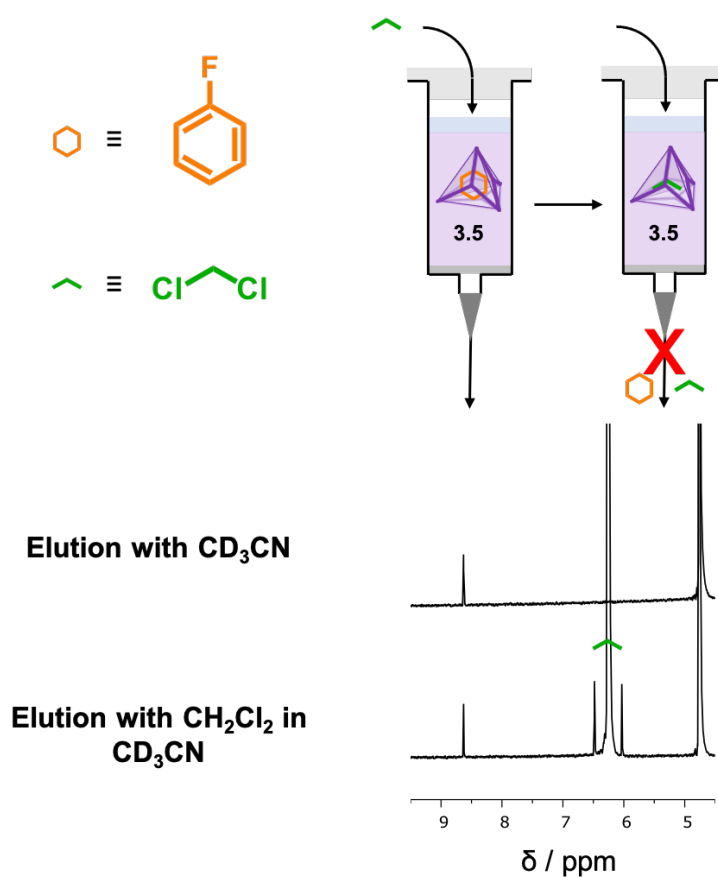
Figure 3.40: Schematic and partial ^{1}H NMR (400 MHz, 298 K) spectra of displacement of fluorobenzene from cage **3.5** on acidic alumina upon addition of dichloromethane in CD$_3$CN, referenced to pyrazine capillary at 8.63 ppm. Full spectra are given in the Experimental.

3.4 Conclusions and Future Work

This chapter has investigated the adsorption of coordination cages on activated alumina from water and acetonitrile. The loadings of cages on to alumina were characterised by adsorption isotherms *via* the solution depletion method and spectroscopic measurements indicated the preservation of the cage MLCT bands following adsorption. A series of guest displacement experiments under flow demonstrated that cages adsorbed from water retained their ability to bind and release guest species. Furthermore, the separation of a diene and a dienophile within adsorbed coordination cages facilitated the controlled initiation of a Diels-Alder reaction upon the addition of a single competing guest. In contrast, the guest displacement experiment performed with cages adsorbed from acetonitrile did not show the release of an initial guest following the addition of a competitive guest.

The experiments performed to-date demonstrate that coordination cages retain their ability to bind and release guest species when adsorbed from water. Coordination cages have been shown to stabilise reactive species in the solution state[26] and, as shown in this chapter, adsorbed cages can also be used to store reactive molecules for subsequent release and reaction; thus, adsorbed cages may find future applications in the storage and stabilisation of more diverse reactive species. Adsorbed cages might also be used in purification and quantitative chemical separations by exploiting the selective guest binding properties of individual cages. Furthermore, the use of coordination cages as homogeneous catalysts continues to be an active area of research[40,41] and the adsorption of catalytically-active cages presents the opportunity to achieve such catalysis heterogeneously. The work of this chapter has focussed on developing methods to demonstrate qualitatively that adsorbed coordination cages are able to bind and release guest species; in order to achieve the applications above, however, new methods of quantifying guest binding within adsorbed coordination cages, both in terms of thermodynamics and kinetics, will also need to be developed to complement more established solution-phase techniques such as Isothermal Titration Calorimetry (ITC).

3.5 Experimental

3.5.1 Subcomponent Synthesis

N2,N4,N6-trimethyl-N2,N4,N6-tris(4-nitrophenyl)-1,3,5-triazine-2,4,6-triamine
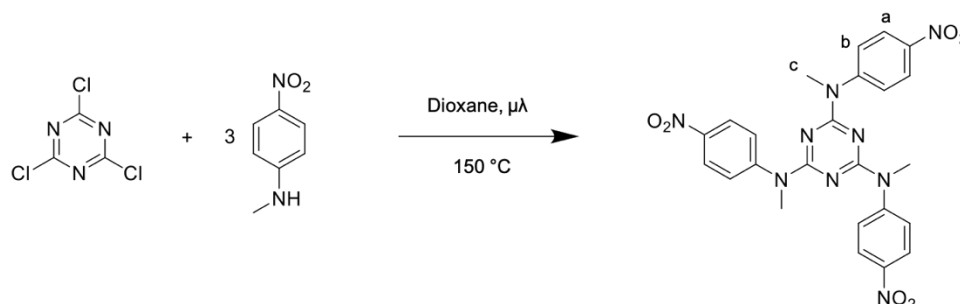
Scheme 3.1: Reaction to form N2,N4,N6-trimethyl-N2,N4,N6-tris(4-nitrophenyl)-1,3,5-triazine-2,4,6-triamine

This compound was prepared *via* a modified literature procedure.[19,29] Cyanuric chloride (0.3786 g, 2.053 mmol) and N-methyl-4-nitroaniline (1.2466 g, 8.193 mmol) were dissolved in dioxane (5.5 mL) and heated in a microwave reactor at 100 °C for 15 minutes and then at 150°C for a further 60 minutes. The resulting precipitate was filtered and washed with water (100 mL), methanol (200 mL), and diethyl ether (50 mL), and dried *in vacuo* to yield pale yellow solid N2,N4,N6-trimethyl-N2,N4,N6-tris(4-nitrophenyl)-1,3,5-triazine-2,4,6-triamine (1.0647 g, 2.003 mmol, 98 %). ^{1}H NMR (400 MHz, CD$_2$Cl$_2$, 298 K, referenced to pyrazine at 8.63 ppm) δ_H = 8.08 (dt, 8 Hz, 2 Hz, H$_a$), 7.44 (dt, 8 Hz, 2 Hz, H$_b$), 3.42 (s, H$_c$).

N2,N4,N6-tris(4-aminophenyl)-N2,N4,N6-trimethyl-1,3,5-triazine-2,4,6-triamine
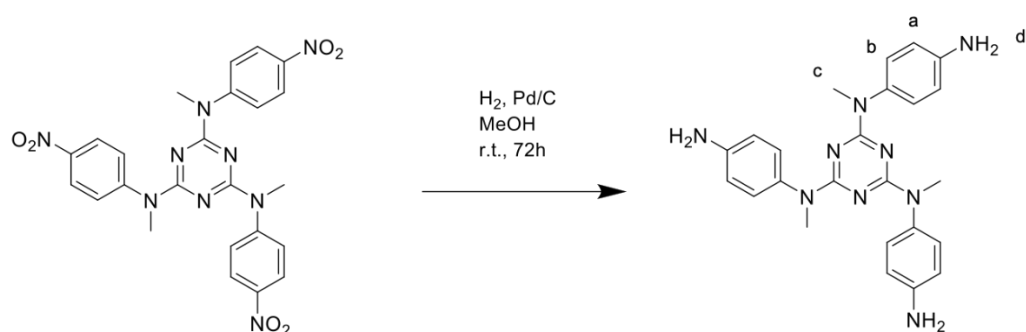
Scheme 3.2: Reaction to form N2,N4,N6-tris(4-aminophenyl)-N2,N4,N6-trimethyl-1,3,5-triazine-2,4,6-triamine

This compound was prepared *via* a modified literature procedure.[19,29] N2,N4,N6-trimethyl-N2,N4,N6-tris(4-nitrophenyl)-1,3,5-triazine-2,4,6-triamine (0.8777 g, 1.651 mmol) was dissolved in methanol (125 mL) and purged with nitrogen. Palladium on carbon (93.1 mg) was added and the solution was placed under H_2 (1 atm, balloon) and stirred at ambient temperature for 72 h. The reaction mixture was then filtered through celite and the solvent was removed *in vacuo* to yield N2,N4,N6-tris(4-aminophenyl)-N2,N4,N6-trimethyl-1,3,5-triazine-2,4,6-triamine (0.5748 g, 1.30 mmol, 79 %). ^{1}H NMR (400 MHz, CD_2Cl_2, 298 K, referenced to pyrazine at 8.63 ppm) δ_H = 6.95 (d, 8 Hz, H_b), 6.55 (d, 8 Hz, H_a), 3.68 (bs, H_d), 3.23 (s, H_c).

Potassium 3-((6-formylpyridin-3-yl)oxy)propane-1-sulphonate
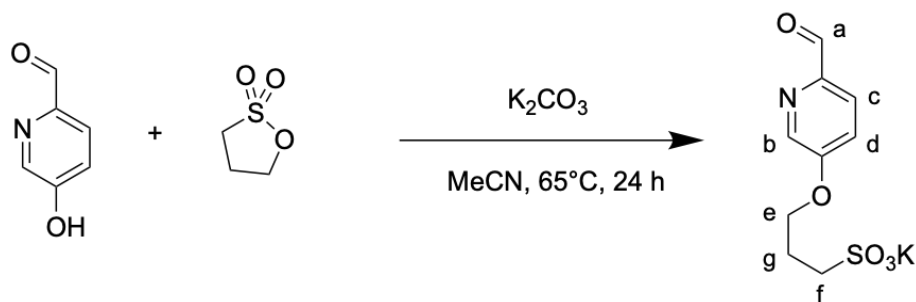
Scheme 3.3: Reaction to form potassium 3-((6-formylpyridin-3-yl)oxy)propane-1-sulphonate

A solution of 1,3-propane sultone (193.6 mg, 1.585 mmol) in acetonitrile (5 mL) was added to a suspension of 5-hydroxypicolinaldehyde (193.0 mg, 1.568 mmol) and potassium carbonate (109.4 mg, 0.792 mmol) in acetonitrile (5 mL). The mixture was purged with nitrogen gas and then stirred at 65 °C for 24 hours. The resulting off-white solid was washed with methanol (2 × 2 mL) and then diethyl ether (10 mL). The solid was dried under a stream of nitrogen gas and then under vacuum to yield potassium 3-((6-formylpyridin-3-yl)oxy)propane-1-sulphonate (201.7 mg, 0.712 mmol, 45 %). ^{1}H NMR (400 MHz, D$_2$O, 298 K, referenced to residual solvent at 4.79 ppm) δ_H = 9.89 (s, H$_a$), 8.47 (s, H$_b$), 8.10 (d, 8 Hz, H$_c$), 7.63 (d, 8 Hz, H$_d$), 4.38 (m, H$_e$), 3.16 (t, 8 Hz, H$_f$), 2.32 (t, 6 Hz, H$_g$).

ESI-MS (Waters Synapt G2-Si, ESI): m/z: 244.0273 (calc. 244.0280, without cation)

^{13}C NMR and 2D experiments could not be collected due to broad peaks, likely due to rapid relaxation, and hence the ^{1}H assignments are speculative.

3.5.2 Cage/Complex Assemblies

Assembly of 3.1[Na]₄
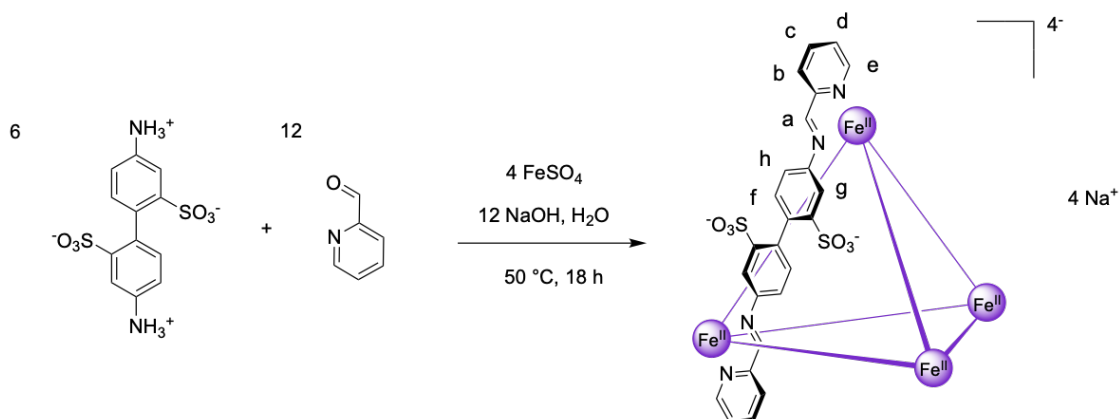
Scheme 3.4: Assembly of **3.1**[Na]₄

This compound was prepared *via* a modified literature procedure.[25] Iron (II) sulphate heptahydrate (0.4569 g, 1.64 mmol) was added to a solution of 4,4'-diamino-[1,1'-biphenyl]-2,2'-disulfonic acid (0.9789 g, 2.40 mmol), picolinaldehyde (0.50 mL, 5.26 mmol) and sodium hydroxide (0.1932 g, 4.83 mmol) in water (20 mL). The solution was degassed via an evacuation/N_2 fill cycle and then stirred at 50 °C for 18 hours. Water (~ 10 mL) was removed *in vacuo* and acetonitrile (~ 30 mL) was added to the vigorously stirred cage solution. The resulting purple precipitate was filtered to yield purple solid **3.1**[Na]₄ (1.9432 g). ¹H NMR (400 MHz, D_2O, 298 K, referenced to pyrazine at 8.63 ppm) δ_H = 9.35 (s, H_a), 8.74 (s, H_b), 8.42 (s, H_c), 7.79 (s, H_d), 7.55 (s, H_e), 7.16 (bs, H_f), 6.46 (s, H_g), 5.85 (s, H_h).

Assembly of 3.2[SO₄]₄
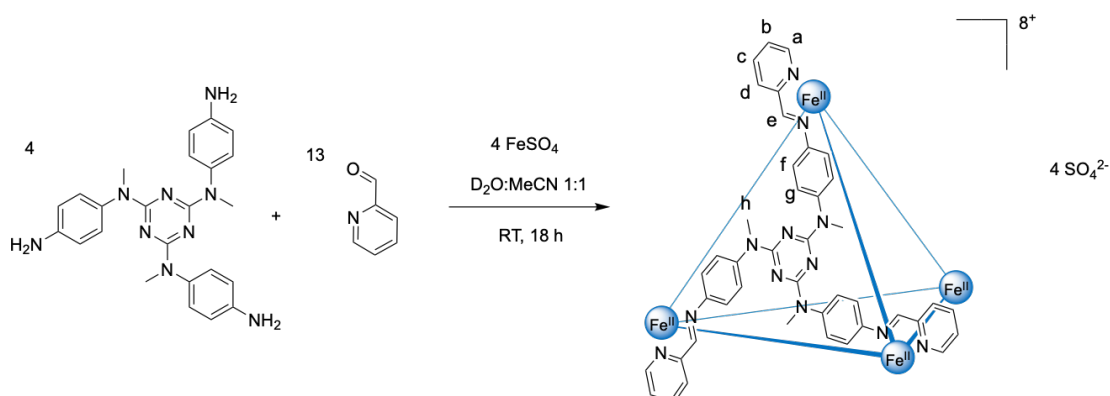
Scheme 3.5: Assembly of **3.2**[SO₄]₄

This compound was assembled *via* the literature procedure.[29] In a glovebox, iron (II) sulphate heptahydrate (22.7 mg, 82 µmol), N2,N4,N6-tris(4-aminophenyl)-N2,N4,N6-trimethyl-1,3,5-triazine-2,4,6-triamine (35.3 mg, 80 µmol), and picolinaldehyde (24.7 µL, 260 µmol) were combined with acetonitrile (5 mL) and D_2O (5 mL). The resulting mixture was stirred for 18 hours at room temperature. The acetonitrile was removed *in vacuo* and the solution diluted with D_2O to a total volume of 10 mL to give a 2 mM solution of **3.2**[SO₄]₄. This stock solution was used without further purification. ^1H NMR (400 MHz, D_2O, 298 K, referenced to acetone at 2.22 ppm) δ_H = 9.03 (s, H_e), 8.60 (d, H_d), 8.43 (t, H_c), 7.74 (t, H_b), 7.47 (m, H_a/H_g), 5.29 (bs, H_f), 3.48 (s, H_h).[29]

Assembly of 3.3[SO₄]
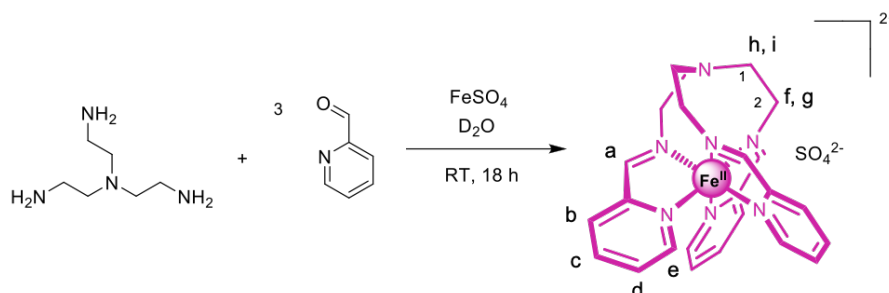
Scheme 3.6: Assembly of **3.3**[SO₄]

In a glovebox, iron (II) sulphate heptahydrate (22.5 mg, 81 µmol), tris(2-aminoethyl)amine (12.3 µL, 82 µmol) and picolinaldehyde (23.1 µL, 242 µL) were dissolved in D_2O (5 mL). The resulting solution was stirred for 18 hours at room temperature to give a 16 mM solution of **3.3**[SO₄]. This stock solution was used without further purification. ¹H NMR (400 MHz, D_2O, 298 K, referenced to pyrazine at 8.63 ppm) δ_H = 9.17 (s, H_a), 8.27 (s, H_b), 8.16 (s, H_c), 7.47 (s, H_d), 7.08 (s, H_e), 3.60 (m, C_2H_f), 3.45 (m, C_2H_g), 3.25 (m, C_1H_h), 3.11 (m, C_1H_i).[34]

Assembly of 3.4[K]
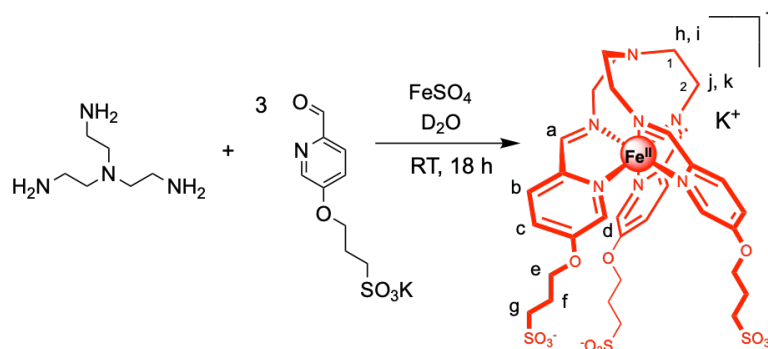
Scheme 3.7: Assembly of **3.4**[K]

A solution of tris(2-aminoethyl)amine (15 µL, 100 µmol) and potassium 3-((6-formylpyridin-3-yl)oxy)propane-1-sulfonate (81.6 mg, 288 µmol) in water (6 mL) was purged with nitrogen gas for 5 minutes. Iron (II) sulphate heptahydrate (26.6 mg, 96 µmol) was added to the mixture and the resulting red solution was stirred at room temperature for 24 hours. The crude mixture was separated into two portions and to each portion acetone (40 mL) was added to precipitate a pink-red solid. Each portion was then washed with acetone (15 mL), dried under nitrogen, dried *in vacuo*, and then recombined to yield **3.4**[K] (82.6 mg, 90 µmol, 94 %). ^{1}H NMR (400 MHz, D$_2$O, 298 K, referenced to acetone at 2.26 ppm) δ_H = 9.15 (bs, H$_a$) 8.33 (bs, H$_b$), 7.78 (bs, H$_c$), 6.97 (bs, H$_d$), 4.13 (bs, H$_e$). 3.58 (bs, C$_2$H$_j$), 3.43 (bs, C$_2$H$_k$), 3.18 (bs, H$_e$)*, 3.11 (bs, C$_1$H$_h$)*, 2.91 (bs, C$_1$H$_i$)*, 2.09 (bs, H$_f$).

The broad peaks for complex **3.4** were likely to have been caused by rapid relaxation and this hindered the collection of ^{13}C and 2D NMR spectra. The ^{1}H assignments have been predicted based on those of **3.3**; "*" denotes where peaks have been challenging to distinguish by ^{1}H NMR alone. ESI-MS, crystallography, and DOSY confirm the formation of a single species of the correct mass and geometry.

ESI-MS (Waters Synapt G2-Si, ESI): m/z: 920.0808 (calc. 920.0869)
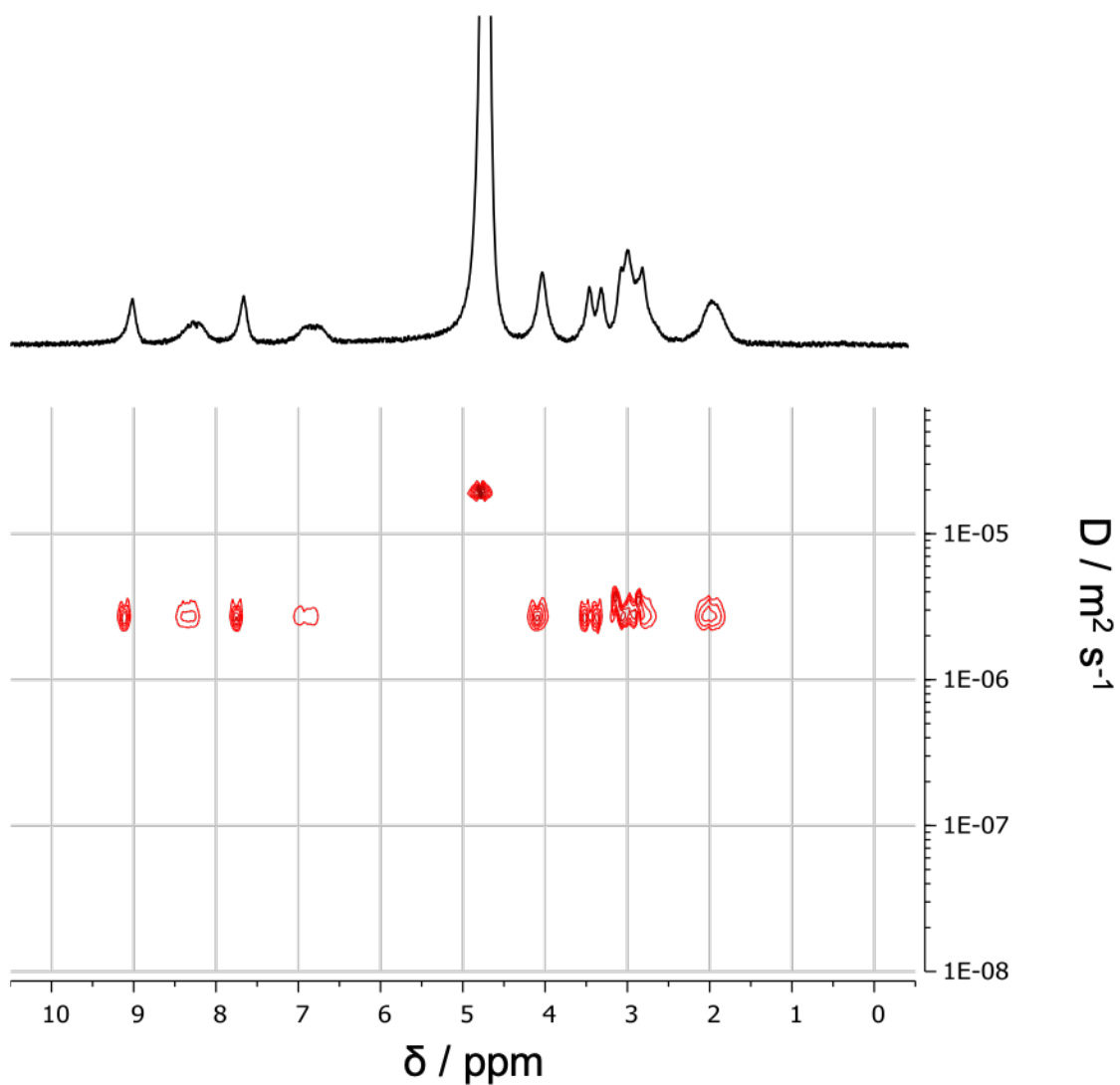
Figure 3.41: DOSY spectrum (400 MHz, D_2O, 298 K) of **3.4**, D = 2.5(5) × 10^{-6} m^2 s^{-1}. 32 scans of 32 points were used in data collection.
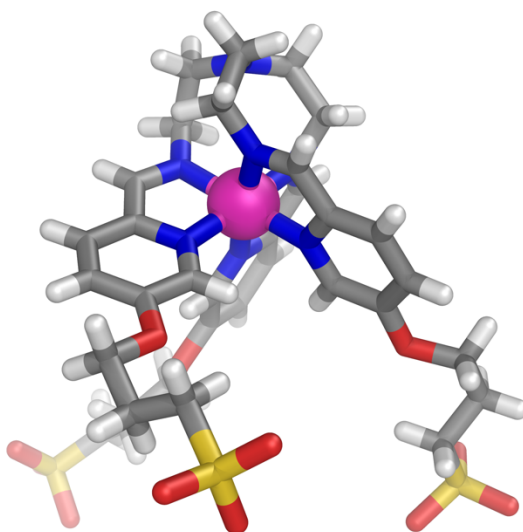
Figure 3.42: Crystal structure of **3.4** (grey – C, white – H, blue – N, red – O, yellow – S, magenta – Fe). Single crystals of **3.4** were grown by vapour diffusion of ethanol into an aqueous solution of **3.4**. Many thanks to Dr Tanya Ronson for structure refinement and image processing.

Crystal Data:

Formula $C_{33}H_{48}FeKN_7O_{15}S_3$, M 973.91, Trigonal, space group P 32 2 1 (#154), a 14.50370(4), b 14.50370(4), c 35.5789(2) Å, γ 120º, V 6481.58(5) Å^3, D_c 1.497 g cm^{-3}, Z 6, crystal size 0.250 by 0.220 by 0.150 mm, colour purple, habit block, temperature 100(2) Kelvin, λ(Synchrotron) 0.6889 Å, μ(Synchrotron) 0.604 mm^{-1}, T(Analytical)$_{min,max}$ 0.995321616693658, 1.0, $2\theta_{max}$ 64.00, hkl range -22 22, -22 22, -54 54, N 125814, N_{ind} 16502(R_{merge} 0.0502), N_{obs} 9499(I > 2σ(I)), N_{var} 682, residuals* R1(F) 0.0781, $wR2(F^2)$ 0.2384, GoF(all) 0.941, $\Delta\rho_{min,max}$ -0.743, 1.688 e$^-$ Å^{-3}.

$^*R1 = \Sigma||F_o| - |F_c||/\Sigma|F_o|$ for $F_o > 2\sigma(F_o)$; $wR2 = (\Sigma w(F_o^2 - F_c^2)^2/\Sigma(wF_c^2)^2)^{1/2}$ all reflections

$w=1/[\sigma^2(F_o^2)+(0.1629P)^2]$ where $P=(F_o^2+2F_c^2)/3$

Assembly of 3.5[NTf₂]₈
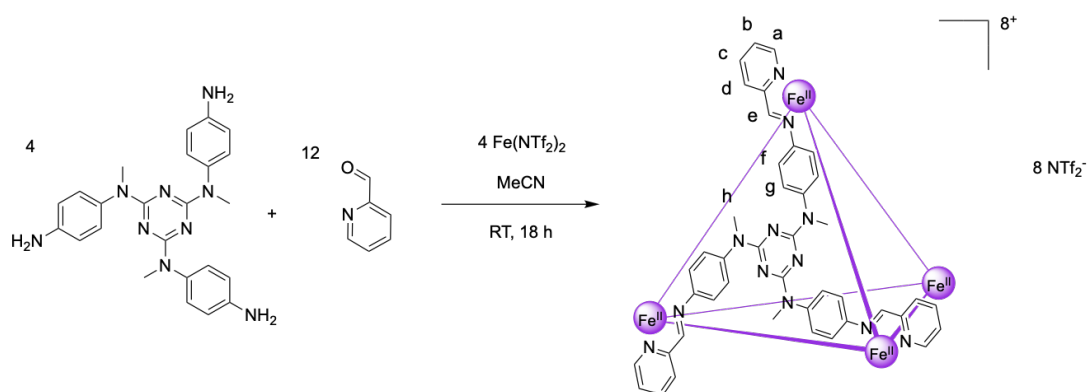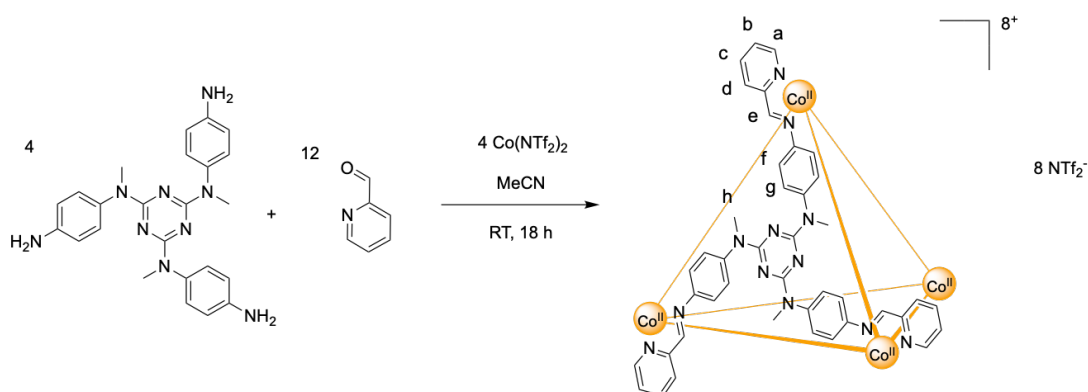

Scheme 3.8: Assembly of **3.5**[NTf₂]

This compound was prepared *via* a modified literature procedure.[29] N2,N4,N6-tris(4-aminophenyl)-N2,N4,N6-trimethyl-1,3,5-triazine-2,4,6-triamine (70.5 mg, 159.7 μmol), picolinaldehyde (46 μL, 484 μmol), and iron (II) bistriflimide[42] (112.1 mg, 160.8 μmol) were dissolved in acetonitrile (5 mL) and stirred at room temperature for 24 hours. The cage product was precipitated with diethyl ether (20 mL), washed with further diethyl ether (15 mL), and dried to air to yield reddish purple amorphous solid **3.5[NTf₂]₈** (151.5 mg, 28.6 μmol, 72 %).

^{1}H NMR (400 MHz, CD₃CN, 298 K, referenced to residual solvent at 1.94 ppm, *ca.* 2 mM)[43]

δ_H = 8.80 – 8.85 (m, H$_e$)*, 8.48 (s, H$_d$), 8.39 (s, H$_c$), 7.74 (s, H$_b$), 7.39 – 7.50 (m, H$_a$/H$_g$), 5.08 – 5.16 (s, H$_f$)*, 3.33 – 3.41 (s, H$_h$)*.

* denotes peak which has been broadened/split by NTf₂⁻ encapsulation

Assembly of 3.6[NTf₂]₈
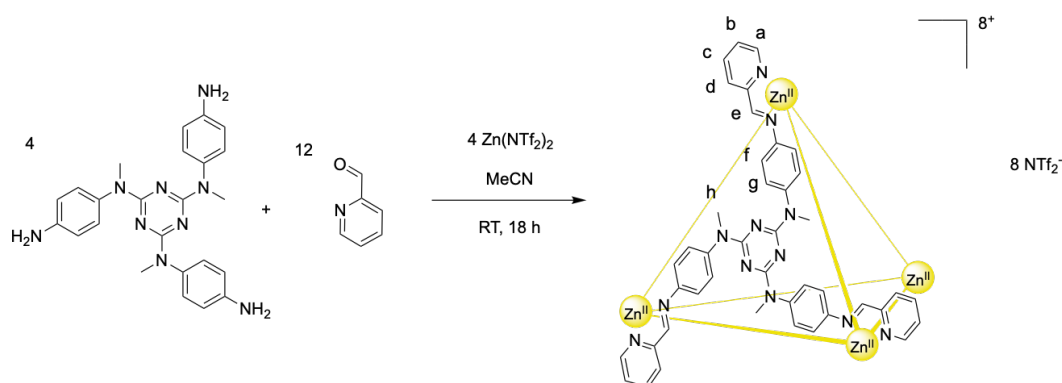
Scheme 3.9: Assembly of **3.6**[NTf₂]

This compound was prepared *via* a modified literature procedure. N2,N4,N6-tris(4-aminophenyl)-N2,N4,N6-trimethyl-1,3,5-triazine-2,4,6-triamine (70.6 mg, 159.9 µmol), picolinaldehyde (46 µL, 484 µmol), and zinc (II) bistriflimide (100.2 mg, 160.2 µmol) were dissolved in acetonitrile (5 mL) and stirred at room temperature for 24 hours. The cage product was precipitated with diethyl ether (20 mL), washed with further diethyl ether (15 mL), and dried to air to yield bright yellow amorphous solid **3.6[NTf₂]₈** (182.3 mg, 34.2 µmol, 85 %). ¹H NMR (400 MHz, CD₃CN, 298 K, referenced to residual solvent at 1.94 ppm, *ca*. 2 mM) δ_H = 8.53 (s, H_e), 8.48 (t, 8 Hz, H_c), 8.24 (d, 8 Hz, H_d), 8.13 (d, 8 Hz, H_a), 7.93 (t, 8 Hz, H_b), 7.47 (d, 8 Hz, H_g), 5.55 (d, 8 Hz, H_f), 3.44 (s, H_h).

Many thanks to Dr Tanya Ronson for her assistance in NMR assignment.

Assembly of 3.7[NTf$_2$]$_8$

Scheme 3.10: Assembly of **3.7**[NTf$_2$]

This compound was prepared *via* the literature procedure.[38] N2,N4,N6-tris(4-aminophenyl)-N2,N4,N6-trimethyl-1,3,5-triazine-2,4,6-triamine (70.7 mg, 160.1 µmol), picolinaldehyde (46 µL, 484 µmol), and cobalt (II) bistriflimide[44] (102.4 mg, 160.7 µmol) were dissolved in acetonitrile (5 mL) and stirred at room temperature for 24 hours. The cage product was precipitated with diethyl ether (20 mL), washed with further diethyl ether (15 mL), and dried to air to yield orange amorphous solid **3.7[NTf$_2$]$_8$** (168.6 mg, 31.7 µmol, 79 %). ^{1}H NMR (400 MHz, CD$_3$CN, 298 K, referenced to residual solvent at 1.94 ppm, *ca*. 2 mM) δ_H = 245.8 (H$_e$), 86.2 (H$_d$), 73.9 (H$_c$), 51.7 (H$_b$), 17.0 (H$_a$), 3.5 (H$_g$), -4.9 (H$_f$), - 23.2 (H$_h$).

3.5.3 UV-Vis Concentration Calibration

Method

Stock solutions of **3.1**[Na]$_4$, **3.2**[SO$_4$]$_4$, **3.3**[SO$_4$], and **3.4**[K] in D$_2$O and **3.5**[NTf$_2$]$_8$, **3.6**[NTf$_2$]$_8$, and **3.7**[NTf$_2$]$_8$ in CH$_3$CN were sequentially diluted and their UV-vis spectra recorded. Calibration curve intercepts were set to zero.
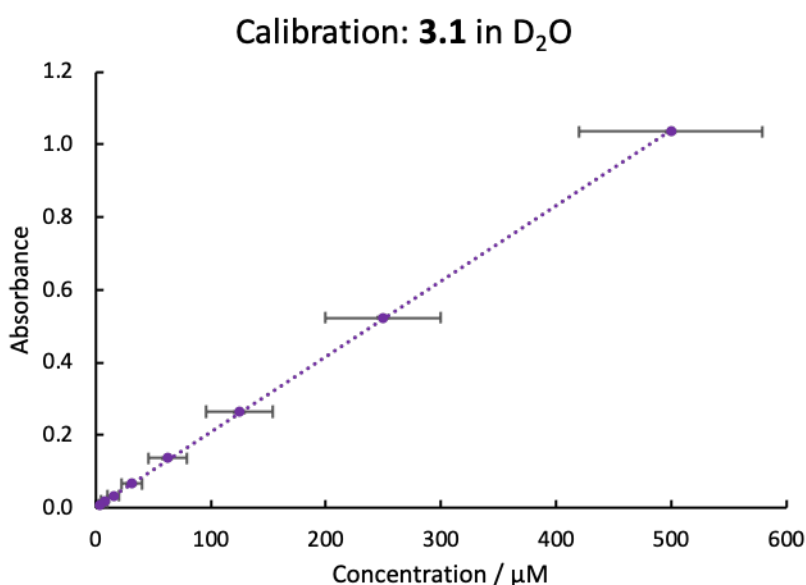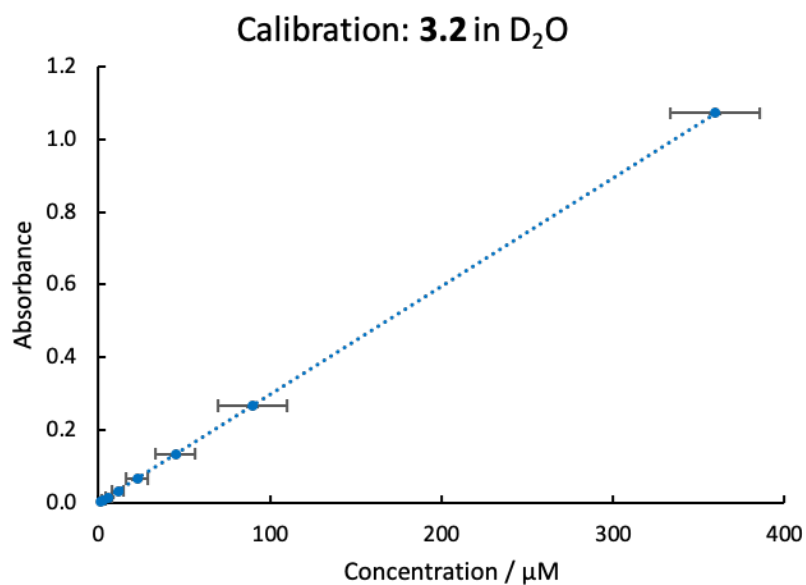
3.1 in D$_2$O

Figure 3.43: UV-vis calibration curve for **3.1** in D$_2$O in the range 0 – 0.5 mM, y = 0.00208 x. The data in Figure 3.41 were collected by Dr Cally Haynes using samples prepared by Mr Hugh Ryan.

Table 3.5: UV-vis calibration data for **3.1** in D$_2$O. Data were collected by Dr Cally Haynes using samples prepared by Mr Hugh Ryan.

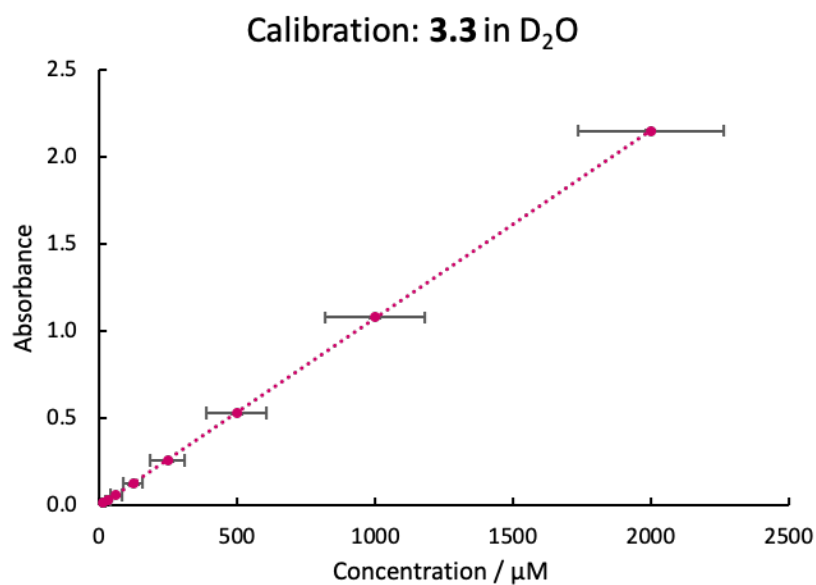| Concentration of 3.1 / µM	Average Absorption at 570 nm
499.6	1.035
249.8	0.523
124.9	0.265
62.5	0.136
31.2	0.067
15.6	0.033
7.8	0.018
3.9	0.009

3.2 in D$_2$O

Figure 3.44: UV-vis calibration curve for **3.2** in D$_2$O in the range 0 – 0.4 mM, y = 0.00298 x. The data in Figure 3.42 were collected by Dr Cally Haynes using samples prepared by Mr Hugh Ryan.

Table 3.6: UV-vis calibration data for **3.2** in D$_2$O. Data were collected by Dr Cally Haynes using samples prepared by Mr Hugh Ryan.

Concentration of 3.2 / µM	Average Absorption at 570 nm
359.5	1.072
89.9	0.266
44.9	0.133
22.5	0.065
11.2	0.031
5.6	0.015
2.8	0.006
1.4	0.001

3.3 in D$_2$O

Figure 3.45: UV-vis calibration curve for **3.3** in D$_2$O in the range 0 – 2 mM, y = 0.00108 x. The data in Figure 3.43 were collected by Dr Cally Haynes using samples prepared by Mr Hugh Ryan.

Table 3.7: UV-vis calibration data for **3.3** in D$_2$O. Data were collected by Dr Cally Haynes using samples prepared by Mr Hugh Ryan.

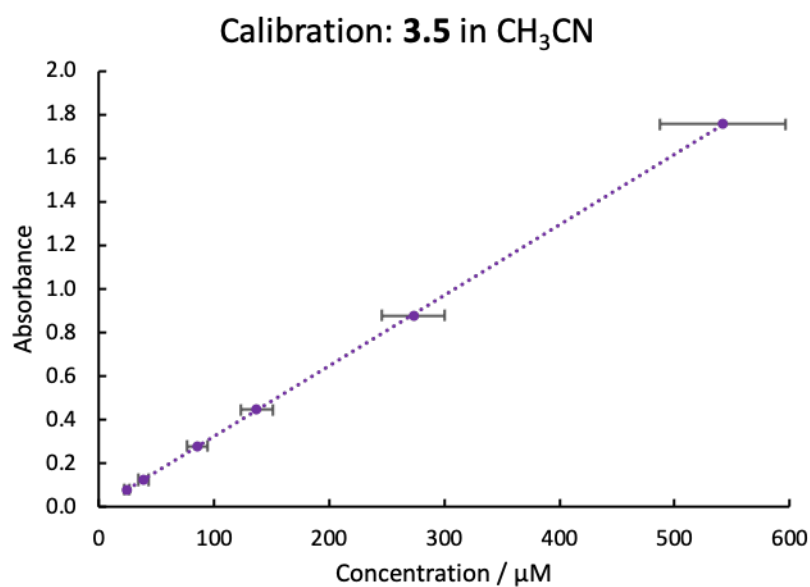| Concentration of 3.3 / µM	Average Absorption at 559 nm
2000.0	2.149
1000.0	1.079
500.0	0.531
250.0	0.261
125.0	0.130
62.5	0.062
31.3	0.031
15.6	0.015

3.4 in D_2O
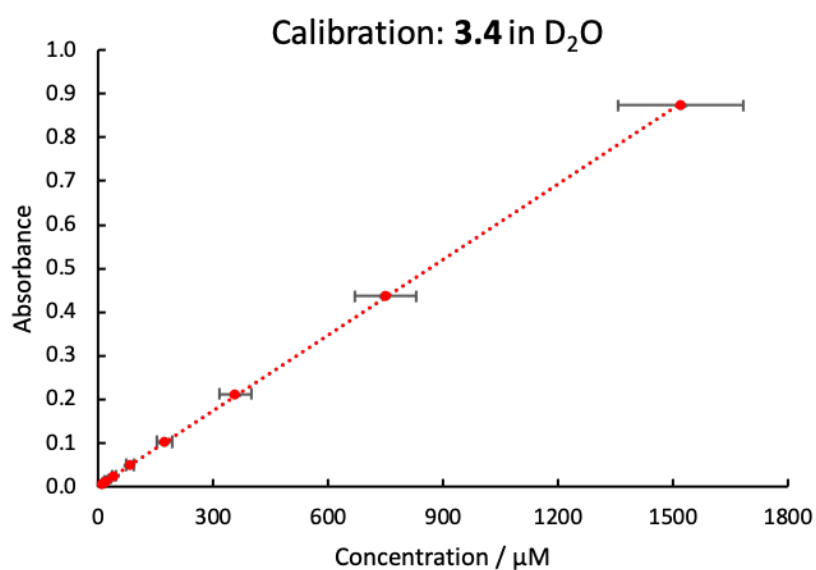
Figure 3.46: UV-vis calibration curve for **3.4** in D_2O in the range 0 – 1.6 mM, y = 0.00058 x.

Table 3.8: UV-vis calibration data for **3.4** in D_2O.

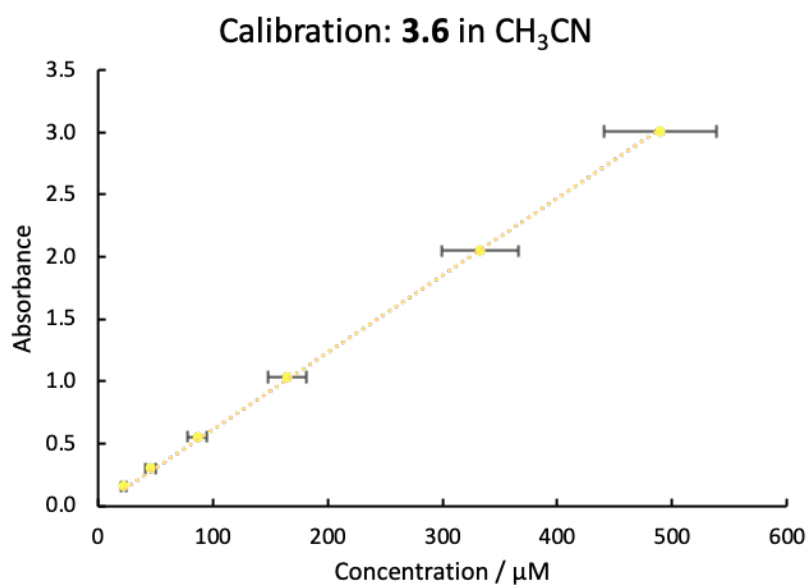| Concentration of 3.4 / μM	Average Absorption at 536 nm
1521.1	0.873
748.6	0.436
357.1	0.212
171.2	0.103
81.6	0.050
39.4	0.024
19.4	0.012
9.5	0.006

3.5 in CH$_3$CN

Figure 3.47: UV-vis calibration curve for **3.5** in CH$_3$CN in the range 0 – 0.6 mM, y = 0.00323 x.

Table 3.9: UV-vis calibration data for **3.5** in CH$_3$CN.

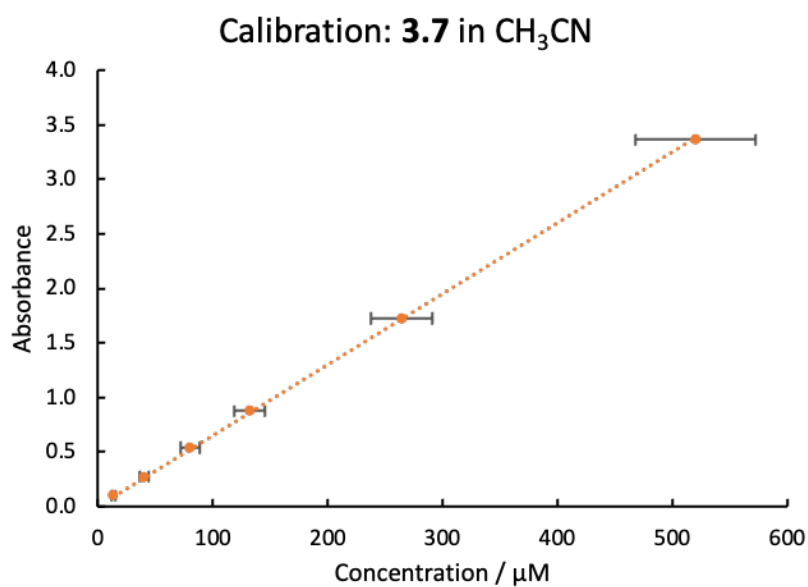| Concentration of 3.5 / µM	Average Absorption at 572 nm
541.9	1.754
273.0	0.878
137.1	0.446
85.5	0.278
38.7	0.125
24.3	0.079

3.6 in CH$_3$CN

Figure 3.48: UV-vis calibration curve for **3.6** in CH$_3$CN in the range 0 – 0.5 mM, y = 0.00617 x.

Table 3.10: UV-vis calibration data for **3.6** in CH$_3$CN.

Concentration of 3.6 / µM	Average Absorption at 372 nm
489.4	3.010
332.4	2.049
165.0	1.034
86.2	0.554
45.4	0.302
22.4	0.158

3.7 in CH₃CN

Figure 3.49: UV-vis calibration curve for **3.7** in CH₃CN in the range $0 – 0.6$ mM, $y = 0.00649$ x.

Table 3.11: UV-vis calibration data for **3.7** in CH₃CN.

Concentration of 3.7 / µM	Average Absorption at 352 nm
520.7	3.366
264.2	1.727
131.9	0.877
80.0	0.540
39.8	0.275
13.1	0.102

3.5.4 Adsorption Isotherms

Method

The adsorption isotherms were collected *via* the solution depletion method. Known masses of alumina adsorbent (200 mg) were added to a series of cage/complex solutions of known concentrations (0 – 1.5 mM) and volumes (2 mL). The samples were equilibrated *via* tumbling for 10 minutes at 40 RPM and then centrifuged for 2 minutes at 3000 RPM. The concentrations of the supernatant solutions were then determined using the UV-vis calibration curves shown above. The depletion of material from solution was attributed to adsorption on the solid support. All of the isotherms were collected at 10% w/v of alumina in water (**3.1** – **3.4**) or acetonitrile (**3.5** – **3.7**) at ambient temperature.

The adsorption isotherm data for species **3.1** – **3.4** were fitted in OriginPro 2017 using the Levenberg Marquardt iteration algorithm with the following, user-defined function:[35]

$$\theta = \theta_{\text{MONO}}\left(\frac{K_S c}{(1 - K_L c)(1 - K_L c + K_S c)}\right)$$

in which θ is the total surface coverage (here In $\mu\text{mol}_{\text{adsorbate}}$ $\text{g}^{-1}_{\text{alumina}}$), θ_{MONO} is the monolayer surface coverage ($\mu\text{mol}_{\text{adsorbate}}$ $\text{g}^{-1}_{\text{alumina}}$), K_S is the surface-adsorbate binding constant (M^{-1}), K_L is the adsorbate-adsorbate binding constant (M^{-1}), and c is the equilibrium adsorbate concentration (M).

The adsorption isotherm data for cages **3.5** – **3.7** were fitted in OriginPro 2020 using the Levenberg Marquardt iteration algorithm with the following, user-defined function:[39]

$$\theta = A\, c^{\frac{1}{n}}$$

in which θ is the total surface coverage (here in $\mu\text{mol}_{\text{adsorbate}}$ $\text{g}^{-1}_{\text{alumina}}$) and A and n are fitted constants. The constant n is not required to have an integer value and thus, in this work, only the magnitudes of the constants A and n are reported and not their units.

3.1 on Acidic Alumina

Table 3.12: Data for the adsorption isotherm of cage **3.1** on acidic alumina from D_2O. The UV-vis measurements for these data were performed by Dr Cally Haynes using samples prepared by Mr Hugh Ryan.

Equilibrium Concentration of 3.1 / µM	Coverage / µmol$_{cage}$ g$_{alumina}$$^{-1}$
1.48	3.96
1.68	2.06
1.93	8.03
2.86	5.97
4.13	10.02
12.01	12.02
56.24	13.53
187.41	14.29

3.2 on Basic Alumina

Table 3.13: Data for the adsorption isotherm of cage **3.2** on basic alumina from D_2O. The UV-vis measurements for these data were performed by Dr Cally Haynes using samples prepared by Mr Hugh Ryan.

Equilibrium Concentration of 3.2 / µM	Coverage / µmol$_{cage}$ g$_{alumina}$$^{-1}$
0.32	1.07
0.25	2.16
0.38	3.08
0.42	2.62
0.76	3.84
4.04	4.58
22.44	5.30
67.91	5.76
106.66	5.74
173.06	6.08

3.3 on Basic Alumina

Table 3.14: Data for the adsorption isotherm of complex **3.3** on basic alumina from D_2O. The UV-vis measurements for these data were performed by Dr Cally Haynes using samples prepared by Mr Hugh Ryan.

Equilibrium Concentration of 3.3 / µM	Coverage / $\mu mol_{complex}\ g_{alumina}^{-1}$
3.45	0.06
5.67	0.13
7.10	0.20
7.66	0.30
13.01	0.49
20.33	0.81
31.58	1.03
37.46	1.23
48.16	1.52
87.25	2.23
136.89	2.81
190.93	3.41
245.31	3.72
328.33	4.30
408.59	4.60
479.40	4.80
564.85	5.01
678.97	5.39
870.49	5.82

3.4 on Acidic Alumina

Table 3.15: Data for the adsorption isotherm of complex **3.4** on acidic alumina from D_2O.

Equilibrium Concentration of 3.4 / μM	Coverage / $\mu mol_{complex}\ g_{alumina}^{-1}$
9.0	0.6
17.0	1.3
17.1	2.0
21.3	2.6
33.1	4.1
45.5	5.5
56.9	6.8
68.3	7.7
89.0	9.3
100.5	10.1
116.7	11.2
141.4	12.5
213.0	15.7
369.6	20.0
640.9	24.0
910.9	27.5
1087.0	28.1

3.5 on Acidic Alumina

Table 3.16: Data for the adsorption isotherm of cage **3.5** on acidic alumina from CH_3CN.

Equilibrium Concentration of 3.5 / µM	Coverage / $\mu mol_{complex}\ g_{alumina}^{-1}$
0.01	0.20
0.24	0.37
1.79	0.48
9.09	0.58
19.69	0.68
28.86	0.71
40.94	0.76
53.65	0.82
103.97	0.82
139.45	1.01
201.25	1.03
294.06	1.14

3.5 on Basic Alumina

Table 3.17: Data for the adsorption isotherm of cage **3.5** on basic alumina from CH_3CN.

Equilibrium Concentration of 3.5 / µM	Coverage / $\mu mol_{complex}\ g_{alumina}^{-1}$
40.97	0.08
89.27	0.12
135.56	0.18
184.12	0.22
231.27	0.26
276.98	0.30

3.6 on Acidic Alumina

Table 3.18: Data for the adsorption isotherm of cage **3.6** on acidic alumina from CH_3CN.

Equilibrium Concentration of 3.6 / µM	Coverage / $µmol_{complex}\ g_{alumina}^{-1}$
0.11	0.18
0.66	0.32
1.28	0.44
3.10	0.62
3.40	0.78
7.45	0.93
8.88	1.00
13.82	1.17
25.39	1.56
35.92	1.95
54.37	2.41
78.29	3.10

3.6 on Basic Alumina

Table 3.19: Data for the adsorption isotherm of cage **3.6** on basic alumina from CH_3CN.

Equilibrium Concentration of 3.6 / µM	Coverage / $µmol_{complex}\ g_{alumina}^{-1}$
46.99	0.05
87.37	0.11
131.28	0.16
170.95	0.20
211.30	0.24
257.53	0.28

3.7 on Acidic Alumina

Table 3.20: Data for the adsorption isotherm of cage **3.7** on acidic alumina from CH_3CN.

Equilibrium Concentration of 3.7 / µM	Coverage / $µmol_{complex}$ $g_{alumina}^{-1}$
1.77	0.18
3.15	0.35
8.04	0.47
12.47	0.56
20.40	0.67
24.56	0.74
35.18	0.84
43.19	0.93
67.19	1.18
94.64	1.36
139.07	1.63
222.65	2.13

3.7 on Basic Alumina

Table 3.21: Data for the adsorption isotherm of cage **3.7** on basic alumina from CH_3CN.

Equilibrium Concentration of 3.7 / µM	Coverage / $µmol_{complex}$ $g_{alumina}^{-1}$
43.28	0.08
85.27	0.17
127.18	0.25
159.40	0.38
207.50	0.47
245.35	0.54

3.5.5 Adsorption Kinetics

Method

The adsorption kinetics of **3.1** on acidic alumina were investigated *via* the solution depletion method. Known masses of alumina adsorbent (200 mg) were added to a series of cage solutions (1.5 mM, 2 mL). The samples were then equilibrated *via* tumbling for a range of different times (15 – 7200 seconds) at 40 RPM and then centrifuged for 2 minutes at 3000 RPM. The concentrations of the supernatant solutions were then determined using the UV-vis calibration curve shown in Figure 3.41. The depletion of material from solution was attributed to adsorption on the solid support.

The kinetics data were fitted in OriginPro 2017 using the Levenberg Marquardt iteration algorithm with the following, user-defined function:[36]

$$\theta = \theta_{MAX}\left(1 - \frac{1}{\theta_{MAX}kt + 1}\right)$$

in which θ is the total surface coverage (μmol$_{adsorbate}$ g^{-1}$_{alumina}$), θ_{MAX} is the maximum surface coverage (μmol$_{adsorbate}$ g^{-1}$_{alumina}$), k is the second-order rate constant (M^{-1} s^{-1}), and t is the equilibration time (s).

Table 3.22: Data for the adsorption kinetics of cage **3.1** on acidic alumina from D$_2$O.

Equilibration Time / s	Coverage / μmol$_{cage}$ g$_{alumina}$$^{-1}$
7380	14.04
3600	13.97
2160	13.80
660	13.77
300	13.54
60	12.24
30	10.83
15	8.73

3.5.6 Visible Transmission Spectroscopy

Method

The samples for transmission spectroscopy were prepared by sandwiching an aqueous suspension of cage/complex **3.1-3.4** on alumina in NVH immersion oil between two glass slides. **3.1** and **3.4** on acidic alumina were measured relative to bare acidic alumina and **3.2** and **3.3** were measured relative to bare basic alumina. Data were smoothed in Origin Pro 2017 using the Adjacent Averaging method at the 10 point level.
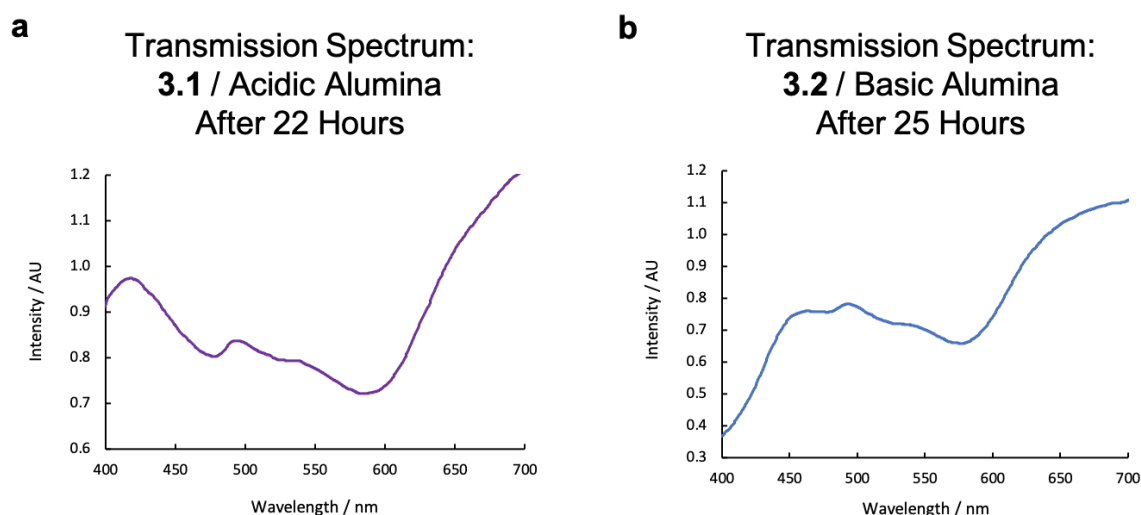

Figure 3.50: a) Visible transmission spectrum of cage **3.1** on acidic alumina after 22 hours, b) Visible transmission spectrum of cage **3.2** on basic alumina after 25 hours. Data collect by Ms Alyssa Smith using samples prepared by Mr Hugh Ryan.

3.5.7 Solution-Phase Host-Guest Chemistry

Neat guests (*ca*. 5 – 20 equivalents) were added to solutions of **3.1** and **3.2** in D_2O (*ca*. 1 – 2 mM) and the samples were allowed to equilibrate for *ca*. 30 minutes at room temperature.

In the ^1H assignments a prime (') denotes where a peak corresponds to the host-guest complex.

FB = fluorobenzene

Cp = cyclopentadiene

NP = N-propylmaleimide

Fluorobenzene⊂3.1

^{1}H NMR (400 MHz, D$_2$O, 298K, referenced to pyrazine at 8.63 ppm) δ_H = 10.89 (s, H$_a$'), 9.35 (s, H$_a$), 9.23 (s, H$_b$'), 8.81 (s, H$_b$), 8.74 (s, H$_e$'), 8.42 (bs, H$_c$/H$_c$'), 8.30 (s, H$_d$'), 7.80 (s, H$_d$), 7.55 (s, H$_e$), 7.45 (s, FB), 7.29 (s, H$_f$'), 7.19 (s, H$_f$), 6.47 (s, H$_g$/H$_g$'), 6.08 (s, H$_h$'), 5.86 (s, H$_h$).

Figure 3.51: ^{1}H NMR (400 MHz, D$_2$O, 298 K) spectrum of cage **3.1** with fluorobenzene, referenced to a pyrazine capillary at 8.63 ppm. Originally reported in reference 27.

Cyclopentadiene⊂3.1

^{1}H NMR (400 MHz, D$_2$O, 298K, referenced to pyrazine at 8.63 ppm) δ_H = 10.22 (s, H$_a$'), 9.35 (s, H$_a$), 9.01 (s, H$_b$'), 8.74 (s, H$_b$), 8.41 (s, H$_c$/H$_c$'), 8.25 (s, H$_e$'), 8.09 (s, H$_d$'), 7.78 (s, H$_d$), 7.55 (s, H$_e$), 7.30 (s, H$_f$'), 7.16 (s, H$_f$), 6.68 (Cp), 6.60 (Cp), 6.47 (s, H$_g$/H$_g$'), 6.01 (s, H$_h$'), 5.85 (s, H$_h$), 5.53 (Cp'), 3.06 (s, Cp), 2.05 (s, Cp').

Figure 3.52: ^{1}H NMR (400 MHz, D$_2$O, 298 K) spectrum of cage **3.1** with cyclopentadiene, referenced to a pyrazine capillary at 8.63 ppm.

Dichloromethane⊂3.1

^{1}H NMR (400 MHz, D$_2$O, 298K, referenced to pyrazine at 8.63 ppm) δ_H = 9.59 (s, H$_a$'), 8.81 (s, H$_b$'), 8.42 (s, H$_c$'), 7.88 (s, H$_d$'), 7.74 (s, H$_e$'), 7.30 (s, H$_f$'), 6.48 (s, H$_g$'), 5.98 (s, H$_h$'), 5.49 (s, DCM).

Figure 3.53: ^{1}H NMR (400 MHz, D$_2$O, 298 K) spectrum of cage **3.1** with dichloromethane, referenced to a pyrazine capillary at 8.63 ppm. Originally reported in reference 27.`

Phloroglucinol with 3.1

^{1}H NMR (400 MHz, D$_2$O, 298 K, referenced to pyrazine at 8.63 ppm) δ_H = 9.46 (s, H$_a$), 8.85 (s, H$_b$), 8.51 (s, H$_c$), 7.88 (s, H$_d$), 7.63 (s, H$_e$), 7.26 (bs, H$_f$), 6.55 (s, H$_g$), 6.11 (phloroglucinol), 5.96 (s, H$_h$).
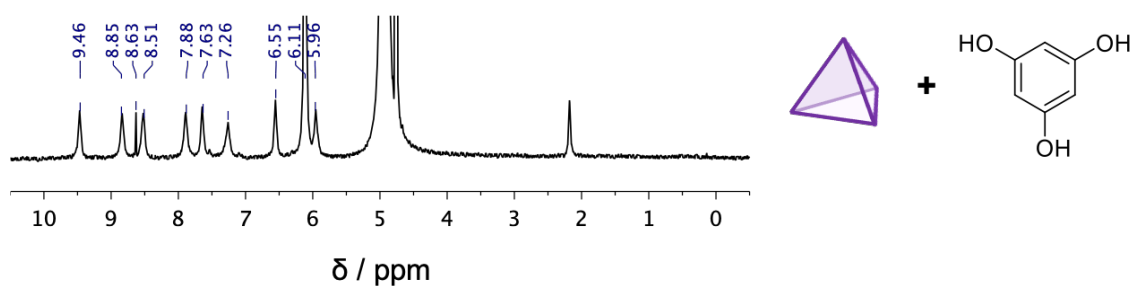

Figure 3.54: ^{1}H NMR (400 MHz, D$_2$O, 298 K) spectrum of cage **3.1** with phloroglucinol, referenced to a pyrazine capillary at 8.63 ppm. The peaks have shifted relative to the empty cage due to the acidity of phloroglucinol.

Pentaerythritol with 3.1

^{1}H NMR (400 MHz, D$_2$O, 298 K, referenced to pyrazine at 8.63 ppm) δ_H = 9.31 (s, H$_a$), 8.69 (s, H$_b$), 8.40 (s, H$_c$), 7.75 (s, H$_d$), 7.53 (s, H$_e$), 7.14 (bs, H$_f$), 6.44 (s, H$_g$), 5.81 (s, H$_h$), 3.60 (pentaerythritol).
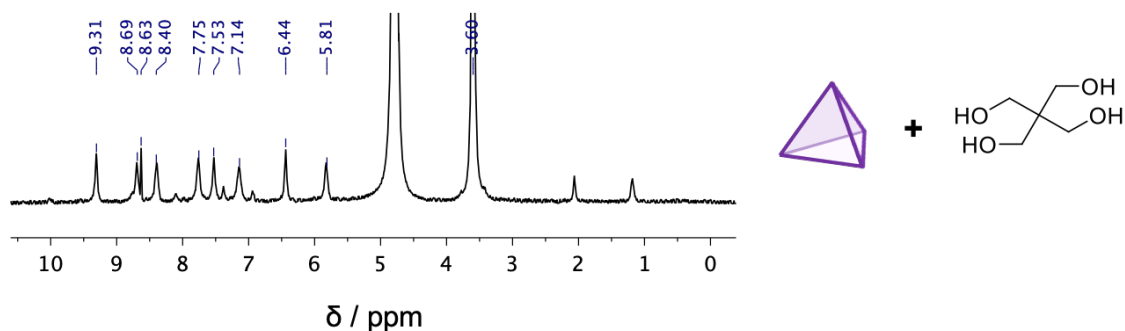

Figure 3.55: ^{1}H NMR (400 MHz, D$_2$O, 298 K) spectrum of cage **3.1** with pentaerythritol, referenced to a pyrazine capillary at 8.63 ppm.

Trifluorobenzene with 3.1

^{1}H NMR (400 MHz, D$_2$O, 298 K, referenced to pyrazine at 8.63 ppm) δ_H = 9.29 (s, H$_a$), 8.67 (s, H$_b$), 8.38 (s, H$_c$), 7.75 (s, H$_d$), 7.51 (s, H$_e$), 7.11 (bs, H$_f$), 6.82 (trifluorobenzene), 6.42 (s, H$_g$), 5.81 (s, H$_h$).
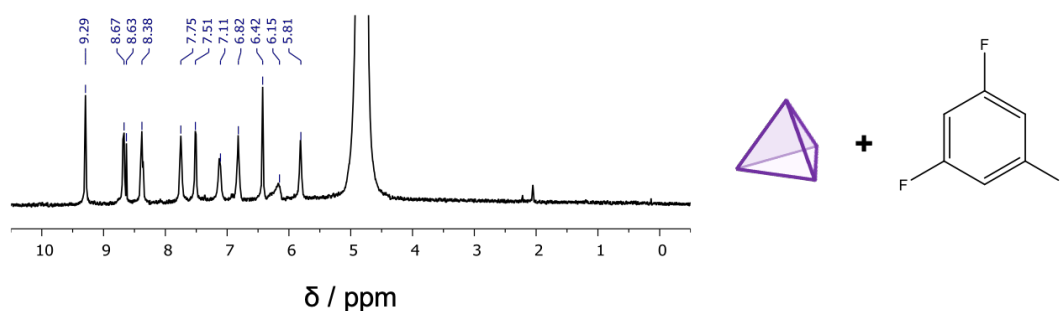

Figure 3.56: ^{1}H NMR (400 MHz, D$_2$O, 298 K) spectrum of cage **3.1** with trifluorobenzene, referenced to a pyrazine capillary at 8.63 ppm.

Fluorobenzene⊂3.2

^{1}H NMR (400 MHz, D$_2$O, 298K, referenced to acetone at 2.22 ppm) δ_H = 9.04 (s, H$_e$'), 8.60 (d, H$_d$'), 8.44 (t, H$_c$'), 7.76 (t, H$_b$'), 7.47 (d, H$_a$'/H$_g$'), 7.22 (FB'), 6.98 (FB'), 6.84 (FB'), 5.92 (bs, H$_f$'), 3.48 (s, H$_h$').
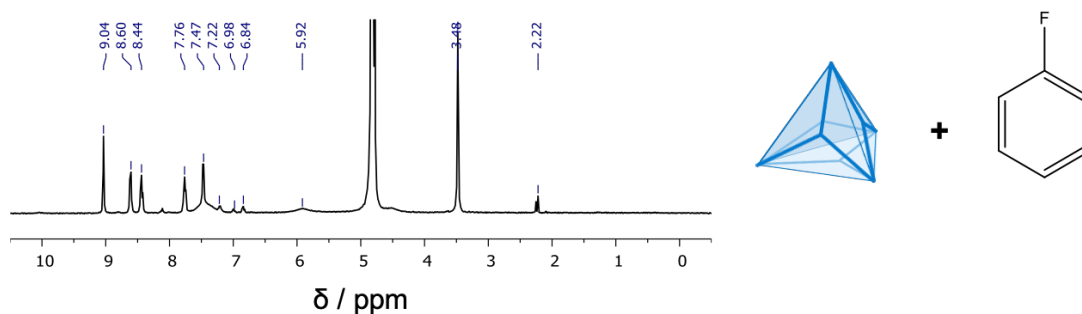

Figure 3.57: ^{1}H NMR (400 MHz, D$_2$O, 298 K) spectrum of cage **3.2** with fluorobenzene, referenced to acetone at 2.22 ppm.

N-propylmaleimide⊂3.2

^{1}H NMR (400 MHz, D$_2$O, 298K, referenced to acetone at 2.22 ppm) δ_H = 9.01 (s, H$_e$'), 8.58 (d, H$_d$'), 8.41 (t, H$_c$'), 7.73 (t, H$_b$'), 7.49 (d, H$_a$'/H$_g$'), 6.82 (NP), 6.62 (NP'), 5.26 (bs, H$_f$'), 3.45 (s, H$_h$'/NP), 1.56 (NP), 0.83 (NP), 0.56 (NP').
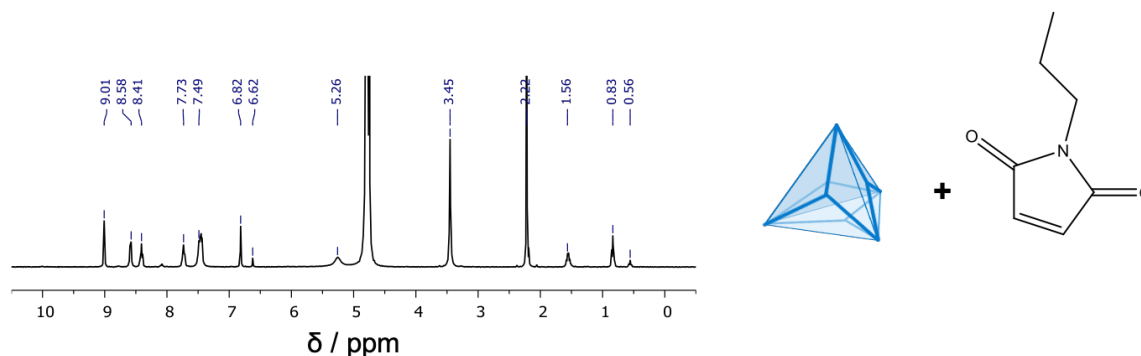

Figure 3.58: ^{1}H NMR (400 MHz, D$_2$O, 298 K) spectrum of cage **3.2** with N-propylmaleimide, referenced to acetone at 2.22 ppm.

Dichloromethane⊂3.2

^{1}H NMR (400 MHz, D$_2$O, 298K, referenced to acetone at 2.22 ppm) δ_H = 9.03 (s, H$_e$'), 8.60 (d, H$_d$'), 8.44 (t, H$_c$'), 7.76 (t, H$_b$'), 7.46 (d, H$_a$'/H$_g$'), 5.92 (bs, H$_f$'), 5.36 (DCM). 3.48 (s, H$_h$').
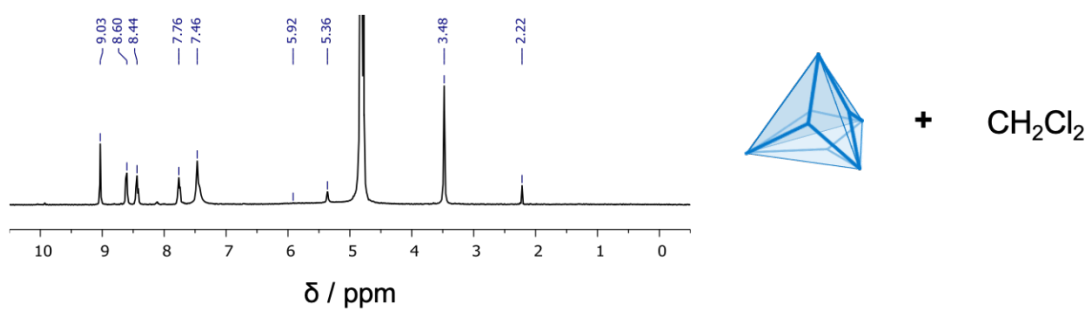

Figure 3.59: ^{1}H NMR (400 MHz, D$_2$O, 298 K) spectrum of cage **3.2** with dichloromethane, referenced to acetone at 2.22 ppm. Originally reported in reference 29.

3.5.8 Thermodynamics and Kinetics of Guest Binding

The thermodynamics and kinetics of cyclopentadiene⊂**3.1** and N-propyl maleimide⊂**3.2** were investigated *via* ^{1}H NMR spectroscopy. An excess of guest (10-20 equivalents) was added to a sample of empty cage (*ca.* 0.5 – 1 mM) and the system's NMR spectrum was recorded at regular intervals. The evolution of the host-guest peaks was fitted to a model of pseudo-first order kinetics and the thermodynamic binding constant was estimated from the final spectrum in the series. All data were fitted in OriginPro 2020 using the functions defined in the following sections.

Cyclopentadiene⊂3.1

The imine peak of cage **3.1** (*ca.* 9.33 ppm) has been shown previously to report of the presence of encapsulated guest species.[25–27] Upon the addition of cyclopentadiene, a new imine peak appears at 10.22 ppm. The kinetics of the uptake of cyclopentadiene were monitored *via* the ratio of the empty cage imine peak at 9.33 ppm to the sum of empty host and host-guest peaks over time.

The following model of pseudo-first order kinetics was used to study cyclopentadiene⊂**3.1**:

$$\frac{\int H}{\int H + \int HG} = A \exp(-kt) + B$$

In which $\int H$ is the integral of the empty host imine peak (9.33 ppm), $\int HG$ is the integral of the host-guest imine peak (10.22 ppm), and A, B, and k are fitted parameters.

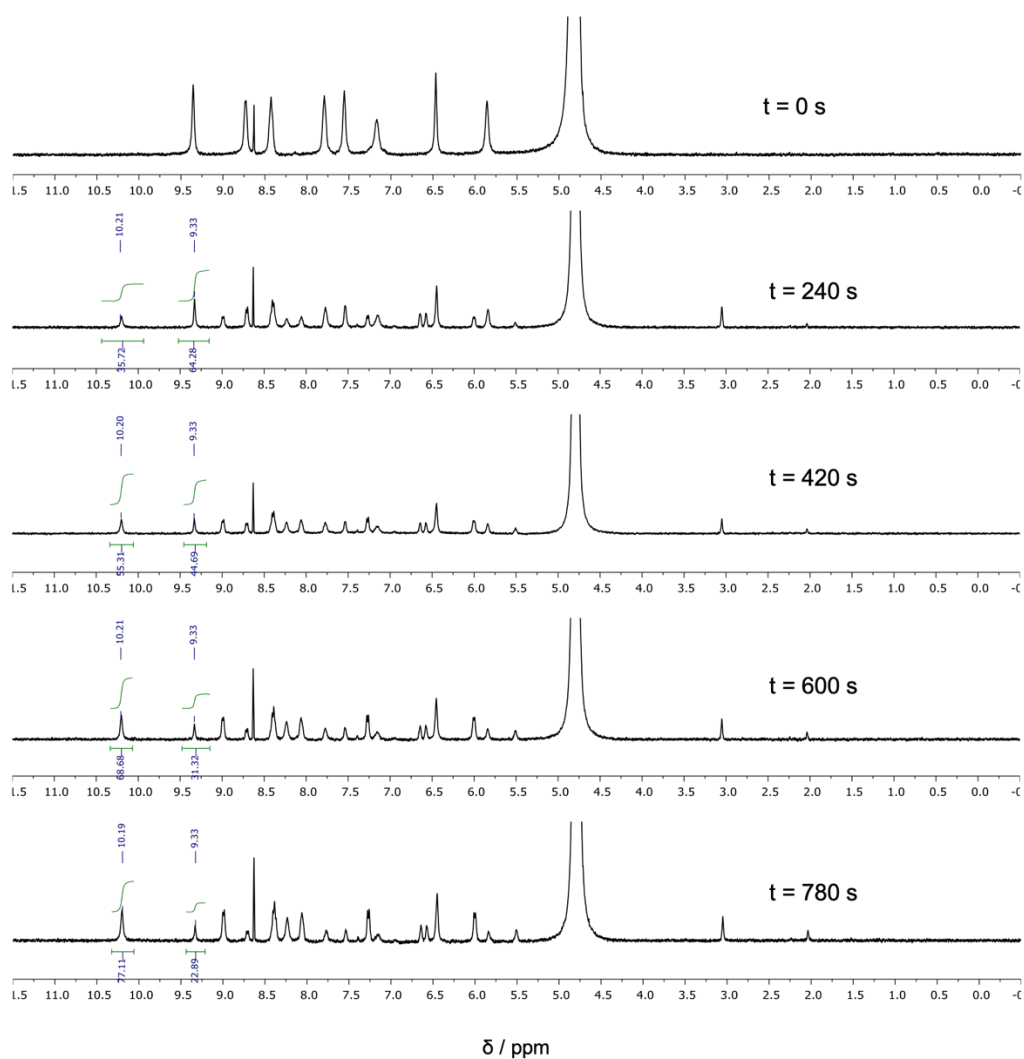Figure 3.60: ^{1}H NMR (400 MHz, D_2O, 298 K) spectra for the time evolution of cyclopentadiene⊂**3.1**.

Figure 3.61: Kinetic plot of the uptake of cyclopentadiene by **3.1**, A = 1, B = 0, k = 1.90(2) × 10^{-3} M^{-1} s^{-1}.

Table 3.23: Kinetics data for the uptake of cyclopentadiene by cage **3.1**.

Time / s	Integral of H	Integral of HG	H/(H+HG)
0	100	0	1
240	64.28	35.72	0.6428
420	44.69	55.31	0.4469
600	31.32	68.68	0.3132
780	22.89	77.11	0.2289

The thermodynamic binding constant for cyclopentadiene⊂**1** was estimated from the ^{1}H NMR spectrum after >3600 s.

Figure 3.62: ^{1}H NMR (400 MHz, D$_2$O, 298 K) spectrum of cyclopentadiene⊂**3.1** after 3600 s, estimated $K_a = 1.4 \times 10^3 \, M^{-1}$.

N-propylmaleimide⊂3.2

Unlike in the case of cage **3.1**, the imine peak of cage **3.2** does not report clearly on the presence of encapsulated guest species and remains at approximately 8.99 ppm, irrespective of the guest species. Upon addition of N-propyl maleimide, however, a peak at 0.45 ppm evolves in the spectrum of cage **3.2**, corresponding to the methyl group of the encapsulated guest. The kinetics of the uptake of N-propyl maleimide by cage **3.2** were thus monitored by the evolution of this peak at 0.45 ppm relative to the integral of the imine peak (*ca*. 8.99 ppm).

The following model of pseudo-first order kinetics was used to study N-propyl maleimide⊂**3.2**:

$$\frac{\int Bound\ Methyl\ Peak}{\int Imine\ Peak} = A\left(1 - \exp(-kt)\right) + B$$
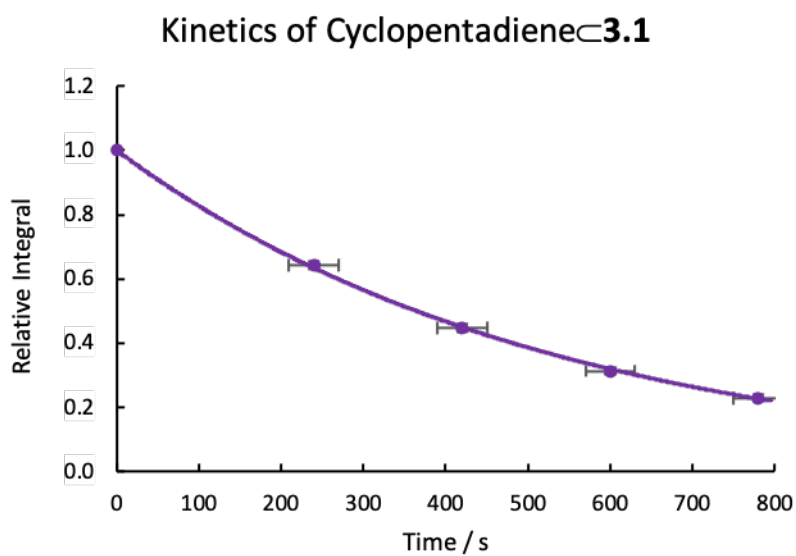
In which A, B, and k are fitted parameters. Note that in the case of full conversion to the host-guest complex, the ratio of integrals should be equal to 0.25 (*i.e.* 1:4). In the following data the imine peak integral was set arbitrarily to 100 and thus A was set to 25.

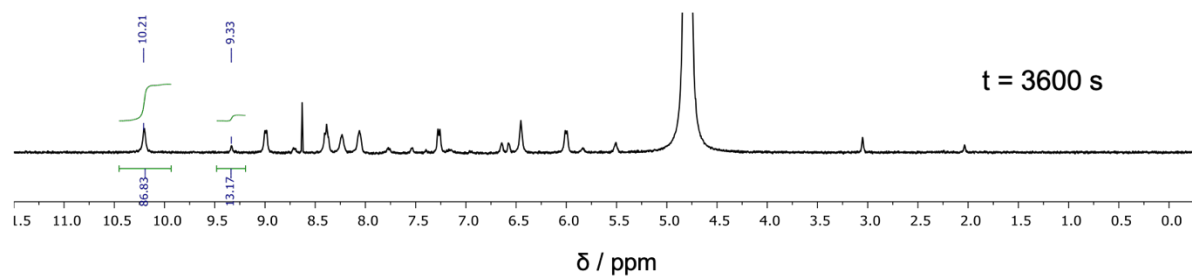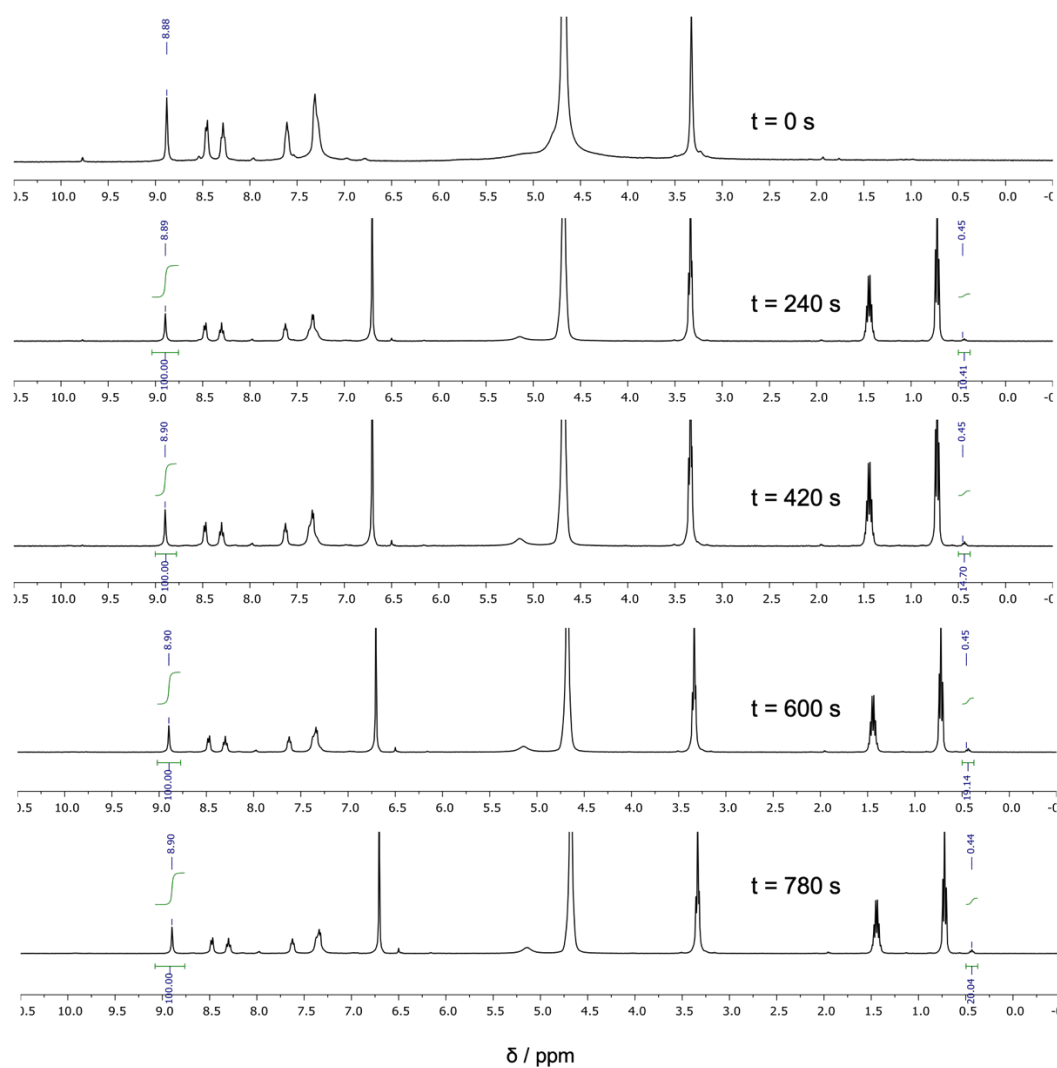Figure 3.63: ^{1}H NMR (400 MHz, D$_2$O, 298 K) spectra for the time evolution of N-propyl maleimide⊂**3.2**.
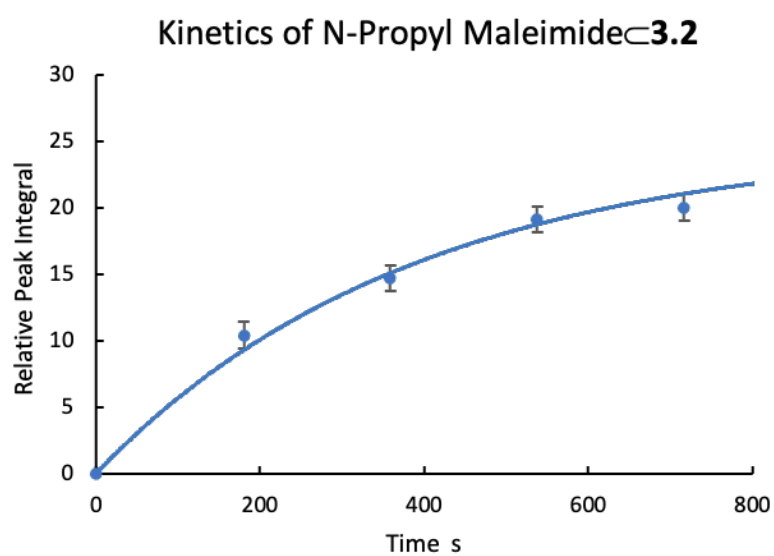
Figure 3.64: Kinetic plot of the uptake of N-propyl maleimide by **3.2**, A = 25, B = 0, k = 2.6(1) × 10^{-3} M^{-1} s^{-1}.

Table 3.24: Kinetics data for the uptake of N-propylmaleimide by cage **3.2**.

Time / s	Relative Peak Integral
0	0.00
180	10.41
359	14.70
538	19.14
717	20.04

The thermodynamic binding constant for N-propylmaleimide⊂**3.2** was estimated from the ^{1}H NMR spectrum after >3600 s.

Figure 3.65: ^{1}H NMR (400 MHz, D$_2$O, 298 K) spectrum of N-propyl maleimide⊂**3.2** after 3600 s, estimated $K_a = 1.5 \times 10^3$ M^{-1}.

3.5.9 Guest Displacement Experiments

Method (Water)

Solid alumina support (1 g) was added to a solution of excess cage/complex in water (*ca*. 5 – 10 mM, 10 mL) and stirred to adsorb the material. The alumina slurry was then loaded into a 5 mL syringe, which contained a cotton wool plug to prevent the alumina from 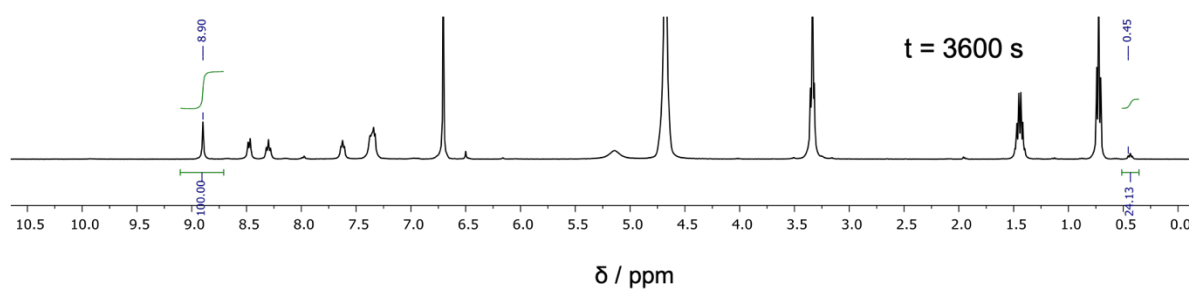passing through the syringe. The "cage column" was washed with water to remove the excess cage/complex. An initial guest solution was eluted slowly through the column (3 mL, 0.1 mL/min) and the column was washed with water to remove the excess guest (*ca*. 25 mL, 5 mL/min). The column was washed with D_2O (5 mL, 5 mL/min) and then eluted with D_2O (3 × 1 mL, 1 mL/min) and then aqueous DCM (3 × 1 mL, *ca*. 200 mM, 1 mL/min). The final D_2O elution and all aqueous DCM elutions were analysed by ^1H NMR. The NMR spectra are referenced to 2 mM pyrazine in D_2O (8.63 ppm) in order to compare guest concentrations between spectra. All spectra were run with 16 scans and receiver gain set to 71.8.

In the guest displacement columns of **3.2**, **3.3**, and **3.4** adsorbed material was observed to slowly leach from the surface at a rate of ~ 7 μM min^{-1} (for **3.2**), ~ 26 μM min^{-1} (for **3.3**), and ~ 15 μM min^{-1} (for **3.4**), by UV-Vis spectroscopy. This gradual adsorbate elution was attributed to the weakly bound electric multilayers observed in the adsorption isotherms. No such material elution was observed for guest displacement columns of **3.1**.

Cage 3.1 on Acidic Alumina with Fluorobenzene/Dichloromethane
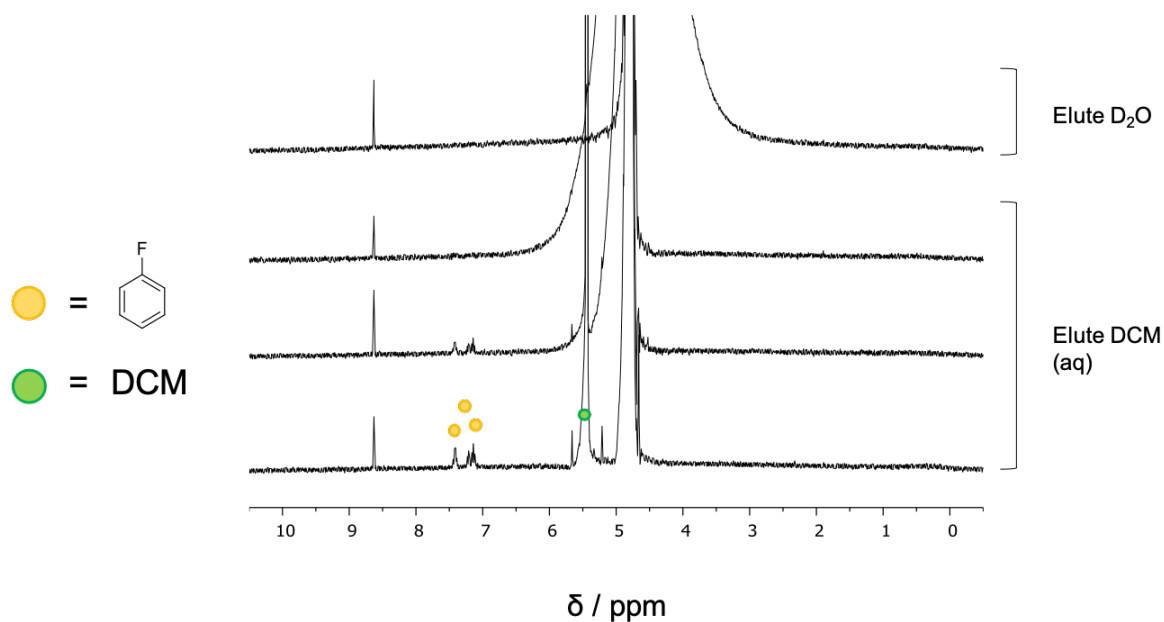
Figure 3.66: ^{1}H NMR (400 MHz, D$_2$O, 298 K) spectra of an experiment to displace fluorobenzene from **3.1** on acidic alumina *via* successive (top to bottom) 1 mL elutions of DCM (aq).

Cage 3.1 on Acidic Alumina with Cyclopentadiene/Dichloromethane
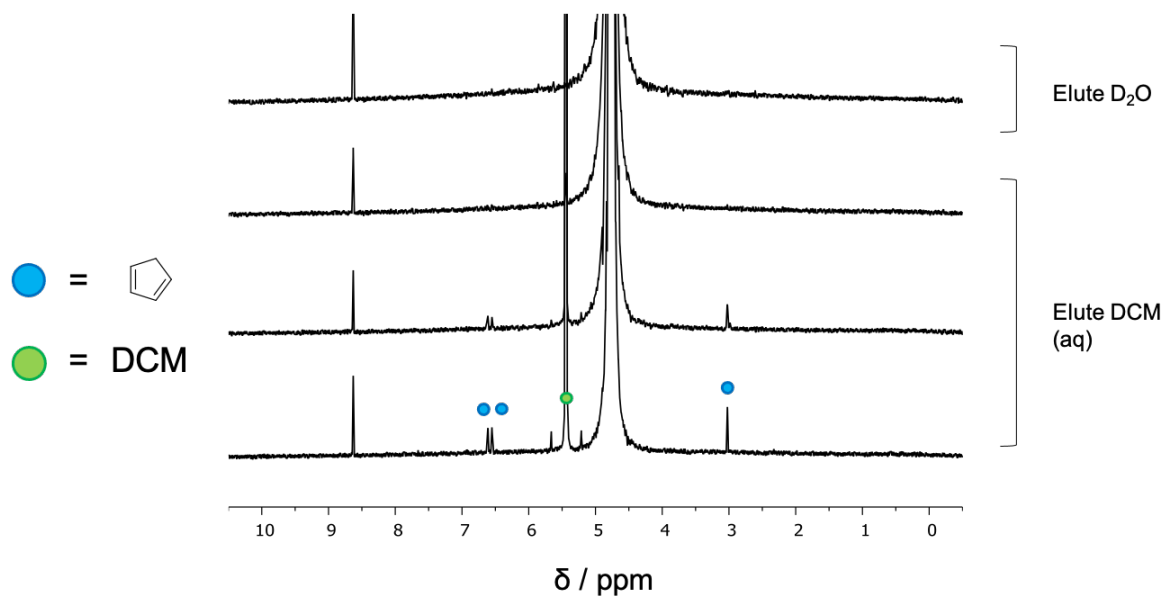
Figure 3.67: ^{1}H NMR (400 MHz, D$_2$O, 298 K) spectra of an experiment to displace cyclopentadiene from **3.1** on acidic alumina *via* successive (top to bottom) 1 mL elutions of DCM (aq).

Cage 3.1 on Acidic Alumina with Cyclopentadiene/Dichloromethane (after two weeks)
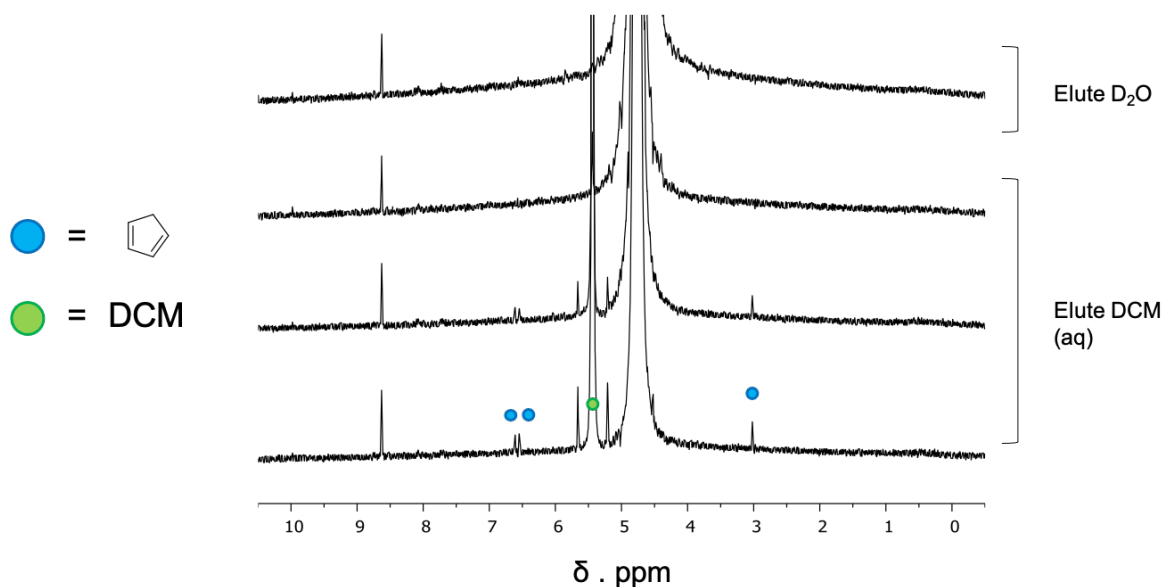
Figure 3.68: ^{1}H NMR (400 MHz, D$_2$O, 298 K) spectra of an experiment to displace cyclopentadiene from **3.1** on acidic alumina *via* successive (top to bottom) 1 mL elutions of DCM (aq), 2 weeks after the initial loading of cyclopentadiene.

The adsorbed cages were loaded with cyclopentadiene and washed with water as described above and then left at room temperature for two weeks. The cage column was then washed with water (*ca.* 25 mL) and D$_2$O (5 mL) and then eluted with 3 × 1 mL D$_2$O and 3 × 1 mL DCM (aq).

Cage 3.1 on Acidic Alumina with Phloroglucinol/Dichloromethane
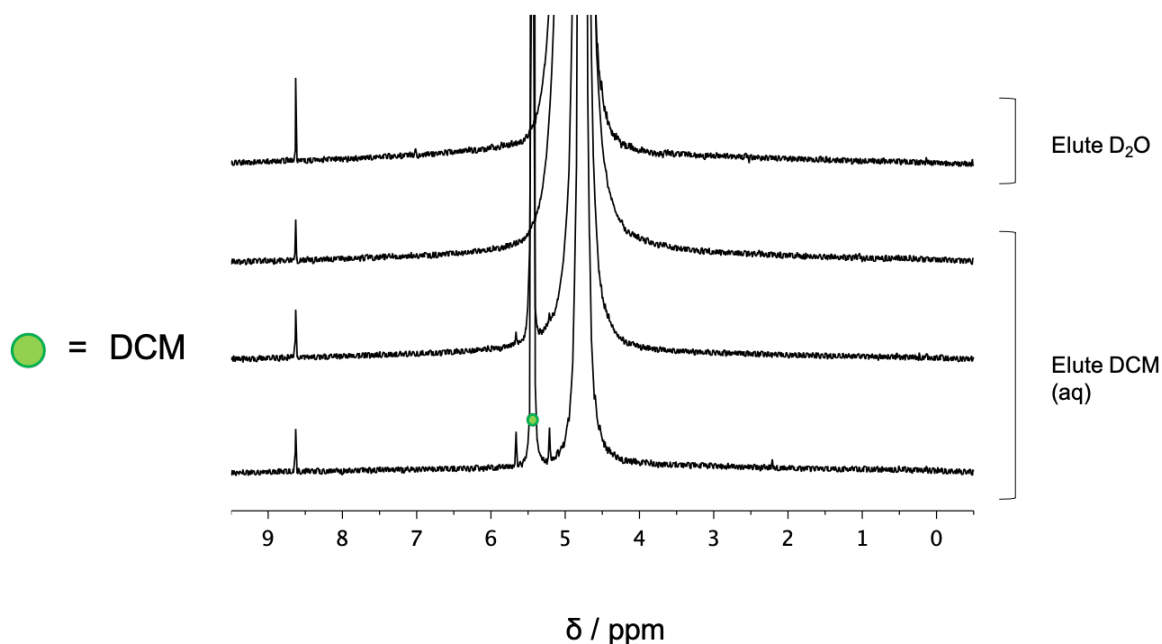
Figure 3.69: ^{1}H NMR (400 MHz, D$_2$O, 298 K) spectra of experiment to show that phloroglucinol, a non-guest for **3.1**, does not bind with adsorbed **3.1** and thus does not elute from a column of **3.1** on acidic alumina following successive (top to bottom) 1 mL elutions with DCM (aq).

Cage 3.1 on Acidic Alumina with Pentaerythritol/Dichloromethane

Figure 3.70: ^{1}H NMR (400 MHz, D$_2$O, 298 K) spectra of experiment to show that pentaerythritol, a non-guest for **3.1**, does not bind with adsorbed **3.1** and thus does not elute from a column of **3.1** on acidic alumina following successive (top to bottom) 1 mL elutions with DCM (aq).

Cage 3.1 on Acidic Alumina with Trifluorobenzene/Dichloromethane

Figure 3.71: ^{1}H NMR (400 MHz, D$_2$O, 298 K) spectra of experiment to show that trifluorobenzene, a non-guest for **3.1**, does not bind with adsorbed **3.1** and thus does not elute from a column of **3.1** on acidic alumina following successive (top to bottom) 1 mL elutions with DCM (aq).

Cage 3.2 on Basic Alumina with Fluorobenzene/Dichloromethane

Figure 3.72: ^{1}H NMR (400 MHz, D$_2$O, 298 K) spectra of experiment to displace fluorobenzene from **3.2** on basic alumina via successive (top to bottom) 1 mL elutions of DCM (aq).

Cage 3.2 on Basic Alumina with N-propyl Maleimide/Dichloromethane
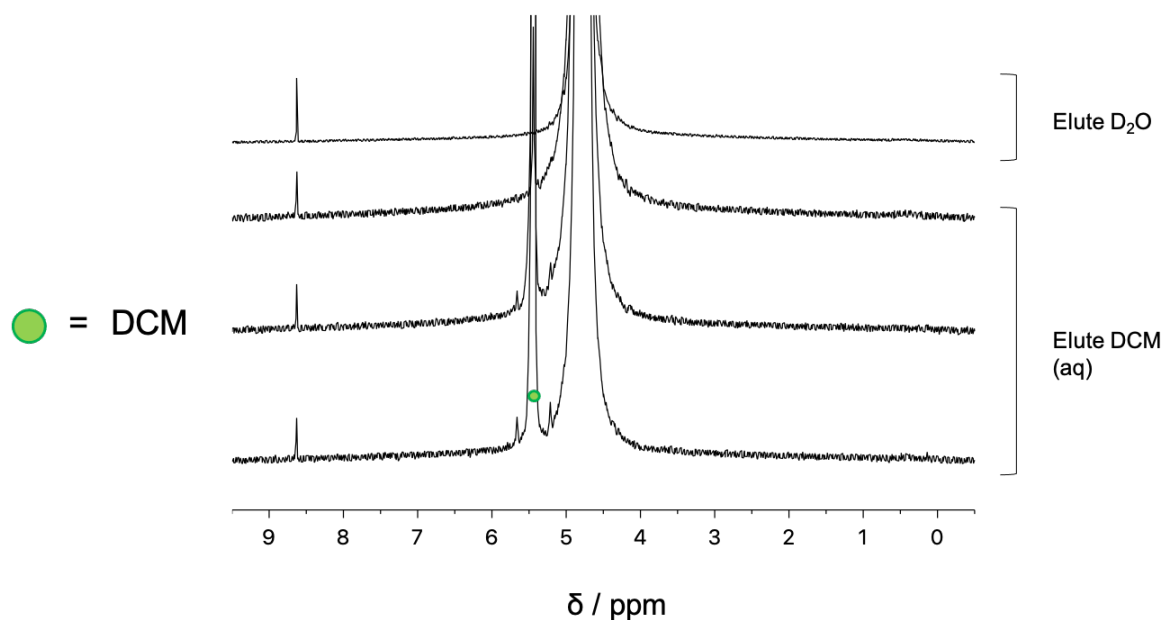

Figure 3.73: ^{1}H NMR (400 MHz, D$_2$O, 298 K) spectra of experiment to displace N-propylmaleimide from **3.2** on basic alumina via successive (top to bottom) 1 mL elutions of DCM (aq).

Complex 3.3 on Basic Alumina with Fluorobenzene/Dichloromethane

Figure 3.74: ^{1}H NMR (400 MHz, D$_2$O, 298 K) spectra of control experiment for displacement of fluorobenzene from **3.3** on basic alumina via successive (top to bottom) 1 mL elutions of DCM (aq).

Complex 3.3 on Basic Alumina with N-propyl Maleimide/Dichloromethane

Figure 3.75: ^{1}H NMR (400 MHz, D$_2$O, 298 K) spectra of control experiment for displacement of N-propylmaleimide from **3.3** on basic alumina *via* successive (top to bottom) 1 mL elutions of DCM (aq).

Complex 3.4 on Acidic Alumina with Fluorobenzene/Dichloromethane
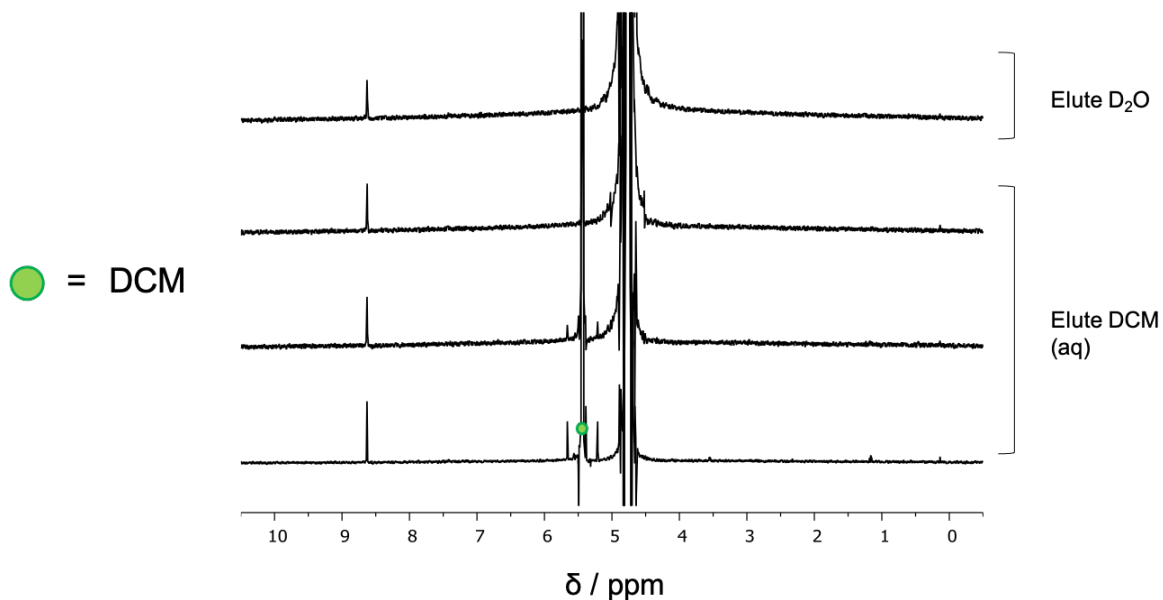
Figure 3.76: ^{1}H NMR (400 MHz, D$_2$O, 298 K) spectra of control experiment for displacement of fluorobenzene from **3.4** on acidic alumina *via* successive (top to bottom) 1 mL elutions of DCM (aq).

Complex 3.4 on Acidic Alumina with Cyclopentadiene/Dichloromethane
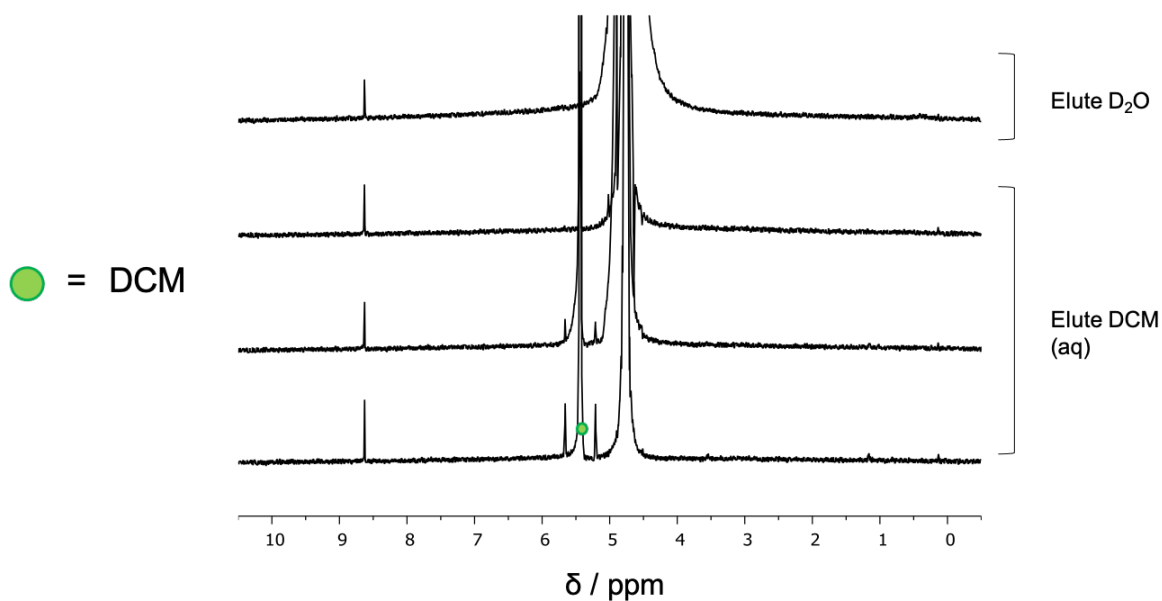
Figure 3.77: ^{1}H NMR (400 MHz, D$_2$O, 298 K) spectra of control experiment for displacement of cyclopentadiene from **3.4** on acidic alumina *via* successive (top to bottom) 1 mL elutions of DCM (aq).

Acidic Alumina with Fluorobenzene/Dichloromethane
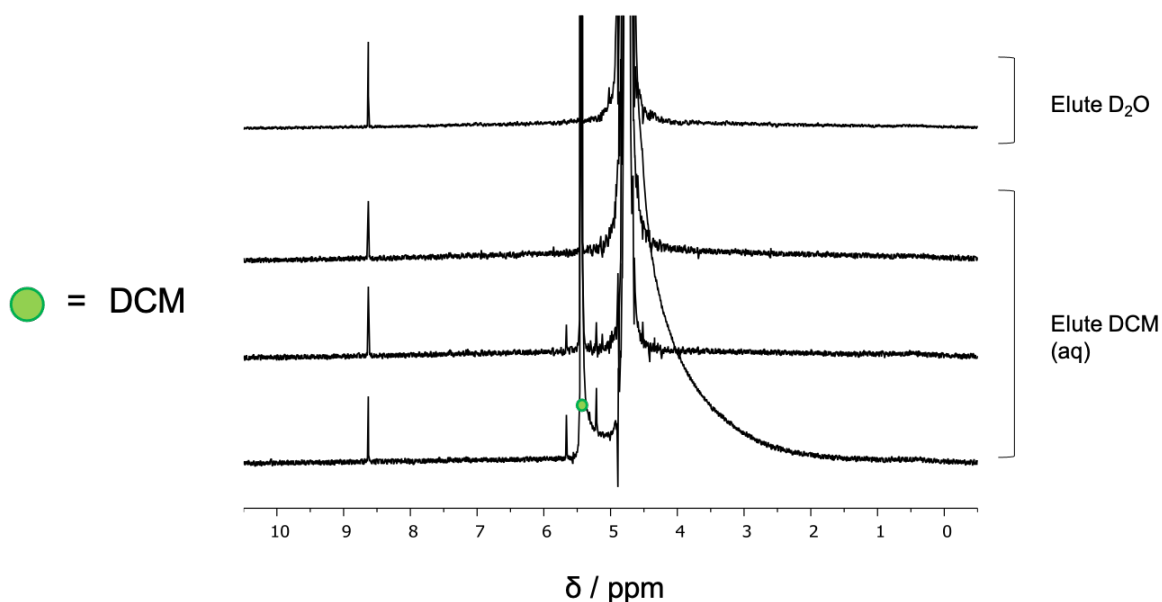
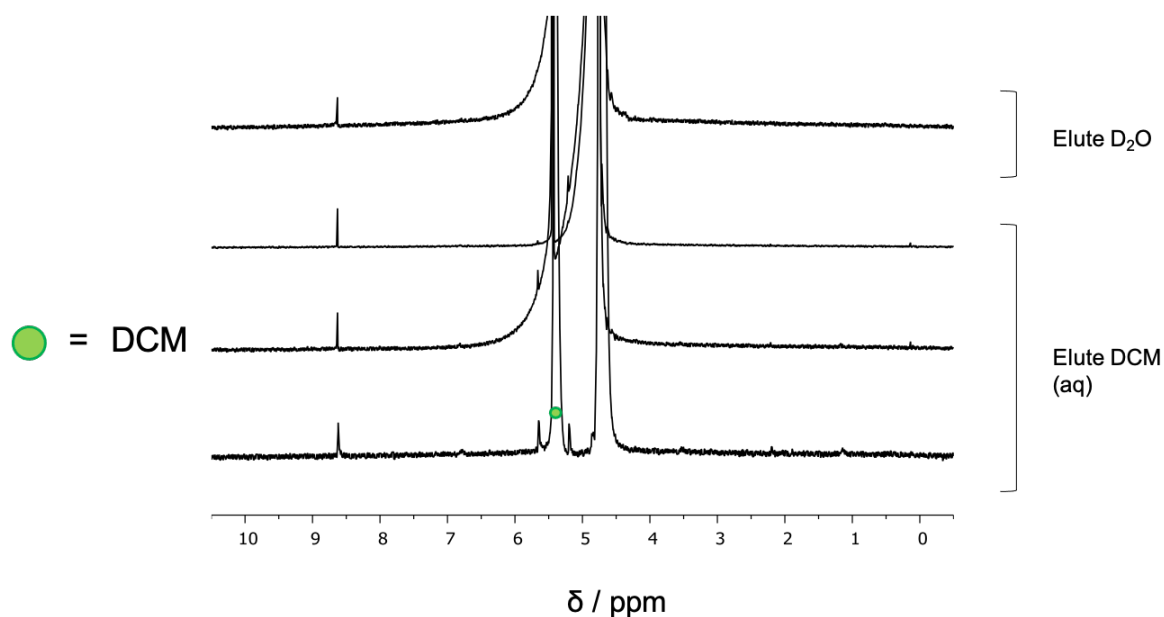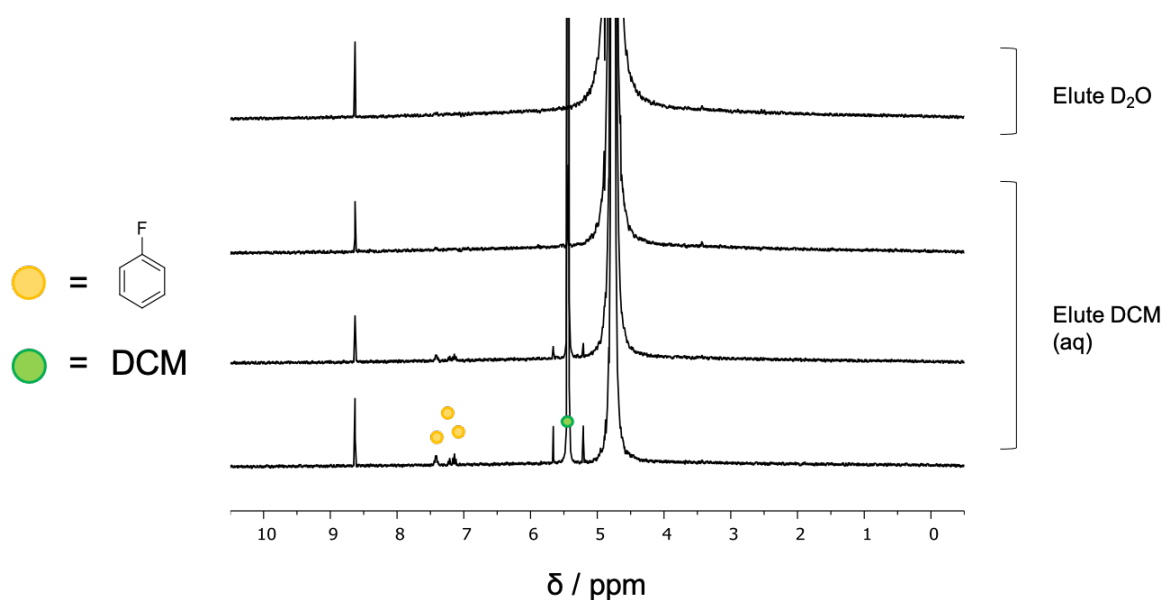Figure 3.78: ^{1}H NMR (400 MHz, D$_2$O, 298 K) spectra of control experiment for displacement of fluorobenzene from bare acidic alumina *via* successive (top to bottom) 1 mL elutions of DCM (aq).

Acidic Alumina with Cyclopentadiene/Dichloromethane
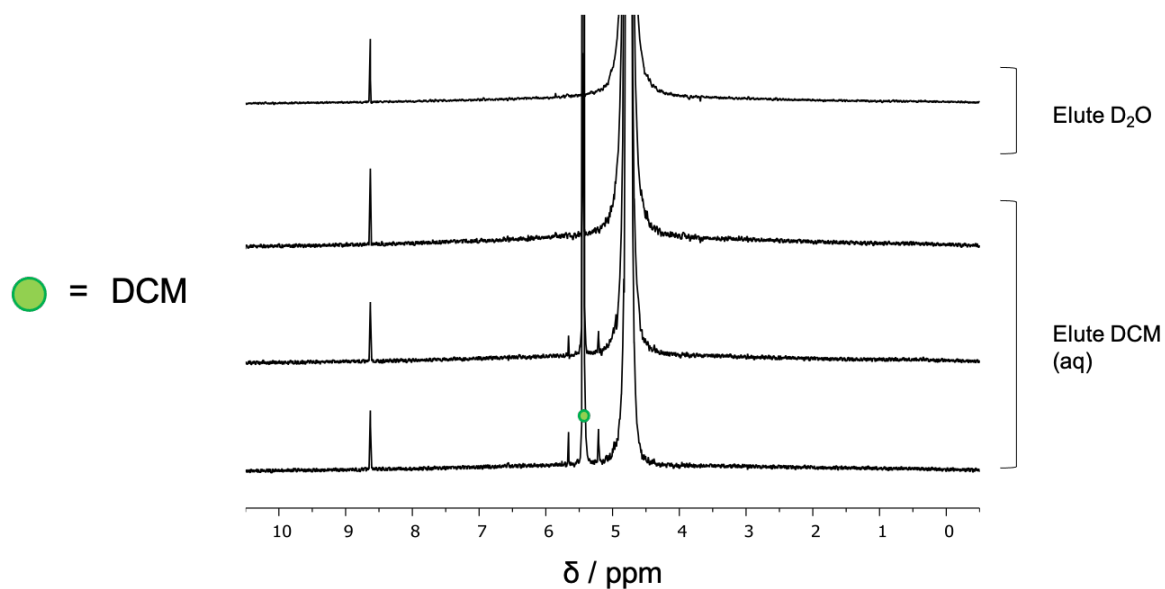
Figure 3.79: ^{1}H NMR (400 MHz, D$_2$O, 298 K) spectra of control experiment for displacement of cyclopentadiene from bare acidic alumina *via* successive (top to bottom) 1 mL elutions of DCM (aq).

Basic Alumina with Fluorobenzene/Dichloromethane
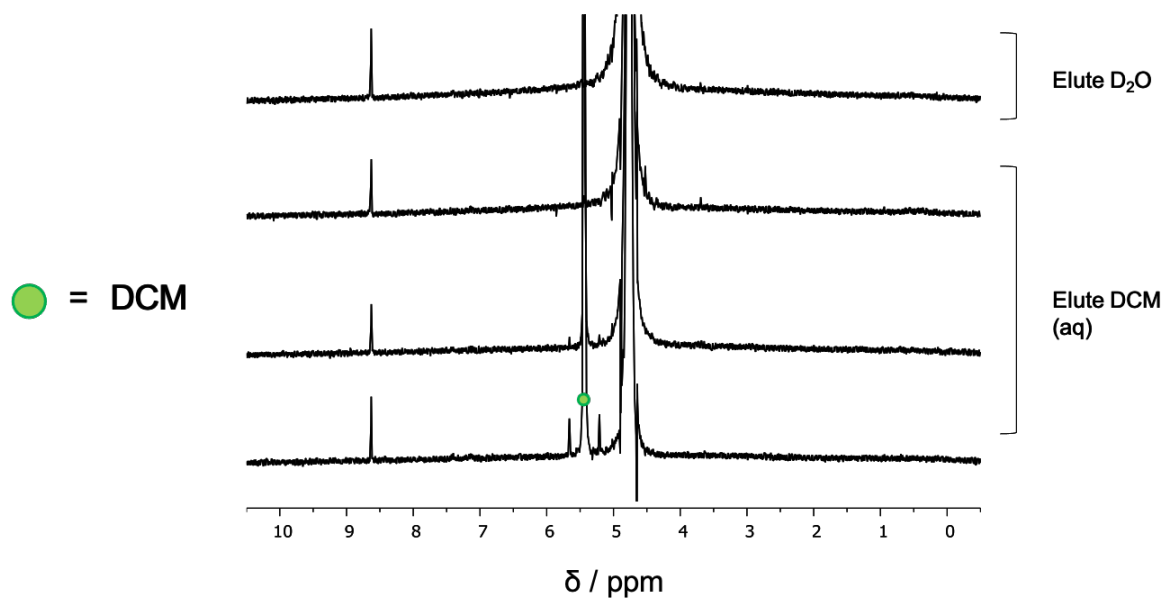
Figure 3.80: ^{1}H NMR (400 MHz, D$_2$O, 298 K) spectra of control experiment for displacement of fluorobenzene from bare basic alumina *via* successive (top to bottom) 1 mL elutions of DCM (aq).

Basic Alumina with N-propyl Maleimide/Dichloromethane

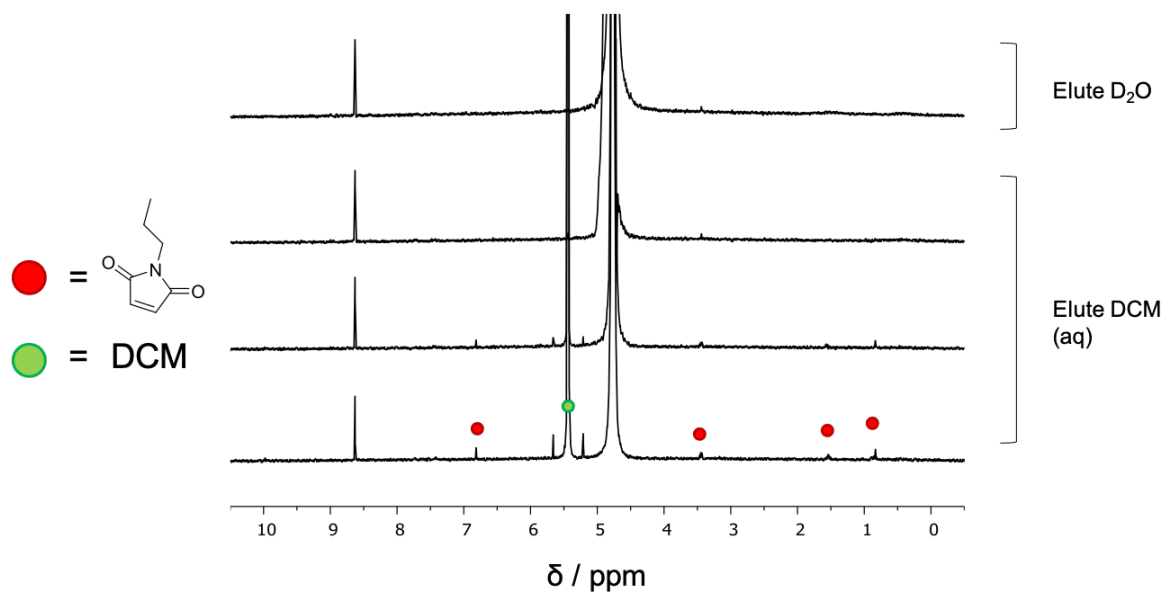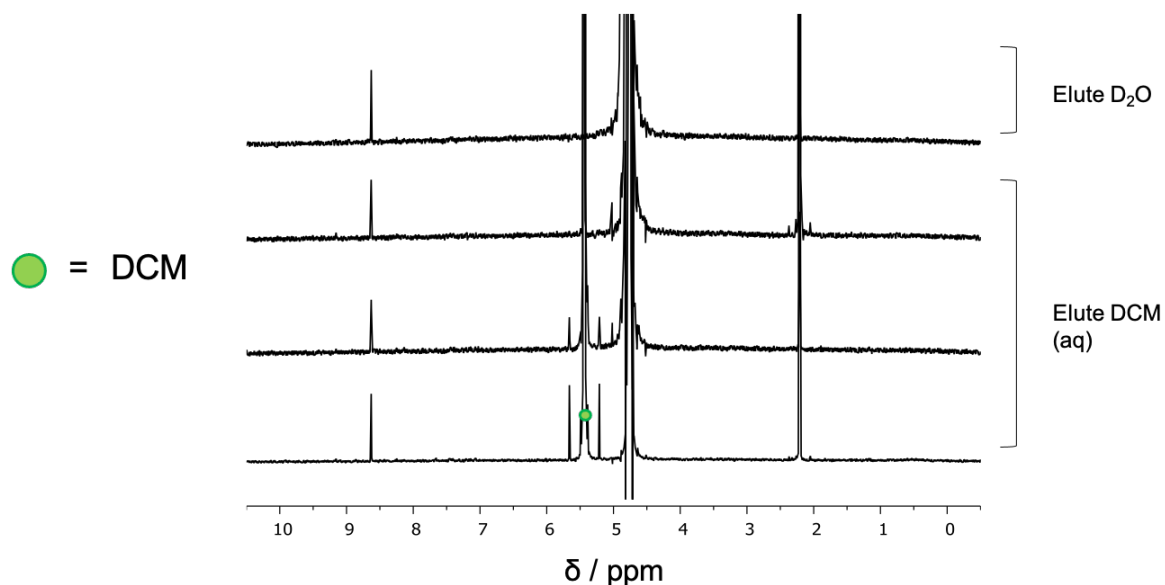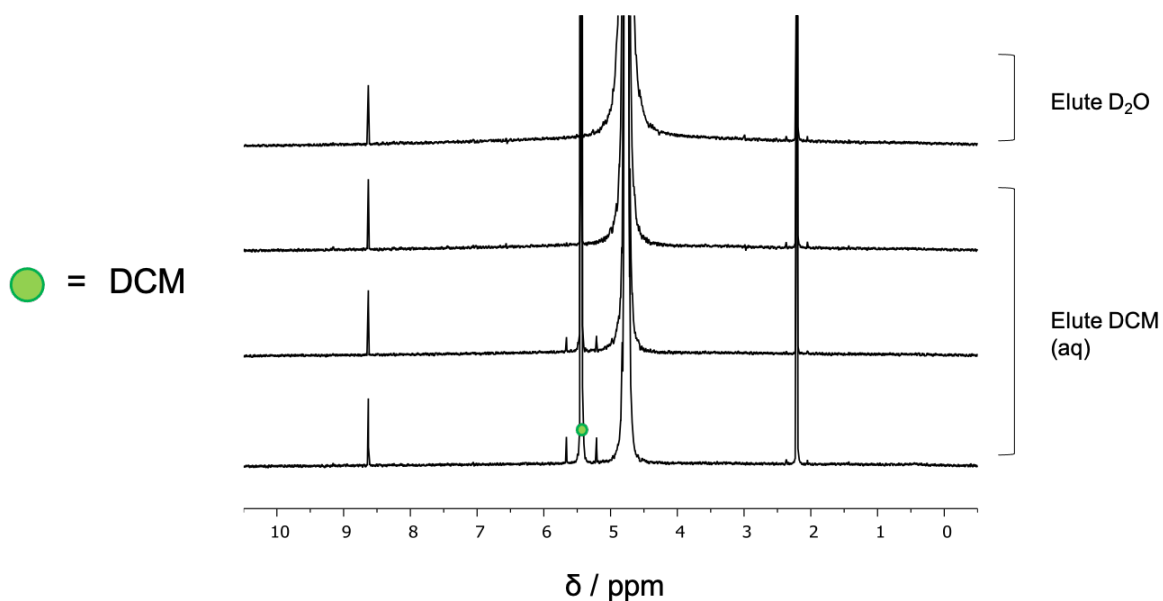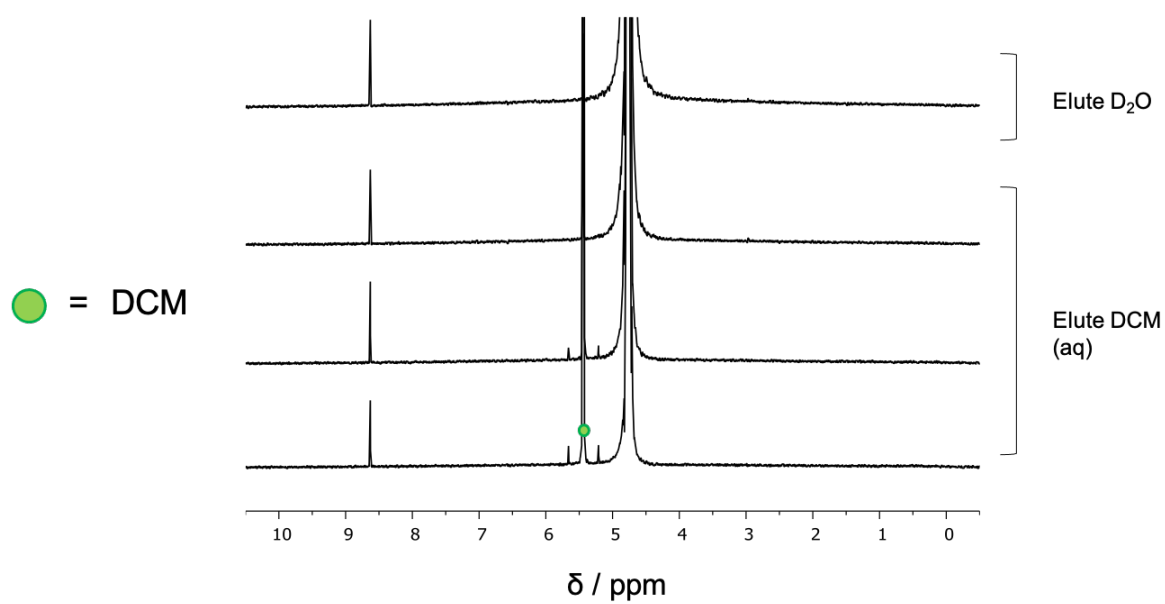Figure 3.81: ^{1}H NMR (400 MHz, D$_2$O, 298 K) spectra of control experiment for displacement of N-propylmaleimide from bare basic alumina *via* successive (top to bottom) 1 mL elutions of DCM (aq).

Method (Acetonitrile)

Solid alumina support (5 g) was added to a solution of excess cage **3.5** in acetonitrile (*ca*. 5 mM, 50 mL) and stirred for *ca*. 1 minute to adsorb the material. The alumina slurry was then loaded into a 12 mL syringe, which contained a cotton wool plug to prevent the alumina from passing through the syringe. The "cage column" was washed with acetonitrile to remove the excess cage. Fluorobenzene in CH_3CN was eluted slowly through the column (*ca*. 30 mM, 6 mL, 0.2 mL/min) and the column was washed with CH_3CN to remove the excess guest (*ca*. 24 mL, 5 mL/min). The column was washed with CD_3CN (5 mL, 5 mL/min) and then eluted with CD_3CN (3 × 1 mL, 1 mL/min) and then DCM in CD_3CN (5 × 1 mL, 1 mL/min). The final CD_3CN elution and all DCM in CD_3CN elutions were analysed by ^1H NMR. The NMR spectra are referenced to 2 mM pyrazine in D_2O (8.63 ppm) in order to compare guest concentrations between spectra. All spectra were run with 16 scans and receiver gain set to 71.8.

Figure 3.82: ^{1}H NMR (400 MHz, CD$_3$CN, 298 K) spectra of an experiment to displace fluorobenzene from **3.5** on acidic alumina via successive (top to bottom) 1 mL elutions of DCM in CD$_3$CN.

3.5.10 Guest Separation Experiments

Method

Acidic alumina (*ca.* 2 g) was added to a solution of excess **3.1** in water (20 mL) and the slurry stirred to adsorb the cage material. The alumina slurry was then loaded into a 5 mL syringe, which contained a cotton wool plug to prevent the alumina from passing through the syringe. The "cage column" was washed with water to remove the excess cage. An aqueous mixture of fluorobenzene and trifluorobenzene (each at 2 mM, 10 mL, 0.34 mL/min) was eluted through the cage column and then the column was washed with water to remove the excess guest and non-guest (*ca.* 25 mL, 5 mL/min). The column was washed with D_2O (5 mL, 5 mL/min) and eluted with D_2O (3 × 1 mL, 1 mL/min) and then aqueous DCM (saturated, *ca.* 0.2 M, 5 × 1 mL, 1 mL/min). The final D_2O elution and all aqueous DCM elutions were analysed by ^1H NMR and ^{19}F NMR. The ^1H NMR spectra were referenced to the residual solvent peak (4.79 ppm) and all spectra were run with 16 scans and receiver gain set to 71.8. The ^{19}F NMR spectra were referenced to hexafluorobenzene in D_2O (-162.9 ppm) and all spectra were run with 128 scans and receiver gain set to 203.

Guest Mixture

The ^1H and ^{19}F NMR spectra of the guest mixture are given in Figure 3.25.

Guest Separation
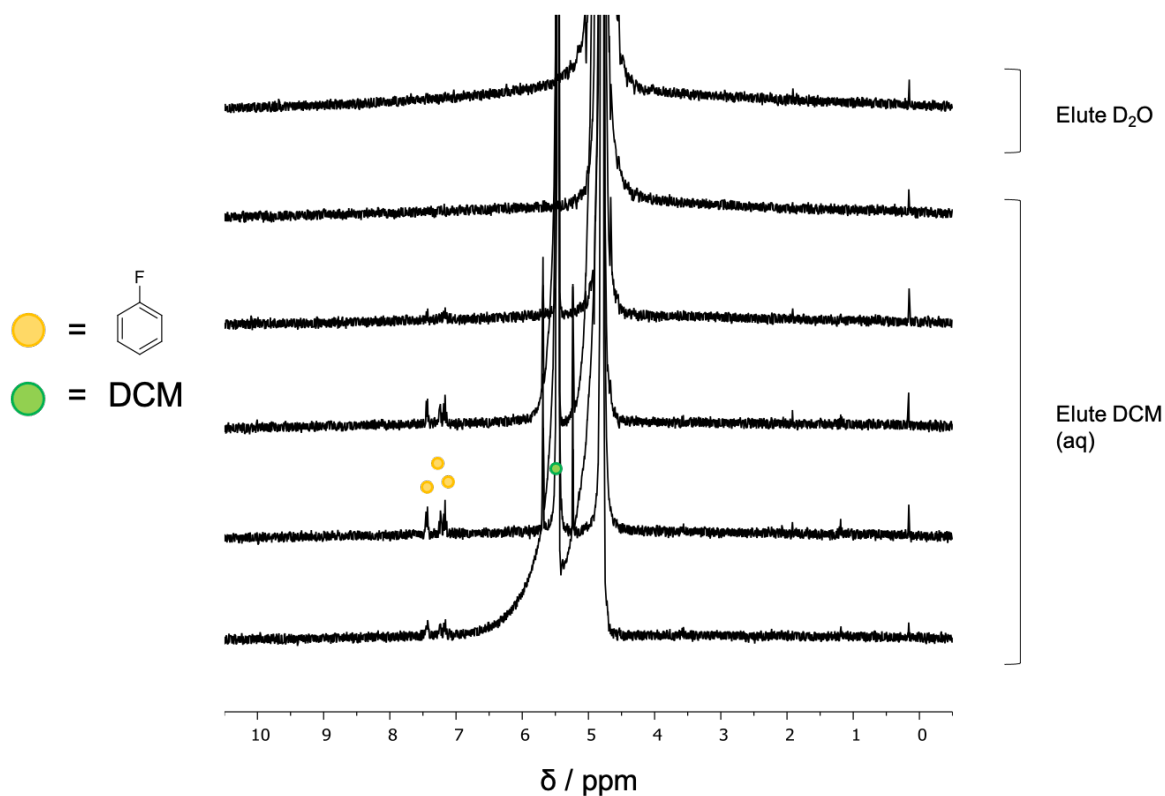
Figure 3.83: ^{1}H NMR (400 MHz, D$_2$O, 298 K) spectra of the separation of fluorobenzene from trifluorobenzene by **3.1** adsorbed on acidic alumina. Following elution with the guest mixture, the "cage column" was eluted with D$_2$O and DCM (aq) to displace the bound fluorobenzene. The spectra are referenced to the residual solvent peak at 4.79 ppm.
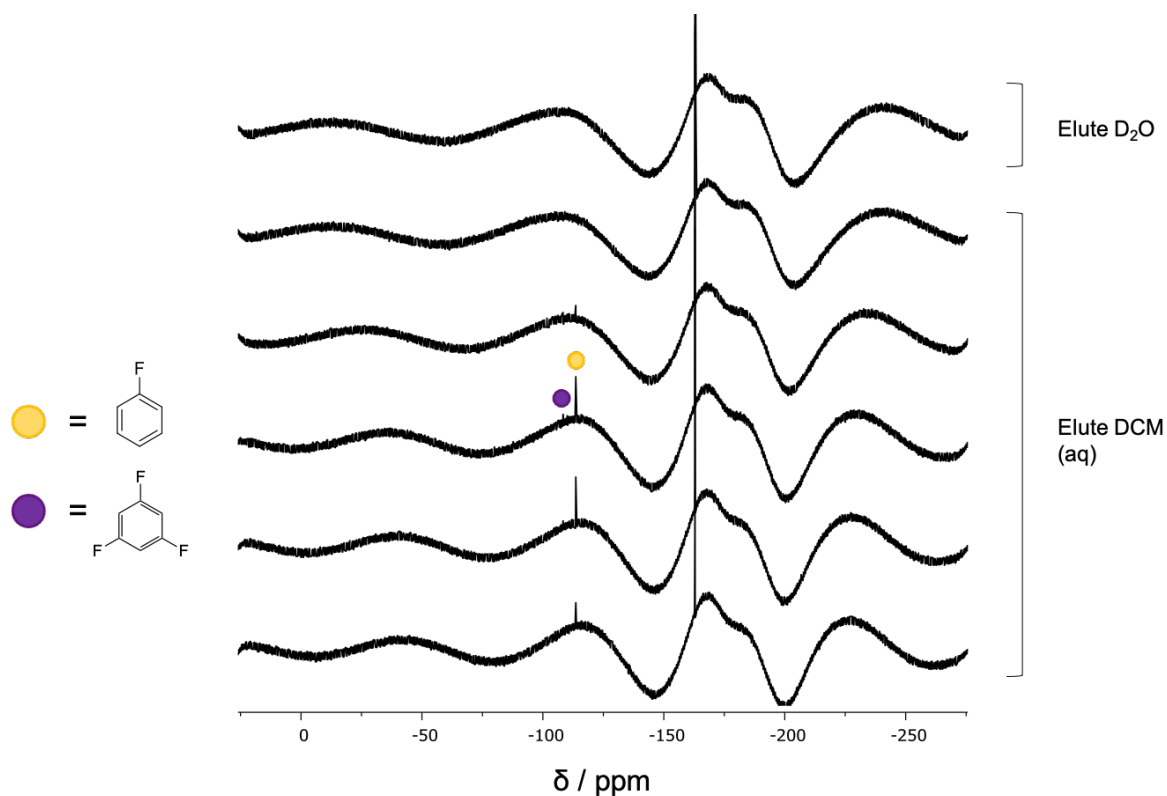
Figure 3.84: ^{19}F NMR (400 MHz, D$_2$O, 298 K) spectra of the separation of fluorobenzene from trifluorobenzene by **3.1** adsorbed on acidic alumina. Following elution with the guest mixture, the "cage column" was eluted with D$_2$O and DCM (aq) to displace the bound fluorobenzene. A minimal concentration of trifluorobenzene was present in the eluate, perhaps due to adsorption to the alumina or weak association with the adsorbed cage **3.1**. The spectra are referenced to hexafluorobenzene at -162.9 ppm.

3.5.11 Reusability of Adsorbed Cages

To test the re-usability of cage **3.1** adsorbed on acidic alumina, we utilised the following method. Acidic alumina (1 g) was added to an aqueous solution of excess cage **3.1** (*ca*. 5 – 10 mM, 10 mL). The alumina slurry was then loaded into a 5 mL syringe, which contained a cotton wool plug to prevent the alumina from passing through the syringe. The "cage column" was washed with water to remove the excess cage/complex. A saturated aqueous solution of fluorobenzene (*ca*. 20 mM) was eluted slowly through the column (3 mL, 0.1 mL/min) and the column was washed with water to remove the excess guest (*ca*. 25 mL, 5 mL/min). The column was washed with D_2O (5 mL, 5 mL/min) and then eluted with D_2O (3 × 1 mL, 1 mL/min) and then aqueous DCM (saturated, *ca*. 0.2 M, 6 × 1 mL, 1 mL/min). The column was then washed with water (*ca*. 25 mL, 5 mL/min) and reloaded with fluorobenzene as before. The column was loaded with fluorobenzene 3 times. The final D_2O elutions and all aqueous DCM elutions were analysed by ^{1}H NMR. The NMR spectra were referenced to 2 mM pyrazine in D_2O (8.63 ppm) in order to compare guest concentrations between spectra. All spectra were run with 16 scans and receiver gain set to 71.8.
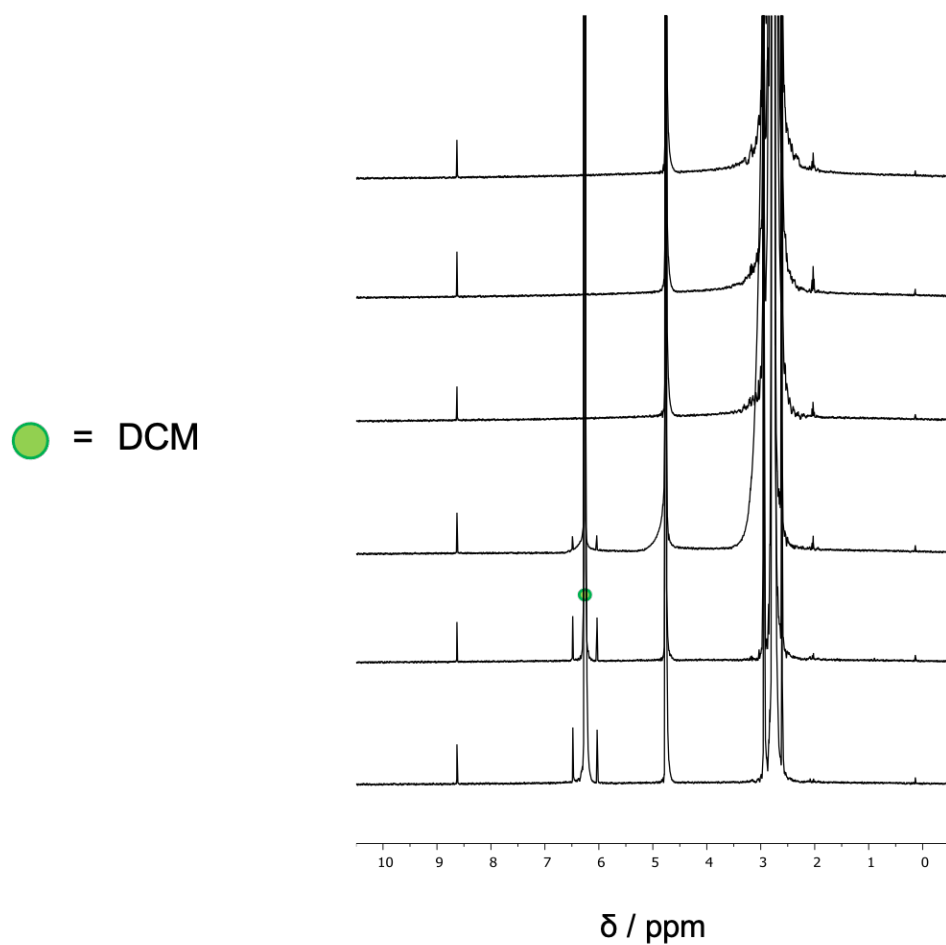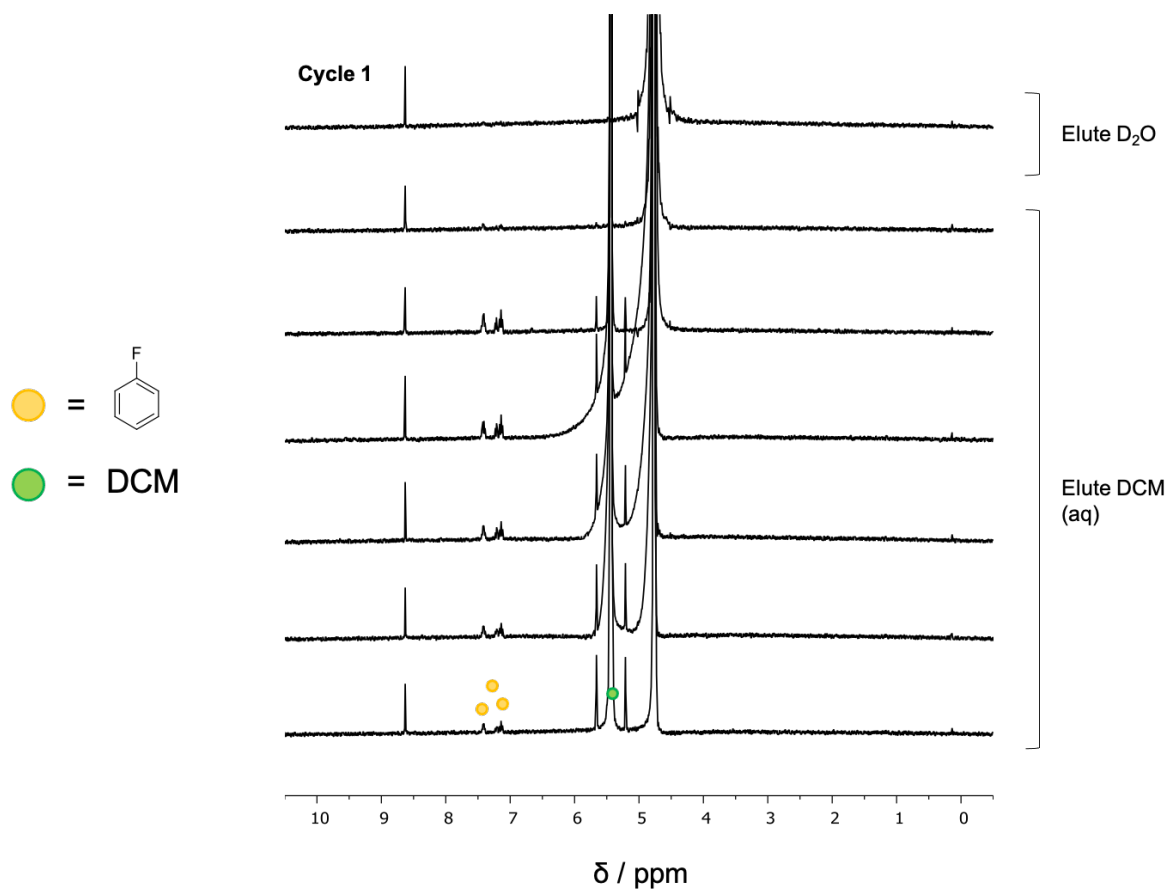
Figure 3.85: ^{1}H NMR (400 MHz, D$_2$O, 298 K) spectra of an experiment to test the reusability of a column of cage **3.1** on acidic alumina in binding and releasing fluorobenzene *via* successive 1 mL elutions of DCM (aq) and subsequent reloading with fluorobenzene. Cycle 1.
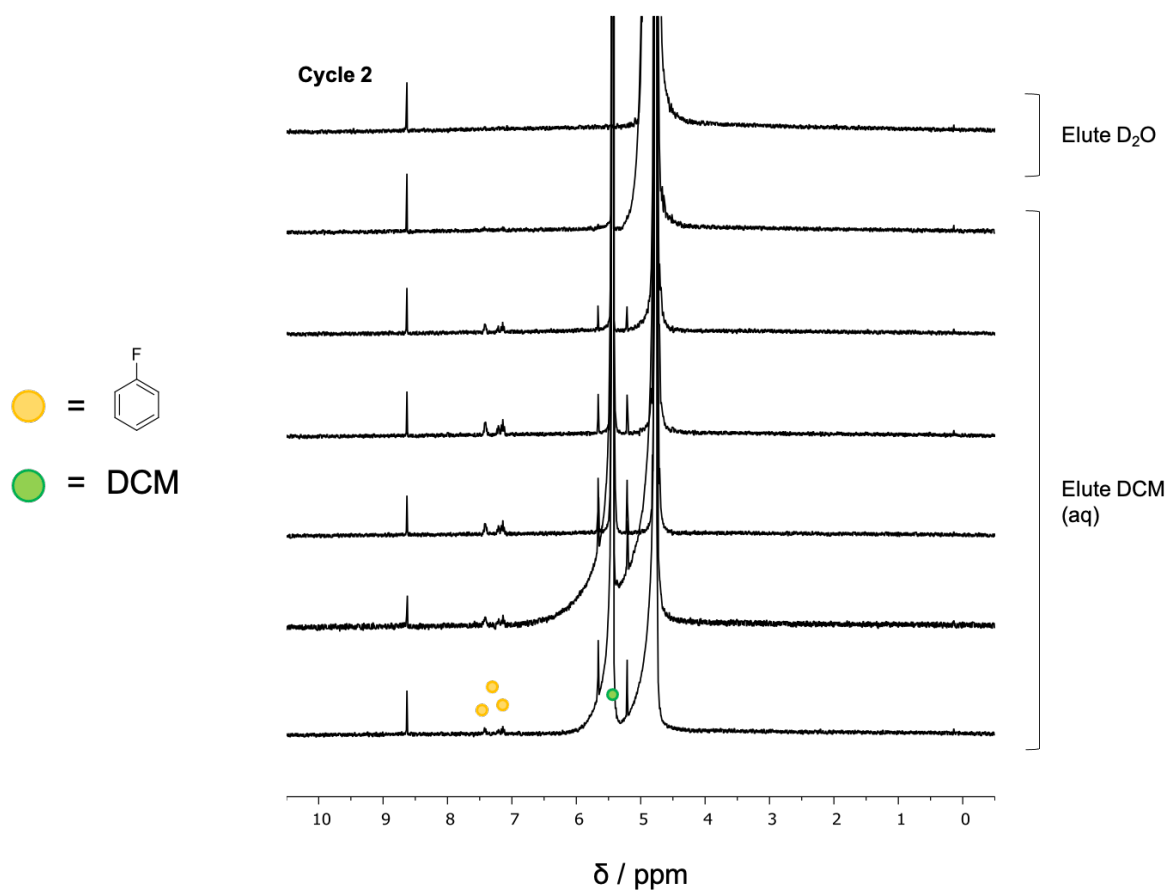
Figure 3.86: ^{1}H NMR (400 MHz, D$_2$O, 298 K) spectra of an experiment to test the reusability of a column of cage **3.1** on acidic alumina in binding and releasing fluorobenzene *via* successive 1 mL elutions of DCM (aq) and subsequent reloading with fluorobenzene. Cycle 2.
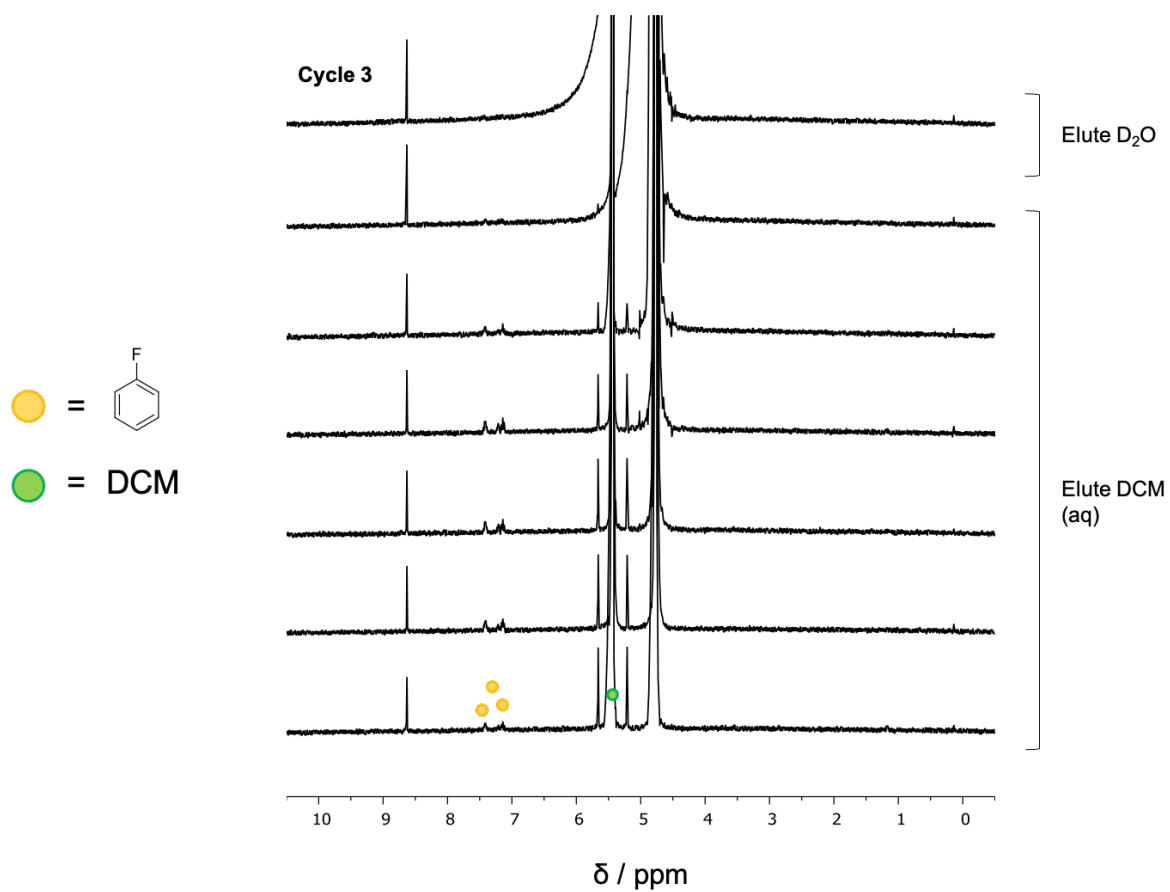
Figure 3.87: ^{1}H NMR (400 MHz, D$_2$O, 298 K) spectra of an experiment to test the reusability of a column of cage **3.1** on acidic alumina in binding and releasing fluorobenzene *via* successive 1 mL elutions of DCM (aq) and subsequent reloading with fluorobenzene. Cycle 3.

3.5.12 Diels-Alder Displacement Experiments

Method 1

In Method 1 the adsorbed cages were loaded with guest species separately and then connected in series.

Acidic alumina (*ca*. 340 mg) was added to a solution of excess **3.1** in HPLC grade water (*ca*. 5 – 10 mM, 3.3 mL) and stirred for *ca*. 1 minute. Basic alumina (*ca*. 1 g) was added to a solution of excess **3.2** in HPLC grade water (*ca*. 2 – 4 mM, 10 mL) and stirred. The two alumina slurries were loaded into separate 3 mL syringes with cotton wool plugs and washed with HPLC grade water to remove the excess cage. The cage column of **3.1** was eluted with aqueous cyclopentadiene (*ca*. 20 mM, 3 mL, 0.1 mL/min) and washed with HPLC grade water (*ca*. 25 mL). The cage column of **3.2** was eluted with aqueous N-propyl maleimide (*ca*. 20 mM, 3 mL, 0.1 mL/min) and washed with HPLC grade water (*ca*. 25 mL). The two cage columns were then stacked vertically and connected (see Figure 3.30a) and washed with D_2O (10 mL). Finally, the stacked system was eluted with D_2O (3 × 1 mL, 1 mL/min) and then aqueous DCM (saturated, *ca*. 0.2 M, 6 × 1 mL, 1 mL/min). The final D_2O elution and all aqueous DCM elutions were analysed by ^1H NMR. The NMR spectra were referenced to 2 mM pyrazine in D_2O (8.63 ppm) in order to compare guest concentrations between spectra. All spectra were run with 16 scans and receiver gain set to 71.8.

The ratio of acidic : basic alumina masses was set to *ca*. 0.33 : 1, which correlates to the inverse of the ratio of monolayer surface coverages seen for **3.1** and **3.2** in their adsorption isotherms.
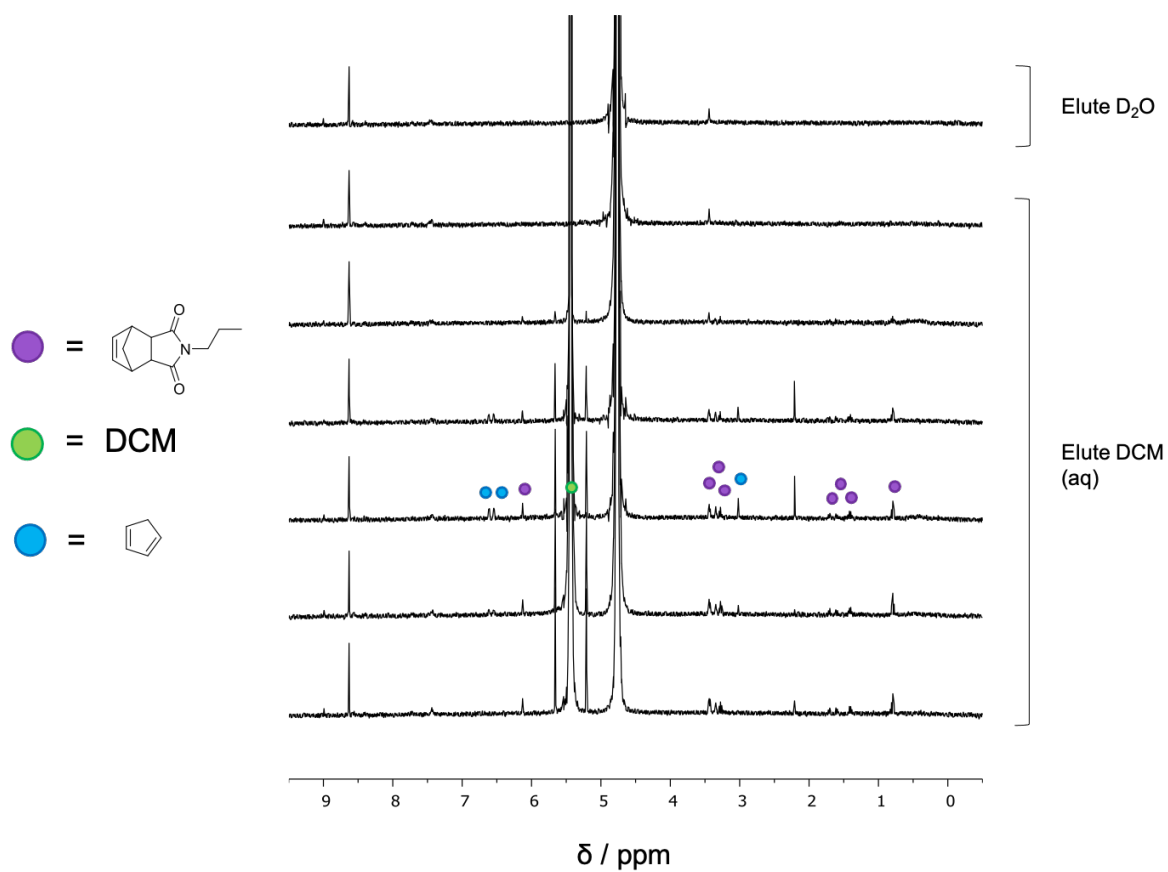
Figure 3.88: ^1H NMR (400 MHz, D_2O, 298 K) spectra of experiment to displace cyclopentadiene and N-propyl maleimide from adsorbed **3.1** and **3.2**, *via* successive 1 mL elutions with DCM (aq), to trigger a Diels-Alder reaction. The cages were loaded separately.

Method 2

In Method 2 the cages were first connected in series and then loaded with guest species.

Acidic alumina (*ca*. 530 mg) was added to a solution of excess **3.1** in HPLC grade water (*ca*. 5 – 10 mM, 5 mL) and stirred for *ca*. 1 minute. Basic alumina (*ca*. 1.54 g) was added to a solution of excess **3.2** in HPLC grade water (*ca*. 2 – 4 mM, 15 mL) and stirred. The two alumina slurries were loaded into separate 3 mL syringes with cotton wool plugs and washed with HPLC grade water to remove the excess cage. The cage columns were then connected in series as shown in Figure 3.30a. The stacked system was eluted with aqueous cyclopentadiene (*ca*. 30 mM, 6 mL, 0.2 mL/min) and washed with HPLC grade water (*ca*. 15 mL) and then eluted with aqueous N-propyl maleimide (*ca*. 30 mM, 6 mL, 0.2 mL/min) and washed with D_2O (*ca*. 15 mL). Finally, the stacked system was eluted with D_2O (3 × 1 mL, 1 mL/min) and then aqueous DCM (saturated, *ca*. 0.2 M, 7 × 1 mL, 1 mL/min). The final D_2O elution and all aqueous DCM elutions were analysed by ^{1}H NMR. The NMR spectra were referenced to 2 mM pyrazine in D_2O (8.63 ppm) in order to compare guest concentrations between spectra. All spectra were run with 16 scans and receiver gain set to 71.8.

The ratio of acidic : basic alumina masses was set to *ca*. 0.33 : 1, which correlates to the inverse of the ratio of monolayer surface coverages seen for **3.1** and **3.2** in their adsorption isotherms.
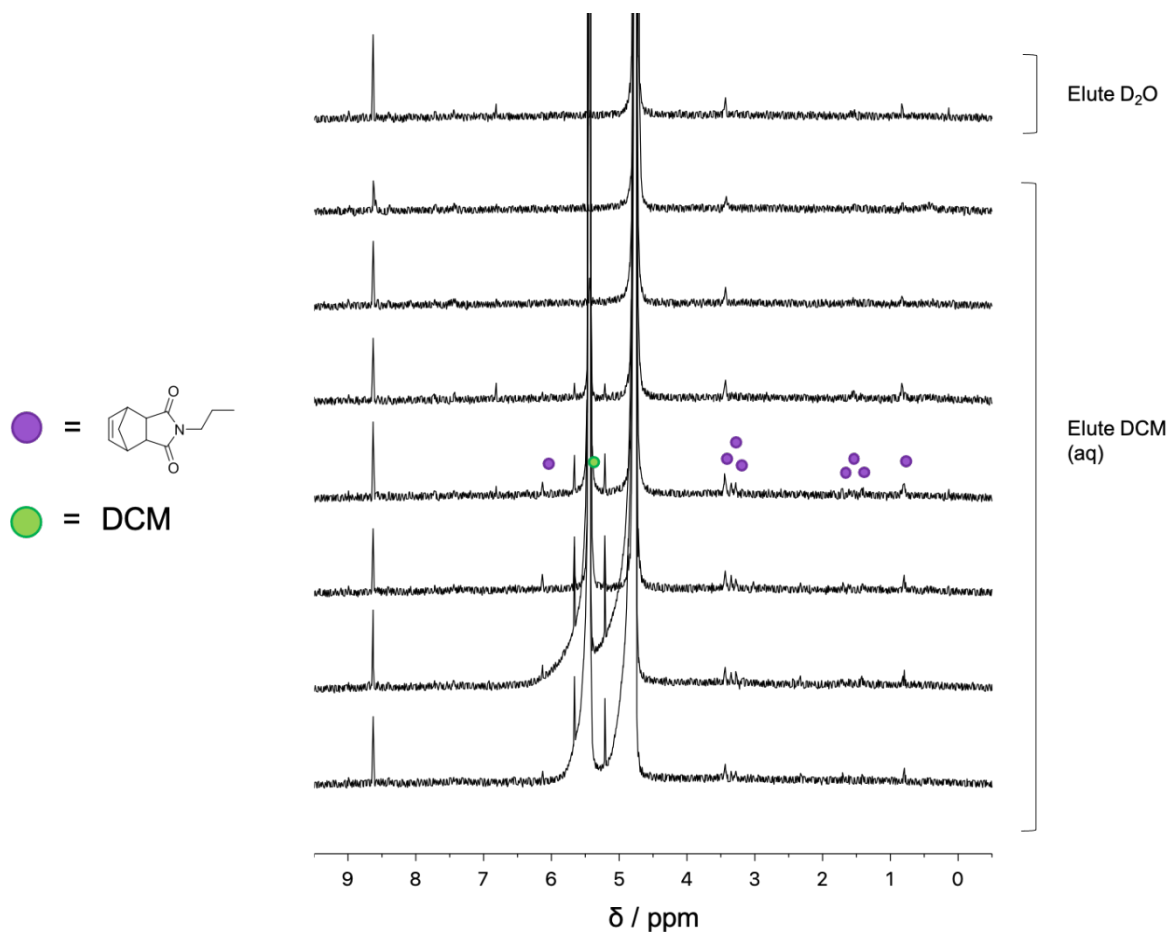
Figure 3.89: ^{1}H NMR (400 MHz, D$_2$O, 298 K) spectra of experiment to displace cyclopentadiene and N-propyl maleimide from adsorbed **3.1** and **3.2**, *via* successive 1 mL elutions with DCM (aq), to trigger a Diels-Alder reaction. The cages were loaded when already stacked.

3.5.13 Change of Solvent System

Method

Solid alumina support (*ca.* 300 mg) was added to a solution of excess cage **3.5** in acetonitrile (3 mL) and stirred to adsorb the material. The alumina slurry was then loaded into a pipette, which contained a cotton wool plug to prevent the alumina from passing through the pipette. The "cage column" was washed with acetonitrile to remove the excess cage and then eluted under gravity with either CD_3CN, D_2O, EtOH, or d_8-THF (*ca.* 0.5 – 1 mL).

^{1}H NMR spectra are given in Figures 3.35 – 3.37

3.6 References

1. Langmuir, I. The Adsorption of Gases on Plane Surfaces of Glass, Mica, and Platinum. *Journal of the American Chemical Society* **40**, 1361–1403 (1918).

2. Everett, D. H. Thermodynamics of adsorption from solution. Part 1.—Perfect systems. *Transactions of the Faraday Society* **60**, 1803–1813 (1964).

3. Bonifazi, D., Mohnani, S. & Llanes-Pallas, A. Supramolecular Chemistry at Interfaces: Molecular Recognition on Nanopatterned Porous Surfaces. *Chemistry - A European Journal* **15**, 7004–7025 (2009).

4. Mali, K. S., Pearce, N., de Feyter, S. & Champness, N. R. Frontiers of supramolecular chemistry at solid surfaces. *Chemical Society Reviews* **46**, 2520–2542 (2017).

5. Lei, S. *et al.* One Building Block, Two Different Supramolecular Surface-Confined Patterns: Concentration in Control at the Solid–Liquid Interface. *Angewandte Chemie* **120**, 3006–3010 (2008).

6. Dmitriev, A., Lin, N., Weckesser, J., Barth, J. v. & Kern, K. Supramolecular assemblies of trimesic acid on a Cu(100) surface. *Journal of Physical Chemistry B* **106**, 6907–6912 (2002).

7. Theobald, J. A., Oxtoby, N. S., Phillips, M. A., Champness, N. R. & Beton, P. H. Controlling molecular deposition and layer structure with supramolecular surface assemblies. *Nature* **424**, 1029–1031 (2003).

8. Jethwa, S. J. *et al.* Supramolecular Corrals on Surfaces Resulting from Aromatic Interactions of Nonplanar Triazoles. *ACS Nano* **11**, 8302–8310 (2017).

9. Peljhan, S. & Kokalj, A. DFT study of gas-phase adsorption of benzotriazole on Cu(111), Cu(100), Cu(110), and low coordinated defects thereon. *Physical Chemistry Chemical Physics* **13**, 20408–20417 (2011).

10. Treier, M. *et al.* An aromatic coupling motif for two-dimensional supramolecular architectures. *Chemical Communications* 4555–4557 (2008) doi:10.1039/b809618j.

11. Beniwal, S. *et al.* Kagome-like lattice of π-π Stacked 3-hydroxyphenalenone on Cu(111). *Chemical Communications* **50**, 8659–8662 (2014).

12. Mekapothula, S. *et al.* Silica bound co-pillar[4+1]arene as a novel supramolecular stationary phase. *Chemical Communications* **56**, 1792–1794 (2020).

13. Busi, M. *et al.* Self-Assembly of Nanosize Coordination Cages on Si(100) Surfaces. *Chemistry - A European Journal* **13**, 6891–6898 (2007).

14. Levi, S. A. *et al.* Direct Observation of Surface-Controlled Self-Assembly of Coordination Cages by Using AFM as a Molecular Ruler. *Angewandte Chemie International Edition* **40**, 1892–1896 (2001).

15. Menozzi, E. *et al.* Surface-Confined Single Molecules: Assembly and Disassembly of Nanosize Coordination Cages on Gold (111). *Chemistry - A European Journal* **10**, 2199–2206 (2004).

16. Frank, M., Funke, S., Wackerbarth, H. & Clever, G. H. SERS spectroscopic evidence for the integrity of surface-deposited self-assembled coordination cages. *Physical Chemistry Chemical Physics* **16**, 21930–21935 (2014).

17. Ramasamy, E. & Ramamurthy, V. Supramolecular-Surface Photochemistry: Assembly and Photochemistry of Host–Guest Capsules on Silica Surface. *Organic Letters* **20**, 4187–4190 (2018).

18. Miyamura, H., Bergman, R. G., Raymond, K. N. & Toste, F. D. Heterogeneous Supramolecular Catalysis through Immobilization of Anionic M4L6Assemblies on Cationic Polymers. *Journal of the American Chemical Society* **142**, (2020).

19. Grommet, A. B. *et al.* Anion Exchange Drives Reversible Phase Transfer of Coordination Cages and Their Cargoes. *Journal of the American Chemical Society* **140**, 14770–14776 (2018).

20. Zhang, D., Ronson, T. K., Mosquera, J., Martinez, A. & Nitschke, J. R. Selective Anion Extraction and Recovery Using a $Fe^{II}_4L_4$ Cage. *Angewandte Chemie International Edition* **57**, 3717–3721 (2018).

21. Tsyganenko, A. A. & Mardilovich, P. P. Structure of alumina surfaces. *Journal of the Chemical Society, Faraday Transactions* **92**, 4843–4852 (1996).

22. Lee, S. Y. *et al.* Adsorption of sodium hexanoate on α-alumina. *Journal of Colloid and Interface Science* **407**, 348–353 (2013).

23. Garbowski, E. & Primet, M. Adsorption of benzene on acidified alumina. *Journal of the Chemical Society, Faraday Transactions 1: Physical Chemistry in Condensed Phases* **83**, 1469–1476 (1987).

24. Gulicovski, J. J., Čerović, L. S. & Milonjić, S. K. Point of Zero Charge and Isoelectric Point of Alumina. *Materials and Manufacturing Processes* **23**, 615–619 (2008).

25. Mal, P., Schultz, D., Beyeh, K., Rissanen, K. & Nitschke, J. R. An Unlockable-Relockable Iron Cage by Subcomponent Self-Assembly. *Angewandte Chemie International Edition* **47**, 8297–8301 (2008).

26. Mal, P., Breiner, B., Rissanen, K. & Nitschke, J. R. White phosphorus is air-stable within a self-assembled tetrahedral capsule. *Science* **324**, 1697–1699 (2009).

27. Smulders, M. M. J., Zarra, S. & Nitschke, J. R. Quantitative Understanding of Guest Binding Enables the Design of Complex Host–Guest Behavior. *Journal of the American Chemical Society* **135**, 7039–7046 (2013).

28. Lever, J., Krzywinski, M. & Altman, N. Points of Significance: Principal component analysis. *Nature Methods* **14**, 641–642 (2017).

29. Bolliger, J. L., Ronson, T. K., Ogawa, M. & Nitschke, J. R. Solvent Effects upon Guest Binding and Dynamics of a $Fe^{II}_4L_4$ Cage. *Journal of the American Chemical Society* **136**, 14545–14553 (2014).

30. Ronson, T. K., Meng, W. & Nitschke, J. R. Design Principles for the Optimization of Guest Binding in Aromatic-Paneled $Fe^{II}_4L_6$ Cages. *Journal of the American Chemical Society* **139**, 9698–9707 (2017).

31. Percástegui, E. G. *et al.* Waterproof architectures through subcomponent self-assembly. *Chemical Science* **10**, 2006–2018 (2019).

32. Percástegui, E. G., Mosquera, J. & Nitschke, J. R. Anion Exchange Renders Hydrophobic Capsules and Cargoes Water-Soluble. *Angewandte Chemie International Edition* **56**, 9136–9140 (2017).

33. Irving, H. & Williams, R. J. P. The stability of transition-metal complexes. *Journal of the Chemical Society (Resumed)* 3192–3210 (1953) doi:10.1039/jr9530003192.

34. Schultz, D. & Nitschke, J. R. Choices of Iron and Copper: Cooperative Selection during Self-Assembly. *Angewandte Chemie International Edition* **45**, 2453–2456 (2006).

35. Ebadi, A., Soltan Mohammadzadeh, J. S. & Khudiev, A. What is the correct form of BET isotherm for modeling liquid phase adsorption? *Adsorption* **15**, 65–73 (2009).

36. Blanchard, G., Maunaye, M. & Martin, G. Removal of heavy metals from waters by means of natural zeolites. *Water Research* **18**, 1501–1507 (1984).

37. Ryan, H. P., Haynes, C. J. E., Smith, A., Grommet, A. B. & Nitschke, J. R. Guest Encapsulation within Surface-Adsorbed Self-Assembled Cages. *Advanced Materials* **33**, 2004192 (2021).

38. Nguyen, B.-N. T. *et al. Coordination cages transport molecular cargoes across liquid membranes*. (2021).

39. Freundlich, H. Über die Adsorption in Lösungen. *Zeitschrift für Physikalische Chemie* **57**, 385–470 (1906).

40. Tan, C. *et al.* Supramolecular Coordination Cages for Asymmetric Catalysis. *Chemistry – A European Journal* **25**, 662–672 (2019).

41. Hong, C. M., Bergman, R. G., Raymond, K. N. & Toste, F. D. Self-Assembled Tetrahedral Hosts as Supramolecular Catalysts. *Accounts of Chemical Research* **51**, 2447–2455 (2018).

42. Sibi, M. P. & Petrovic, G. Enantioselective radical reactions: The use of metal triflimides as Lewis acids. *Tetrahedron Asymmetry* **14**, 2879–2882 (2003).

43. Fulmer, G. R. *et al.* NMR Chemical Shifts of Trace Impurities: Common Laboratory Solvents, Organics, and Gases in Deuterated Solvents Relevant to the Organometallic Chemist. *Organometallics* **29**, 2176–2179 (2010).

44. Riddell, I. A. *et al.* Anion-induced reconstitution of a self-assembling system to express a chloride-binding $Co_{10}L_{15}$ pentagonal prism. *Nature Chemistry* **4**, 751–756 (2012).

Chapter 4: Coordination Cages as Scaffolds for Permanently Porous Liquids

This chapter explores the use of coordination cages as frameworks for the synthesis of porous, liquid materials. The modular nature of subcomponent self-assembly is well-suited to the synthesis of liquid materials because previously reported polytopic ligands can be combined with liquid monotopic subcomponents to generate liquid coordination cages. This chapter presents the progress to-date towards the synthesis of a liquid cage salt, "hetero-cage" system, in which the counterions of highly cationic liquid coordination cages are highly anionic coordination cages. Furthermore, an investigation of the thermal properties of liquid coordination cages is presented, with a particular emphasis on tuning the glass transition temperatures of the cages towards temperature-controlled host-guest chemistry.

4.1 Introduction

This section draws on material published in "*Engineering Permanent Porosity into Liquids*".

4.1.1 Porous Liquids

In 2007, Stuart James published a paper in which he postulated the concept of liquid materials with permanent intrinsic porosity.[1] James made the following distinction between "intrinsic" and "extrinsic" porosity; "extrinsic" porosity refers to the transient cavities which form in any liquid phase due to the random motion of molecules over time, whereas "intrinsic" porosity is concerned with permanent pores existing within the liquid molecules themselves. James also presented three ways in which permanent porosity might be engineered into liquid phases, which he classed as Type I, II, and III porous liquids. Type I permanently porous liquids are single-component neat liquid systems in which the individual molecules contain permanent, rigid internal cavities which cannot be intermolecularly "self-filled" (Figure 4.1). In contrast, Type II liquids consist of rigid hosts dissolved in a solvent which is sterically prevented from entering the host cavities. Finally, Type III liquids are dispersions of microporous frameworks in solvents which are sterically prevented from entering the framework cavities. Since their conception in 2007, there have been a number of reports of the formation of permanently porous liquids; a selection of these is outlined below.
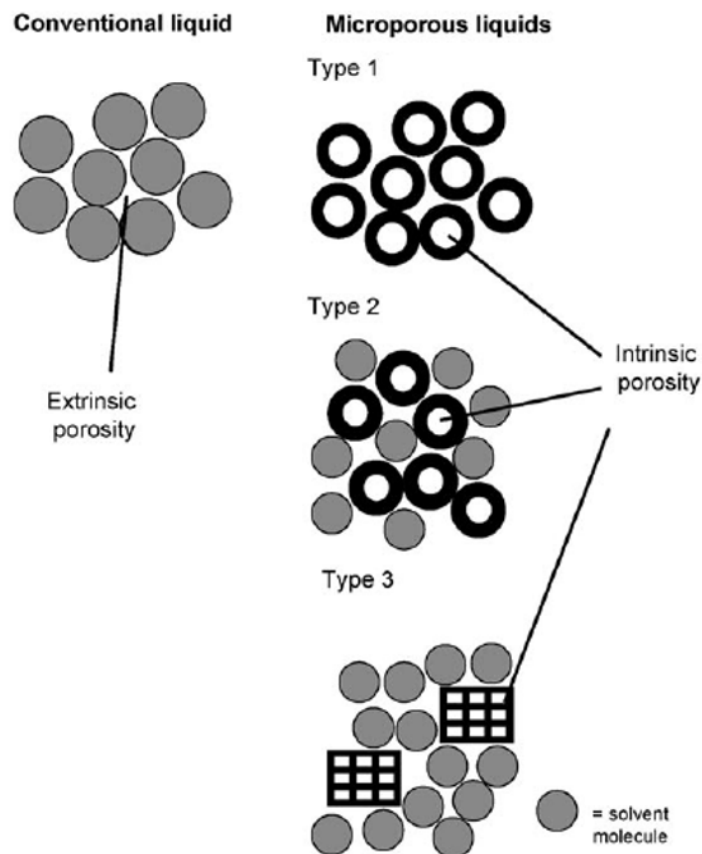
Figure 4.1: The three types of microporous liquid proposed by James in 2007.[1] Figure 4.1 is reproduced with permission from reference 1.

4.1.2 Type I Porous Liquids

James defined Type I porous liquids as neat liquids with permanent microporosity and one of the earliest strategies towards the synthesis of Type I porous liquids was reported by him and Cooper in 2012.[1,2] In this work, the melting points of previously reported rigid iminospherand cages,[3] formed *via* the condensation of 1,3,5-triformylbenzene and a range of diamines, were depressed *via* functionalisation with a range of alkyl chains (Figure 4.2). James *et al.* observed that the cage functionalised with pendant n-octyl (*n*-C_8) chains underwent a transition to a liquid-like phase at *ca.* 50 °C and even behaved as a Newtonian fluid at temperatures above 80 °C; a Newtonian fluid is defined as a fluid species in which, in simple shear and at constant temperature and pressure, the shear stress is proportional to the shear rate *via* the dynamic viscosity.[4] Further rheometric analysis of this cage found that the gel point occurred at 58 °C and 53 °C at oscillation rates of 1.0 Hz and 0.1 Hz, respectively; the gel point is defined as the temperature at which the shear storage modulus (*G'*) and shear loss modulus (*G''*) are equal

and above which a given system is formally a fluid. Whilst this strategy was effective in the depressing the melting points of these cages, the authors concluded that these systems could not be termed "permanently porous" liquids in their neat states due to the easy penetration of the cage cavities by the alkyl chains. Subsequent work by James and Del Pópolo *et al.* presented a joint computational and synthetic study of cages decorated with longer alkyl chains and also branched alkyl chains, such as n-C_{20} and neo-C_{14}.[5] The computational study determined that cavities of cages with long, linear chains (n-C_{12} and n-C_{20}) did not remain empty over the duration of the simulation (100 ns); in contrast, shorter alkyl chains (n-C_5) and branched alkyl chains (neo-C_{14}) did not result in complete occupation of the cage cavities and thus these materials were described as permanently microporous. Furthermore, additional simulations of the dissolution of methane in cages functionalised with n-C_5, n-C_{12}, and neo-C_{14} showed that methane was much more soluble in the cages with empty cavities present (n-C_5 and neo-C_{14}) and that methane absorbed preferentially within the cage cavities than the alkyl chain region.
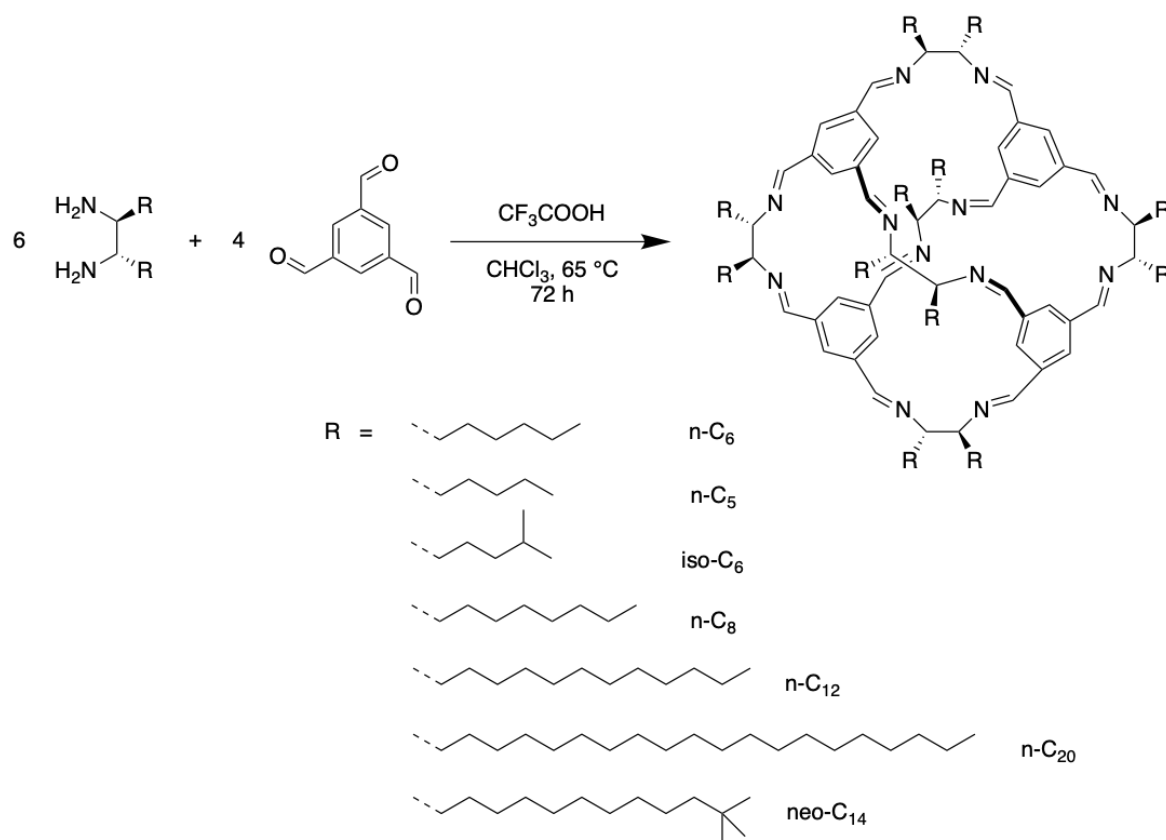

Figure 4.2: The alkylated organic cages studied by James, Cooper, and Del Pópolo.[2,5]

In 2015, Dai *et al.* reported another approach for synthesising porous liquids in which the surfaces of hollow silica spheres were functionalised with fluidifying polymer chains.[6] In Dai's work, a positively-charged organosilane was employed to form a monolayer on the silica surface thereby forming a positively-charged "corona" around the spheres (Figure 4.3). The chloride counteranions were then exchanged to a poly(ethylene glycol) sulphonate "canopy" to form an optically transparent liquid at room temperature. Finally, Dai demonstrated that this hollow silica sphere liquid could be used in the separation of N_2 and CO_2; the poly(ethylene glycol) matrix of the liquid assisted in the initial dissolution of CO_2 and the significant proportion of free volume, arising from the empty silica spheres, resulted in increased diffusivity through the material. More recently, Dai has reported a significantly different strategy to form porous liquids *via* the supramolecular complexation of the countercations of anionic organic cages.[7] Dai demonstrated that dicyclohexano-18-crown-6 was able to abstract the potassium countercation of an anionic organic cage and the resulting Type I porous liquid was able to absorb and release CO_2 with a capacity between that of 18-crown-6 and the parent organic cage (Figure 4.4). The permanent porosity of the liquid was also confirmed by Positron Annihilation Lifetime Spectroscopy (PALS). PALS is a technique which probes for the existence of empty pores in a material by injecting a positron source, such as ^{22}Na, into the porous material; the lifetime of the positron can then be correlated to the porosity of the material, *e.g. via* the Tao-Eldrup model.[8–10] In contrast to the Type I liquid, the same anionic organic cage combined with 15-crown-5 formed a solid material when combined in a 2:1 ratio (2 equivalents of crown ether) and a Type II porous liquid when 15-crown-5 was added in excess.
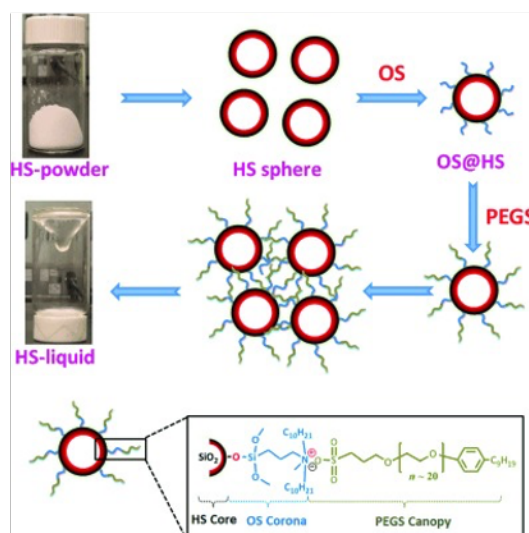
Figure 4.3: Dai's surface-functionalisation approach to forming a hollow silica sphere (HS) porous liquid.[6] Figure 4.3 is reproduced with permission from reference 6.
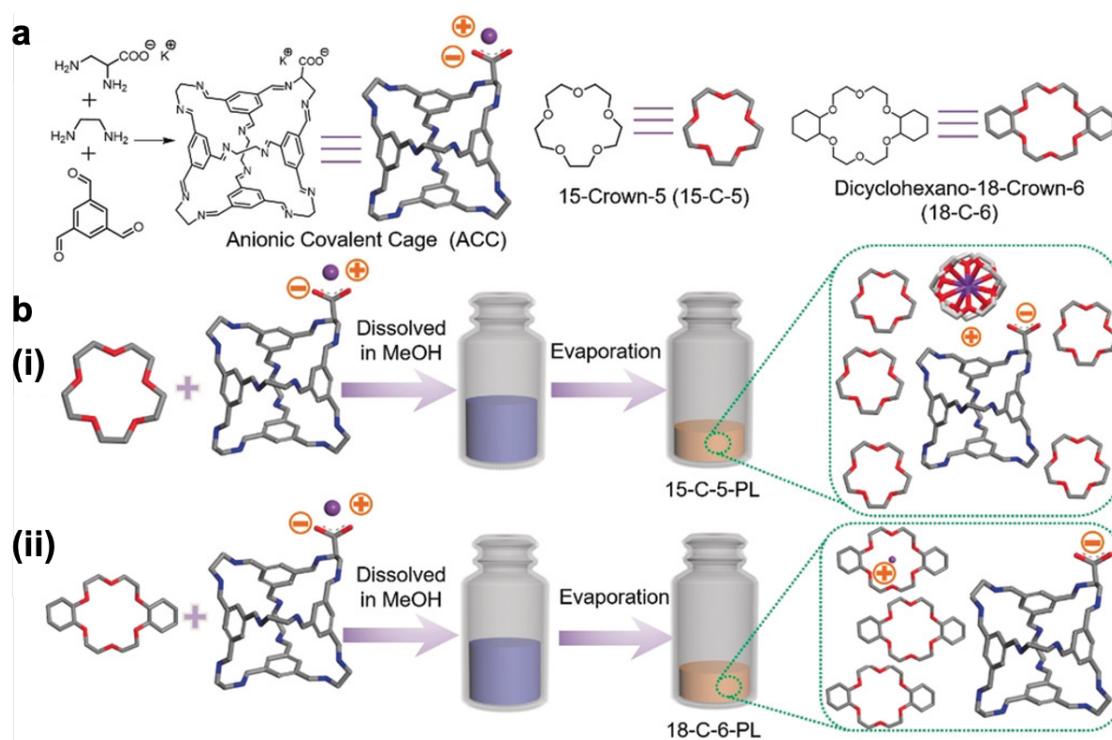
Figure 4.4: Dai's supramolecular complexation approach to forming a porous liquid based on an anionic covalent cage; a) Formation of the anionic covalent cage, b) (i) Combination of the anionic cage with 15-C-5 to form a Type II porous liquid, (ii) Combination of the anionic cage with dicyclohexano-18-C-6 to form a Type I porous liquid.[7] Figure 4.4 is reproduced with permission from reference 7.

In 2020, Nitschke *et al.* reported the synthesis of a Type I permanently porous liquid.[11] This porous liquid was formed *via* subcomponent self-assembly (see Section 1.3) in which a newly synthesised aniline, functionalised with poly(ethylene glycol) (PEG), was combined with a previously reported trialdehyde ligand and zinc (II) triflimide, in acetonitrile (Figure 4.5).[12] Upon removal of the assembly solvent, however, the coordination cage remained fluid due to the incorporation of the PEG chains at the vertices of the cages. Additionally, the PEG termini were functionalised with imidazolium cations which electrostatically prevented the termini from entering the cavities of the cages, thereby critically ensuring that the material remained permanently porous; this hypothesis was also confirmed by PALS. The authors demonstrated that the liquid coordination cage was able to bind chlorofluorocarbons (CFCs) and isomers of butanol in its neat, solvent-free state and, furthermore, that the guests could be removed *in vacuo* thereby recycling the cage.


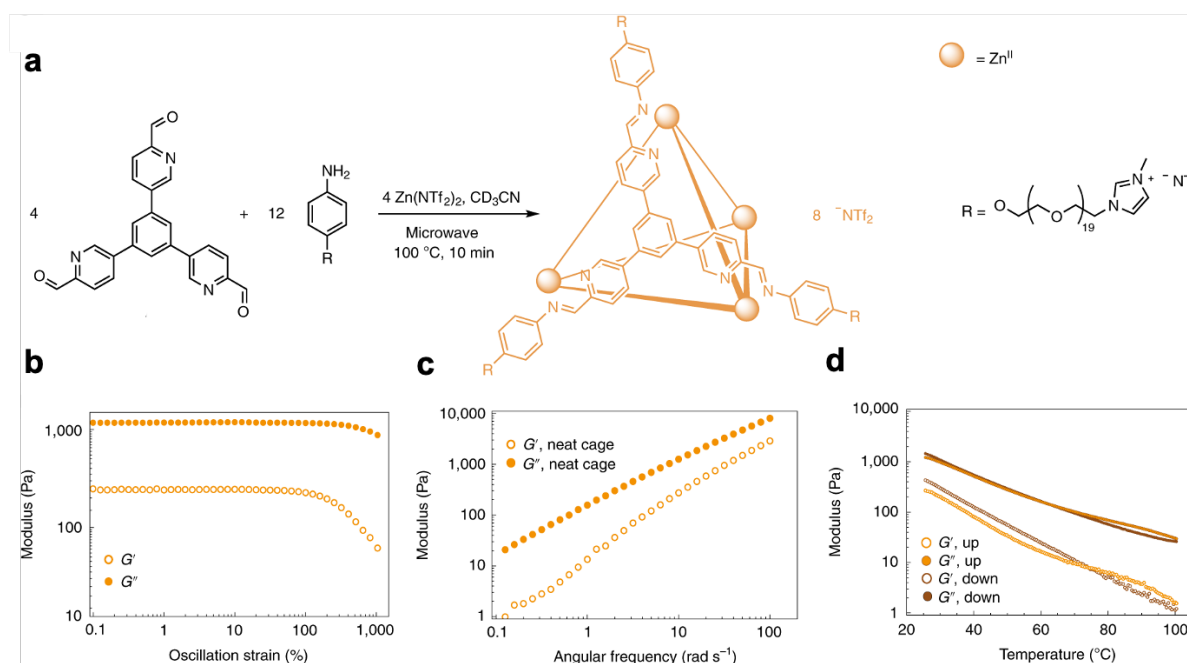Figure 4.5: Nitschke's Type I porous liquid coordination cage; a) Self-assembly of the liquid cage from molecular subcomponents, b) Dynamic rheological analysis of the liquid cage, c) Frequency-dependent rheological analysis of the liquid cage, d) Temperature-dependent rheological analysis of the liquid cage (5 °C min^{-1}, 25 – 100 °C, 10 rad s^{-1}, 1 % strain.[11] Figure 4.5 is adapted with permission from reference 11.

4.1.3 Type II Porous Liquids

Unlike single-component neat liquid Type I porous liquids, James defined Type II porous liquids as empty hosts dissolved in solvents which are sterically excluded from the liquid pores.[1] This increase in allowed system complexity for Type II porous liquids has facilitated a broader range of approaches to their synthesis, *i.e.* a solution of any given rigid host can be called a Type II porous liquid if it can be shown that the solvent molecules do not occupy the cavities of the host species. Some examples of reported Type II systems are illustrated below.

In 2015, Cooper and James *et al.* published two examples of Type II porous liquids, both of which were based on the condensation of 1,3,5-triformylbenzene with diamines.[8] The first of these examples utilised an organic cage functionalised with 6 crown ethers groups which was dissolved in 15-crown-5 (Figure 4.6). PALS measurements confirmed the presence of permanent pores in the liquid and Cooper and James demonstrated that their Type II porous liquid was able to dissolve up to 8 times as much methane as the neat 15-crown-5 over the range of 30 – 50 °C, per unit mass. Cooper and James' second example employed a ligand-scrambling approach in which two different diamines were used in the condensation reaction to form the organic cages (Figure 4.7a). The resulting "scrambled cages" were observed to possess increased solubility in common organic solvents than the parent cages due to their increased structural disorder and formed Type II porous liquids when they were dissolved in hexachloropropene. Similarly to the crown ether system, this scrambled cage porous liquid exhibited enhanced methane solubility. Cooper and James also demonstrated a guest displacement system in which xenon gas was first stored within the porous liquid and then subsequently displaced by the addition of a competing guest, chloroform (Figure 4.7b); in contrast, the xenon gas was not displaced following the addition of a non-competing guest, 1-t-butyl-3,5-dimethylbenzene. Furthermore, in 2019, Cooper reported a study in which high-throughput automation was employed to discover new porous liquid systems of scrambled cages and sterically-excluded solvents.[13] This approach led to the discovery of 29 new cage-solvent systems, from 11 diamines and 6 solvents, which were able to store up to 55 % more xenon than Cooper's original scrambled cage Type II porous liquid.
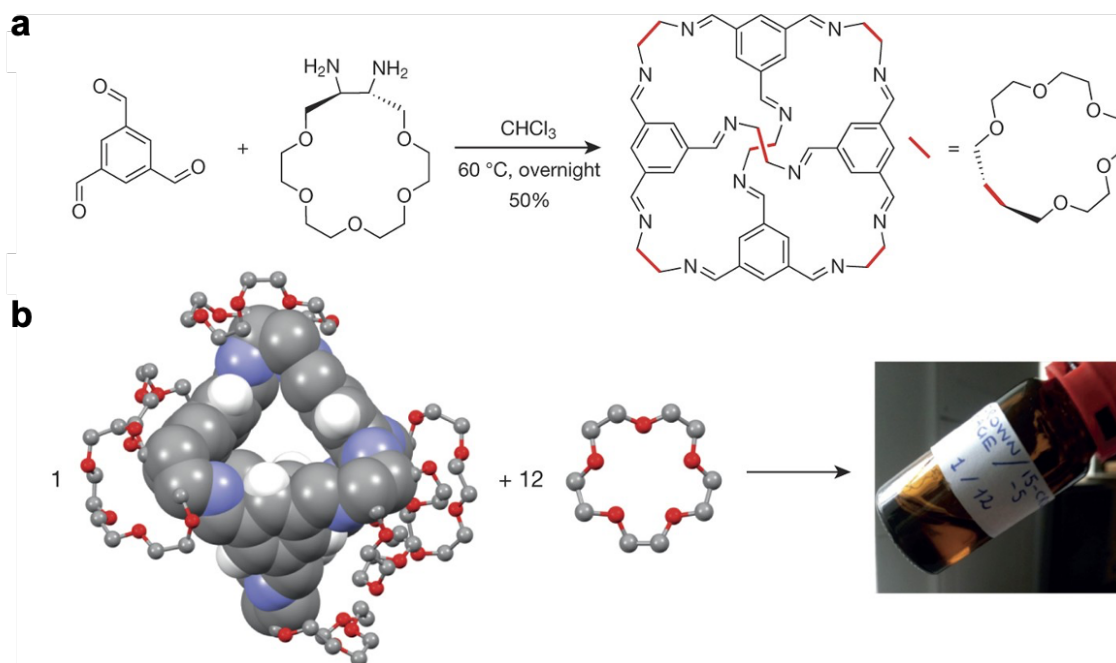
Figure 4.6: Cooper's crown-ether based Type II porous liquid; a) Formation of the crown-ether-functionalised organic cage, b) The crown-ether cage combined with 12 equivalents of 15-C-5 to form a concentrated solution of the Type II porous liquid.[8] Figure 4.6 is reproduced with permission from reference 8.
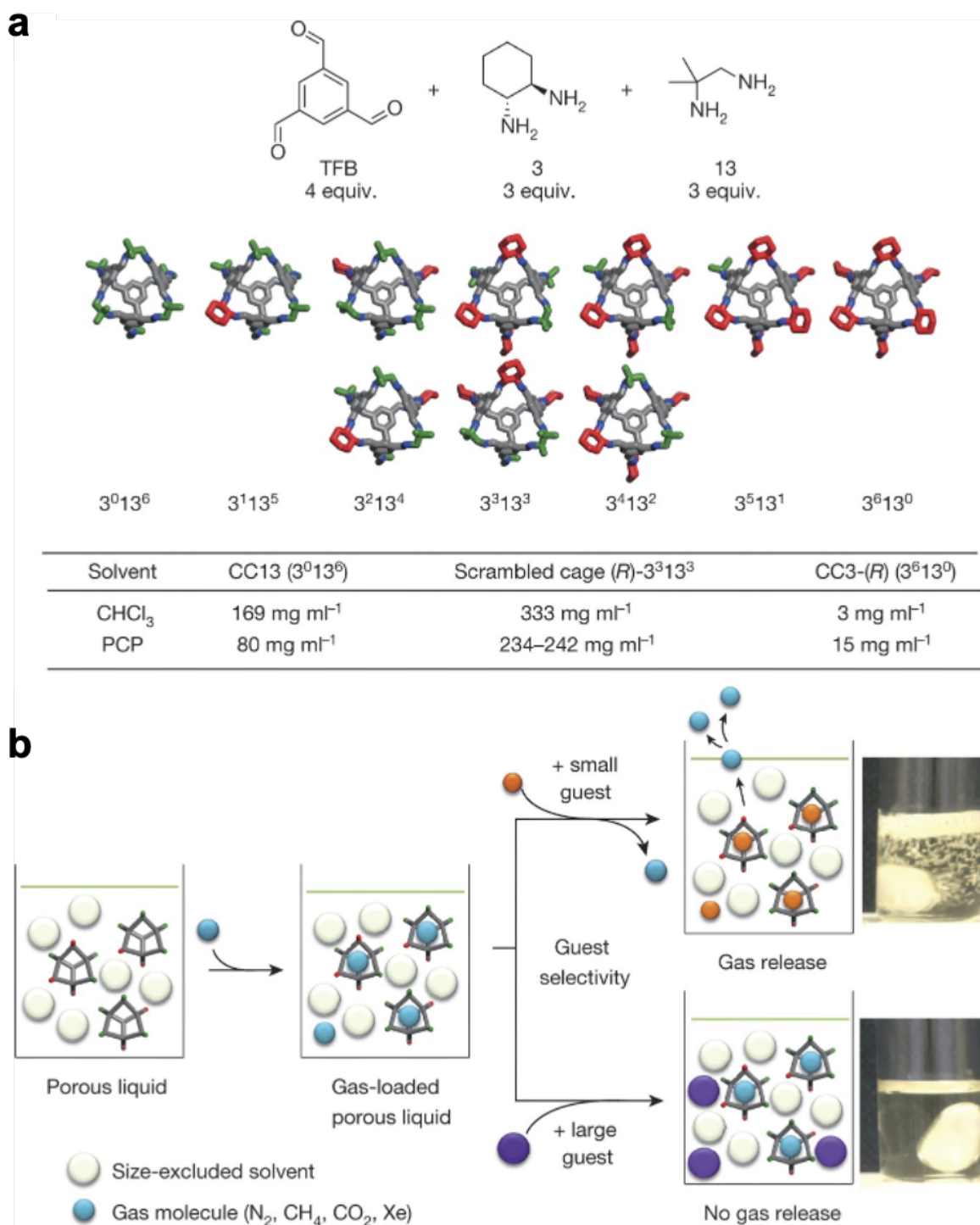
Figure 4.7: Cooper's ligand-scrambling approach to forming Type II porous liquids; a) Condensation of triformylbenzene (TFB) with two different diamines (molecules "3" and "13") to form a statistical mixture of covalent cages, and the solubilities of the resulting cages in chloroform ($CHCl_3$) and hexachloropropene (PCP), b) The addition of a small guest (orange circle) results in the displacement of gases stored in the porous liquid, whereas no gas release occurs following the addition of a large guest (purple circle).[8] Figure 4.7 is reproduced with permission from reference 8.

141

4.1.4 Type III Porous Liquids

In contrast to the more synthetically challenging Type I and Type II porous liquids, James defined Type III permanently porous liquids as microporous frameworks dispersed in sterically hindered solvents.[1] The literature contains a wide array of metal-organic frameworks and thus Type III porous liquids can be fabricated by immersing these frameworks in suitable solvents. For example, in 2014, Chen, Sun, and Smit *et al.* reported the use of zeolitic imidazolate framework-8 (ZIF-8) suspended in glycol-2-methylimidazole as a material for the capture of carbon dioxide.[14] Whilst this material was not identified as a Type III porous liquid in the original publication, the authors commented that the kinetic diameter of the glycol molecules (4.5 Å) was larger than the ZIF-8 pore diameter (3.4 Å) and thus, retrospectively, this material can be labelled as a Type III porous liquid. The authors demonstrated that their Type III porous liquid was selective for carbon dioxide over nitrogen, hydrogen, and methane, and that the low sorption enthalpy of -29 kJ mol^{-1} facilitated recovery of the sorbent material.

More recently, in 2018, ZIF-8 was again used to construct Type III porous liquids in three separate studies by Dai, Liu, and Costa Gomes.[15–17] Dai *et al.* investigated suspensions of ZIF-8 in the bulky ionic liquid 8,8′-(3,6-dioxaoctane-1,8-diyl)bis(1,8-Diazabicyclo[5.4.0]undec-7-en-8-ium) bis(trifluoromethanesulfonyl)imide ([DBU-PEG][NTf$_2$]) and the resulting Type III porous liquids exhibited enhanced carbon dioxide adsorption capacities over the pure ionic liquid.[15] Liu *et al.* demonstrated that a colloidal suspension of ZIF-8 in *N*-butyl pyridinium bis(trifluoromethyl sulfonyl)imide ([Bpy][NTf$_2$]) was stable with respect to aggregation on the timescale of months.[16] Finally, Costa Gomes *et al.* formed Type III liquids by dispersing ZIF-8 in trihexyltetradecylphosphonium bis(trifluoromethylsulfonyl)imide ([P$_{6,6,6,14}$][NTf$_2$]) and the resulting material was able to reversibly absorb up to 150 % more nitrogen and 100 % more methane than the neat ionic liquid.[17]

4.1.5 Porous Salts

In 2020, Bloch *et al.* reported the synthesis of a new solid, ionic material in which both the cationic and anionic components were coordination cages (Figure 4.8a).[18] The authors adopted a salt metathesis method, in which methanolic solutions of an anionic copper cuboctahedron, [Cu$_{24}$(SO$_3$-bdc)$_{24}$]$^{24-}$, and a cationic zirconium tetrahedron, [Zr$_{12}$(μ_3-O)$_4$(μ_2-OH)$_{12}$(Cp)$_{12}$(Me$_2$-bdc)$_6$]$^{4+}$, were combined to precipitate the "charged cage salt" whilst the counter-cations and

counter-anions remained in solution. The XPS and EDX analyses of the newly formed salt showed the presence of both copper and zirconium and both the infrared and diffuse reflectance UV-Vis spectra of the salt contained bands which were present in the starting cages. Furthermore, the authors were able to grow single crystals of the charged cage salt suitable for single crystal diffraction (Figure 4.8b). Interestingly, however, the composition of the material varied with the metathesis reaction time. When the metathesis reaction was allowed to proceed quickly (< 30 minutes), the ^{1}H NMR spectrum of the salt digested in DMSO indicated that the amorphous material formed had the charge-ideal cuboctahedron:tetrahedron ratio of 1:6; conversely, when the metathesis reaction proceeded more slowly, as in the case of crystallisation, the authors observed a ratios as low as 1:3. Finally, the authors observed, *via* N_2 and CO_2 adsorption isotherms, that the charged cage salt was intensively more porous that the original cages due to the removal of non-porous counterions. This study thus paved the way for ionic materials in which both components are supramolecular species.
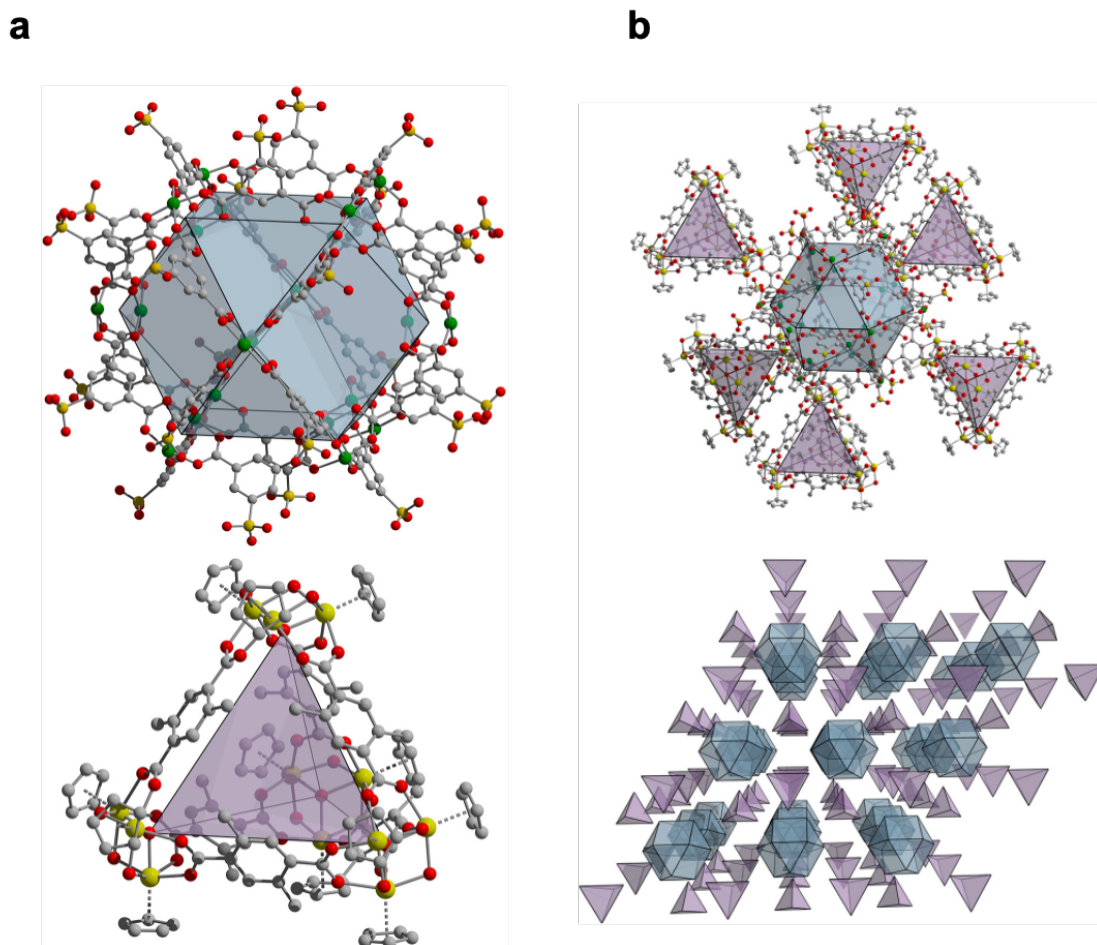
Figure 4.8: Bloch's solid cage salt formed *via* ion metathesis; a) Anionic copper cuboctahedron $[Cu_{24}(SO_3\text{-}bdc)_{24}]^{24-}$ (top) and cationic zirconium tetrahedron $[Zr_{12}(\mu_3\text{-}O)_4(\mu_2\text{-}OH)_{12}(Cp)_{12}(Me_2\text{-}bdc)_6]^{4+}$ (bottom), b) Crystal structure of the doubly porous salt $X_{16}\bullet[Cu_{24}(SO_3\text{-}bdc)_{24}]\bullet[Zr_{12}(\mu_3\text{-}O)_4(\mu_2\text{-}OH)_{12}(Cp)_{12}(Me_2\text{-}bdc)_6]_2$.[18] Figure 4.8 is adapted with permission from reference 18.

4.1.6 Aims and Objectives

Nitschke's 2020 Type I porous liquid demonstrated the potential of subcomponent self-assembly for synthesising porous liquids.[11] However, Nitschke's system also had two main drawbacks, namely the proportion of free pore volume and the range of molecules encapsulated. If the unfunctionalised cage is taken as the "pore", *i.e.* the cage assembled with regular aniline rather than the poly(ethylene glycol)-functionalised aniline, then the proportion of pore in Nitschke's liquid is only *ca*. 24 wt% due to the mass of the pendant poly(ethylene glycol) chains and the triflimide counteranions (see Figure 4.9). Furthermore, the use of a small

trialdehyde ligand (see Figure 4.5) restricted the range of prospective guest molecules to weakly binding isomers of butanol and propanol and to small chlorofluorocarbons.
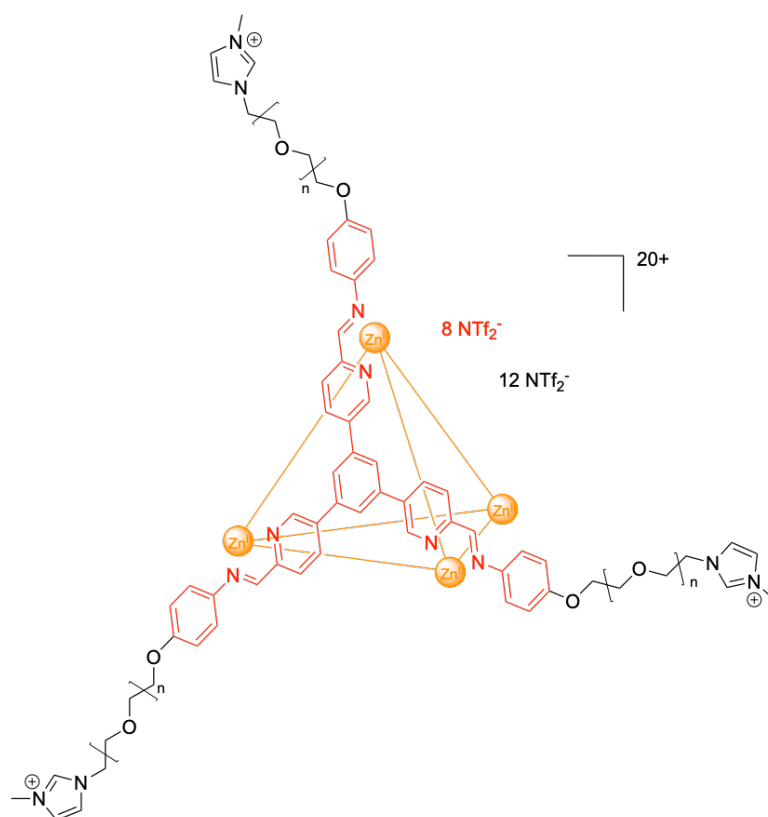
Figure 4.9: Estimation of the weight percentage of cage in Nitschke's first Type I porous liquid; Red highlight mass – 4977.58 g mol^{-1} (calculated), total mass – *ca*. 21098.98 g mol^{-1}, pore proportion ~ 24 wt%.

The following sections explore methods by which the porosity of liquid coordination cages can be increased *via* a new generation of cages based on Bolliger's previously reported triazine-centred tritopic aniline assembled with a pyridine aldehyde bearing a poly(ethylene glycol) tail. The first section investigates the use of a newly synthesised highly anionic coordination cage in the synthesis of a cage salt material in which the non-coordinating anions of a highly cationic liquid cage are exchanged for this highly anionic coordination cage *via* a salt metathesis approach. The second section of this chapter investigates the effect of varying the length of the fluidifying pendent poly(ethylene glycol) tail on the glass transition temperatures of the resulting cage materials.

4.2 Coordination Cages as Liquid Cage Salts

4.2.1 Preliminary Work

In her doctoral thesis "*Coordination Cages as a Scaffold for Permanently Porous Liquids*" and in unpublished work, Dr Lillian Ma reported the formation of an ionic "hetero-cage" system (referred to as a "liquid cage salt" from here onwards), in which the cationic component was liquid coordination cage **4.A** and the anionic component was coordination cage **4.B** (Figure 4.10a).[19] Much like Bloch, Ma utilised an ion metathesis approach in which cages **4.A** and **4.B** were combined in cold water and subsequently washed with ethyl acetate to remove the tetramethylammonium triflimide by-product (Figure 4.10b). Ma combined cages **4.A** and **4.B** in 1:1, 1:3, and 1:5 ratios and analysed the resulting materials by NMR, TGA, and DSC; of these ratios, the 1:5 system is nominally charge-balanced. Ma observed, by ^{19}F NMR spectroscopy, that these systems contained progressively fewer triflimide counterions as the proportion of cage **4.B** increased and ultimately no triflimide counterions were observed for the charge-balanced 1:5 system; thus, in the 1:5 system, the counterions of cage **4.A** were fully exchanged from triflimide to cage **4.B**. Furthermore, Ma also observed a broad glass transition feature and a melting point (177.6 °C) for the 1:5 system, by DSC, which suggested that material behaved as a solid suspension of cage **4.B** in cage **4.A** at room temperature. Ma concluded her work by hypothesising that a more negatively charged anionic cage component would reduce the proportion of solid cage required to charge-balance the highly cationic liquid cage, thereby increasing the likelihood of liquid behaviour at room temperature. Such a system would mark a significant milestone in the field of porous liquids because the resulting liquid material would contain two independently tunable pores, both of which would have the potential to bind molecular guests. Ma's 1:5 system and her concluding hypothesis thus form the initial basis for this work.
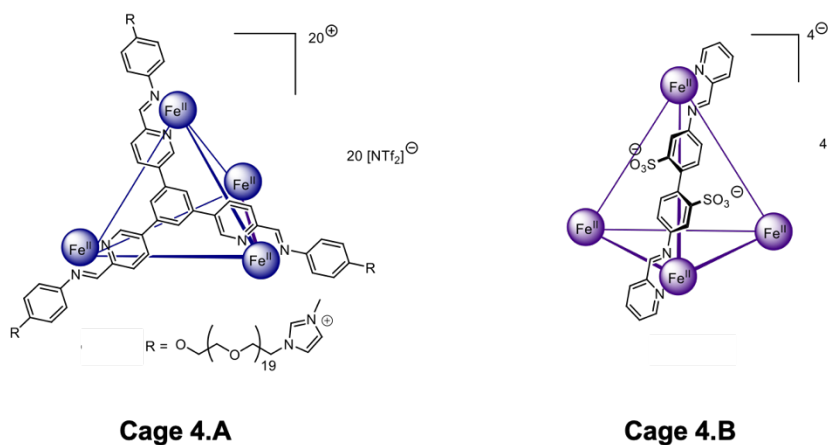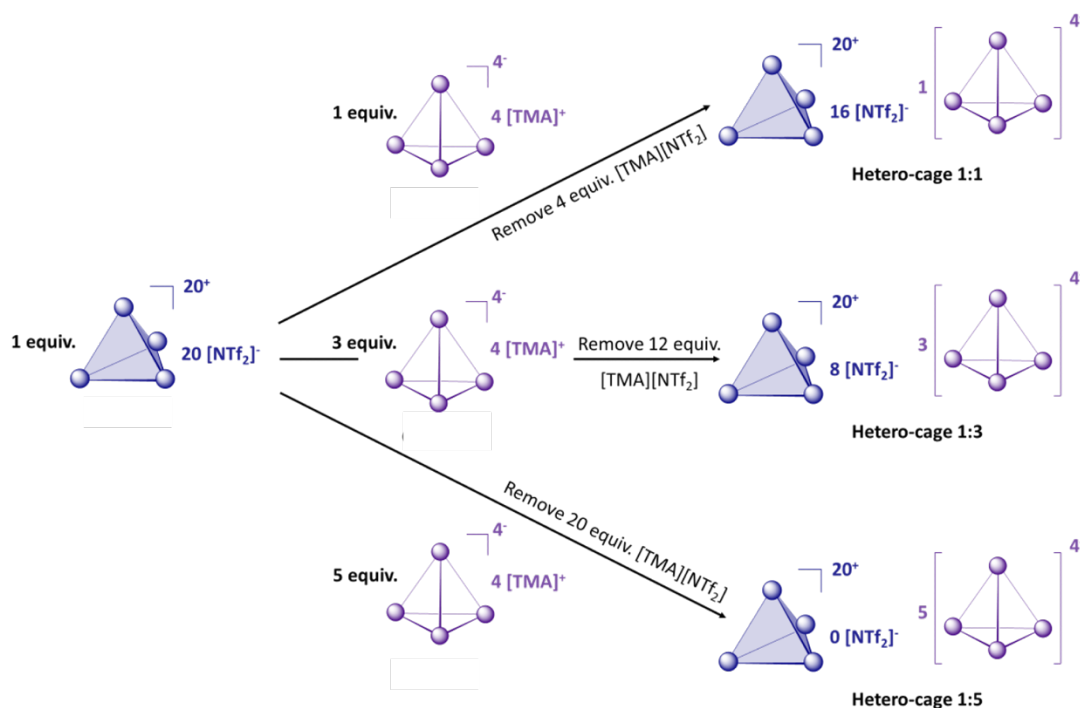
Figure 4.10: a) Cages **4.A** and **4.B** used in Lillian Ma's hetero-cage research, b) Formation of Ma's 1:1, 1:3, and 1:5 hetero-cage systems.[19] Figure 4.10 is adapted with permission from reference 19.

4.2.2 A Highly Anionic Coordination Cage

In her preliminary studies of liquid cage salts Dr Lillian Ma observed that a charge-balanced 1:5 mixture of liquid cage **4.A** and solid cage **4.B** resulted in the formation of a flaky solid species in which the counterions of cage **4.A** were fully exchanged from triflimide to cage **4.B**.

Ma hypothesised that a highly negatively-charged solid coordination cage would be able to act as the counterion for a highly positively-charged liquid coordination cage to form a porous ionic liquid system in which both ionic components were coordination cages.

Cage **4.1** was assembled from the same sulphonated ditopic aniline used by Ma in cage **4.B** and the negatively-charged sulphonated aldehyde described in Chapter 3 (*vide supra*) to form a coordination cage with a -16 charge for further liquid cage salt studies (Figure 4.11a). Single crystals of cage **4.1** for X-ray diffraction were grown by the vapour diffusion of ethanol into an aqueous solution of cage **4.1** (Figure 4.11b).
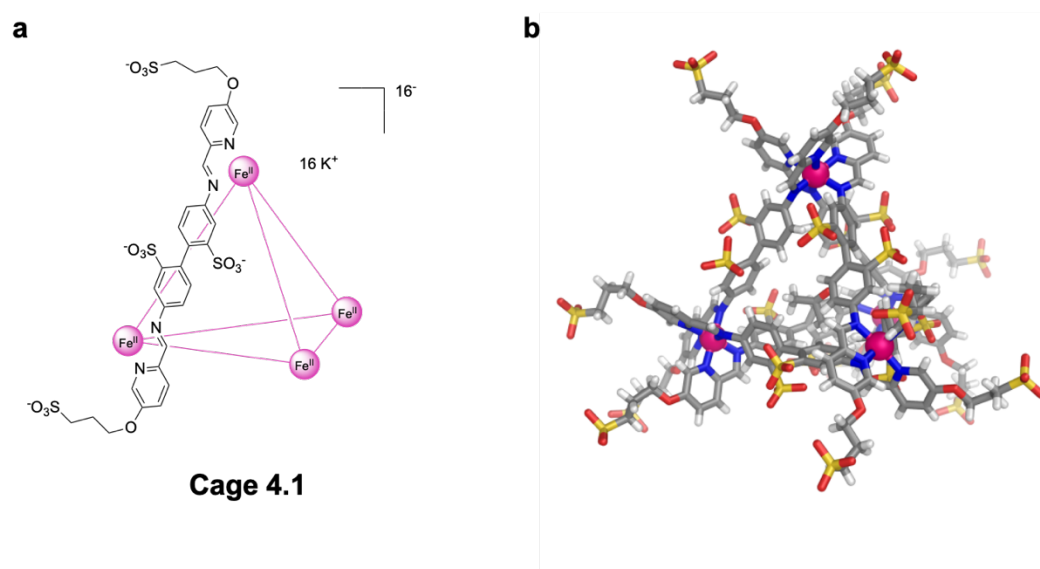
Figure 4.11: a) Highly anionic cage **4.1**, b) Single-crystal X-Ray structure of cage **4.1** (grey – C, white – H, blue – N, red – O, yellow – S, hot pink – Fe) - data collected by Mr Hugh Ryan, structure refinement by Dr Tanya Ronson. Note – complete structure refinement is still in-progress as of June 2021.

The thermal properties of cage **4.1** were studied by DSC and TGA (Figure 4.12). The DSC trace of **4.1** is generally featureless with a small exotherm at *ca.* 180 °C, perhaps corresponding to a melting point, and an onset of decomposition at *ca.* 318 °C. The TGA trace of **4.1** shows a loss of solvent (water) of *ca.* 15 % below 200 °C, due to the solvent trapped during precipitation, and an onset of decomposition at *ca.* 300 °C, in good agreement with the DSC trace.

Figure 4.12: a) TGA profile for cage **4.1**, b) DSC profile for cage **4.1**. These analyses were performed by Georgie Robertson using samples prepared by Mr Hugh Ryan.

Whilst the guest-binding properties of **4.1** were not investigated thoroughly, cage **4.1** was observed to bind fluorobenzene in D_2O by ^{1}H and ^{19}F NMR (see Section 4.4.3). Fluorobenzene was chosen as a useful molecular probe for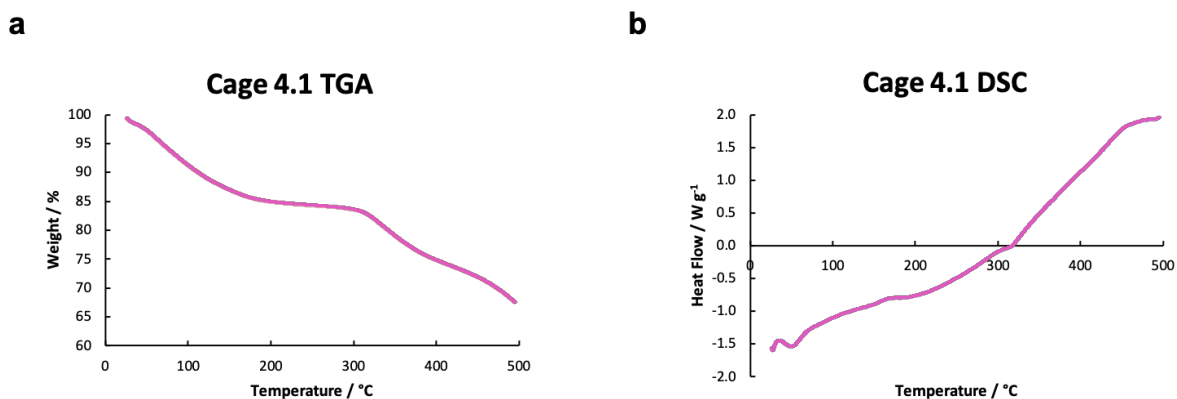 subsequent verification that the cavity of cage **4.1** remained intact after ion metathesis (*vide infra*) and thus, in this work, the binding of fluorobenzene inside **4.1** was studied only qualitatively.

4.2.3 A Highly Cationic Liquid Coordination Cage

In her preliminary studies of liquid cage salt systems Dr Lillian Ma used liquid cage **4.A**, based on the same tritopic aldehyde ligand used in her published work, as the liquid component.[11] The small cavity of cage **4.A**, however, resulted in the encapsulation of only small molecules such as propanol and butanol; thus, the larger triazine-centred liquid cage **4.2** was chosen for further liquid cage salt studies in order to increase the diversity of prospective guest species for encapsulation (Figure 4.13).[20,21] As described in Chapter 1 (*vide supra*), cage **4.2** has already been used to transport molecular cargo in response to thermal stimuli when combined with an ionic liquid auxiliary. The physical properties of cage **4.2**, such as viscosity and storage/loss moduli, and its use in liquid cage salt systems, however, have not been investigated previously.
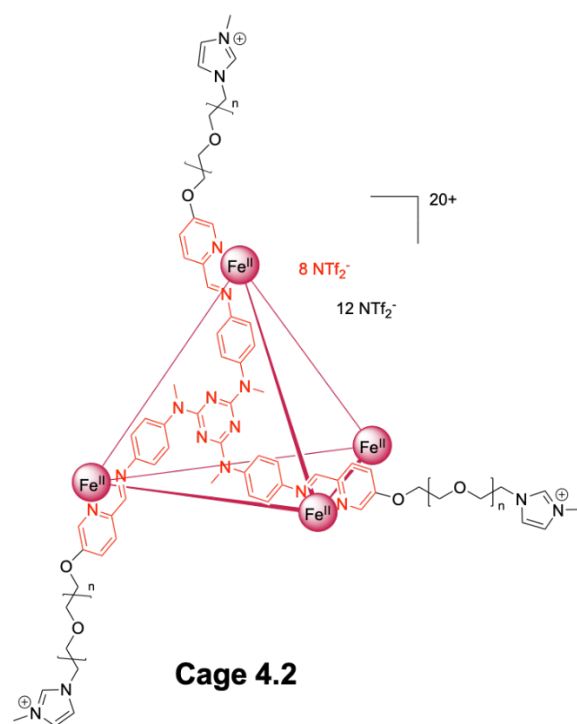
Figure 4.13: Highly cationic liquid coordination cage **4.2**; Red highlight mass – 5299.80 g mol^{-1} (calculated), total mass – *ca*. 21421.20 g mol^{-1}, pore proportion ~ 25 wt%.

Cage **4.2** was assembled *via* the literature procedure and its thermal properties were investigated *via* DSC and TGA (Figure 4.14).[20,21] The DSC trace of cage **4.2** shows a glass transition at -40.4 °C (onset -43.7 °C). The TGA trace of cage **4.2** shows that very little solvent remained in the sample after drying under a dynamic vacuum (< 5 % by mass) and the trace exhibits an onset of decomposition at *ca*. 300 °C. Using the same method described in Section 4.1.6, the proportion of pore of cage **4.2** was estimated to be 25 wt% (see Figure 4.13).

a

Cage 4.2 TGA

b

Cage 4.2 DSC

Figure 4.14: a) TGA profile for cage **4.2**, b) DSC profile for cage **4.2**. These analyses were performed by Georgie Robertson using samples prepared by Mr Hugh Ryan.

Whilst the guest-binding properties of cage **4.2** were not investigated extensively, cage **4.2** was observed to bind fluorobenzene in acetonitrile (see Section 4.4.3); as with cage **4.1** in Section 4.2.2, fluorobenzene was used as a molecular probe for the cavity of cage **4.2** following ion metathesis.
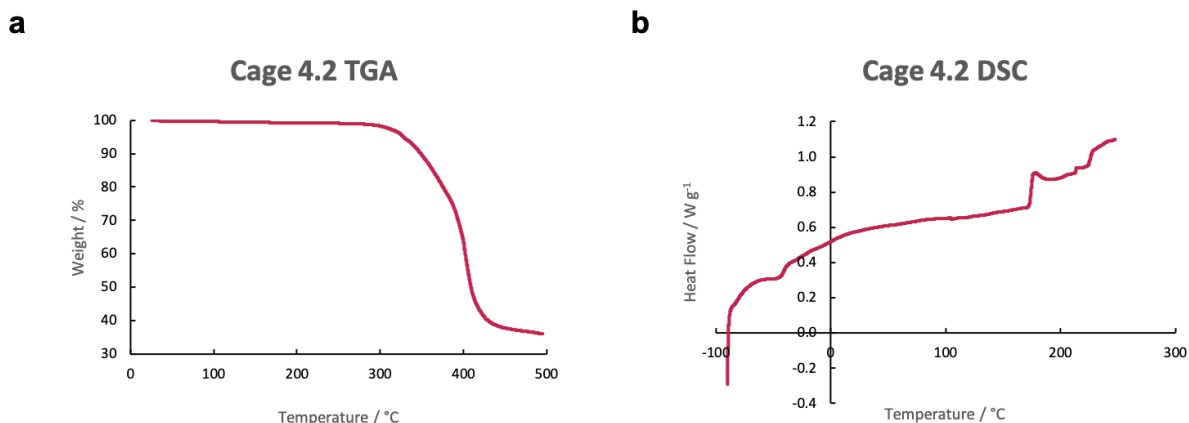
4.2.4 Towards A Liquid Cage Salt

An ion metathesis approach was taken to form a cage salt material from highly anionic cage **4.1** and highly cationic liquid cage **4.2** (Figure 4.15). Cage **4.1** in water was combined with cage **4.2** in methanol and the resulting mixture was washed with ethyl acetate to remove the potassium triflimide by-product (see Section 4.4.4) to yield an intensely red, solid, flaky material [**4.1**]$_5$•[**4.2**]$_4$, referred to from here onwards as salt **4.1•4.2**. The ^{1}H NMR spectrum of **4.1•4.2** in D$_2$O shows the persistence of the broad peaks observed separately for cages **4.1** and **4.2** in D$_2$O (Figure 4.16a). The ^{19}F NMR spectrum of **4.1•4.2** indicates that almost all of the triflimide ions were removed during the washes with ethyl acetate, relative to the ^{19}F NMR spectrum of cage **4.2** in D$_2$O (Figure 4.16b). Furthermore, the triflimide signal at -74.9 ppm which remained in the ^{19}F NMR spectrum of **4.1•4.2** in D$_2$O corresponds to triflimide bound within the cavity of cage **4.2**. The addition of fluorobenzene to **4.1•4.2** in D$_2$O resulted in the appearance of a new ^{19}F signal at -106.6 ppm corresponding to fluorobenzene bound in cage **4.1** (Figure 4.16b). Thus the ^{19}F NMR spectra of **4.1•4.2** in D$_2$O indicate that the counterions

of cage **4.2** were successfully exchanged from triflimide to cage **4.1** and that both cage cavities remained intact following ion metathesis.
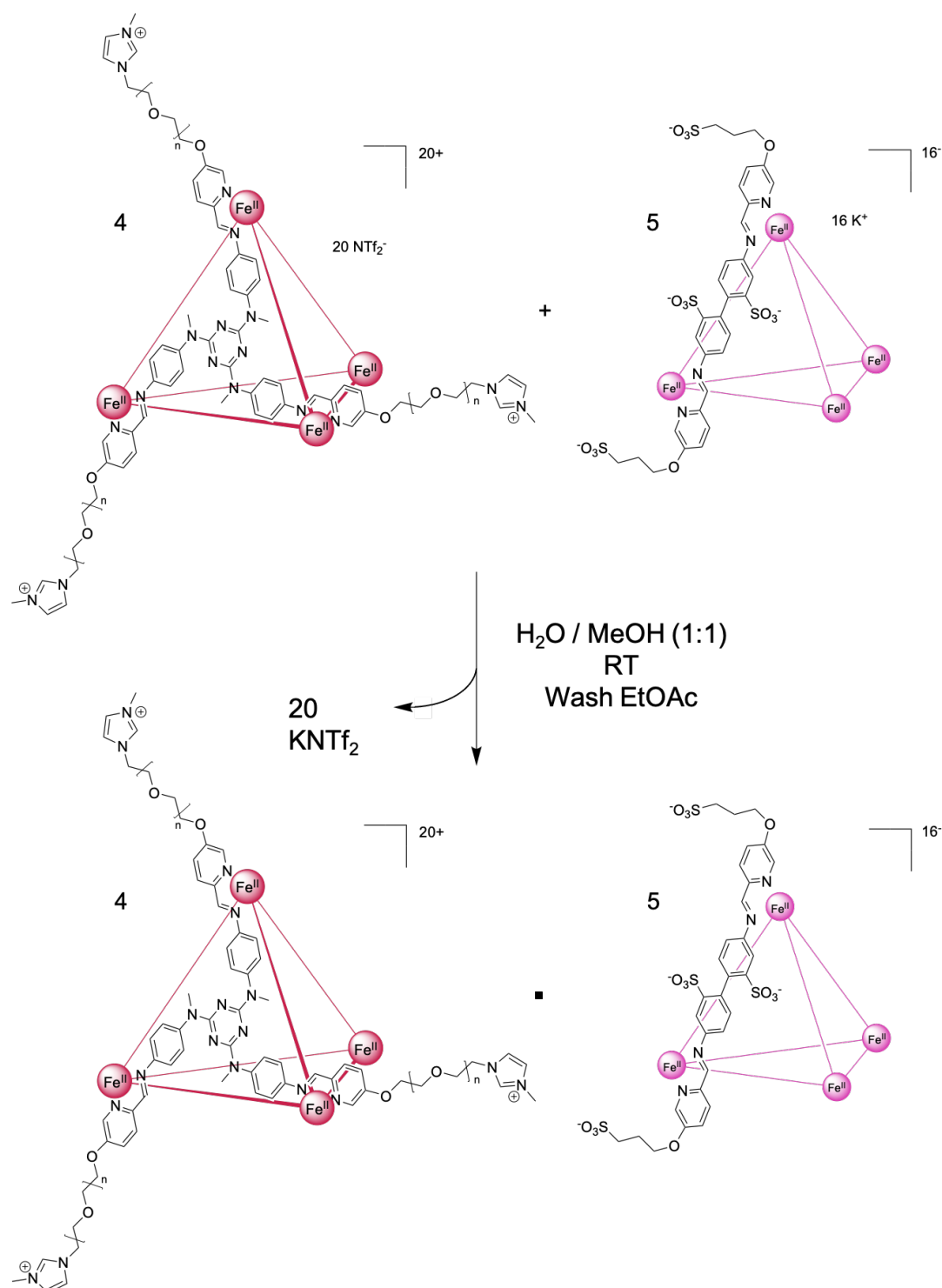

Figure 4.15: Ion metathesis approach to the formation of the cage salt material **4.1•4.2**; Cage **4.1** in water was combined with cage **4.2** in methanol and the mixture was washed with ethyl acetate to remove the excess potassium triflimide.
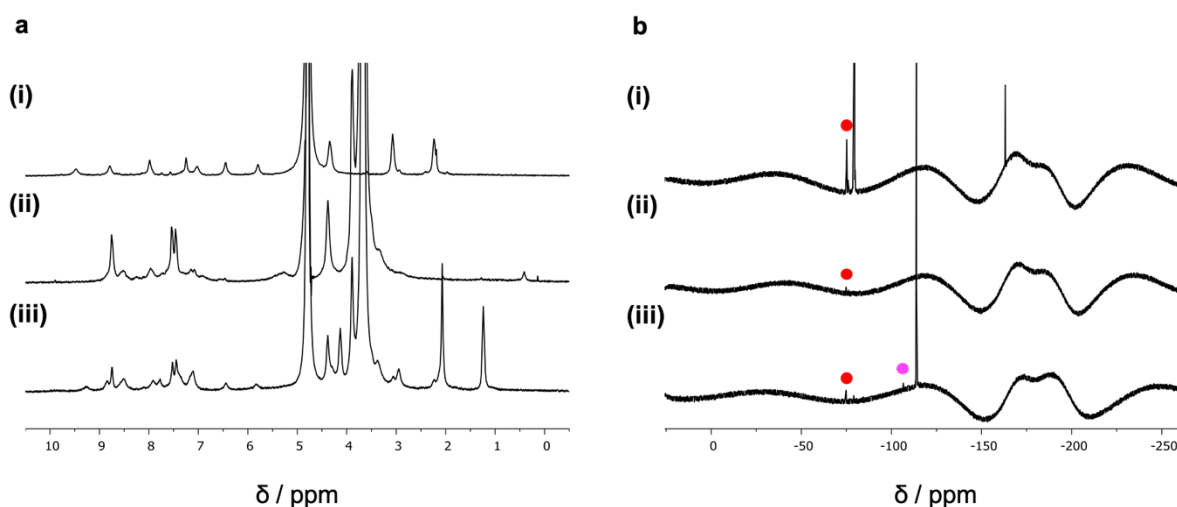
Figure 4.16: a) ^{1}H NMR spectra (D$_2$O, 298 K) for the formation of **4.1•4.2**; i) Cage **4.1** (500 MHz), ii) Cage **4.2** (400 MHz), iii) Cage salt **4.1•4.2** (400 MHz), b) ^{19}F NMR spectra (298 K, 400 MHz, D$_2$O) for the formation of **4.1•4.2**; i) Cage **4.2** – -74.9 (NTf$_2^-$ in cage **4.2**, red circle), -79.0 (free NTf$_2^-$), -162.9 (hexafluorobenzene), ii) Cage salt **4.1•4.2** – -74.9 (NTf$_2^-$ in cage **4.2**, red circle), iii) Cage salt **4.1•4.2** with fluorobenzene – -74.9 (NTf$_2^-$ in cage **4.2**, red circle), -79.0 (free NTf$_2^-$), -106.6 (fluorobenzene in cage **4.1**, pink circle), -114.0 (free fluorobenzene). All shifts in ppm.

The thermal properties of **4.1•4.2** were investigated by DSC and TGA. The TGA profile of **4.1•4.2** indicates the loss of water, *ca*. 10 wt%, below 100 °C and the onset of decomposition at *ca*. 300 °C (Figure 4.17a). The DSC profile of **4.1•4.2** shows a broad glass transition at -44.2 °C (onset -49.6 °C) in the first upwards sweep and another broad feature in range 30 – 70 °C. Interestingly, the second upwards sweep does not show this second broad feature thereby suggesting that this feature results from the two cages blending in the first upwards sweep.

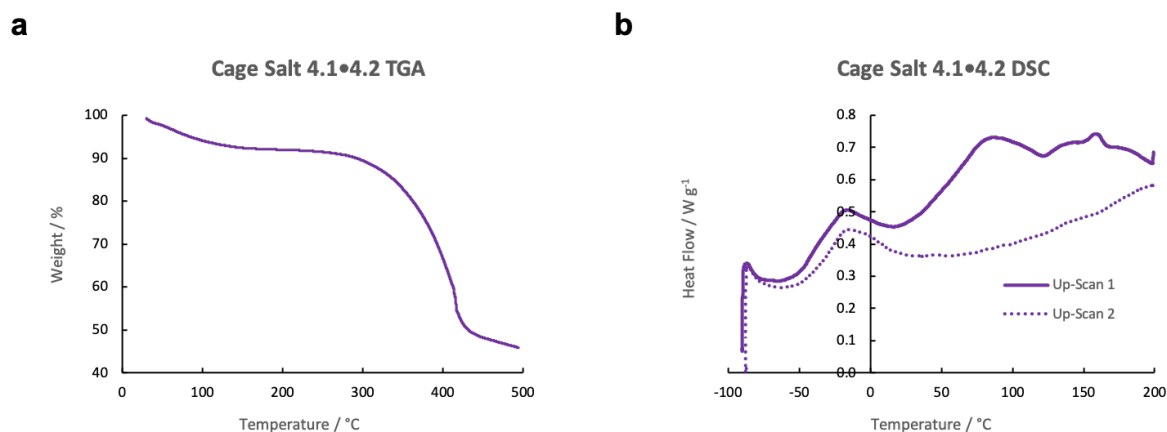Figure 4.17: a) TGA profile for cage salt **4.1•4.2**, b) DSC profile for cage salt **4.1•4.2**. These analyses were performed by Georgie Robertson using samples prepared by Mr Hugh Ryan.

As discussed in Section 4.1.6, one of the drawbacks of Nitschke's first generation of liquid coordination cages was that the coordination cage pore only accounted for *ca.* 24 wt% of the overall liquid material. In an analogous manner to the analysis performed in Section 4.1.6, the proportion of cage pore in **4.1•4.2** is *ca.* 39 wt% and thus **4.1•4.2** represents a significant improvement in the porosity of the overall material of *ca.* 15 wt%. Unfortunately, as discussed above, the material appears as a flaky solid like the hetero-cages studied by Ma and thus cannot be described as a porous liquid.

4.2.5 Conclusions and Future Work

The sections above demonstrate that a cage salt material was synthesised *via* an ion metathesis approach from a highly cationic liquid coordination cage and a highly anionic solid coordination cage. ^{19}F NMR spectroscopy demonstrated that both of the cage cavities remained intact following the ion metathesis reaction and thus the cage salt material retained its porosity. Unfortunately, however, the cage salt was a flaky solid material and thus cannot be described as a porous liquid.

The next stage in the development of a liquid cage salt will require an investigation of the liquid component of the salt. One possible method of ensuring fluidity could be to increase the length of the pendent poly(ethylene glycol) chains to increase the liquid-like nature of the liquid cage; this method would, unfortunately, come at the expense of some of the proportion of cage pores in the material, for example an increase in chain length from 1000 g mol^{-1} to 1500 g mol^{-1}

would result in a decrease in pore proportion from *ca*. 39 wt% to *ca*. 30 wt%. Alternatively, an increase in the polydispersity of the poly(ethylene glycol) chains would result in increased heterogeneity and possibly more liquid-like behaviour; such polydispersity could be achieved by assembling the liquid cage component with a blend of subcomponents synthesised from different poly(ethylene glycol) starting materials.

If one of the above approaches is successful in forming a liquid cage salt, the resulting material would then need to be characterised by ^{1}H and ^{19}F NMR to demonstrate that both of the cage cavities remain intact following ion metathesis. The material would also require rheometric analysis to demonstrate that the material is a fluid phase, as well as other characterisation techniques such as DSC and TGA. Furthermore, the DSC trace of the cage salt system formed to-date suggests that blending of the two constituent cages might occur during the first heating cycle and thus an investigation of the effect of thermal history on the state of the system should also be conducted, perhaps by ^{1}H and ^{19}F NMR. Additionally, porous liquids have already shown great promise in gas sorption, *e.g.* CO_2 and CH_4, and the resulting liquid cage salt material would be expected to bind gaseous guests in its neat state, as well as liquid and solid guests; thus, the gas sorption properties of the liquid material, relative to its component cages, should also be investigated.

4.3 Tuning the Glass Transition Temperature of Liquid Coordination Cages

4.3.1 Preliminary Work

Nitschke's first example of a Type I permanently porous liquid exhibited a glass transition at approximately -44 °C, corresponding to the thermal activation of the poly(ethylene glycol) chains anchored to the coordination cage vertices.[11] In his master's dissertation, "*Thermal Properties of PEG-imidazolium Functionalised Liquid Coordination Cages*", Dani Besenyöi, under the supervision of Mr Hugh Ryan, investigated the effect of decreasing the length of the pendent poly(ethylene glycol) chains on the glass transition temperature of liquid cages assembled with Bolliger's previously reported triazine-centred tritopic aniline.[22] Besenyöi hypothesised that guest binding within solvent-free liquid/glass-like coordination cages could be gated by equilibrating the coordination cage above and below its glass transition temperature (Figure 4.18); above the glass transition temperature the material would behave as a fluid phase and thus guest binding/exchange could occur whereas below the glass transition temperature the material would behave as a solid phase and guest binding/exchange would be kinetically inhibited. Besenyöi observed that decreasing the pendant poly(ethylene glycol) chain length from an average molecular weight of 1000 g mol^{-1} to an average molecular weight of 400 g mol^{-1} resulted in an increase in the glass transition temperature of the cage material from -44 °C to *ca*. -23 °C, depending on the metal centre at the cage vertices (Fe^{II}, Zn^{II}, and Co^{II}). Furthermore, the choice of counterion has been reported to have a significant effect on imidazolium-based ionic liquids;[23] Besenyöi also briefly investigated the effect of the choice of counterion (triflimide, triflate, nitrate, and perchlorate) on the glass transition temperature of a PEG-imidazolium ionic liquid, as a prelude to an investigation of the effect of the choice of counterion on the glass transition temperature of liquid/glass-like coordination cages. Besenyöi observed, however, that the choice of counterion had a smaller effect on the glass transition temperature of the ionic liquid (*ca*. 5 – 6 °C) that the poly(ethylene glycol) chain length had on the liquid cages (*ca*. 20 °C); thus, he concluded that future studies would benefit from a continued investigation of the effect of the chain length on the glass transition temperatures of liquid cages. Both Ma's and Besenyöi's research thus constitute the basis for the following section.
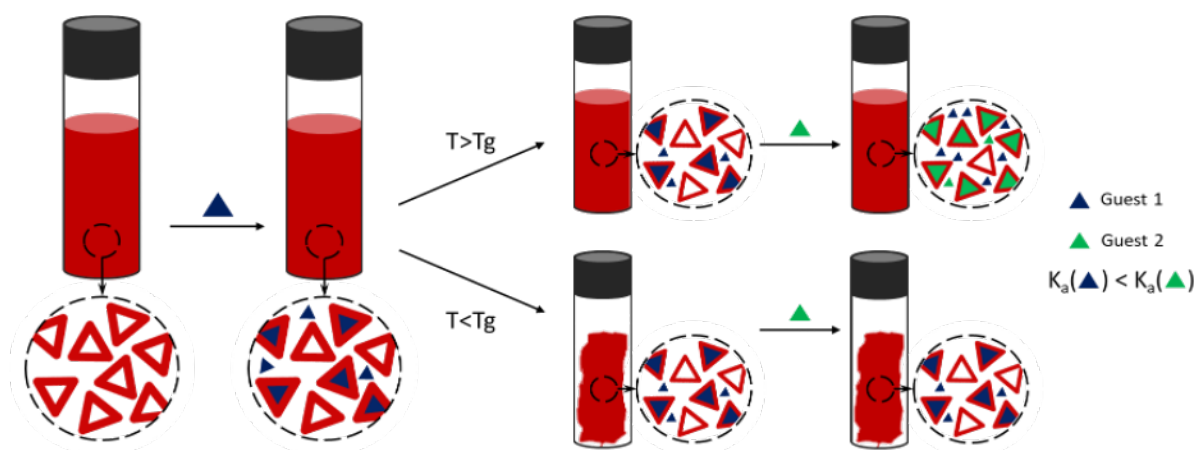
Figure 4.18: Schematic of the guest-binding "kinetic trap" gated by the glass transition of liquid/glass-like cages; following the addition of an initial guest (Guest 1, blue triangle), above its glass transition temperature the cage material is liquid-like and the initial guest can be exchanged for a competitive guest (Guest 2, green triangle), whereas the guest exchange is inhibited below the material's glass transition temperature.[22] Figure 4.18 is reproduced with permission from reference 22.

4.3.2 Effect of Pendent Chain Length

In order to investigate the effect of pendent chain length more thoroughly, ligands **A** and **B** - with pendent chain lengths of ~1000 g mol^{-1} and ~200 g mol^{-1}, respectively - were synthesised and assembled with Bolliger's triazine-centred tritopic aniline and a range of metal vertices and the thermal properties of the resulting liquid/glass-like cages were then studied by DSC and TGA (Figure 4.19).

a   b

Cage	T_g / °C
Cage **4.2** – Fe[II], PEG ~ 1000 g mol^{-1}	-40.4
Cage **4.3** – Zn[II], PEG ~ 1000 g mol^{-1}	-42.9
Cage **4.4** – Co[II], PEG ~ 1000 g mol^{-1}	-41.9
Cage **4.9** – Fe[II], PEG ~ 400 g mol^{-1} *	-22.2
Zn[II], PEG ~ 400 g mol^{-1} *	-24.9
Co[II], PEG ~ 400 g mol^{-1} *	-23.2
Cage **4.5** – Fe[II], PEG ~ 200 g mol^{-1}	-25.4
Cage **4.6** – Zn[II], PEG ~ 200 g mol^{-1}	-27.9
Cage **4.7** – Co[II], PEG ~ 200 g mol^{-1}	-24.6
Cage **4.8** – Fe[II], PEG ~ "400" g mol^{-1} **	-31.9

Figure 4.19: a) The general liquid/glass-like cage framework, n = ~ 16-24 (~ 1000 g mol^{-1}, ligand **A**), ~ 7-8 (~ 400 g mol^{-1}), ~ 3-4 (~ 200 g mol^{-1}, ligand **B**), b) The glass transition temperatures of the cages assembled, * - data collected by Besenyöi,[22] ** - here a 1:3 mixture of ligand **A**:**B** was used in the assembly to have a statistical average of (~ 400 g mol^{-1}).

As discussed in the previous section, Besenyöi observed an increase of *ca.* 20 °C in the glass transition temperature of his liquid cages upon decreasing the pendent poly(ethylene glycol) chain length from ~ 1000 g mol^{-1} to ~ 400 g mol^{-1}, relative to the liquid cage first synthesised by Ma. Cages **4.2** – **4.4**, assembled with a chain length of ~ 1000 g mol^{-1}, show a similar glass transition temperature to that observed by Ma. In contrast to the work done by Besenyöi, the data in Figure 4.19 indicate that reduction of the chain length from ~ 400 g mol^{-1} to ~ 200 g mol^{-1} (cages **4.5** – **4.7**) resulted in a significantly smaller change to the glass transition (*ca.* 3 °C). Cages **4.5** – **4.7**, however, were glass-like by inspection. Cage **4.8** was formed from a 1:3 mixture of ~ 1000 g mol^{-1} (ligand **A**) and ~ 200 g mol^{-1} (ligand **B**) in order to mimic the average chain length of Besenyöi's cages (~ 400 g mol^{-1}) but with increased disorder at the vertices of the cage. Cage **4.8** and Besenyöi's cage **4.9** were observed to diffuse at the same rate in acetonitrile by DOSY (see Sections 4.4.2 and 4.4.5) thereby suggesting a similar hydrodynamic radius - or, perhaps more formally, solvo-dynamic radius – but the low-resolution mass spectra of the two cages indicate that, as anticipated, the distribution of masses of cage **4.8** is much larger (see Sections 4.4.2 and 4.4.5). Interestingly, cage **4.8** exhibited a broad glass transition at *ca.* 9 °C lower than Besenyöi's cage **4.9** and this observation is attributed to the increase in chain heterogeneity at the vertices of the cage. Cage **4.8** was liquid-like by inspection but, due

to the overall reduction in chain length relative to cage **4.2** (*vide supra*), contains 37 wt% pore and thus cage **4.8** represents a significant increase in the proportion of cage pore in the material over Nitschke's first example.

4.3.3 Conclusions and Future Work

The preceding section presented a short investigation of the effect of the length of the fluidifying poly(ethylene glycol) chains on the glass transition temperature of liquid coordination cages. Previous work has shown that decreasing the polymer length from ~ 1000 g mol^{-1} to ~ 400 g mol^{-1} resulted in an increase of *ca*. 20 °C in the glass transition temperature; in this work, a further decrease in chain length to ~ 200 g mol^{-1} resulted in very little change (*ca*. 2 – 3 °C) in the glass transition temperature. In contrast, increasing the heterogeneity in the lengths of the polymer chains whilst maintaining an average of ~ 400 g mol^{-1} resulted in a depression of the glass transition temperature of *ca*. 9 °C, thereby increasing the proportion of pore in the material, relative to the previously published example, but maintaining its fluid properties (by inspection).

The next stage in this development of a new generation of liquid coordination cages will require an investigation of the material properties of the cages formed thus far. The cages formed with polymer chains of ~ 400 g mol^{-1} appear liquid by inspection but rheometric analysis will be required in order to demonstrate that they are fluid phases, *i.e.* their loss moduli exceed their storage moduli. Nitschke's first example of a liquid coordination cage bound gaseous chlorofluorocarbons and small alcohols but was otherwise limited in the range of prospective guest species due to the small cage cavity; having demonstrated that the cages are fluid phases, future efforts might wish to explore the host-guest chemistry of these new, larger liquid cages in the neat state towards both gaseous and condensed guests.

4.4 Experimental

4.4.1 Subcomponent Synthesis
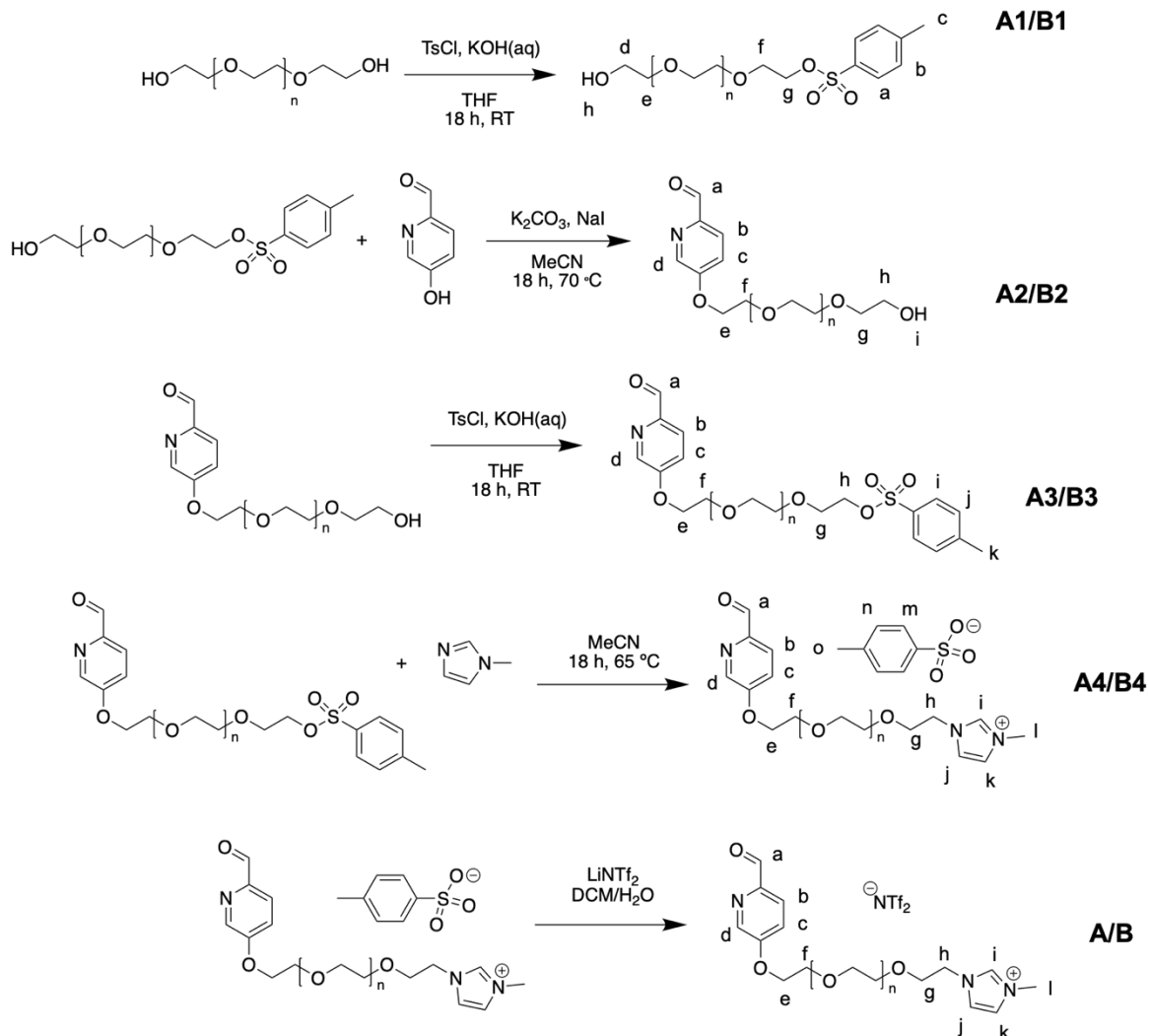
Scheme 4.1: Synthesis of ligands **A** (n ~ 16 – 24) and **B** (n ~ 3 – 4).

Ligand **A**:

This compound was prepared by a modified literature procedure[21] combined with the procedure worked on by Maureen Georges[20]. The ^{1}H NMR peaks were assigned in comparison to Georges' work.

Precursor **A1**

A solution of potassium hydroxide (265.5 mg, 4.732 mmol) in water (3 mL) was added dropwise to a stirred solution of polyethylene glycol ($M_r \sim 1000$ g mol^{-1}, 10.0532 g, 10.053 mmol) in THF (100 mL). p-Toluenesulphonyl chloride (267.1 mg, 1.401 mmol) was then added and the reaction mixture was stirred at room temperature for 18 hours. The solvent was removed *in vacuo* and the crude product was extracted with DCM (3 × 30 mL), washed with water (3 × 30 mL), dried over anhydrous magnesium sulphate, filtered under gravity, and finally the solvent was removed *in vacuo*. The crude product was purified by flash column chromatography on silica (DCM/MeOH, 6 %) and dried under a stream of nitrogen gas to yield precursor **A1** (1.078 g, 0.934 mmol, 67 %). ^{1}H NMR (400 MHz, CD$_3$CN, 298 K, referenced to residual solvent at 1.94 ppm) δ_H = 7.79 (d, 8 Hz, H$_a$), 7.44 (d, 8 Hz, H$_b$), 4.11 (m, H$_g$), 3.55 – 3.75 (m, H$_d$, H$_e$, H$_f$, H$_{PEG}$), 2.83 (bs, H$_h$), 2.45 (s, H$_c$).

Precursor **A2**

A mixture of precursor **A1** (1.0554 g, 0.914 mmol), potassium carbonate (634.7 mg, 4.592 mmol), sodium iodide (25.5 mg, 0.170 mmol), and 5-hydroxypicolinaldehyde (123.0 mg, 0.999 mmol) in acetonitrile (10 mL) was stirred at 70 °C for 18 hours. The reaction mixture was then filtered under gravity and the solvent removed *in vacuo*. The crude product was extracted with DCM (3 × 30 mL), washed with water (3 × 30 mL), dried over anhydrous magnesium sulphate, and filtered under gravity. Finally, the solvent was removed *in vacuo* and the product dried under a stream of nitrogen gas to yield precursor **A2** (984.4 mg, 0.891 mmol, 97 %). ^{1}H NMR (400 MHz, CD$_3$CN, 298 K, referenced to residual solvent at 1.94 ppm) δ_H = 9.91 (s, H$_a$), 8.45 (d, 2 Hz, H$_d$), 7.92 (d, 9 Hz, H$_b$), 7.45 (dd, 9 Hz, 2 Hz, H$_c$), 4.28 (m, H$_e$), 3.83 (m, H$_f$), 3.35 – 3.75 (m, H$_g$, H$_h$, H$_{PEG}$), 2.77 (m, H$_i$).

Precursor **A3**

A solution of potassium hydroxide (187.8 mg, 3.347 mmol) in water (1 mL) was added dropwise to a solution of **A2** (957.2 mg, 0.866 mmol) in THF (30 mL). p-Toluenesulphonyl

chloride (334.9 mg, 1.757 mmol) was then added and the resulting mixture was stirred at room temperature for 18 hours. The solvent was then removed *in vacuo* and the product was extracted with DCM (3 × 30 mL), washed with water (3 × 30 mL), dried over anhydrous magnesium sulphate, and filtered under gravity. The crude product was purified by flash column chromatography on silica (DCM/MeOH 6 %) and then the product was dried under a stream of nitrogen gas to yield precursor **A3** (872.2 mg, 0.692 mmol, 80 %). ^{1}H NMR (400 MHz, CD$_3$CN, 298 K, referenced to residual solvent at 1.94 ppm) δ_H = 9.91 (s, H$_a$), 8.45 (d, 2 Hz, H$_d$), 7.92 (d, 9 Hz, H$_b$), 7.79 (d, 8 Hz, H$_i$), 7.45 (m, H$_c$, H$_j$), 4.28 (m, H$_e$), 4.11 (m, H$_h$), 3.83 (m, H$_f$), 3.35 – 3.75 (m, H$_g$, H$_{PEG}$), 2.44 (s, H$_k$).

Precursor **A4**

A solution of **A3** (734.4 mg, 0.583 mmol) and 1-methylimidazole (0.15 mL, 1.882 mmol) in acetonitrile (6.5 mL) was stirred at 65 °C for 18 hours. The solvent was removed *in vacuo* and the crude product was washed with diethyl ether (5 × 50 mL) and dried under a stream of nitrogen gas to yield precursor **A4** (679.7 mg, 0.507 mmol, 87 %). ^{1}H NMR (400 MHz, CD$_3$CN, 298 K, referenced to residual solvent at 1.94 ppm) δ_H = 9.91 (s, H$_a$), 8.69 (s, H$_i$), 8.44 (d, 2 Hz, H$_d$), 7.92 (d, 9 Hz, H$_b$), 7.59 (d, 8 Hz, H$_m$), 7.45 (m, H$_c$, H$_j$), 7.36 (s, H$_k$), 7.14 (d, 8 Hz, H$_n$), 4.28 (m, H$_h$), 3.85 (s, H$_l$), 3.83 (m, H$_e$), 3.35 – 3.80 (m, H$_f$, H$_g$, H$_{PEG}$), 2.33 (s, H$_o$).

Ligand **A**

A mixture of **A4** (632.7 mg, 0.472 mmol) and lithium bistriflimide (220.4 mg, 0.768 mmol) in water (5 mL) was stirred at room temperature for 1 hour. DCM (75 mL) was added and the biphasic mixture was then stirred vigorously at room temperature for 1 hour. The phases were then separated and the organic phase was washed with water (3 × 30 mL), dried over anhydrous magnesium sulphate, and filtered under gravity. The solvent was then removed *in vacuo* and the product dried under a stream of nitrogen gas to yield ligand **A** (665.6 mg, 0.459 mmol, 97 %). ^{1}H NMR (400 MHz, CD$_3$CN, 298 K, referenced to residual solvent at 1.94 ppm) δ_H = 9.91 (s, H$_a$), 8.60 (s, H$_i$), 8.45 (d, 2 Hz, H$_d$), 7.92 (d, 9 Hz, H$_b$), 7.35 – 7.45 (m, H$_c$, H$_j$, H$_k$), 4.27 (m, H$_h$), 3.84 (s, H$_l$), 3.83 (m, H$_e$), 3.35 – 3.80 (m, H$_f$, H$_g$, H$_{PEG}$).

Ligand **B**:

This compound was synthesised by modifying the first step of the literature procedure and in conjunction with Georges' work.[20,21] The ^{1}H NMR peaks were assigned in comparison to Georges' work.

Precursor **B1**

A solution of potassium hydroxide (1.2540 g, 22.4 mmol) in water (5 mL) was added dropwise to a mixture of polyethylene glycol ($M_r \sim 200$ g mol^{-1}, 18.7802 g, 93.9 mmol) and p-toluenesulphonyl chloride (1.6809 g, 8.82 mmol) in THF (75 mL). The resulting mixture was stirred at room temperature for 18 hours. The solvent was removed *in vacuo* and the crude product was extracted with DCM (3 × 30 mL), washed with water (6 × 30 mL), dried over anhydrous magnesium sulphate, filtered, and dried in vacuo. The crude product was then purified *via* flash column chromatography on silica (DCM/MeOH 4 %) and dried under a stream of nitrogen gas to yield pale yellow oil precursor **B1** (496.3 mg, 1.40 mmol, 16 %). ^{1}H NMR (500 MHz, CD$_3$CN, 298 K, referenced to residual solvent at 1.94 ppm) δ_H = 7.79 (d, 10 Hz, H_a), 7.44 (d, 10 Hz, H_b), 4.11 (m, H_g), 3-35 – 3.75 (m, H_d, H_e, H_f. H_{PEG}), 2.73 (bs, H_h), 2.44 (s, H_c).

TOF MS (Waters G2-S, ASAP): m/z = 349.1315 (calculated 349.1231), major species

Precursor **B2**

A mixture of precursor **B1** (433.2 mg, 1.22 mmol), potassium carbonate (860 mg, 6.22 mmol), sodium iodide (25 mg, 0.17 mmol), and 5-hydroxypicolinaldehyde (195 mg, 1.58 mmol) in acetonitrile (10 mL) was stirred at 65 °C for 48 hours. The reaction mixture was then filtered under gravity and dried *in vacuo*. The crude product was extracted with DCM (3 × 30 mL), washed with water (3 × 30 mL), dried over anhydrous magnesium sulphate, filtered, dried in *vacuo*, and then finally dried under a stream of nitrogen gas to yield pale yellow oil precursor **B2** (259 mg, 0.85 mmol, 69 %). ^{1}H NMR (500 MHz, CD$_3$CN, 298 K, referenced to residual solvent at 1.94 ppm) δ_H = 9.91 (s, H_a), 8.46 (t, 3 Hz, H_d), 7.92 (d, 10 Hz, H_b), 7.45 (dd, 10 Hz, 3 Hz, H_c), 4.28 (m, H_e), 3.84 (m, H_f), 3.35 – 3.75 (m, H_g, H_h, H_{PEG}), 2.75 (bs, H_i).

TOF MS (Waters G2-S, ASAP): m/z = 300.1438 (calculated 300.1442), major species

163

Precursor **B3**

A solution of potassium hydroxide (120.2 mg, 2.14 mmol) in water (*ca.* 1 mL) was added dropwise to a solution of precursor **B2** (230 mg, 0.75 mmol) and p-toluenesulphonyl chloride (269.4 mg, 1.41 mmol) in THF (10 mL) and the resulting mixture was stirred at room temperature for 18 hours. The reaction mixture was then dried *in vacuo* and the crude product was extracted with DCM (3 × 30 mL), washed with water (3 × 30 mL), dried over anhydrous magnesium sulphate, filtered, and dried *in vacuo*. The crude product was then purified *via* flash column chromatography on silica (DCM/MeOH 4 %) and dried under a stream of nitrogen gas to yield pale yellow oil precursor **B3** (249.2 mg, 0.54 mmol, 72 %). ^{1}H NMR (500 MHz, CD$_3$CN, 298 K, referenced to residual solvent at 1.94 ppm) δ_H = 9.92 (s, H$_a$), 8.45 (m, H$_d$), 7.92 (d, 10 Hz, H$_b$), 7.79 (d, 10 Hz, H$_i$), 7.44 (m, H$_c$, H$_j$), 4.28 (m, H$_e$), 4.11 (m, H$_h$), 3.84 (m, H$_f$), 3.35 – 3.75 (m, H$_g$, H$_{PEG}$), 2.44 (m, H$_k$).

TOF-MS (Agilent 6230 LC/TOF, ESI): m/z = 454.1544 (calculated 454.1530), major species

Precursor **B4**

A solution of precursor **B3** (244.2 mg, 0.53 mmol) and 1-methylimidazole (0.2 mL, 2.51 mmol) in acetonitrile (5 mL) was stirred at 65 °C for 18 hours. The solvent was removed *in vacuo* and the crude product was washed with ether (15 × 10 mL) and dried under a stream of nitrogen gas to yield yellow oil precursor **B4** (215.6 mg, 0.40 mmol, 75 %). ^{1}H NMR (400 MHz, CD$_3$CN, 298 K, referenced to residual solvent at 1.94 ppm) δ_H = 9.92 (s, H$_a$), 8.70 (s, H$_i$), 8.43 (d, H$_d$), 7.92 (d, 7 Hz, H$_b$), 7.59 (d, 6 Hz, H$_m$), 7.45 (m, H$_c$, H$_j$), 7.36 (s, H$_k$) 7.14 (d, 7 Hz, H$_n$), 4.26 (m, H$_h$), 3.85 (s, H$_l$), 3.83 (m, H$_e$), 3.79 (m, H$_f$, H$_g$) 3.35 – 3.75 (m, H$_{PEG}$), 2.33 (s, H$_o$).

This species was not observed by TOF-MS

Ligand **B**:

A mixture of **B4** (215.6 mg, 0.40 mmol) and lithium bistriflimide (309.7 mg, 1.07 mmol) in water (5 mL) was stirred at room temperature for *ca.* 5 minutes. DCM (50 mL) was added and the biphasic mixture was then stirred vigorously at room temperature for a further 5 minutes. The phases were then separated and the organic phase was washed with water (3 × 25 mL), dried over anhydrous magnesium sulphate, and filtered under gravity. The solvent was then removed *in vacuo* and the product dried under a stream of nitrogen gas to yield ligand **B** (214.6 mg, 0.33 mmol, 83 %). ^{1}H NMR (400 MHz, CD$_3$CN, 298 K, referenced to residual solvent at

1.94 ppm) δ_H = 9.91 (s, H_a), 8.53 (m, H_i), 8.43 (m, H_d), 7.92 (d, 9 Hz, H_b), 7.43 (m, H_j), 7.30 (m, H_c, H_k), 4.25 (m, H_h), 3.82 (s, H_l), 3.35 – 3.75 (m, H_e, H_f, H_g, H_{PEG}).

TOF-MS (Waters G2-S, ASAP): m/z = 364.1869 (364.1872), major species

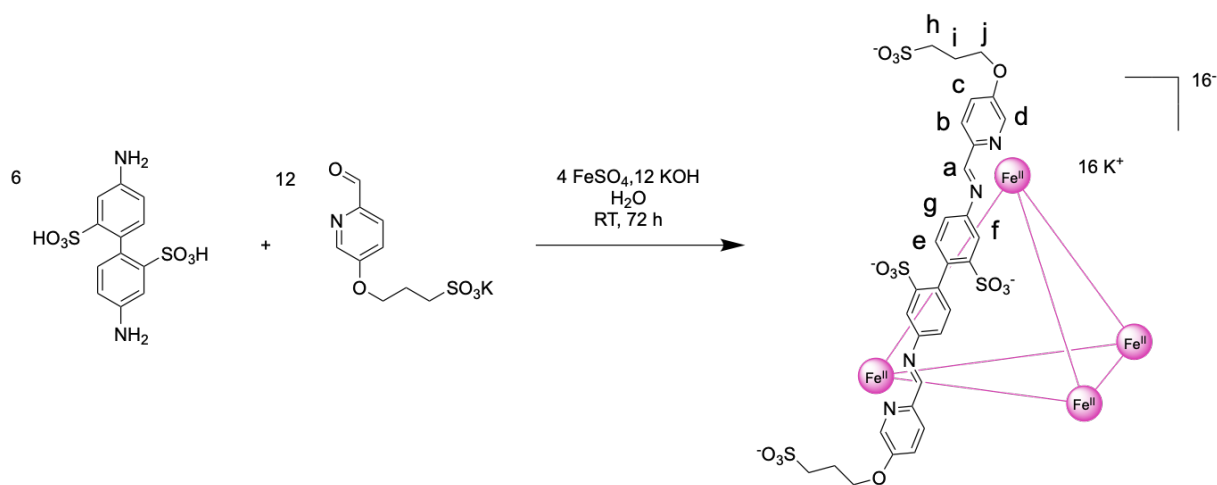**N2,N4,N6-tris(4-aminophenyl)-N2,N4,N6-trimethyl-1,3,5-triazine-2,4,6-triamine**:

This compound was synthesised as described in Section 3.5.1.

Potassium 3-((6-formylpyridin-3-yl)oxy)propane-1-sulphonate:

This compound was synthesised as described in Section 3.5.1.

4.4.2 Cage Assemblies

Cage **4.1**

Scheme 4.2: Assembly of cage **4.1**.

Potassium 3-((6-formylpyridin-3-yl)oxy)propane-1-sulfonate (54.4 mg, 192.0 µmol), 4,4'-diamino-[1,1'-biphenyl]-2,2'-disulfonic acid (39.3 mg, *ca*. 96.3 µmol), potassium hydroxide (12 mg, 213.9 µmol), and iron (II) sulphate heptahydrate (18.4 mg, 66.2 µmol) were dissolved in D_2O (2 mL) and stirred at room temperature for 72 hours. The cage was precipitated with acetone (10 mL), washed with further acetone (10 mL), and dried to air to yield dark pink solid cage **4.1** (88.6 mg, 15.7 µmol)*. ^{1}H NMR (400 MHz, D_2O, 298 K, referenced to residual solvent at 4.79 ppm) $\delta_H = 9.47$ (bs, H_a), 8.80 (bs, H_b), 7.97 (bs, H_c), 7.24 (bs, H_d), 7.03 (bs, H_e), 6.44 (bs, H_f), 5.79 (bs, H_g), 4.34 (bs, H_j), 3.07 (bs, H_h), 2.23 (bs, H_i).

* - TGA trace indicates a large proportion of solvent in the precipitate and thus a yield has not been given.

The broad peaks for cage **4.1** were likely to have been caused by rapid relaxation and this hindered the collection of ^{13}C and 2D NMR spectra. The ^{1}H assignments have been predicted based on those of cage **3.1**. Crystallography confirms the formation of cage **4.1**.
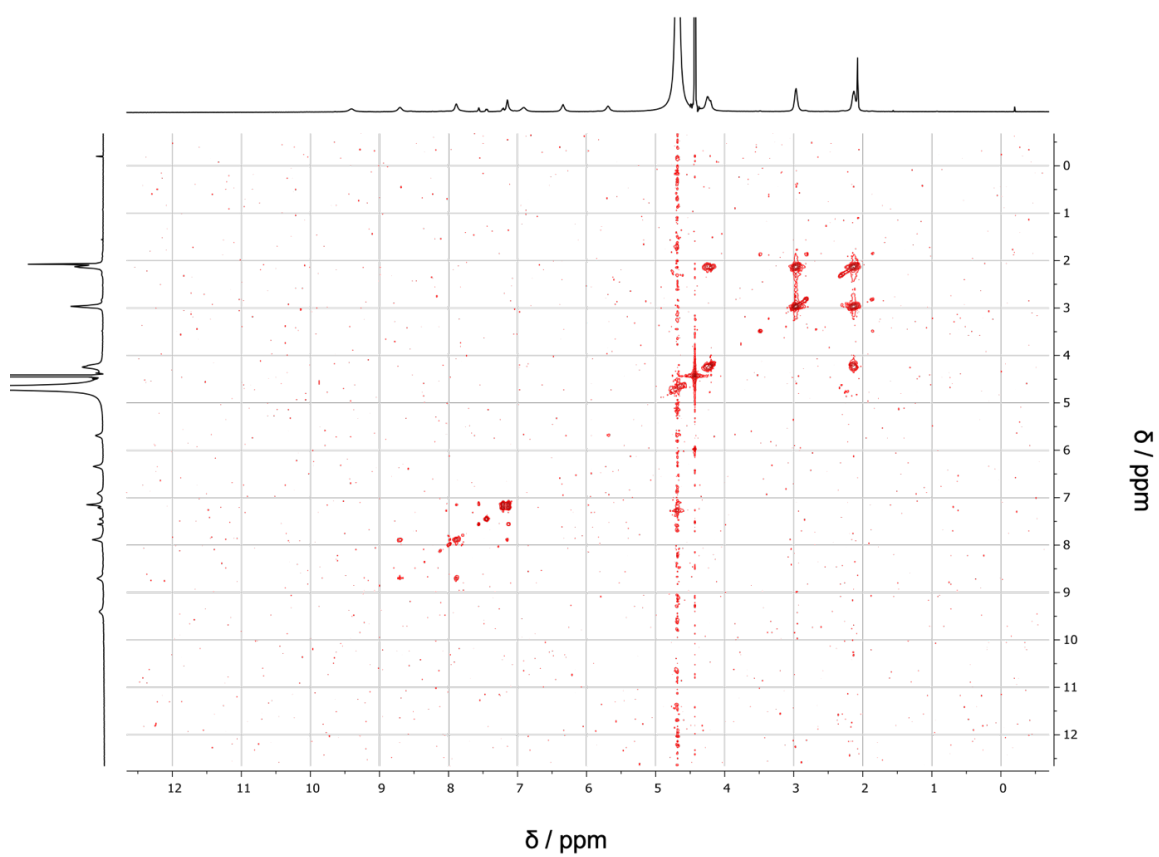
Figure 4.20: COSY spectrum (500 MHz, D$_2$O, 298 K) of cage **4.1**. Data acquired by NMR Service, Department of Chemistry, using a sample prepared by Mr Hugh Ryan.

DSC and TGA data for cage **4.1** are provided in Section 4.2.2.

Cage **4.2**
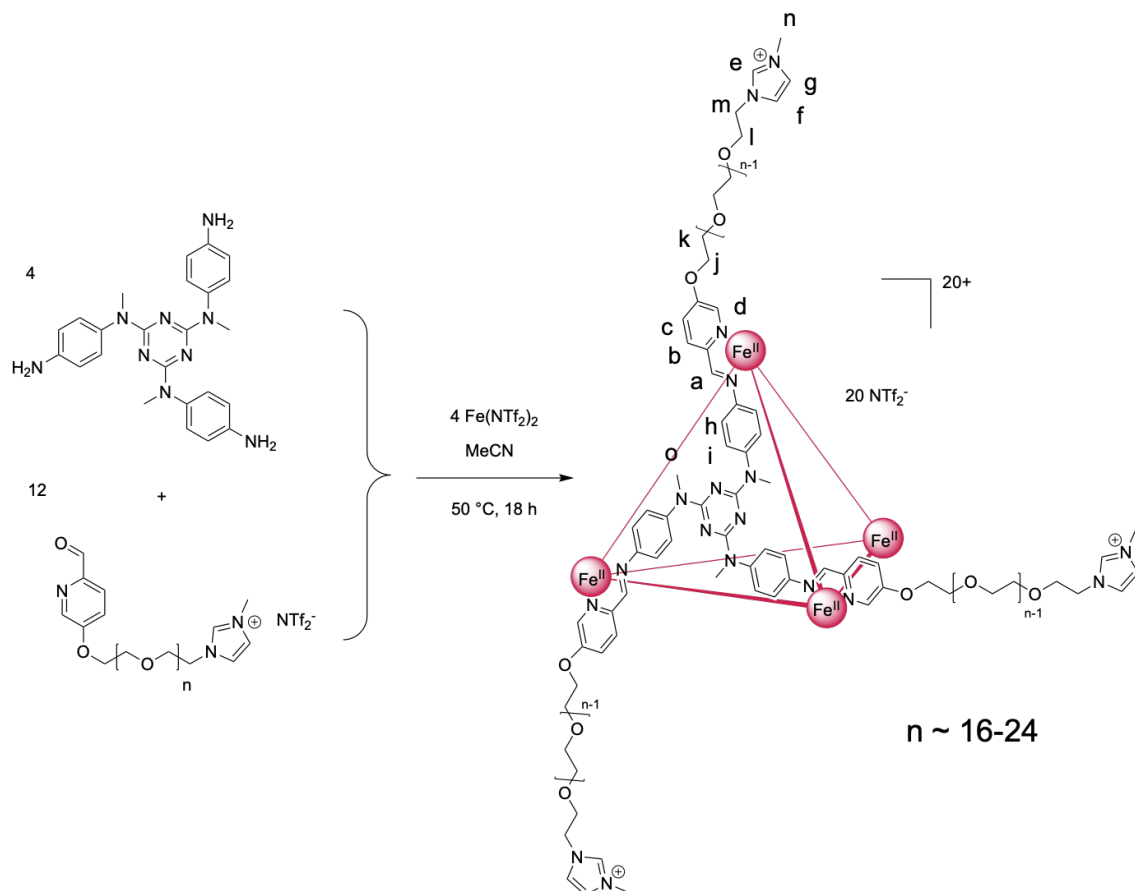
Scheme 4.3: Assembly of cage **4.2**.

This cage was assembled *via* the literature procedure.[21] N2,N4,N6-tris(4-aminophenyl)-N2,N4,N6-trimethyl-1,3,5-triazine-2,4,6-triamine (11.7 mg, 26.5 µmol), ligand **A** (115.1 mg, 79.3 µmol), and iron (II) bistriflimide[24] (18.3 mg, 26.2 µmol) were dissolved in CD_3CN (2 mL) and stirred at 50 °C for 18 hours. The cage was precipitated with diethyl ether (8 mL), washed with further diethyl ether (2 × 5 mL), and dried under a stream of nitrogen gas to yield a dark red sticky liquid cage **4.2** (114.5 mg, 5.3 µmol, 81 %). ^{1}H NMR (400 MHz, CD_3CN, 298 K, referenced to residual solvent at 1.94 ppm) δ_H = 8.70 (s, H_a), 8.67 (s, H_a)*, 8.58 (s, H_e), 8.42 (m, H_b), 7.88 (d, 9 Hz, H_c), 7.44 (m, H_f), 7.35 (m, H_g, H_i), 7.01 (s, H_d), 5.08 (m, H_h), 4.27 (m, H_j, H_m), 3.84 (s, H_n), 3.79 (m, H_k, H_l), 3.35 – 3.75 (m, H_o, H_{PEG}).

*denotes peak arising from host-guest complex with NTf_2^-

168

DSC and TGA data for cage **4.2** are provided in Section 4.2.3.
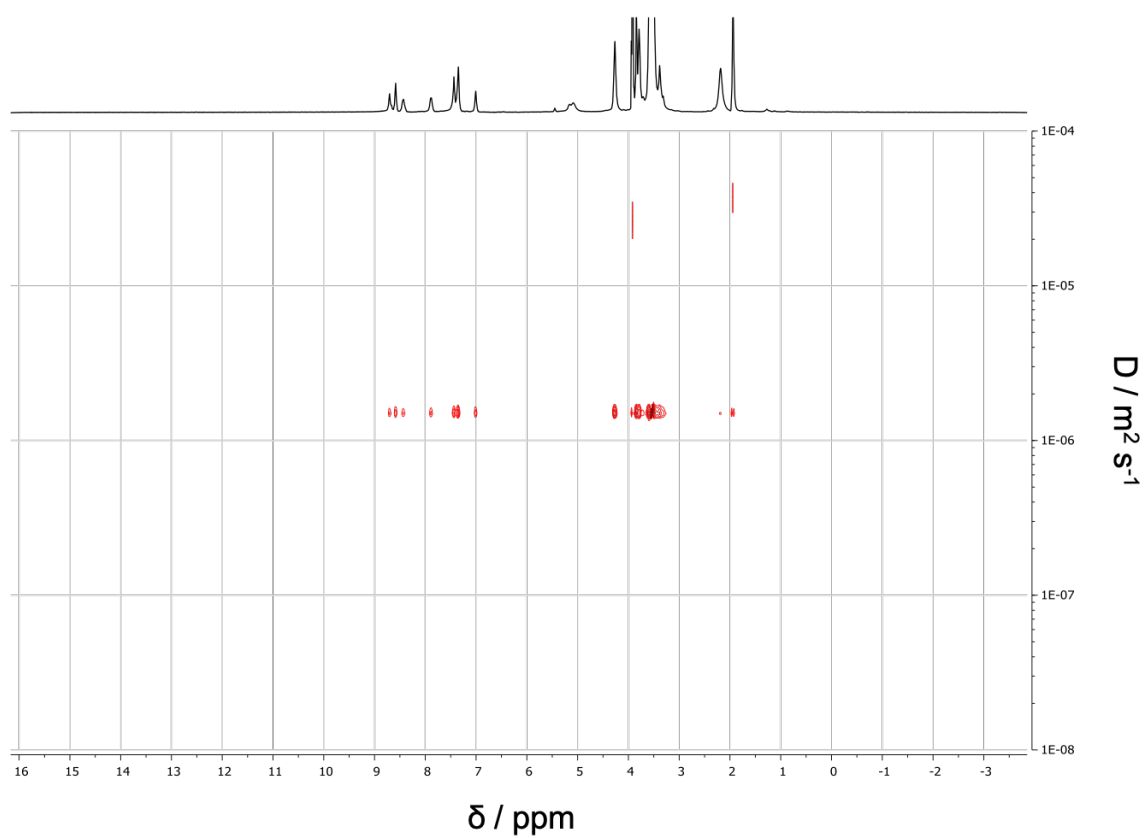
Figure 4.21: DOSY spectrum of cage **4.2** in CD$_3$CN (298 K, 400 MHz), D ~ 1.5 × 10^{-6} m^2 s^{-1}.
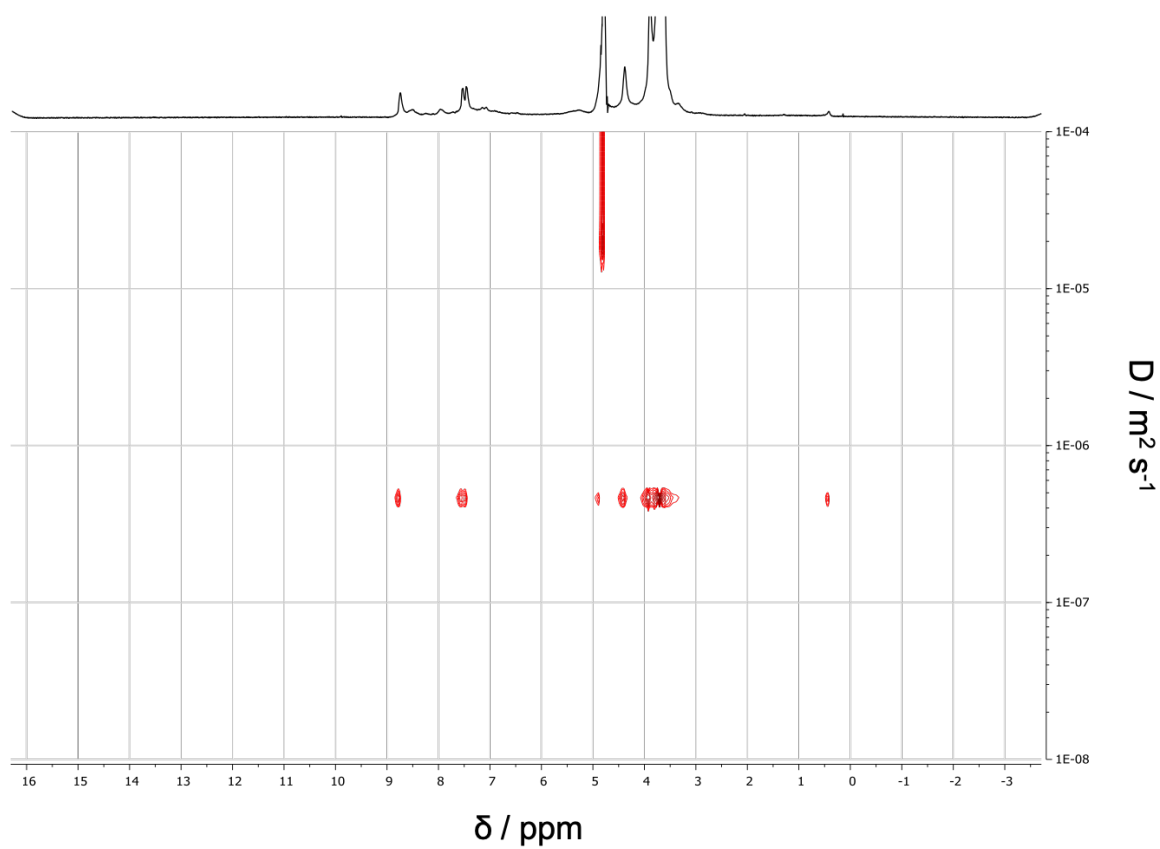
Figure 4.22: DOSY spectrum of cage **4.2** in D_2O (298 K, 400 MHz), D ~ 4.6×10^{-7} m^2 s^{-1}.

Cage **4.3**
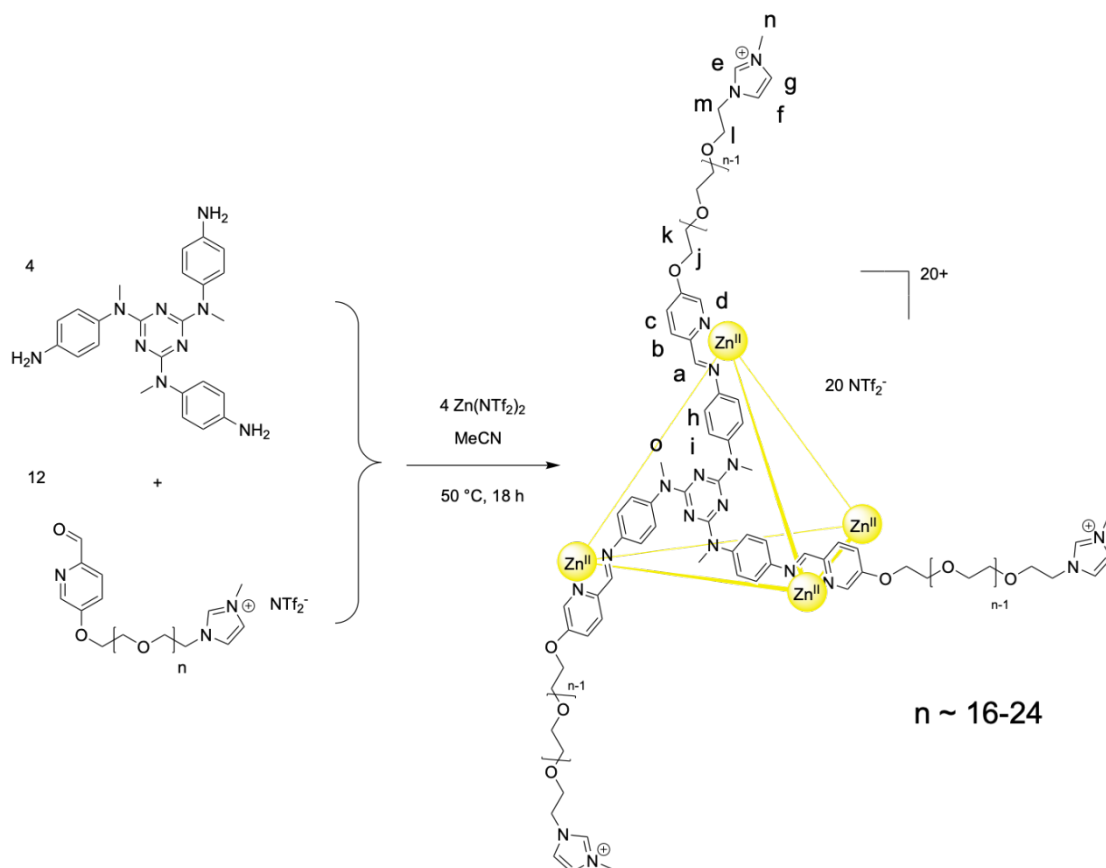
Scheme 4.4: Assembly of cage **4.3**.

This cage was assembled *via* the protocol given in Maureen Georges' dissertation.[20] N2,N4,N6-tris(4-aminophenyl)-N2,N4,N6-trimethyl-1,3,5-triazine-2,4,6-triamine (11.6 mg, 26.3 μmol), ligand **A** (115.2 mg, 79.3 μmol), and zinc (II) bistriflimide (18.4 mg, 29.4 μmol) were dissolved in distilled acetonitrile (2 mL) and stirred at 50 °C for 18 hours. The cage was precipitated with diethyl ether (10 mL), washed with further diethyl ether (2 × 10 mL), and dried under a stream of nitrogen gas to yield a dark yellow sticky liquid cage **4.3** (135.0 mg, 6.3 μmol, 96 %). ^{1}H NMR (400 MHz, CD$_3$CN, 298 K, referenced to residual solvent at 1.94 ppm) δ_H = 8.59 (s, H$_e$), 8.41 (s, H$_a$), 8.18 (d, 11 Hz, H$_b$), 7.93 (d, 10 Hz, H$_c$), 7.81 (s, H$_d$), 7.44 (m, H$_f$, H$_i$), 7.35 (s, H$_g$), 5.54 (d, 10 Hz, H$_h$), 4.33 (s, H$_j$), 4.27 (m, H$_m$), 3.84 (s, H$_m$), 3.79 (m, H$_k$, H$_l$), 3.35 – 3.75 (m, H$_o$, H$_{PEG}$).
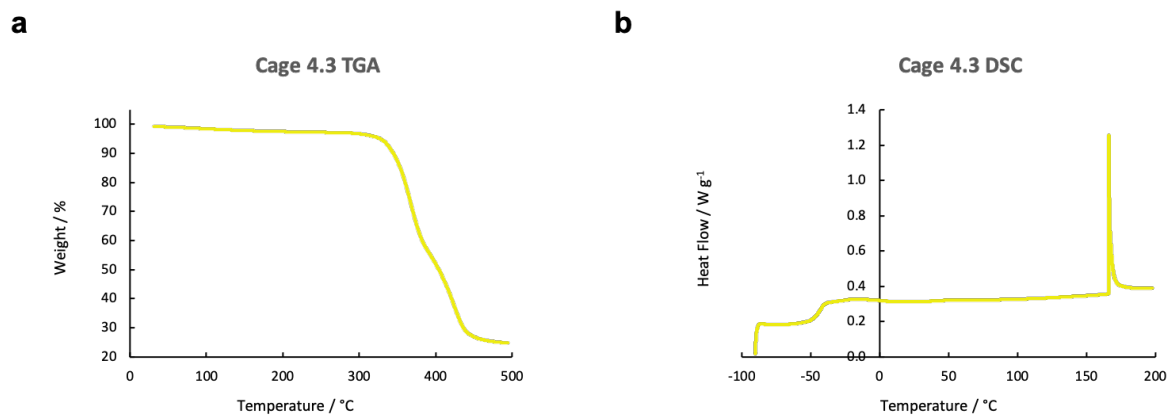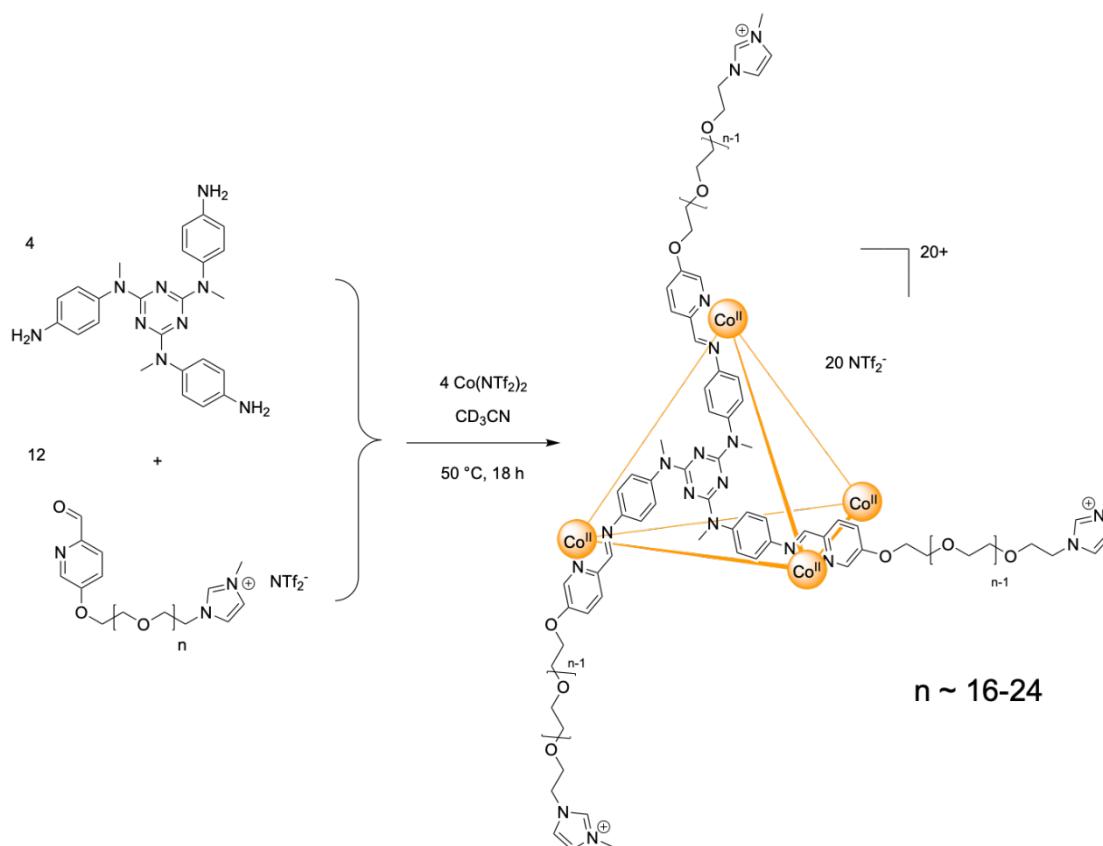
a Cage 4.3 TGA

b Cage 4.3 DSC

Figure 4.23: a) TGA profile for cage **4.3**, b) DSC profile for cage **4.3** – the exotherm at *ca.* 160 °C is likely to be an artefact only. These analyses were performed by Georgie Robertson using samples prepared by Mr Hugh Ryan.

Cage **4.4**

Scheme 4.5: Assembly of cage **4.4**.

This cage was assembled *via* the protocol given in Maureen Georges' dissertation.[20] N2,N4,N6-tris(4-aminophenyl)-N2,N4,N6-trimethyl-1,3,5-triazine-2,4,6-triamine (11.6 mg, 26.3 μmol), ligand **A** (114.3 mg, 78.8 μmol), and cobalt (II) bistriflimide[24] (18.4 mg, 28.9 μmol) were dissolved in CD$_3$CN (2 mL) and stirred at 50 °C for 18 hours. The cage was precipitated with diethyl ether (8 mL), washed with further diethyl ether (2 × 5 mL), and dried under a stream of nitrogen gas to yield a dark orange sticky liquid cage **4.4** (122.8 mg, 5.7 μmol, 87 %). ^{1}H NMR (400 MHz, CD$_3$CN, 298 K, referenced to residual solvent at 1.94 ppm) δ_H = 251.6, 107.3, 82.3, 12.3, 8.6, 7.4, 4.3, 3.3 – 3.8 (m), 3.2, 3.0, 2.7, 2.3, 1.7, 1.4, 1.2, 0.9, -0.4, -0.7, -5.0, -23.8.
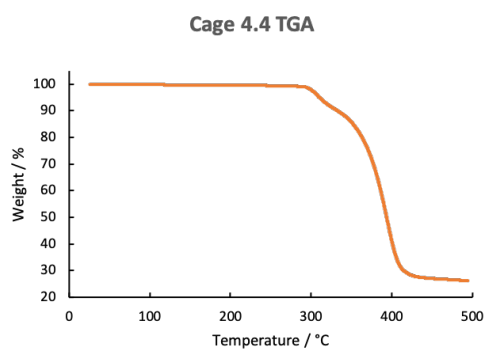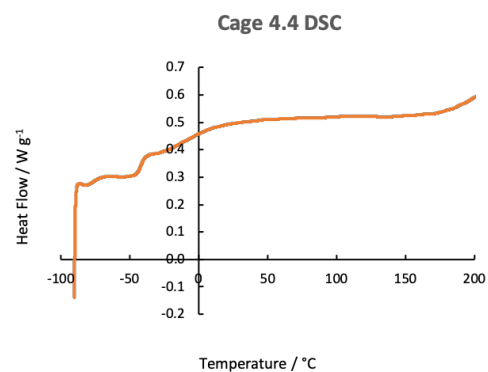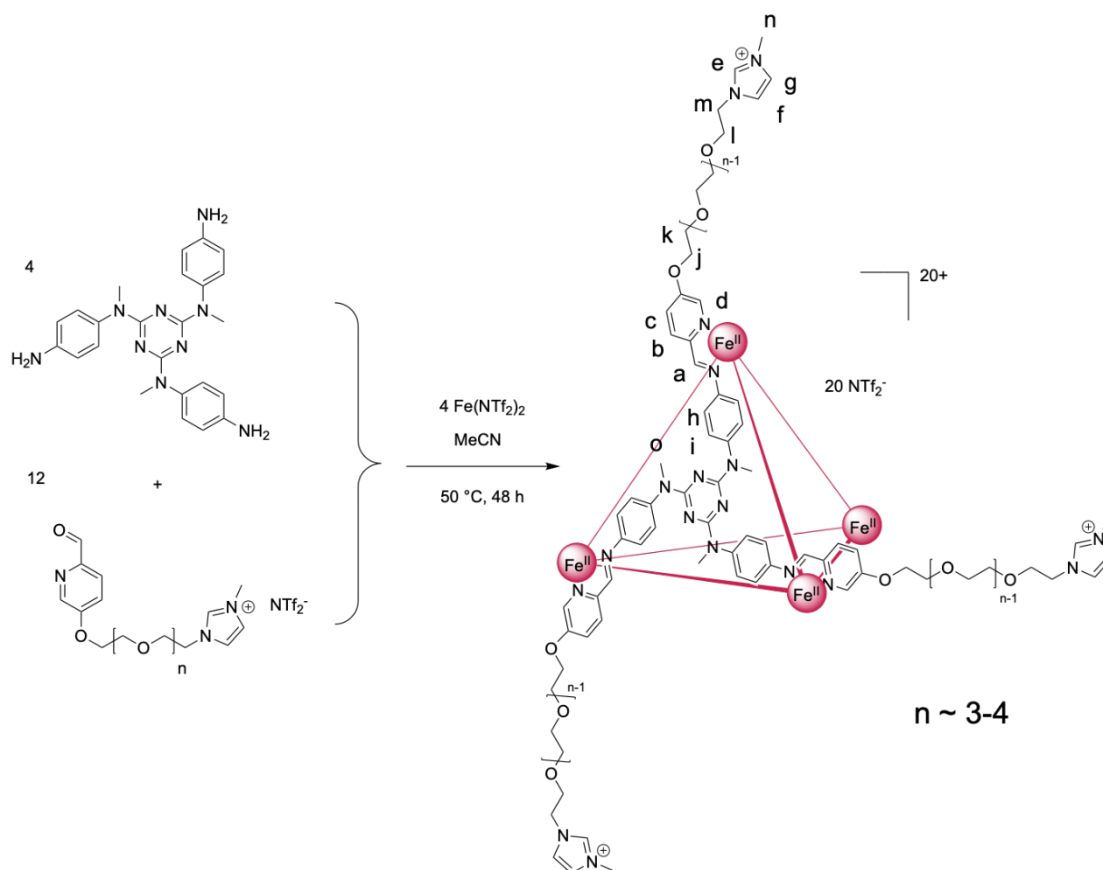
^{1}H NMR peaks are consistent with Georges' reported peaks.[20]

Figure 4.24: a) TGA profile for cage **4.4**, b) DSC profile for cage **4.4**. These analyses were performed by Georgie Robertson using samples prepared by Mr Hugh Ryan.

Cage **4.5**

Scheme 4.6: Assembly of cage **4.5**.

N2,N4,N6-tris(4-aminophenyl)-N2,N4,N6-trimethyl-1,3,5-triazine-2,4,6-triamine (13.7 mg, 31.0 μmol), ligand **B** (60.9 mg, 93.6 μmol), and iron (II) bistriflimide[24] (22.1 mg, 31.7 μmol) were dissolved in distilled acetonitrile (2 mL) and stirred at 50 °C for 48 hours. The cage was precipitated with diethyl ether (10 mL), washed with further diethyl ether (2 × 10 mL), and dried under a stream of nitrogen gas to yield a dark red glassy cage **4.5** (86.9 mg, 7.4 μmol, 95 %). ^{1}H NMR (400 MHz, CD$_3$CN, 298 K, referenced to residual solvent at 1.94 ppm) δ_H = 8.70 (s, H$_a$), 8.45 (m, H$_b$, H$_e$), 7.84 (m, H$_c$), 7.36 (m, H$_f$, H$_g$, H$_i$), 7.00 (s, H$_d$), 5.08 (bs, H$_h$), 4.26 (m, H$_j$, H$_m$), 3.94 (s, H$_n$), 3.35 – 3.75 (m, H$_k$, H$_l$, H$_o$, H$_{PEG}$). ^{19}F NMR (400 MHz, CD$_3$CN, 298 K, referenced to hexafluorobenzene at -162.9 ppm) δ_F = -74.0 (bound NTf$_2^-$), -79.1 (free NTf$_2^-$).
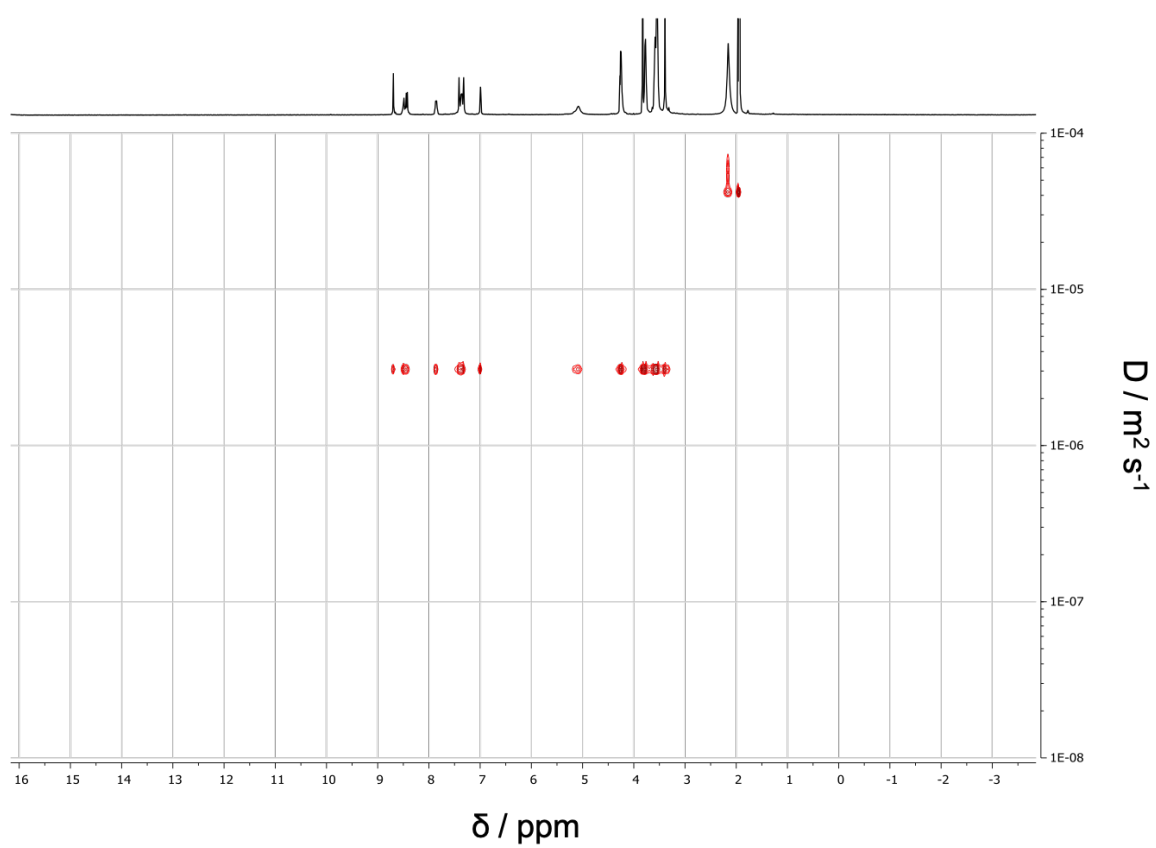
Figure 4.25: DOSY spectrum of cage **4.5** in CD₃CN (298 K, 400 MHz), D ~ 3.1 × 10⁻⁶ m²
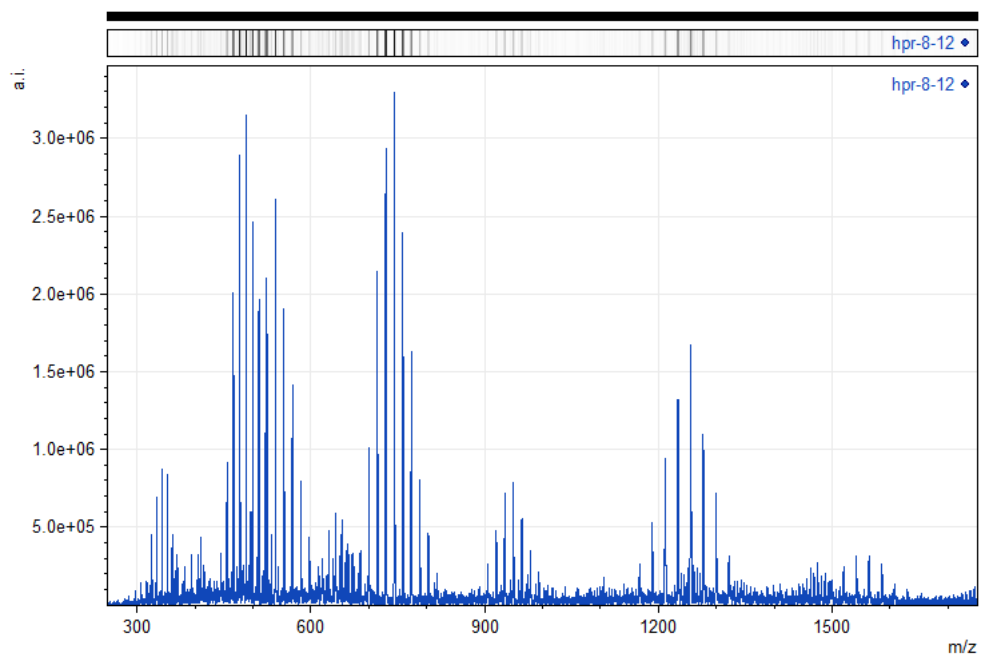s⁻¹.

Figure 4.26: Low-resolution mass spectrum of cage **4.5**. Data collected by Ms Zifei Lu and Mr Samuel Clark, using a sample prepared by Mr Hugh Ryan, on a Micromass Quattro LC.
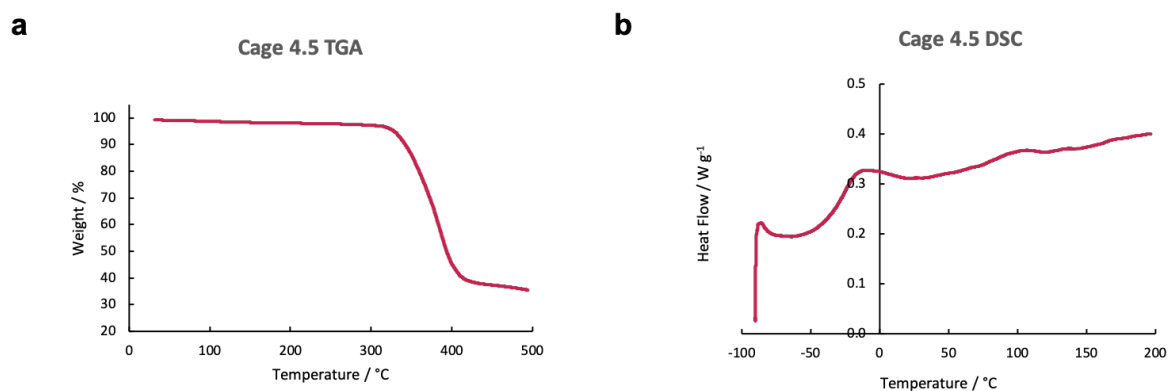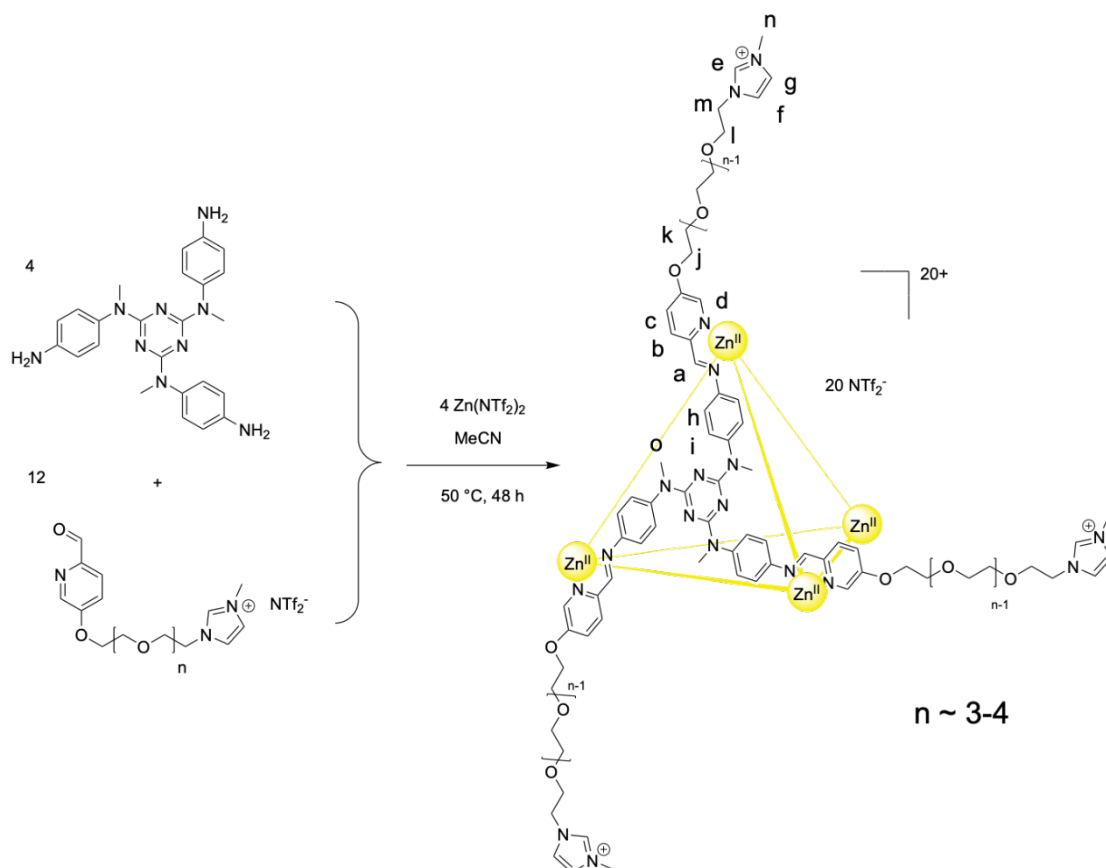

Figure 4.27: a) TGA profile for cage **4.5**, b) DSC profile for cage **4.5**. These analyses were performed by Georgie Robertson using samples prepared by Mr Hugh Ryan.

Cage **4.6**

Scheme 4.7: Assembly of cage **4.6**.

N2,N4,N6-tris(4-aminophenyl)-N2,N4,N6-trimethyl-1,3,5-triazine-2,4,6-triamine (13.8 mg, 31.3 µmol), ligand **B** (62.7 mg, 96.8 µmol), and zinc (II) bistriflimide (21.0 mg, 33.6 µmol) were dissolved in distilled acetonitrile (2 mL) and stirred at 50 °C for 48 hours. The cage was precipitated with diethyl ether (10 mL), washed with further diethyl ether (2 × 10 mL), and dried under a stream of nitrogen gas to yield a dark yellow glassy cage **4.6** (82.0 mg, 6.9 µmol, 88 %). ^{1}H NMR (400 MHz, CD$_3$CN, 298 K, referenced to residual solvent at 1.94 ppm) δ_H = 8.49 (bs, H$_e$), 8.43 (s, H$_a$), 8.18 (d, 9 Hz, H$_b$), 7.90 (d, 9 Hz, H$_c$), 7.78 (s, H$_d$), 7.44 (m, H$_f$, H$_i$), 7.32 (s, H$_g$), 5.53 (d, 8 Hz, H$_h$), 4.30 (s, H$_j$), 4.26 (m, H$_m$), 3.95 (s, H$_n$), 3.35 – 3.75 (m, H$_k$, H$_l$, H$_o$, H$_{PEG}$). ^{19}F NMR (400 MHz, CD$_3$CN, 298 K, referenced to hexafluorobenzene at -162.9 ppm) δ_F = -75.1 (bound NTf$_2^-$), -79.1 (free NTf$_2^-$).
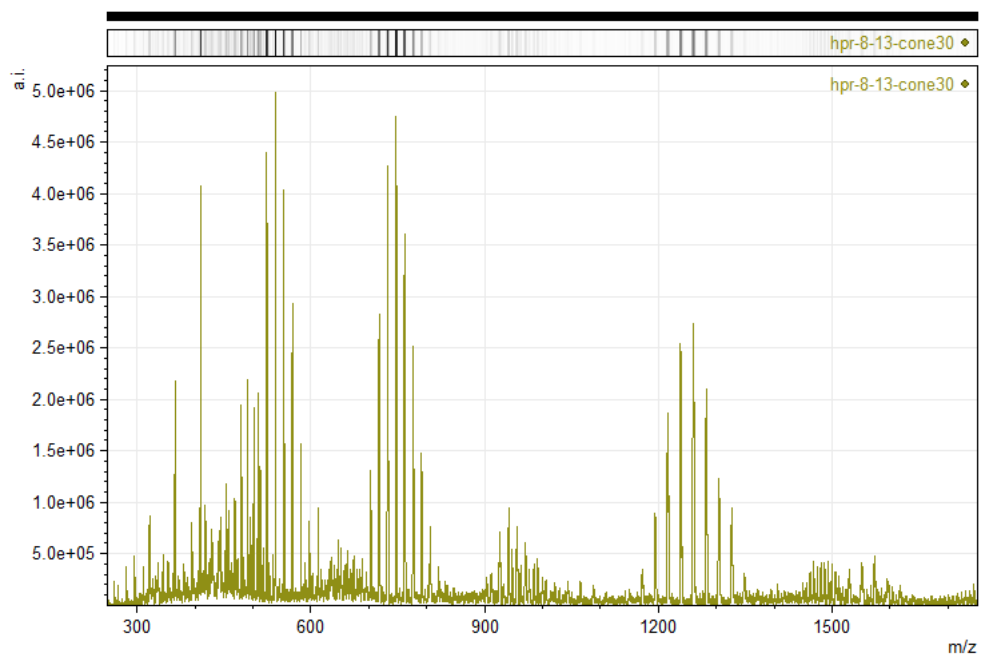
Figure 4.28: Low-resolution mass spectrum of cage **4.6**. Data collected by Ms Zifei Lu and Mr Samuel Clark, using a sample prepared by Mr Hugh Ryan, on a Micromass Quattro LC.

Figure 4.29: a) TGA profile for cage **4.6**, b) DSC profile for cage **4.6**. These analyses were performed by Georgie Robertson using samples prepared by Mr Hugh Ryan.

Cage **4.7**
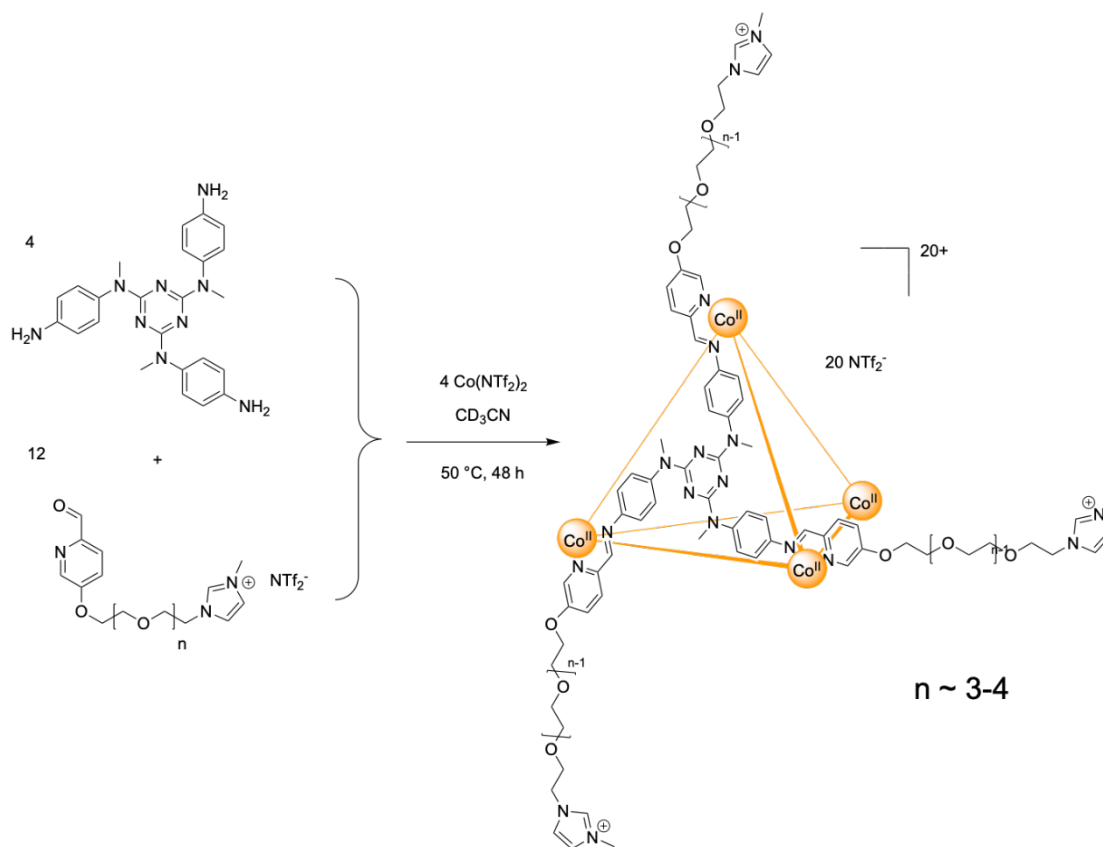
Scheme 4.8: Assembly of cage **4.7**.

N2,N4,N6-tris(4-aminophenyl)-N2,N4,N6-trimethyl-1,3,5-triazine-2,4,6-triamine (13.7 mg, 31.0 μmol), ligand **B** (60.4 mg, 92.8 μmol), and cobalt (II) bistriflimide[24] (20.8 mg, 32.6 μmol) were dissolved in distilled acetonitrile (2 mL) and stirred at 50 °C for 48 hours. The cage was precipitated with diethyl ether (10 mL), washed with further diethyl ether (2 × 10 mL), and dried under a stream of nitrogen gas to yield a dark orange glassy cage **4.7** (75.0 mg, 6.3 μmol, 82 %). ^{1}H NMR (400 MHz, CD$_3$CN, 298 K, referenced to residual solvent at 1.94 ppm) δ_H = 252.4, 106.0, 81.6, 12.4, 8.5, 8.3, 8.1, 7.2, 3.0 – 5.0 (m), 2.8, 2.5, 2.2, 0.8 – 2.0 (m), -0.4, -0.7, -0.8, -5.0, -23.7. ^{19}F NMR (400 MHz, CD$_3$CN, 298 K, referenced to hexafluorobenzene at -162.9 ppm) δ_F = -78.1 (free NTf$_2^-$), -100.6 (bound NTf$_2^-$).

^{1}H NMR peaks are broadly consistent with those observed for cage **4.4**.

Figure 4.30: Low-resolution mass spectrum of cage **4.7**. Data collected by Ms Zifei Lu and Mr Samuel Clark, using a sample prepared by Mr Hugh Ryan, on a Micromass Quattro LC.
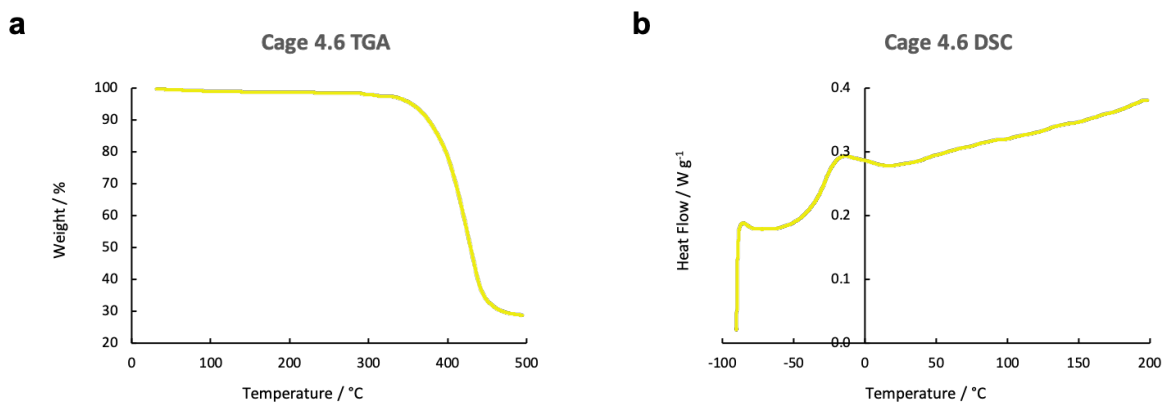

Figure 4.31: a) TGA profile for cage **4.7**, b) DSC profile for cage **4.7**. These analyses were performed by Georgie Robertson using samples prepared by Mr Hugh Ryan.

Cage **4.8**
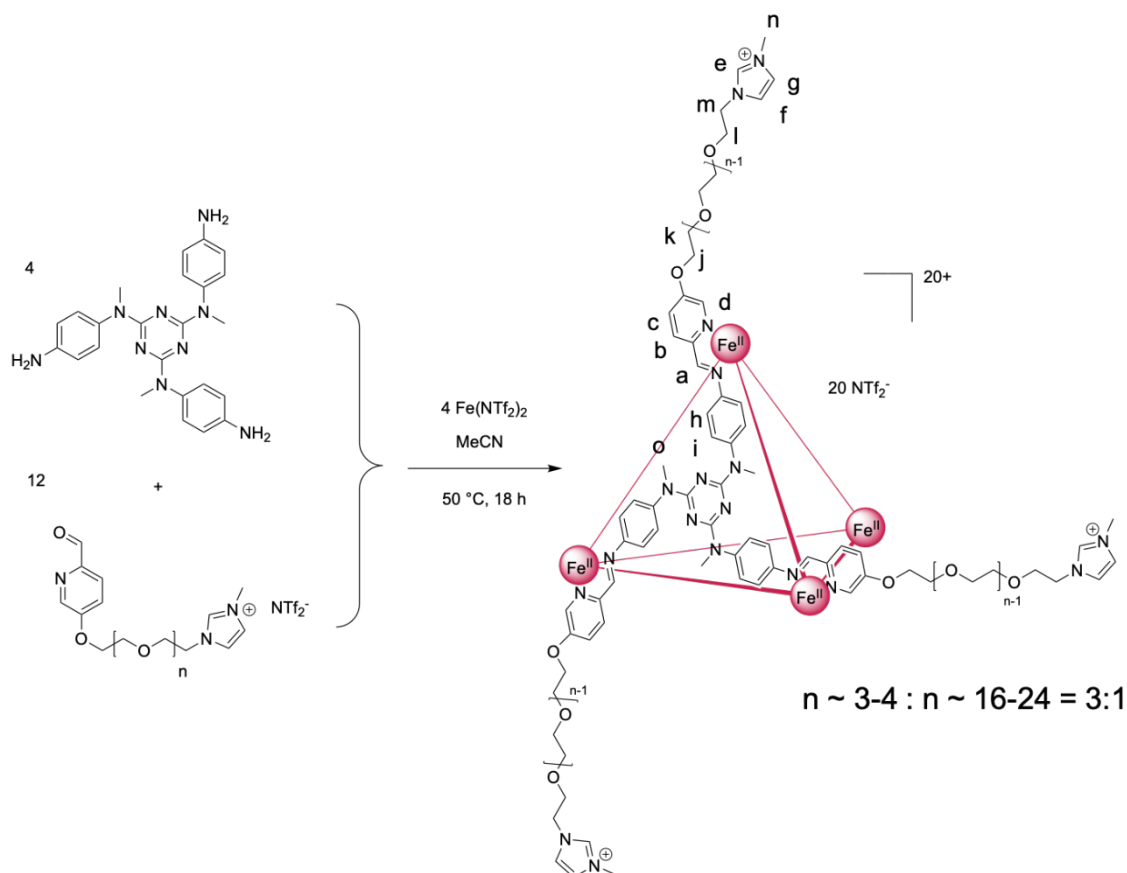
Scheme 4.9: Assembly of cage **4.8**.

N2,N4,N6-tris(4-aminophenyl)-N2,N4,N6-trimethyl-1,3,5-triazine-2,4,6-triamine (11.8 mg, 26.7 µmol), ligand **A** (28.7 mg, 19.8 µmol), ligand **B** (39.9 mg, 61.3 µmol), and iron (II) bistriflimide[24] (18.8 mg, 27.0 µmol) were dissolved in distilled acetonitrile (2 mL) and stirred at 50 °C for 18 hours. The cage was precipitated with diethyl ether (10 mL), washed with further diethyl ether (2 × 10 mL), and dried under a stream of nitrogen gas to yield a dark red sticky liquid cage **4.8** (91.0 mg, 7.7 µmol, quantitative). ^{1}H NMR (400 MHz, CD$_3$CN, 298 K, referenced to residual solvent at 1.94 ppm) δ_H = 8.70 (s, H$_a$), 8.58 (s, H$_e$), 8.47 (m, H$_b$), 7.88 (bs, H$_c$), 7.30 – 7.40 (m, H$_f$, H$_g$, H$_i$), 7.00 (bs, H$_d$), 5.09 (bs, H$_h$), 4.27 (m, H$_j$, H$_m$), 3.35 – 3.85 (m, H$_k$, H$_l$, H$_n$, H$_o$, H$_{PEG}$).
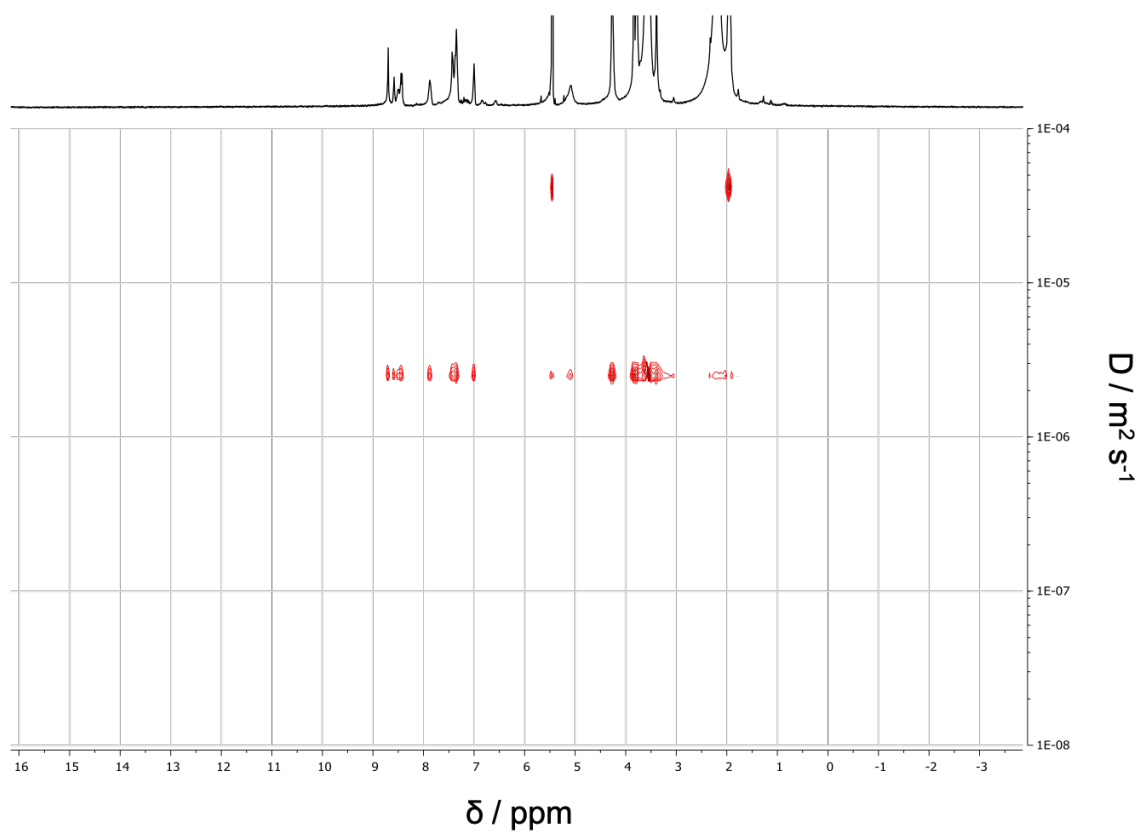
Figure 4.32: DOSY spectrum of cage **4.8** in CD_3CN (298 K, 400 MHz), D ~ 2.5×10^{-6} m^2 s^{-1}.
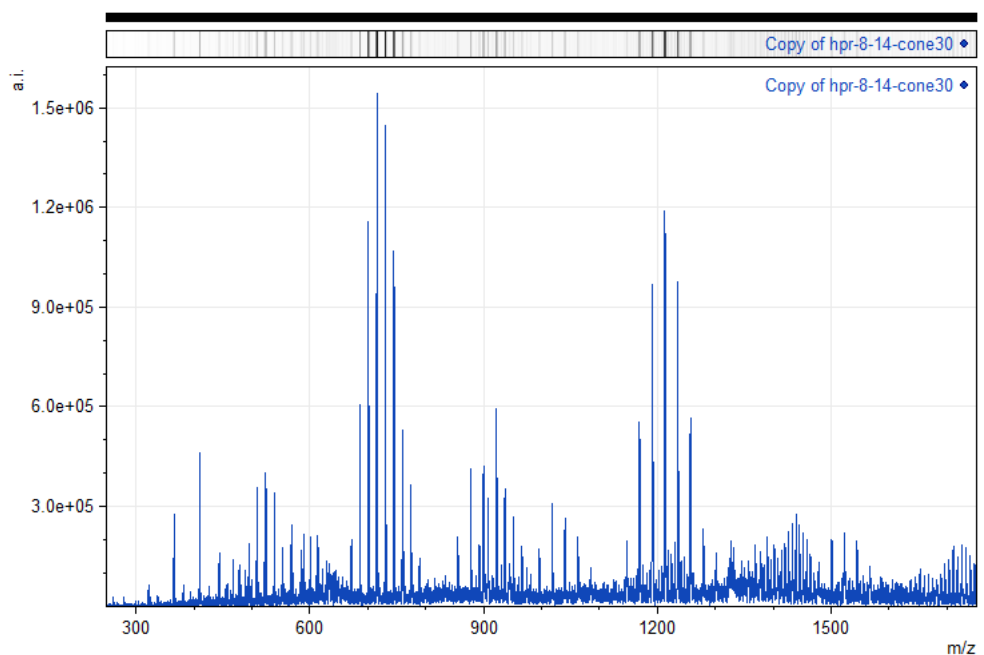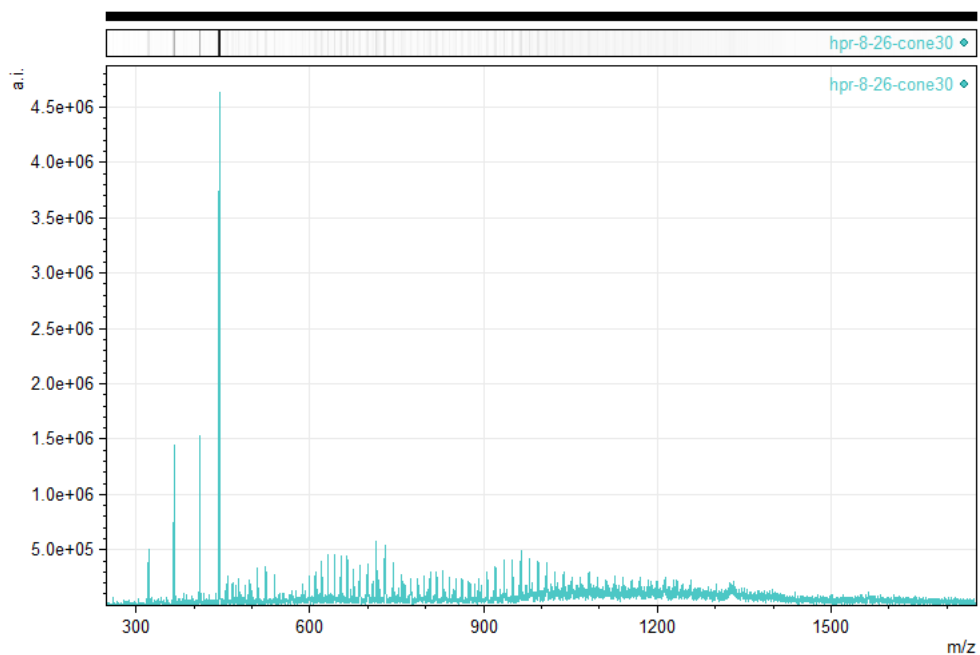
Figure 4.33: Low-resolution mass spectrum of cage **4.8**. Data collected by Ms Zifei Lu and Mr Samuel Clark, using a sample prepared by Mr Hugh Ryan, on a Micromass Quattro LC.
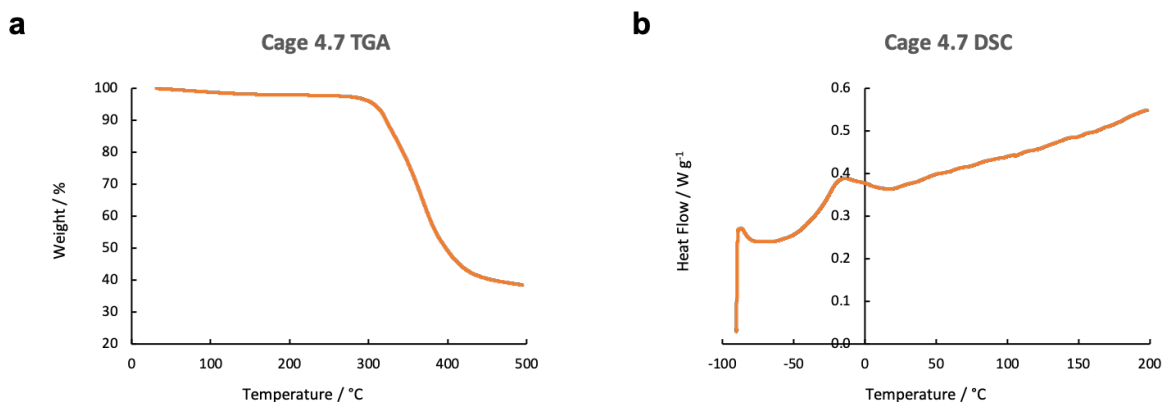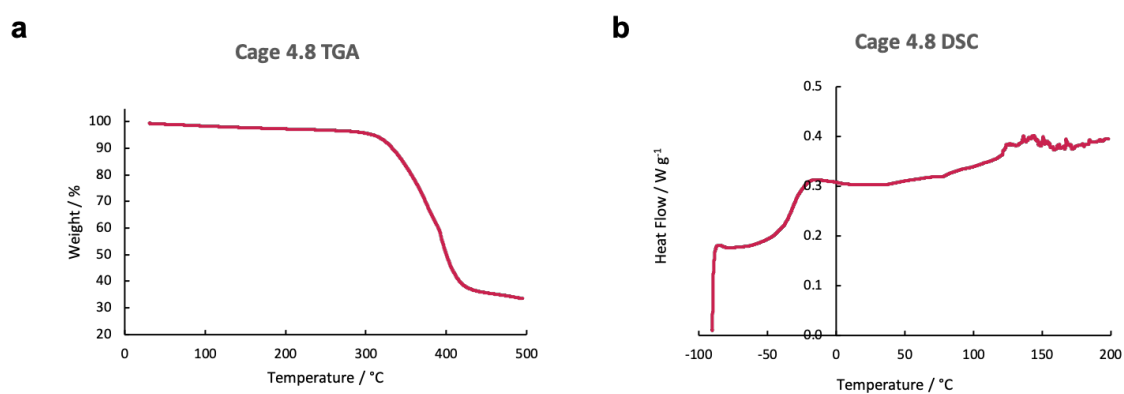

Figure 4.34: a) TGA profile for cage **4.8**, b) DSC profile for cage **4.8**. These analyses were performed by Georgie Robertson using samples prepared by Mr Hugh Ryan.

4.4.3 Solution-Phase Host-Guest Chemistry
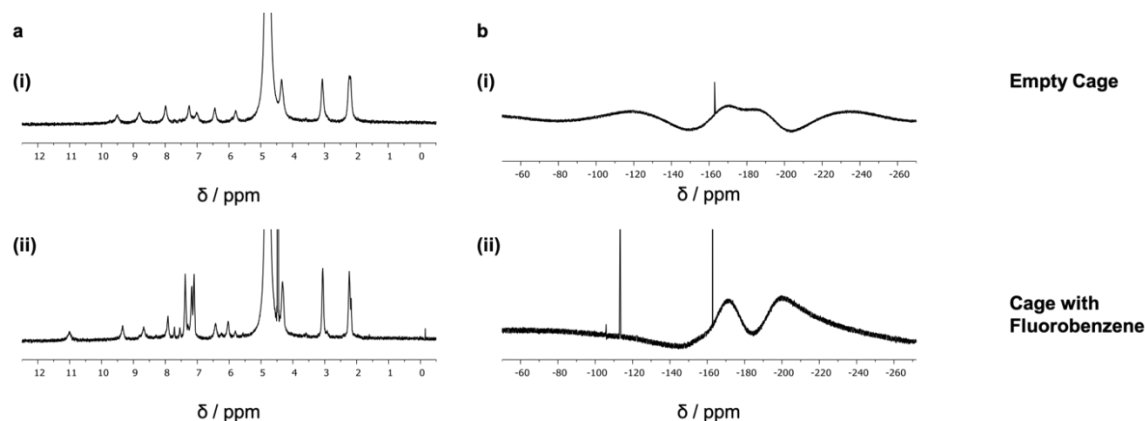
Figure 4.35: a) ^{1}H NMR (500 MHz, D$_2$O, 298 K); i) Cage **4.1**, ii) Cage **4.1** with fluorobenzene, b) ^{19}F NMR (D$_2$O, 298K); Cage **4.1** (400 MHz) - -162.9 (hexafluorobenzene reference), ii) Cage **4.1** with fluorobenzene (500 MHz) – -105.8 (bound fluorobenzene), -113.3 (free fluorobenzene), -162.9 (hexafluorobenzene reference). Shifts in ppm.
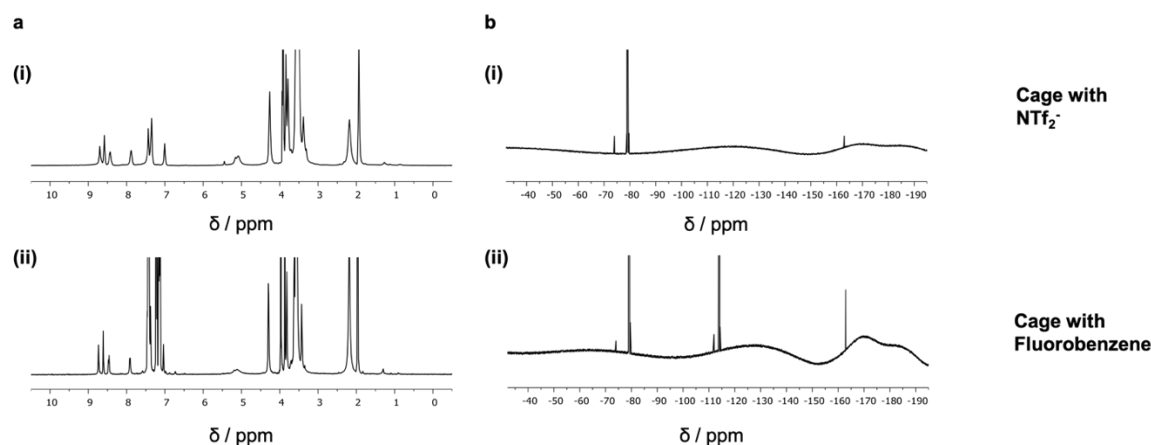
Figure 4.36: a) ^{1}H NMR (CD$_3$CN, 298 K); i) Cage **4.2** (400 MHz), ii) Cage **4.2** with fluorobenzene (500 MHz), b) ^{19}F NMR (CD$_3$CN, 298K); Cage **4.2** (400 MHz) – -74.0 (bound NTf$_2^-$), -79.1 (free NTf$_2^-$), -162.9 (hexafluorobenzene reference), ii) Cage **4.2** with fluorobenzene (500 MHz) – -74.0 (bound fluorobenzene), -79.1 (free fluorobenzene), -111.93 (bound fluorobenzene), -113.93 (free fluorobenzene), -162.9 (hexafluorobenzene reference). Shifts in ppm.
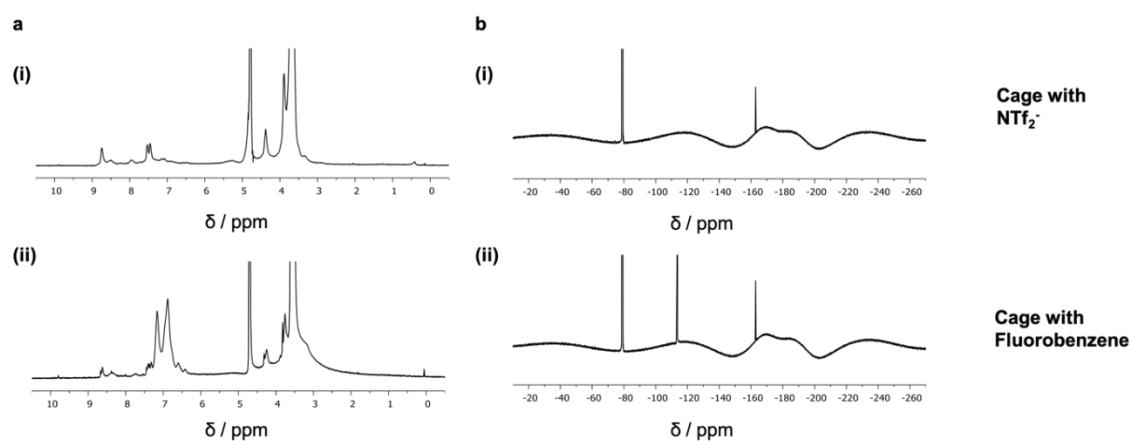
Figure 4.37: a) ^{1}H NMR (D$_2$O, 298 K); i) Cage **4.2** (400 MHz), ii) Cage **4.2** with fluorobenzene (500 MHz), b) ^{19}F NMR (400 MHz, D$_2$O, 298K); Cage **4.2** – -74.9 (bound NTf$_2^-$), -79.0 (free NTf$_2^-$), -162.9 (hexafluorobenzene reference), ii) Cage **4.2** with fluorobenzene – -79.0 (free NTf$_2^-$), -113.5 (free fluorobenzene), -162.9 (hexafluorobenzene reference). Shifts in ppm.

4.4.4 Cage Salt Formation

Cage **4.1** (5.8 mg, ~ 0.82 µmol) in water (1 mL) was added to cage **4.2** (16.3 mg, ~ 0.76 µmol) in methanol (1 mL) and the resulting mixture was washed with ethyl acetate (3 × 10 mL) and then dried under a stream of nitrogen gas to yield flaky red solid salt [**4.1**]$_5$•[**4.2**]$_4$ (16.4 mg, ~ 0.19 µmol, approximately quantitative). ^{1}H NMR (400 MHz, D$_2$O, 298 K, referenced to residual solvent at 4.79 ppm) δ_H = 9.27 (bs), 8.84 (bs), 8.75 (bs), 7.93 (bs), 7.78 (bs), 7.53 (bs), 7.44 (bs), 6.43 (bs), 5.83 (bs), 4.39 (bs), 4.14 (bs), 3.89 (bs), 3.35 – 3.75 (m), 3.06 (bs), 2.95 (bs), 2.07 (bs), 1.24 (bs).

DSC and TGA data for [**4.1**]$_5$•[**4.2**]$_4$ are provided in Section 4.2.4.

4.4.5 Miscellaneous
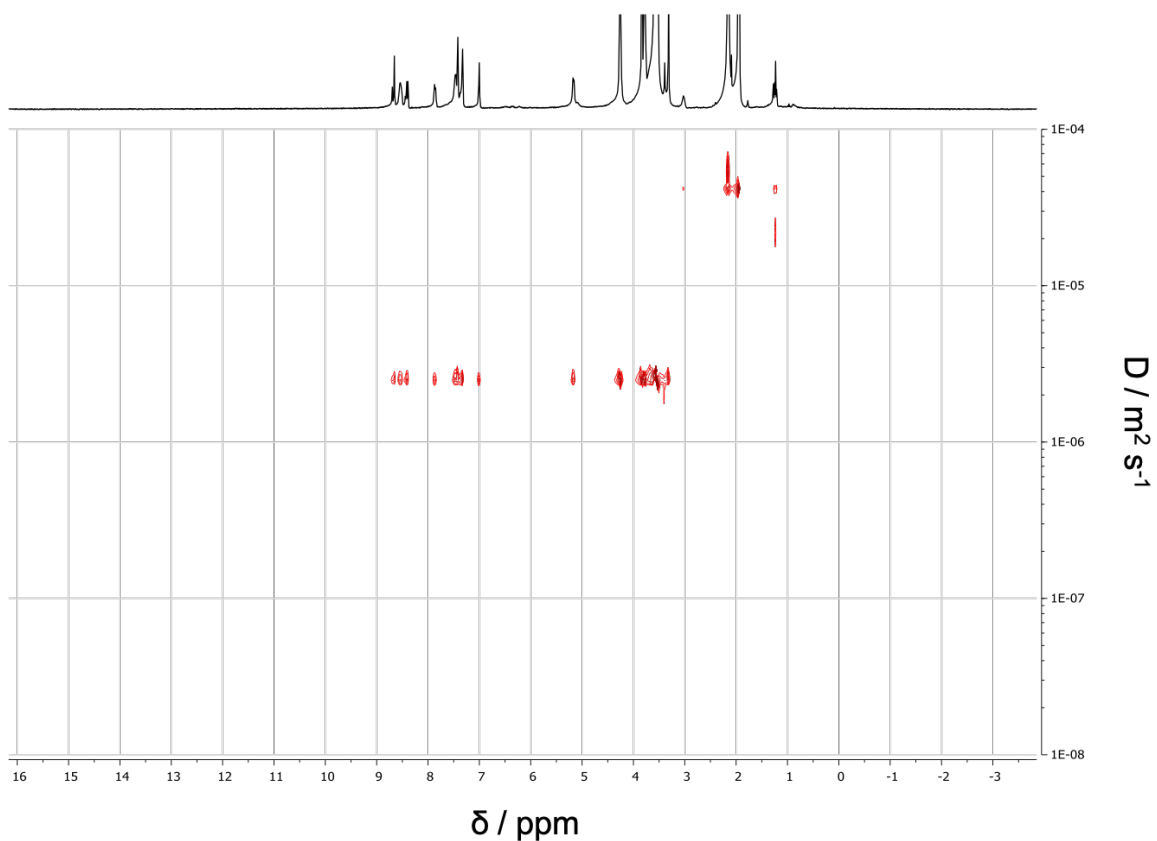
Figure 4.38: DOSY spectrum of Besenyöi's iron (II) cage **4.9** assembled with poly(ethylene glycol) chains of ~ 400 g mol^{-1} in CD$_3$CN (298 K, 400 MHz), D ~ 2.6 × 10^{-6} m^2 s^{-1}. Data collected by Mr Hugh Ryan using a sample prepared by Mr Dani Besenyöi.

Figure 4.39: Low-resolution mass spectrum of Besenyöi's iron (II) cage **4.9** assembled with poly(ethylene glycol) chains of ~ 400 g mol^{-1}. Data collected by Ms Zifei Lu and Mr Samuel Clark, using a sample prepared by Mr Dani Besenyöi, on a Micromass Quattro LC.

4.5 References

1. O'Reilly, N., Giri, N. & James, S. L. Porous Liquids. *Chemistry - A European Journal* **13**, 3020–3025 (2007).

2. Giri, N. *et al.* Alkylated organic cages: From porous crystals to neat liquids. *Chemical Science* **3**, 2153–2157 (2012).

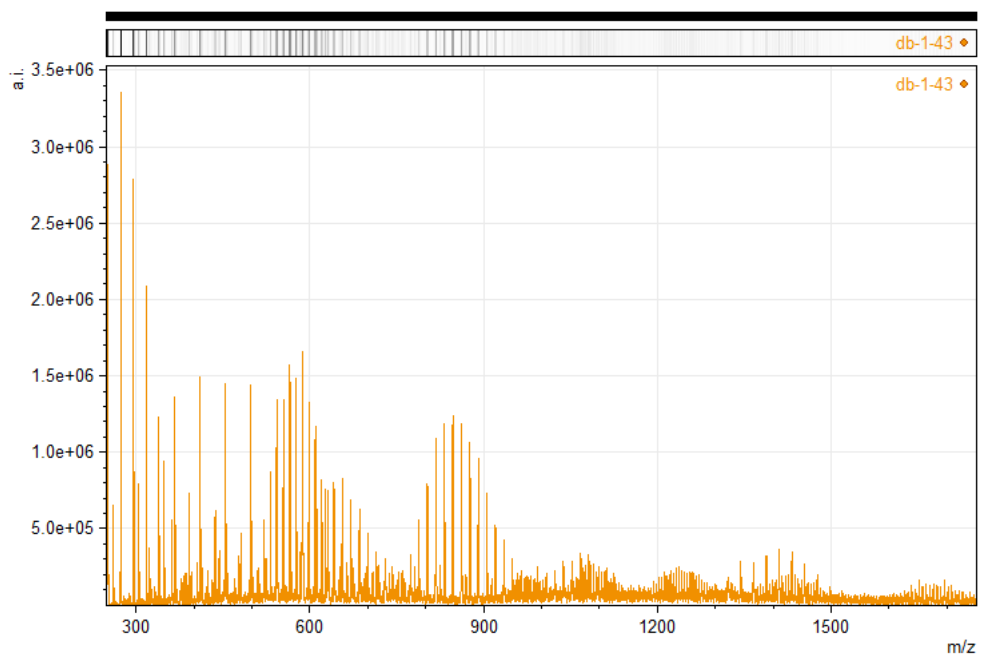3. Tozawa, T. *et al.* Porous organic cages. *Nature Materials* **8**, 973–978 (2009).

4. Chhabra, R. P. Non-Newtonian fluids: An introduction. in *Rheology of Complex Fluids* 3–34 (Springer New York, 2010). doi:10.1007/978-1-4419-6494-6_1.

5. Melaugh, G., Giri, N., Davidson, C. E., James, S. L. & del Pópolo, M. G. Designing and understanding permanent microporosity in liquids. *Physical Chemistry Chemical Physics* **16**, 9422–9431 (2014).

6. Zhang, J. *et al.* Porous liquids: A promising class of media for gas separation. *Angewandte Chemie International Edition* **54**, 932–936 (2015).

7. Jie, K. *et al.* Transforming Porous Organic Cages into Porous Ionic Liquids via a Supramolecular Complexation Strategy. *Angewandte Chemie International Edition* **59**, 2268–2272 (2020).

8. Giri, N. *et al.* Liquids with permanent porosity. *Nature* **527**, 216–220 (2015).

9. Tao, S. J. Positronium annihilation in molecular substances. *The Journal of Chemical Physics* **56**, 5499–5510 (1972).

10. Eldrup, M., Lightbody, D. & Sherwood, J. N. The temperature dependence of positron lifetimes in solid pivalic acid. *Chemical Physics* **63**, 51–58 (1981).

11. Ma, L. *et al.* Coordination cages as permanently porous ionic liquids. *Nature Chemistry* **12**, 270–275 (2020).

12. Jiménez, A. *et al.* Selective Encapsulation and Sequential Release of Guests Within a Self-Sorting Mixture of Three Tetrahedral Cages. *Angewandte Chemie International Edition* **53**, 4556–4560 (2014).

13. Kearsey, R. J., Alston, B. M., Briggs, M. E., Greenaway, R. L. & Cooper, A. I. Accelerated robotic discovery of type II porous liquids. *Chemical Science* **10**, 9454–9465 (2019).

14. Liu, H. *et al.* A hybrid absorption-adsorption method to efficiently capture carbon. *Nature Communications* **5**, (2014).

15. Shan, W. *et al.* New Class of Type III Porous Liquids: A Promising Platform for Rational Adjustment of Gas Sorption Behavior. *ACS Applied Materials and Interfaces* **10**, 32–36 (2018).

16. Liu, S. *et al.* Porous Liquid: A Stable ZIF-8 Colloid in Ionic Liquid with Permanent Porosity. *Langmuir* **34**, 3654–3660 (2018).

17. Costa Gomes, M., Pison, L., Červinka, C. & Padua, A. Porous Ionic Liquids or Liquid Metal-Organic Frameworks? *Angewandte Chemie International Edition* **57**, 11909–11912 (2018).

18. Gosselin, E. J. *et al.* A Charged Coordination Cage-Based Porous Salt. *Journal of the American Chemical Society* **142**, 9594–9598 (2020).

19. Ma, L. Coordination Cages as a Scaffold for Permanently Porous Liquids. (2019).

20. Georges, M. Reversible Directed Phase Transfer of $M_4^{II}L_4$ and $M_4^{II}L_6$ Cages. (2017).

21. Nguyen, B.-N. T., Grommet, A. B., Tron, A., Georges, M. C. A. & Nitschke, J. R. Heat Engine Drives Transport of an $Fe^{II}_4L_4$ Cage and Cargo. *Advanced Materials* **32**, 1907241 (2020).

22. Besenyői, D. Thermal Properties of PEG-imidazolium Functionalised Liquid Coordination Cages. (2020).

23. López-Martin, I., Burello, E., Davey, P. N., Seddon, K. R. & Rothenberg, G. Anion and Cation Effects on Imidazolium Salt Melting Points: A Descriptor Modelling Study. *ChemPhysChem* **8**, 690–695 (2007).

24. Sibi, M. P. & Petrovic, G. Enantioselective radical reactions: The use of metal triflimides as Lewis acids. *Tetrahedron Asymmetry* **14**, 2879–2882 (2003).

Chapter 5: Concluding Remarks

Metal-organic coordination cages of many geometries and sizes have been reported in the literature. Such species have been shown to encapsulate a wide range of molecular guests and these encapsulation phenomena have facilitated the application of coordination cages in areas such as chemical separations and catalysis. To-date, the literature contains many studies of coordination cages in the solution state but comparatively fewer examples of coordination cages in condensed phases. The objectives of this thesis have been to investigate the use of coordination cages adsorbed on solid supports and coordination cages as neat liquids.

Chapter 3 studied the adsorption of two previously reported coordination cages on activated alumina from both aqueous and organic media. A series of guest displacement experiments demonstrated that the cages adsorbed from water retained their ability to bind and release guest species. The host-guest chemistry of the adsorbed cages was then used to achieve a simple chemical separation and to spatially separate a pair of Diels-Alder components prior to their subsequent release and reaction. This study presents an early step in the development the application of coordination cages on solid phases and establishes a foundation from which future studies can progress. The development of catalytically-active coordination cages continues to be an area of active interest and hence future studies of adsorbed cages might include the translation of homogenous catalysis within coordination cages into heterogeneous catalysis; it is the opinion of this author that the heterogeneous catalysis described above is perhaps both the most challenging and exciting direction for this work and may lead to industrially-relevant applications, if suitable cage candidates can be found.

Chapter 4 presented the investigation to-date of a new generation of liquid/glass-like coordination cages. The main focus of this chapter was the formation of a new porous ionic liquid, *via* ion metathesis, in which both ionic components are coordination cages. The characterisation of the materials formed herein suggests that the ion metathesis approach adopted is successful in forming cage salt materials but the current salt material is a flaky, glassy solid, by inspection. The next step in the development of the liquid cage salt is likely to be the tuning of the peripheral polymer chains to engender fluidity; if such tuning is successful in forming a liquid material, the resulting porous liquid would, to this author's knowledge, be the first example of a single-component Type I porous liquid in which there are two distinguishable pores. This liquid cage salt would, therefore, represent a significant

advance in the development of porous liquids. Many of the porous liquids reported in the literature have only focussed on the binding of gaseous guests; in contrast, the known host-guest chemistry of coordination cages suggests this liquid cage salt would be expected to bind guests in condensed phases, as well as gaseous guests, thereby increasing its scope for future applications.

As the number of reported coordination cages continues to grow one might expect the demand for new applications of coordination cages to increase. In combination, these research chapters have demonstrated that the utility of coordination cages extends to solid and neat liquid phases and thus future studies and applications of coordination cages need not be limited to the solution state.

Appendix

Isotherm Theory

Langmuir Model

An adsorption isotherm relates the quantity of material adsorbed on a given surface to the quantity of material in the bulk phase. One of the earliest models of adsorption was developed by Irving Langmuir for the adsorption of gases on plane surfaces.[1,2] Langmuir made the following assumptions in his basic model:

1. The surface consists of a finite number of identical adsorption sites.
2. Adsorption exhibits no cooperativity, *i.e.* the occupation of one site does not affect the occupation of another site.
3. Adsorption sites can, at most, be singly occupied, *i.e.* binary site occupation.

Under these assumptions, the Langmuir model of adsorption has the following form:

$$\theta = \theta_{\text{MAX}} \frac{bP}{1+bP} \qquad \text{(A1)}$$

In which θ is the surface coverage, θ_{MAX} is the surface coverage at saturation, b is a thermal constant, and P is the gas pressure.

Equation A1 indicates that, initially ($bP << 1$), the surface coverage increases quasi-linearly with gas pressure. As the gas pressure continues to increase ($bP >> 1$), however, the surface coverage plateaus at θ_{MAX}. The determination of an adsorption isotherms therefore yields the surface coverage for a given gas pressure in contact with the surface and the maximal surface coverage. Equation A1 can be neatly derived within the grand canonical ensemble, *i.e.* a system which is able to exchange both particles and energy with its surroundings. Consider a surface of M identical sites on which N particles are adsorbed with an energy $-\varepsilon$ per adsorbed particle:

$$\Xi(N,V,T) = \sum_N \sum_i \exp(-\beta E_i) \exp(\beta\mu N) \qquad \text{(A2)}$$

In which $\varXi$ is the grand partition function, V is the system volume, T is the system temperature, β is the inverse of thermal energy, E_i is the energy of microstate i, and μ is the chemical potential.

A2 can be explicitly computed, however, by recognising that, for a given value of N, the sum over microstates i can be evaluated as $^{M}C_N$, *i.e.* a binomial factor, thus:

$$\Xi(N, V, T) = \sum_N \frac{M!}{N!(M-N)!} \exp\left(\beta N(\mu + \varepsilon)\right) \qquad (A3)$$

$$\Xi(N, V, T) = (1 + \exp\left(\beta N(\mu + \varepsilon)\right))^M \qquad (A4)$$

The expectation value of N, $<N>$, is then:

$$<N> = \frac{\partial \ln\Xi}{\partial \beta\mu} = M \frac{exp(\beta(\mu+\varepsilon))}{1 + exp(\beta(\mu+\varepsilon))} \qquad (A5)$$

The pressure of an ideal gas has the following dependence on the chemical potential:

$$P \sim \exp(\beta\mu) \qquad (A6)$$

Combining A5 and A6:

$$<N> = M \frac{exp(\beta\varepsilon)P}{1 + exp(\beta\varepsilon)\,P} \qquad (A7)$$

Finally, note that equations A1 and A7 have the same functional form and thus the Langmuir model has been derived from statistical mechanics.

Brunauer-Emmett-Teller (BET) Model

The Langmuir model derived in the previous section predicts that the adsorbed gaseous species forms a surface monolayer in the limit of high pressure, *i.e.* all surface adsorption sites are occupied by a single adsorbate. A later model by Brunauer, Emmett, and Teller extended the Langmuir model to the formation of adsorbed multilayers, *i.e.* further adsorption on the surface monolayer.[3] Consider a surface consisting of sub-regions s_i on which there are i layers of adsorbate. At equilibrium, s_i must be constant for all i, thus the following are true:

$$a_1 p s_0 = b_1 s_1 \exp\left(\frac{-E_1}{RT}\right) \qquad \text{(A8)}$$

$$a_2 p s_1 + b_1 s_1 \exp\left(-\frac{E_1}{RT}\right) = b_2 s_2 \exp\left(\frac{-E_2}{RT}\right) + a_1 p s_0 \qquad \text{(A9)}$$

In which p is the gas pressure, E_i is the heat of adsorption of the i'th layer, and a_i and b_i are constants.

Equation A8 states that, at equilibrium, the rate of deposition on to the bare surface (LHS) must be equal to the rate of desorption from the first layer (RHS). Equation A9 is extends this to say that the sum of the rates of deposition and desorption on to/from the first layer (LHS) must be equal to the sum of the rates of deposition on to the bare surface and desorption from the second layer (RHS). The insertion of A8 into A9 (blue) reduces A9 to A10:

$$a_2 p s_1 = b_2 s_2 \exp\left(\frac{-E_2}{RT}\right) \qquad \text{(A10)}$$

Extending these arguments to the general case, the following is true:

$$a_i p s_{i-1} = b_i s_i \exp\left(\frac{-E_i}{RT}\right) \qquad \text{(A11)}$$

The total area of the surface, A, is:

$$A = \sum_{i=0}^{\infty} s_i \qquad \text{(A12)}$$

The total volume of gas adsorbed, v, is:

$$v = v_0 \sum_{i=0}^{\infty} i s_i \qquad \text{(A13)}$$

In which v_0 is the volume of gas per unit surface area when the adsorbed gas forms a monolayer.

The total volume of gas adsorbed, relative to the volume of gas in one monolayer is then:

$$\frac{v}{Av_0} = \frac{v}{v_m} = \frac{\sum_{i=0}^{\infty} is_i}{\sum_{i=0}^{\infty} s_i} \qquad \text{(A14)}$$

In which v_m is the volume gas in one monolayer.

Assuming that $E_i = E_L$, the heat of liquefaction, for $i \geq 2$, and that $b_i/a_i = g$, a constant, *i.e.* that multilayers of adsorbed material behave like a condensed state, some further simplifications can be made. Let:

$$s_i = cx^i s_0 \qquad \text{(A15)}$$

In which:

$$c = \frac{a_1 g}{b_1} \exp\left(\frac{E_1 - E_L}{RT}\right) \qquad \text{(A16)}$$

$$x = \frac{p}{g} \exp\left(\frac{E_L}{RT}\right) \qquad \text{(A17)}$$

Inserting A15, A16, and A17 into A14 yields:

$$\frac{v}{v_m} = \frac{c s_0 \sum_{i=1}^{\infty} i x^i}{s_0 (1 + c \sum_{i=1}^{\infty} x^i)} \qquad \text{(A18)}$$

The summations in A18 can be solved analytically to yield:

$$\frac{v}{v_m} = \frac{cx}{(1-x)(1-x+cx)} \qquad \text{(A19)}$$

In the case of gas adsorption, in the limit of high gas pressure the surface coverage must tend to infinity, *i.e.* the saturated vapour pressure is reached and any additional material condenses on the surface, thus x is equal to unity, hence more generally $x = p/p_0$, in which is the gas saturation pressure. Inserting this expression for x into A19 yields the BET isotherm model:

$$v = \frac{v_m c p}{(p_0 - p)\left(1 + (c-1)\left(\frac{p}{p_0}\right)\right)} \qquad \text{(A20)}$$

Equation A20 predicts an S-shaped isotherm in which the surface coverage is concave to the pressure axis at low pressure ($p \ll p_0$) but becomes convex to the pressure axis at high pressure ($p \sim p_0$).

This derivation has been reproduced from the original paper "*Adsorption of Gases in Multimolecular Layers*" by Brunauer, Emmett, and Teller.[3]

     Everett Model

The Langmuir and BET models derived in the previous sections were for the adsorption of gases on surfaces, *i.e.* a single adsorbing species. In contrast, adsorption from solution is a two-component system in which solvent and solute molecules compete for adsorption sites.[4] This system can be expressed by the following equilibrium:

$$S_{ads} + A_{sol} \rightleftharpoons S_{sol} + A_{ads} \qquad (A21)$$
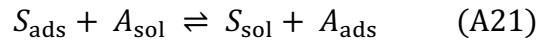
In which S and A denote solvent and adsorbate molecules and the subscripts 'ads' and 'sol' denote adsorbed and solution states respectively.

The equilibrium constant for A21 may be written as follows:

$$K_{ads} = \frac{X_{A_{ads}} X_{S_{sol}}}{X_{A_{sol}} X_{S_{ads}}} \qquad (A22)$$

In which K_{ads} is the equilibrium constant for adsorption and X_i denotes the mole-fraction of species i.

Combining A21 and A22 yields:

$$X_{A_{ads}} = \frac{K_{ads} X_{A_{sol}}}{1 + X_{A_{sol}}(K_{ads}+1)} \qquad (A23)$$

Equation A23 describes the Everett model of adsorption from solution. In the case of a strongly binding adsorbate, *i.e.* $K_{ads} \gg 1$, equation A23 reduces to the following:

$$X_{A_{ads}} = \frac{K_{ads} X_{A_{sol}}}{1 + K_{ads} X_{A_{sol}}} \qquad (A24)$$

Equation A24 has the same form as equation A1 and hence, for a strongly binding adsorbate, Langmuir-like adsorption behaviour is expected. Equation A24 is more commonly cast with concentration as the independent variable and has the following form:

$$\theta = \theta_{\text{MAX}} \frac{K_{\text{ads}}c}{1 + K_{\text{ads}}c} \qquad \text{(A25)}$$

In which c is the solution concentration of solute in equilibrium with the solute adsorbed on the surface.

The value of K_{ads} can give an estimate of the change in Gibbs free energy of adsorption *via* the following fundamental relation from thermodynamics:

$$\Delta G_{\text{ads}} = -RT ln(K_{\text{ads}}) \qquad \text{(A26)}$$

The Gibbs energy of adsorption contains both enthalpic (ΔH_{ads}) and entropic (ΔS_{ads}) terms. For chemisorption, the enthalpy of adsorption (ΔH_{ads}) would be similar to the strength of a typical chemical bond (~200 kJ mol^{-1}). In contrast, the enthalpy change for physisorption would be expected to be an order of magnitude smaller (~20 kJ mol^{-1}).

Solution-Phase BET Model

In their derivation of the gas-phase model of multilayer adsorption, Brunauer, Emmett, and Teller made the critical assumption that the surface coverage tends to infinity as the gas vapour saturates. This reduces the number of fitted parameters in their model (Equation A20) from three to two (v_{m} and c). This assumption, however, does not necessarily hold in the solution phase. In 2009, Ebadi, Mohammadzadeh, and Khudiev published their development of a solution-phase analogue of the BET model in which a third parameter was introduced so that this critical assumption was not required:[5]

$$\theta = \theta_{\text{MONO}} \left(\frac{K_S c}{(1 - K_L c)(1 - K_L c + K_S c)} \right) \qquad \text{(A27)}$$

In which θ is the surface coverage, θ_{MONO} is the monolayer surface coverage, K_S is the adsorbate-surface interaction parameter (c.f. K_{ads}), K_L is the adsorbate-adsorbate interaction parameter (for multilayer interactions), and c is the equilibrium adsorbate concentration. Equation A27 has three fitted parameters - θ_{MONO}, K_S, and K_L – and hence cannot be reduced to a linear form. Nevertheless, Ebadi *et al.* demonstrated that their model produced much better fits for previously published sets of adsorption data than the basic Langmuir model without assumptions about the asymptotic behaviours of the systems or the saturation concentrations of the adsorbates.

Solution Depletion Method

In this work, the adsorption isotherms were determined *via* the solution depletion method. This method is essentially a procedure of mass balance; a known quantity of adsorbent is added to a solution of adsorbate of known concentration and volume and, following equilibration, the reduction in the solution concentration (*i.e.* depletion) is attributed to adsorption on the adsorbent. The method requires a method to determine the equilibrium adsorbate concentration; in this work UV-Vis spectroscopy was used to calibrate the adsorbate concentration because the metal-to-ligand charge transfer (MLCT) of the coordination cages give rise to strong electronic transitions in the visible region. The Beer-Lambert Law was used in these calibrations:

$$A = \varepsilon l c \qquad (A28)$$

In which A is the absorbance of the solution, ε is the extinction coefficient of the species in solution at a given wavelength, l is the pathlength of UV-Vis cuvette, and 'c' is the solute concentration.

This method was chosen because it is experimentally facile but nevertheless can produce meaningful data. Other methods, such as Quartz Crystal Microbalance (QCM),[6] have been successfully utilised in quantifying adsorption but require more specialised equipment.

References

1. Langmuir, I. The Adsorption of Gases on Plane Surfaces of Glass, Mica, and Platinum. *Journal of the American Chemical Society* **40**, 1361–1403 (1918).

2. Atkins, P. W. & de Paula, Julio. *Atkins' Physical Chemistry*. (Oxford University Press, 2014).

3. Brunauer, S., Emmett, P. H. & Teller, E. Adsorption of Gases in Multimolecular Layers. *Journal of the American Chemical Society* **60**, 309–319 (1938).

4. Everett, D. H. Thermodynamics of adsorption from solution. Part 1.—Perfect systems. *Transactions of the Faraday Society* **60**, 1803–1813 (1964).

5. Ebadi, A., Soltan Mohammadzadeh, J. S. & Khudiev, A. What is the correct form of BET isotherm for modeling liquid phase adsorption? *Adsorption* **15**, 65–73 (2009).

6. Kaimaki, D. M. *et al.* Multiscale Approach Linking Self-Aggregation and Surface Interactions of Synthesized Foulants to Fouling Mitigation Strategies. *Energy and Fuels* **33**, 7216–7224 (2019).